Universität zu Köln

Functional characterization of PRC2 dimerization on chromatin and structural analyses of AIFM1 interaction with binding partners MIA40 and AK2

Inaugural-Dissertation

zur

Erlangung des Doktorgrades

der Mathematisch-Naturwissenschaftlichen Fakultät

der Universität zu Köln

vorgelegt von

Egor Alekseevic Pavlenko

geboren in

Kormilowka (Russische Föderation)

angenommen im Jahr 2025

Köln 2024

Berichterstatter

Erstgutachter: Dr. Simon Poepsel

Zweitgutachter: Prof. Dr. Ulrich Baumann

ERKLÄRUNG ZUR DISSERTATION

[redacted]

ACKNOWLEDGEMENTS

I would like to extend my deepest gratitude to my supervisor and mentor, Simon. In Germany, the supervisor of a PhD thesis is referred to as a ‘Doktorvater’, symbolizing the close relationship and pivotal role this person plays in one’s academic journey. In every sense, I have been incredibly fortunate to have Simon as my mentor. He embodies all the qualities one could hope for in such a role: unwavering support for my ambitions, invaluable opportunities for personal and professional growth and a constant challenge to think critically and apply scientific concepts rigorously.
When I joined Simon’s group, my interest was rooted in epigenetics and especially the method of cryo-EM. Relatively early, what started as a 'side project' on PRC2 soon became the central focus of my thesis. Knowing my interests, Simon facilitated a collaboration with AG Riemer, which allowed me to gain hands-on experience with every aspect of cryo-EM. Furthermore, he gave me the opportunity to learn model building under Kelly’s guidance in Cambridge. On that note, I’d like to express my gratitude to Kelly and her group for accepting me to visit her group and personally teaching me the ins and out of this process.
Simon’s support extended beyond academia; when I became a father, Simon went above and beyond to help me balance the demands of my PhD and my family responsibilities. His encouragement was both professional and personal, for which I am profoundly grateful. The 'short’ discussions I had with Simon are legendary within our group. My son even asked me,‘¿Tú hablas con jefe?’ on a regular bases to describe our frequent and intensive conversations. These discussions—about experiments, results, and their implications—were as crucial to my growth as a scientist. Generating and analyzing data, critically evaluating and debating scientific ideas are essential aspects of the scientific endeavor, and Simon fostered an environment where these activities thrived. I am equally grateful to the incredible group of people Simon assembled. Special thanks go to Christian Sommereisen, Linda Zirden, Till Rüngeler, Fabian Basler and our lab technician, Juliane Renn. Juliane and I occasionally butted heads but always found solutions and shared many funny moments. Christian and I not only shared a workspace but also countless inside jokes. Till and I bonded over our mutual frustrations with our proteins, while Linda and I supported each other through challenges, often exchanging valuable scientific and personal advice
I would also like to acknowledge our collaborators, including members of the Nogales Lab—Eva, Trinity, and Paul—as well as Alex and Jan from the Riemer lab and Pascal and Robert from the Hänsel-Hertsch lab in Cologne. I am especially grateful to Paul, a brilliant scientist with whom Simon and I had extensive discussions about the PRC2 project. The challenges of this work are captured in the name we humorously adopted at a Heidelberg conference: ‘The Polycomb Depressive Complex’. Despite these challenges, everyone’s collective perseverance resulted in the publication of one paper, with another under revision at the time of writing this thesis.
I’d also like to thank Prof. Dr. Baumann for serving as the second corrector of my thesis and Prof. Dr. Behrmann and Prof. Dr. Krüger for being members of my thesis advisory committee and providing invaluable input to advance my project.
To my wife, Dr. Susy Prieto Huarcaya: you are the cornerstone of my life. Your positivity, humor, decisiveness, insightfullnes and much more make you the perfect match for my (sometimes) difficult nature. Your perspectives, both scientific and personal, have been invaluable in helping me navigate challenges and progress in my work. I am also grateful for the two beautiful additions to my family. My son, Lucas, has taught me to optimize my time in the lab so I can maximize the moments I spend with him. His joy and the sense of responsibility he instills in me are unmatched. This year, I was blessed to also welcome my daughter, Nadia, whose presence, alongside Lucas, gives me renewed strength to persevere every day.
Ich möchte mich bei meinen Geschwistern und vor allem bei meinen Eltern bedanken. Dank ihnen durfte ich viele prägende Erfahrungen machen, wie beispielsweise die Disziplin und den nötigen Biss, den ich durch den Kampfsport entwickelt habe, oder die Gelassenheit, die ich beim Tauchen erlernt habe. Sie haben stets großen Wert auf meine schulische Ausbildung und persönliche Entwicklung

gelegt und mir während meines Studiums den Rücken freigehalten. Dadurch haben sie mir eine solide akademische Grundlage ermöglicht, ohne die diese Doktorarbeit nicht möglich gewesen wäre.

ABSTRACT

Polycomb Repressive Complex 2 (PRC2) and Apoptosis-Inducing Factor Mitochondrial 1 (AIFM1) are critical regulators of cellular processes, yet aspects of their molecular mechanisms remain incompletely understood. This thesis explores two distinct aspects of these proteins to advance our understanding of epigenetic and mitochondrial regulation.

The first part examines the functional significance of PRC2 automethylation and dimerization on chromatin. PRC2 is an essential epigenetic regulator that catalyzes mono-, di-, and trimethylation of lysine 27 on histone 3 (H3K27me1/me2/me3), with H3K27me3 being crucial for transcriptional silencing, embryonic development and cellular differentiation. The methyltransferase activity required for H3K27me3 deposition depends on allosteric activation through methyl-lysine binding to the regulatory subunit EED. Recent findings suggest that automethylation of the catalytic subunit, enhancer of zeste homolog 2 (EZH2), enhances PRC2 activity, although the mechanism has been unclear. Based on structural insights from cryo-electron microscopy (cryo-EM), a novel mechanism was proposed in which automethylation promotes dimerization of PRC2 on chromatin, thereby targeting the well-known activating mechanism via the regulatory subunit EED. Through a combination of biochemical assays and transcriptomic approaches, this study investigates the role of PRC2 dimerization and automethylation in regulating enzymatic function and the specific mechanism *in vitro* and in a cellular context. This discovery of automethylation-coupled dimerization offers new insights into the regulatory mechanisms of chromatin-modifying complexes, revealing a novel layer of PRC2 activation.

The second part of this thesis explores the structural dynamics of AIFM1, a multifunctional mitochondrial flavoprotein. While AIFM1 is traditionally linked to caspase-independent apoptosis, recent studies highlight its role in the mitochondrial disulfide relay import pathway, where it facilitates protein import and directly interacts with Mitochondrial Intermembrane Space Import and Assembly Protein 40 (MIA40). Additionally, adenylate kinase 2 (AK2), an essential enzyme in adenine nucleotide metabolism and a substrate of the disulfide relay pathway, was identified as an interaction partner of AIFM1. However, the precise mechanisms and functional consequences of these interactions remain to be fully elucidated. Using cryo-EM, this study investigates how interactions of MIA40 and AK2 with AIFM1 influence the conformational state, stability and function. The findings provide insights into the structural basis of these interactions and their implications for mitochondrial function.

Together, these findings provide novel insights into the molecular mechanisms regulating PRC2 and AIFM1, contributing to our understanding of epigenetic regulation and mitochondrial function.

ZUSAMMENFASSUNG

Polycomb Repressive Complex 2 (PRC2) und der Apoptosis-Inducing Factor Mitochondrial 1 (AIFM1) sind zentrale Regulatoren des Chromatins und Mitochondriums. Dennoch sind Aspekte ihrer molekularen Regulation noch nicht ausreichend verstanden.
Der erste Teil der Arbeit untersucht die funktionelle Bedeutung von Automethylierung und Dimerisierung bei PRC2. Dieser Proteinkomplex ist ein epigenetischer Regulator, der die Mono-, Di- und Trimethylierung von Lysin 27 auf Histon 3 (H3K27me1/me2/me3) katalysiert, wobei H3K27me3 eine zentrale Rolle bei der Transkriptionsrepression spielt. Für die Katalyse von H3K27me3 ist eine allosterischen Aktivierung durch die Bindung von methylierten Lysinen an die regulatorische Untereinheit EED nötig. Es wurde gezeigt, dass auch die Automethylierung der katalytischen Untereinheit, Enhancer of Zeste Homolog 2 (EZH2), die PRC2-Aktivität steigert, jedoch blieb der genaue Mechanismus bislang unklar. Auf Basis struktureller Erkenntnisse von Kooperationspartner wurde eine Hypothese für einen Mechanismus aufgestellt, bei dem PRC2 auf Chromatin dimerisiert und den bekannten Aktivierungsmechanismus über die regulatorische Untereinheit EED nutzt. Eine Kombination aus komplexen biochemischen Assays und zellulären Experimenten wird genutzt, um die Dimerisierung und Automethylierung von PRC2 *in vitro* und in einem zellulären Kontext zu charakterisieren.
Der zweite Teil der Arbeit untersucht die Struktur von AIFM1, einem mitochondrialen Flavoprotein. Klassisch, wird AIFM1 mit der caspase-unabhängigen Apoptose in Verbindung gebracht. Allerding wurde gezeigt, dass AIFM1 eine wichtige Rolle bei dem Proteinimport von der Protein-Disulfid-Isomerase Mitochondrial Intermembrane Space Import and Assembly Protein 40 (MIA40) spielt und diese auch in einem stabilen Komplex bindet. Zudem wurde Adenylatkinase 2 (AK2), ein Enzym des Adeninnukleotidstoffwechsels, von Kooperationspartnern als weiterer Bindungspartner von AIFM1 identifiziert. Die genauen Mechanismen und funktionellen Konsequenzen dieser Interaktionen, die diese Bindungen auf das Enzym haben, sind jedoch noch weitgehend ungeklärt. In dieser Arbeit wird die Struktur von MIA40 und AK2 gebundenen AIFM1 untersucht. Die Ergebnisse liefern Einblicke in die strukturelle Basis dieser Interaktionen und deren Bedeutung für AIFM1.
Zusammenfassend liefern die in dieser Arbeit gewonnenen Erkenntnisse neue Einblicke in die molekularen Mechanismen von PRC2 und AIFM1.

2. TABLE OF CONTENTS

3. LIST OF FIGURES

4. LIST OF TABLES

5. ABBREVIATIONS

A

aa: Amino acid

AEB2: Adipocyte Enhancer-Binding Protein 2

AIFM1: Apoptosis-inducing factor mitochondrial 1

AK2: Adenylate kinase 2

AMP/ADP/ATP: Adenosine mono-/di-/triphosphate

APS: Ammonium persulfate

B

bME: β-Mercaptoethanol

bp: Base pair

C

CBB: Coomassiebrilliant blue

CI/CII/C/III/CIV/CV: Complex I/II/III/IV/V of the mitochondrial electron transport chain

Cryo-EM: Cryogenic electron microscopy

CTC: charge–transfer complex

CTF: Contrast transfer function

Cyt C: Cytochrome c (Cyt c)

D

DBS: DNA binding site

ddH2O: Double-distilled water

DEG: Differentially expressed genes

DNA: Deoxyribonucleic acid

DTT: Dithiothreitol

E

EBD: EED-binding domain

EDTA: Ethylenediaminetetraacetic acid

EED: Embryonic ectoderm development

EMSA: Electrophoretic Mobility Shift Assay

EPOP: Elongin BC and PRC2 associated protein

ETC: Electron transport chain

EZH2: Enhancer of Zeste Homolog 2

F

FBS: Fetal bovine serum

FRET: Förster resonance energy transfer

G

GFP: Green fluorescent protein

GSEA: Gene set enrichment analysis

N

NAD: Nicotinamide adenine dinucleotide

Nanog: Nanog homeobox

Nes: Nestin

NLS: Nuclear localization signal

NLS: Nuclear localization signal

O

OM: Outer membrane

P

PAGE: Polyacrylamide gel electrophoresis

PAL: PRC2 associated LCOR isoform

Pax6: Paired box 6

PBS: Phosphate-buffered saline

PcG: Polycomb group

PCL: Polycomb-like proteins

PCL: Polycomb-like proteins

PCR: Polymerase chain reaction

PHD1: PHD finger protein 1

PIC: Protease inhibitor cocktail

POU5F1: POU domain, class 5, transcription factor 1

PRC: Polycomb repressive complex

PRE: Polycomb response elements

PTM: Post-translational modifications

R

RB: Retinoblastoma protein

RBBP: Retinoblastoma Binding Protein 4

RMSD: root mean square deviation

RNA: Ribonucleic acid

S

SAH: S-adenosylhomocysteine

SAL: SET activation loop

SAM: S-Adenosyl-L-methionine

SBD: SANT1 binding domain

SDS: Sodium dodecyl sulfate

SEC: Size-exclusion chromatography

SET: Su(var)3–9, Enhancer-of-zeste and Trithorax

SOX2: SRY (sex determining region Y)-box 2

SRM: Stimulation response motif

SUZ12: Suppressor of Zeste 12

H

H2AK119Ub: Histone H2A lysine 119

H3K27: Histone H3 lysine 27

H3K36: Histone H3 lysine 36

H3K4: Histone H3 lysine 4

HAT: Histone acetyltransferase

HDAC: Histone deacetylase

HMT: Histone methyl transferase

I

IM: Inner membrane

IMS: Intermembrane space

J

JARID2: Jumonji, and AT-rich interaction domain 2

K

KDM: Lysine demethylase

L

LB: Lysogeny broth

M

MESC: Mouse cmbryonic stem cells

MIA40: Mitochondrial intermembrane space import and assembly protein 40

MIM: Mitochondrial inner membrane

MLS: Mitochondrial targeting sequences

MTF2: Metal regulatory transcription factor 2

MW: molecular weight

T

TBS: Tris-buffered Saline

TCA: Tricarboxylic acid

TIM: Translocase of the inner membrane

TOM: Translocase of the outer membrane

TrxG: Trithorax group

Tubb3: tubulin beta-3 chain

U

UV: Ultraviolet

W

WT: Wild-type

Y

YFP: Yellow fluorescent protein

Tubb3: tubulin beta-3 chain

Table 1:Names of the canonical amino acids and their one letter code

Name	Single Letter Code
Alanine	A
Arginine	R
Asparagine	N
Aspartic Acid	D
Cysteine	C
Glutamic Acid	E
Glutamine	Q
Glycine	G
Histidine	H
Isoleucine	I
Leucine	L
Lysine	K
Methionine	M
Phenylalanine	F
Proline	P
Serine	S
Threonine	T
Tryptophan	W
Tyrosine	Y
Valine	V

6. INTRODUCTION

CHAPTER I: FUNCTIONAL CHARACTERIZATION OF PRC2 DIMERIZATION ON CHROMATIN

6.1. Chromatin: A condensed story of epigenetic regulation

6.1.1. Epigenetics: Breaking a dogma

In multicellular organisms, all cells share the same genetic information. However, cells exhibit changes in their cellular states during development and differentiation leading to diverse phenotypes and functions. These dynamic events result from coordinated transcriptional regulation, controlled by diverse signals directing gene expression.
Traditionally, the dogma of biology states that genetic information is stored as deoxyribonucleic acid (DNA). DNA is transcribed to messenger ribonucleic acid (mRNA) molecules, the sequence of which is then translated into proteins.[1] The term 'epigenetics', first introduced by Waddington in the 1940s, refers to mechanisms that operate beyond 'traditional' genetics, such as DNA methylation or histone modification. The epigenetic field is rapidly evolving, expanding our understanding of gene regulation beyond the confines of the DNA sequence.[2, 3]
Genomic DNA comprises ~ 6 billion bases in humans and needs to be condensed roughly 10,000 times to reside within the limited space of the nucleus in eukaryotic cells.[4] This is achieved by forming a complex system of genomic DNA, proteins and non-coding RNA, called chromatin. The dynamic structure of chromatin allows it to respond to environmental influences, thus shaping cellular behaviour, development, and physiological responses. Understanding how these epigenetic modifications operate can uncover the molecular basis of complex cellular mechanisms and diseases, thus paving the way for innovative therapeutic strategies. For example, the compaction of DNA on multiple level is required to fit inside the nucleus but at the same time still has to be accessible for the transcription machinery.[5, 6] Therefore, studying epigenetics down to the molecular level deepens our understanding of precise mechanism governing biological function.

6.1.2. Nucleosomes: The building block of chromatin

To understand chromatin organization, it is important to understand the structure of chromatin and its components. In the 1950s, the structure of the 'naked' DNA was solved using X-ray crystallography. A series of studies revealed that the DNA is composed of four bases (adenine, thymine, cytosine, and guanine) that form a double-stranded molecule organized into a double helix.[7-9] However, the subsequent higher-order organization of chromatin took another 20 years to be understood.[10] Electron microscopic studies – which gave us the iconic 'beads on a string' images (Figure 1, left)[11, 12] – in combination with nuclease digestion experiments [4, 13] revealed a repetitive structural unit of DNA wrapped around a histone core, named the nucleosome.[10, 14]

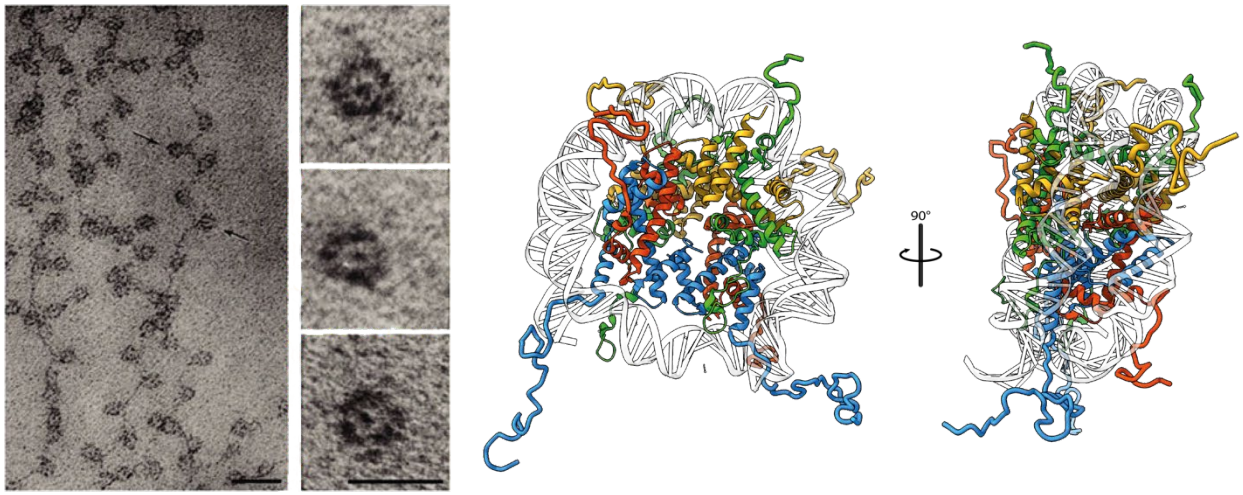

Figure 1: Beads on a string chromatin and nucleosome structure

Left: *Electron microscopic image of chromatin. It shows the chromatin organization of nucleosomes and DNA in the 'beads on string' model. (Olins et al. [10]).* ***Right:*** *Nucleosome structure (PDB:1KX5) obtained by X-ray crystallography. It shows the four canonical histones wrapped around by 145 bp of DNA. The histone tails are extruding from the octamer core. (Green: H2A; Yellow: H2B; Blue: H3; Red:H4)*

The nucleosome is formed by 145-147 base pairs (bp) of DNA that are wrapped in 1.67 left-handed superhelical turns around an octameric histone core consisting of four canonical histones; H2A, H2B, H3, and H4 (Figure 1: right).[15, 16] These histones are small, basic proteins (11-15 kDa), which are highly conserved in eukaryotes. Their structure comprises a globular C-terminal domain and an unstructured basic N-terminal region, the so-called histone tails that protrude from the core.[17] The C-terminal domain of all four canonical histones mainly consists of a 'histone fold' motif, which is comprised of two short α-helices α1 and α3 (9-14aa) that flank a longer central α-helix α2 (~ 29aa) connected by short loops.[15] The histones associate via these four helix bundles, whereas H2A-H2B and H3-H4 respectively form a stable dimer. The H3-H4 dimer further self-associates via an H3:H3 interface into a tetramer. Thus, one H2A-H2B dimer assembles on either side of the tetramer with an H2B:H4 interface.[15, 18-20] This assembly exposes multiple DNA binding sites that bend and position the DNA around the histone octamer via interactions with the phosphate backbone.[16, 21] Several nucleosomes are connected by 10-50 bp of exposed linker DNA and can be compacted and spatially organized via the linker histone H1.[14, 22]

As the carrier of genetic information, DNA is targeted by transcription factors and enzymes for proper gene expression. However, chromatin and its histones form an additional layer of gene regulation (Figure 2). Histone variants, the higher-order chromatin structure, and especially the histone tails, which are targets for various post-translational modifications (PTMs), modulate epigenetic signalling.[17, 23-25]

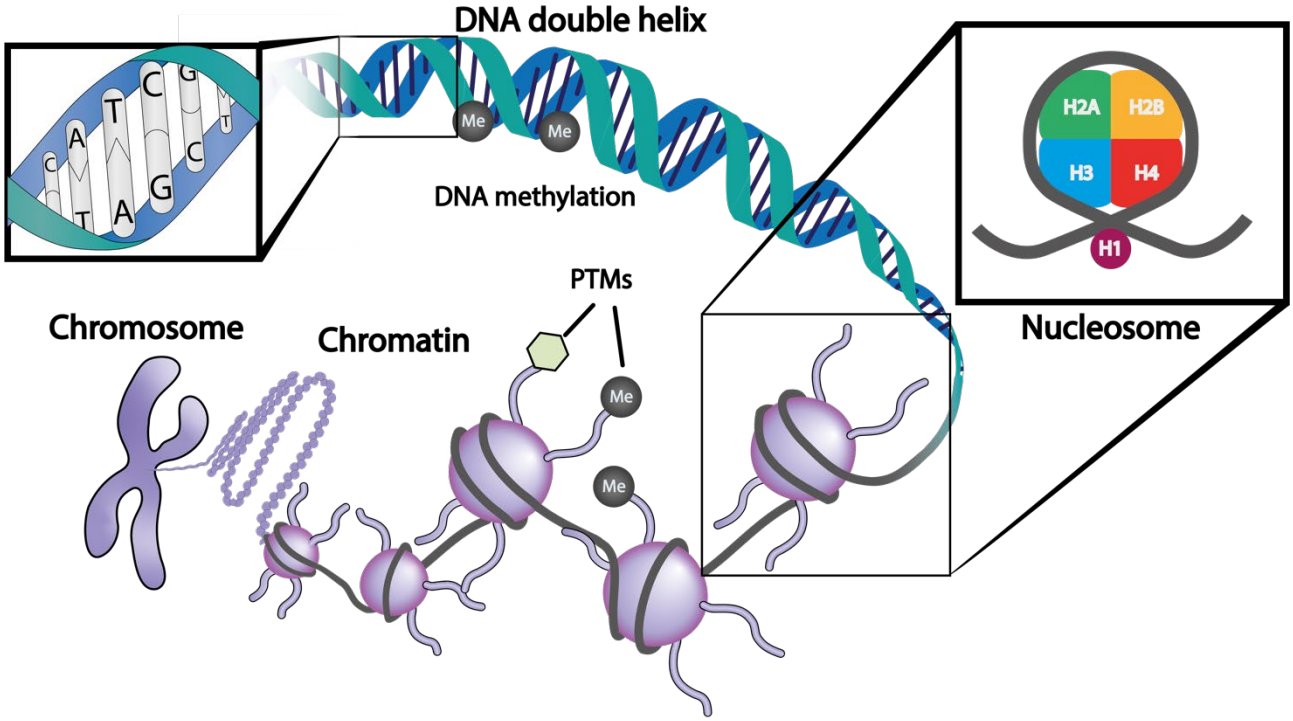

Figure 2: Schematic illustration of chromatin organization

DNA is the basic layer of genetic information. It is a double-stranded molecule formed by adenine, thymine, cytosine and guanine, and organized in a double helix. The DNA is wrapped around histone octamers to form nucleosomes, which are connected by 'linker' DNA. Most nucleosomes contain two copies of the four histones H2A, H2B, H3, and H4 and are further organized by the linker histone H1. Nucleosomes are further organized into chromatin, which undergoes higher-order folding and compaction. The highest level of this hierarchical organization results in the formation of chromosomes. PTMs on histone tails (acetylation, ubiquitination, methylation, and phosphorylation and others) as well as DNA methylation contribute to the regulation of chromatin structure and thus gene expression.

6.1.3. Post-translation modifications: Deciphering the histone code

Extensive studies have shown that histone modifications influence histone-histone and histone-DNA interactions, thus affecting the overall chromatin structure.[26-28] Histone post-translational modifications (PTMs) are chemical alterations on histone proteins – the addition of chemical groups such as acetyl- [29, 30], methyl[31, 32], phosphoryl [33, 34], ubiquitin[35], and other groups – to specific amino acid side chains predominantly located on the histone tails.[36] Multiple residues on the different histone tails can be modified with different PTMs, providing a high degree of combinatorial potential and diversity. Moreover, distinct modification patterns exist, resulting in biological specificity and recognition by specific proteins and protein activities.[37-41] The complex information that histones and their PTMs carry is also referred to as the 'histone code'.[17, 36]

PTMs can promote gene activation by relaxing the chromatin ("euchromatin") or to gene repression by compacting chromatin ("heterochromatin") through the recruitement of effector proteins that recognize specific modifications.[42] This proteins can affect pre-existing modifications by guiding the deposition of new PTMs on the same or neighbouring histone tails or by inducing nucleosome repositioning. Thus, PTMs act as a regulatory code essential to fine-tune gene expression patterns, maintain genome stability, and orchestrate cellular processes during development and in response to environmental cues.[17, 43] The importance of PTMs underscores the necessity for precise regulation, which is maintained by a network of pathways involving enzymes that recognize ("readers"), deposit ("writers"), or remove histone PTMs ("erasers").[43, 44]

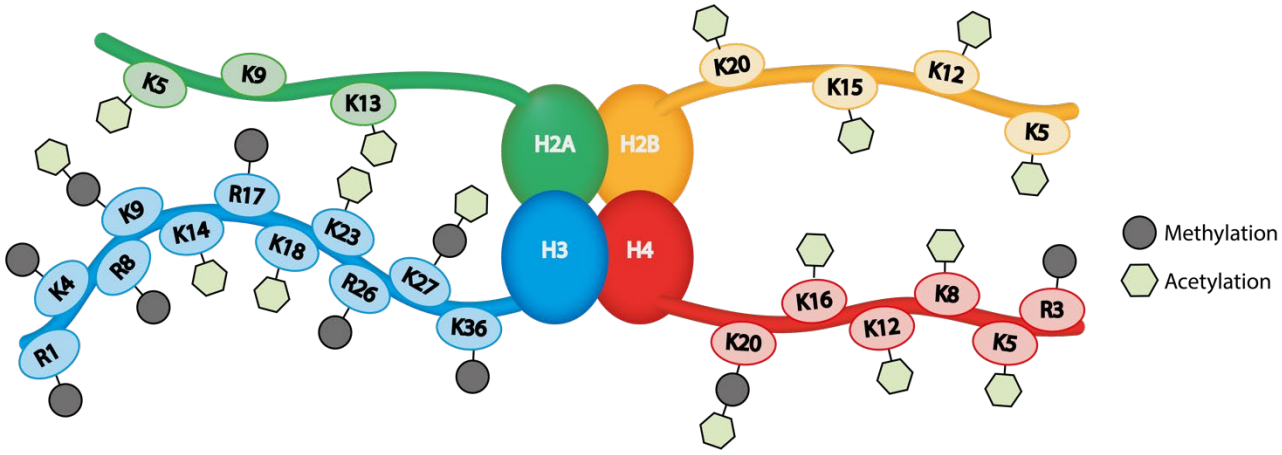

Figure 3: Simplified depiction of histone residues targeted for methylation and acetylation

Histone tails undergo various post-translational modifications, recognized by epigenetic and transcriptional regulators. The figure shows residues of the four canonical histones—H2A, H2B, H3, and H4—that can be acetylated (hexagon) or methylated (circle). (Derived from Turner [45] and Ramazi et al.[46])

6.1.4. Epigenetic regulators: Writer, readers and erasers

Either individually or in combination, each PTM plays a unique role in cellular function. To explore mechanisms that control epigenetic regulation, this chapter will focus on two of the most common and well-studied histone modifications: acetylation and methylation. (Figure 3).[32]

Acetylation mainly occurs on lysines of H3 and H4, neutralizing the positive charge of the respective residue and thus potentially affecting the affinity between DNA and histones, favoring a less dense, decompacted chromatin structure, associated with transcriptional activation.[47-49] Accordingly, this PTM is prevalent at active enhancers and promoters.[49] The deposition of a new acetyl group is catalyzed by histone acetyltransferases (HATs), and removed by histone deacetylases (HDACs), which ultimately favors chromatin condensation and transcriptional repression.[50] Acetylated lysine can be recognized by proteins with bromodomains, which can mediate chromatin remodeling and transcriptional activation.[51-55]

In contrast, histone methylation can occur on lysines or arginines and is mediated by histone methyltransferases (HMTases), including histone lysine methyltransferases and protein/histone arginine methyltransferases.[56, 57] Methylated lysines can be recognized by chromodomains. Depending on the specific amino acid residue, and the number of methyl groups added (mono-, di-, or trimethylation), specific enzymes can facilitate either gene activation or repression.[58-60] This dynamic PTM can also be removed by histone lysine demethylases (KDMs).[61, 62]

The epigenetic regulators can exert different effects on gene expression depending on the location of PTMs within the gene and the surrounding chromatin context. For instance, trimethylation of lysine 39 on histone 3 (H3K36me3) represses transcription when located on a gene promoter but activates it when located within the gene body.[60, 63] Similarly, di- or trimethylation of lysine 4 on histone H3 (H3K4me2/3) is enriched in actively transcribed promoters.[64, 65] Conversely, trimethylation of lysine 9 (H3K9me3) or lysine 27 on histone 3 (H3K27me3) is associated with two types of repressed chromatin domains and gene silencing.[66, 67] On one hand, H3K9me3 is considered a mark of constitutive heterochromatin, leading to irreversible gene silencing, [68, 69] while H3K27me3 is associated with facultative heterochromatin and reversible silencing of cell-lineage-specific genes.[70, 71]

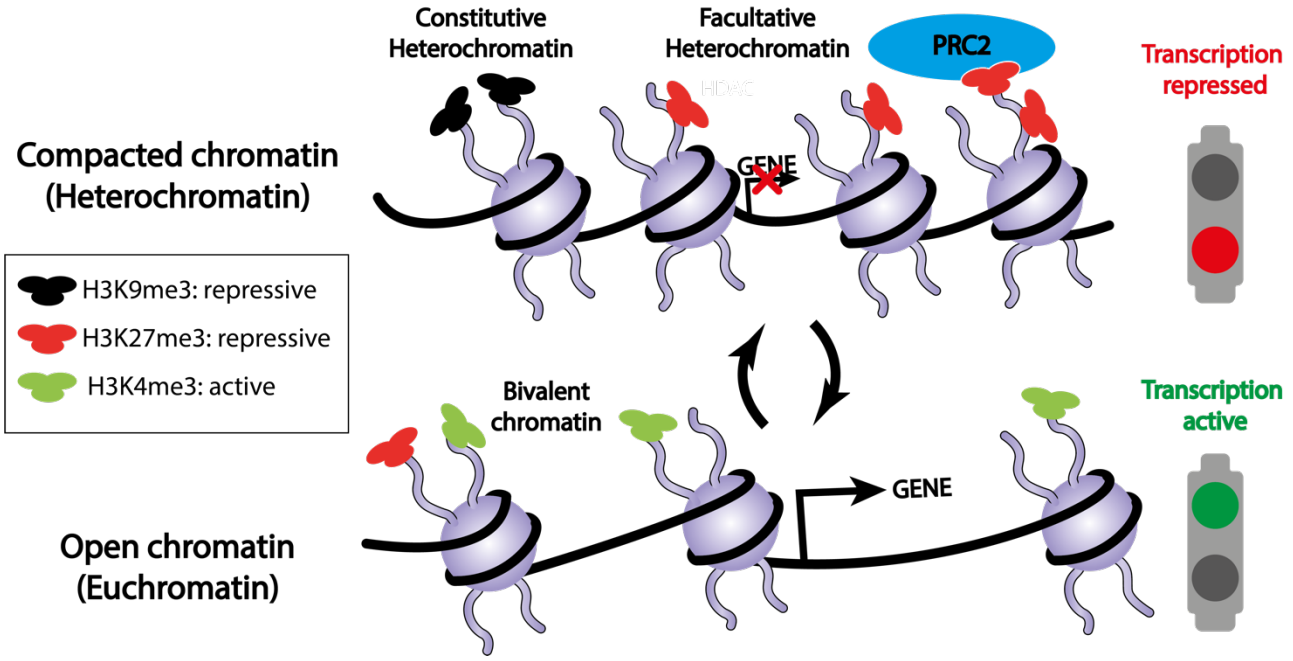

Figure 4: Exemplary effects of methylation on chromatin organization

Top left: *H3K9me3 is a hallmark of constitutive heterochromatin, associated with irreversible gene silencing.* ***Top right:*** *H3K27me3 is a mark of facultative heterochromatin. An epigenetic regulator that reads H3K27me3 and catalyzes H3K27 methylation is PRC2. Specific histone demethylases can remove this repressive mark.* ***Bottom left:*** *The active H3K4me3 and repressive H3K27me3 marks can coexist at the same locus, known as bivalent chromatin. Depending on environmental stimuli, this chromatin state is poised for either transcriptional activation or repression.* ***Bottom right:*** *H3K4me3 is a PTM associated with active transcription.*

The repressive PTMs H3K9me3 and H3K27me3 contribute to gene silencing through different mechanisms. H3K9me3 is recognized by Heterochromatin Protein 1 (HP1), which oligomerizes and interacts with other repressive marks, compacting and spreading the heterochromatin.[32, 72] While the mechanism by which H3K27me3 functions is not entirely understood, studies suggest that H3K27me3 is a target for recruiting additional proteins, that facilitate silencing.[70, 73] Intriguingly, the repressive H3K27me3 can coexist with the activating H3K4me3 mark at the same locus.[74, 75] Genes within this so-called bivalent chromatin exhibit low transcription in stem cells but are either strongly silenced or expressed upon differentiation, indicating that these genes are poised for either repression or activation, ready to respond rapidly to instructive stimuli.[75] This complex interplay underscores the importance of precise enzymatic regulation of epigenetic modifications.

6.2. PRC2: A very complex complex

6.2.1. Polycomb: A historical perspective of the masterminds shaping cell fate

Historically, the term 'Polycomb' refers to the phenotype caused by mutations identified in the mid-20th century in the model organism *Drosophila melanogaster*.[76, 77] During embryonal development, the dynamics of gene activation and silencing leads to the differential expression of homeotic (HOX) genes responsible for the anterior-posterior segmentation of the *Drosophila* body. The Polycomb (Pc) phenotype affects the correct anterior-posterior segmentation.[76] Subsequent genetic analyses identified additional genes that resulted in a phenotype similar to Pc, revealing their role as general repressors of HOX genes. These genes were collectively termed the Polycomb group (PcG) genes and proteins.[78-80]
Later, another set of genes was discovered to antagonize PcG gene function and named Trithorax group (TrxG) genes according to the phenotype cause by mutating them.[79, 81-83] The proteins encoded by both sets of genes, were found to target the same genes, with TrxG proteins activating them and PcG proteins silencing them.[84] Only much later, TrxG and PcG proteins were shown to function as epigenetic regulators by catalyzing histone modifications with antagonistic functions.[80, 85-87] TrxGs primarily methylate H3K4, whereas PcGs mainly methylated H3K27 or ubiquitinate lysine 119 on histone H2A (H2AK119ub).[80] Both protein groups are critical for the ‘cellular’ or ‘transcriptional memory’ that maintains a transcriptional state of cells stably and heritably across cell divisions, which is essential for development, cellular differentiation and maintaining cellular identity.[88, 89]
The characterization of PcG proteins from *Drosophila* revealed their assembly into two main multi-protein complexes: Polycomb repressive complex 1 (PRC1) and PRC2.[66, 90] This classification has since been extended to include the Polycomb repressive deubiquitinase (PR DUB) and the DNA-binding Pho repressive complex (PhoRC).[91-93] Focusing on the two main complexes, PRC1 ubiquitinates lysine 118 on histone H2A (H2AK118ub) or H2AK119 in mammals,[94, 95] whereas PRC2 methylates H3K27 to all three methylation states.[96, 97] Both complexes work synergistically to establish and propagate heterochromatin. For instance, they play a critical role in processes such as X chromosome inactivation in females.[98-101]
PcG genes are also essential for early developmental processes, including cellular differentiation, pluripotency, and maintenance of cell type identity.[97, 102] Their importance in critical developmental events is underlined by their frequent mutation in cancer. Dysregulation of these genes leads to a variety of diseases, affects tumour immunity, and can result in embryonic lethality.[65, 103]

6.2.2. Polycomb repressive complex 2 (PRC2): A complex protein complex

PRC2 is an HMTase complex that catalyzes the transfer of methyl groups from S-Adenosyl-L-methionine (SAM) to H3K27, resulting in its mono-, di- and trimethylation (H3K27me1/2/3) and S-adenosylhomocysteine (SAH) (Figure 5:left).[66, 90, 104, 105] H3K27me2 is the most prevalent of the three methylation states, accounting for approximately 50-70% of H3K27 methylation, and is predominantly found in intergenic regions. In contrast, H3K27me1 and H3K27me3 have a prevalence of approximately 5%, in bodies of actively transcribed genes, and 5-10% respectively.[106-109] Functionally, the different methylation states fulfil different roles. Most studies focus on H3K27me3 because it is an important hallmark of facultative heterochromatin. H3K27me2 was proposed to block H3K27 by preventing acetylation and thus hindering aberrant transcriptional activation,[106, 110] whereas H3K27me1 in humans is directly linked to active genes.[111-113] However, the exact functional significance and specificity of each methylation state of H3K27 and the mechanism of differential deposition in the genome are not completely understood.[73]

The core complex composition of PRC2 is highly conserved and consists of the minimal protein subunits required for catalytic activity: Enhancer of Zeste Homolog 2 (EZH2) or its less active ortholog EZH1, Embryonic Ectoderm Development (EED) and Suppressor of Zeste 12 (SUZ12) (Figure 5:left). [66, 86, 104, 105, 114, 115] The knockout of either of these subunits results in the previously described Pc phenotype in *Drosophila* [116, 117] and non-viable mice, emphasizing the important role of PRC2.[118-120]

Due to the stabilizing effect of histone tail binding, the core complex was expanded with the Retinoblastoma Binding Protein 4 or 7 (RBBP4/RBBP7; formerly Retinoblastoma-binding protein p46/48, RBAP46/48).[86, 121] Additional subunits have been identified that modulate PRC2 function, including Adipocyte Enhancer-Binding Protein 2 (AEBP2), Jumonji, and AT-Rich Interaction Domain 2 (JARID2).[122, 123]

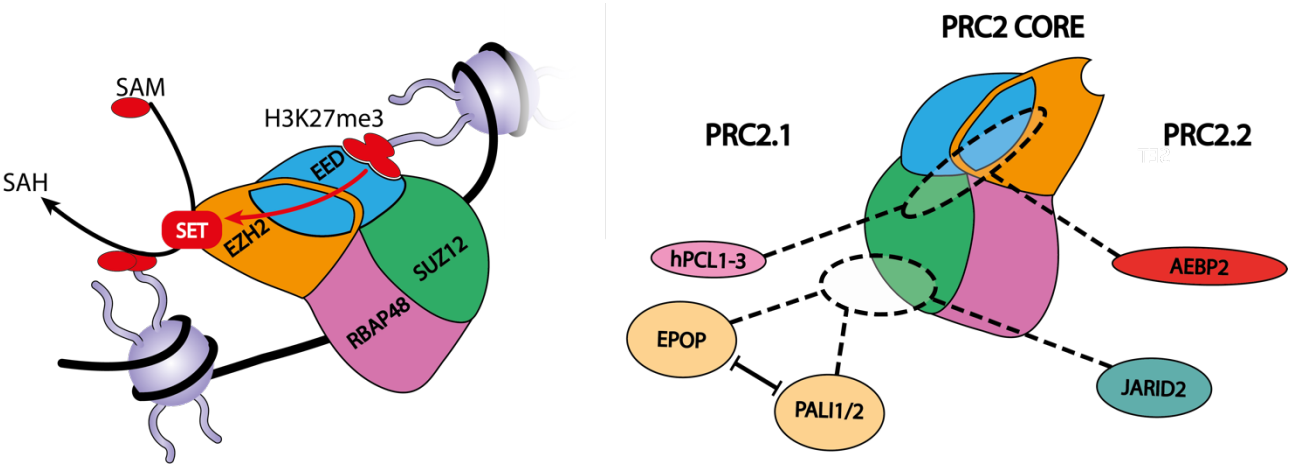

Figure 5: Schematic representation of PRC2 reaction and PRC2 subcomplexes

Left**: Schematic organisation of the core subunits of PRC2 and its engagement with the nucleosome substrate. The EZH2 subunit with its catalytic SET domain facilitates H3K27 methylation with SAM as a methyl donor. The product H3K27me3 is also an allosteric activator (red arrow) of PRC2, binding EED.* ***Right: Accessory subunits of PRC2.1 and PRC2.2 (*adapted from Healy et al*[124])

The catalytic subunit, EZH2, contains a Su(var)3–9, Enhancer-of-zeste and Trithorax (SET) domain, which is folded into a β-sheet rich structure with a catalytic tyrosine at the center.[125] In contrast to other homologues, the isolated SET domain of EZH1/2 is in an autoinhibitory state and requires activation from other PRC2 subunits.[86, 126, 127] While SUZ12 has no catalytic function, it is an integral structural part of PRC2 that holds all core subunits, as well as additional subunits together.[128-130] EED, which is key for EZH2 activation recognizes its catalytic product H3K27me3 as an allosteric activator, which is an essential mechanism for local spreading of this repressive mark.[131, 132]

The PRC2 core complex is essential for the establishment and maintenance of H3K27me3 marks, with the functional interplay between its subunits being crucial for enzymatic activity. Additional subunits that associate with the core PRC2 further refine its functionality, resulting in the formation of distinct subcomplexes with unique roles. The binding of accessory proteins to the core complex gives rise to two major PRC2 variants: PRC2.1 and PRC2.2 (Figure 5: right).). PRC2.1 is comprised of the core, supplemented by one of the Polycomb-like proteins (PCL) PHD finger protein 1 **(**PHF1;hPCL1), Metal regulatory transcription factor 2 (MTF 2; hPCL2) or PHF19 (hPCL3) (homologues to Pcl1-3 in *Drosophila*), as well as Elongin BC and PRC2 Associated Protein (EPOP) or PRC2 associated LCOR isoform 1/2 (PALI1/2).[124, 133, 134] PRC2.2 comprises AEBP2 and JARID2 as accessory proteins. The two complexes are mutually exclusive in their composition: AEBP2 is incompatible with hPCLs, and JARID2 with EPOP/PALI binding. [135-141] These cofactors bind mostly to the N-terminal region of SUZ12 and RBAP48.[130, 137, 142]
Functionally, the accessory subunits of the two PRC2 variants affect the enzymatic activity and recruitment to chromatin.[134] Through a wing-helix domain of the PCLs PRC2 gets recruited to unmethylated GC-rich DNA sequences.[133] EPOP and PALI1/2 have, so far, only been identified as components of PRC2.1 with their functional impact remaining elusive. It is hypothesized that PALI1/2 might stimulate PRC2 activity[138] and that EPOP forms a competing Elongin BC complex that impedes PRC2 binding.[96, 140]
In contrast to PRC2.1, the roles of the accessory subunits of PRC2.2 is well understood. AEBP2 and JARID2 form a stable, stoichiometric complex with the core PRC2.[128, 143, 144] AEBP2 is a zinc-finger protein that stimulates PRC2 activity and stabilizes the complex structurally.[86, 128, 129, 145, 146] JARID2 contains a catalytically inactive Jumonji C (JmjC) histone demethylase domain, an ARID domain, as well as a zinc-finger that can interact with nucleosome DNA and help facilitate PRC2 binding to the chromatin.[123, 147] Furthermore, lysine 116 of JARID2 is a substrate of PRC2, which strongly stimulates its enzymatic activity.[148, 149] The role of accessory subunits underscores the complexity of PRC2 regulation, which extends beyond simple complex composition and involves dynamic interactions with chromatin and other regulatory factors.

6.2.3. PRC2 regulation

As important as understanding the composition of PRC2 is, it is just as crucial to understand its recruitment to specific genomic loci and the effect of its chromatin environment. In *Drosophila* both PRC1 and PRC2 target specific DNA binding sites, so-called Polycomb response elements (PREs).[150, 151] The insertion of PREs in a transgenic construct and integration into the the genome causes spreading of H3K27me3 in proximity to these insertions. Removal of PREs, on the other hand, resulted in the Pc phenotype and dilution of H3K27me3, indicating that PREs are sufficient for PRC recruitment.[152-155] In mammals, the mechanism of PRC2 recruitment is less understood due to the absence of PRE equivalents. While some transcription factors have been reported to interact with PRC2, their contribution to recruitment appears context-dependent[156-158]
Instead, PRC2 is was shown to get recruited by CpG-rich, unmethylated DNA.[133, 159-164] Both the PRC2 core complex and its accessory subunits interact with exposed DNA, emphasizing the multifaceted nature of its DNA interaction.[73, 159, 165] Particularly, cis-regulatory binding elements of the accessory subunits PCLs were uggested to include recognition of specific DNA shape.[133, 160]
Recent studies reveal that RNA interacts with PRC2, sparking hypotheses regarding its regulatory role. Both EZH2 and SUZ12 bind a wide range of RNA, raising questions about their functional relevance in PRC2 recruitment.[134, 166-168] On one hand, noncoding RNA was show to guide PRC2 to specific loci or prevent chromatin binding.[169-172] On the other, RNA interactions can inhibit PRC2's catalytic activity.[173, 174] However, studies showed that regions interacting with RNA are important for catalytic activity, rather than the RNA-binding itself. This function operates independently of RNA leaving its regulatory role unclear.[175]

Further, since both PRC1 and PRC2 were shown to have overlapping binding patterns, a complementary function was suggested. (See: Polycomb: A historical perspective of the masterminds shaping cell fate).[85] . Multiple studies indicate a reciprocal relationship between the two complexes. Initially, canonical PRC1 was thought to recognize H3K27me3 via its chromodomains.[176, 177] In this hierarchical model PRC1 actvity was assumed downstream from PRC2.[178] However, deletion of PRC2 subunits in mouse embryonic stem cells (mESCs) reduced but did not eliminate PRC1 binding at target loci and had minimal impact on H2AK119ub deposition.[179] This suggested far less dependency of PRC1 on PRC2 actvitiy. Instead, PRC1 was shown to promote PRC2 recruitment through H2AK119ub deposition.[180] AEBP2 and particularly JARID2 of PRC2.2 recognize this PTM and direct the complex to target loci.[181, 182] Furthermore, the core subunit EED interacts directly with PRC1 indicating more functional overlaps between PRC1 and PRC2.[183]
One crucial aspect of PRC2 regulation is the interaction with histone PTMs. PRC2 activity is regulated in a feed-forward like manner, where its catalytic product H3K27me3 enhances the activity of PRC2. H3K27me3 binds the allosteric site within EED, resulting in a significantly increased catalytic activity.[131, 184] This positive feedback loop allows for the spreading of H3K27me3 and gene silencing. One example of this mechanism is the re-establishment of this repressive mark into newly synthesized chromatin during S-phase. A similar mechanism of trimethyl-lysine mediated activation was shown for the trimethylated lysine 116 of JARID2.[148] In addition to H3K27, PRC2 automethylates its subunits SUZ12 and EZH2.[66, 165] The automethylation of three lysines on EZH2 results in an increase of enzymatic activity in a yet unknown manner. [185, 186] *In-vitro* PRC2 exhibits higher activity in oligonucleosomes compared to mononucleosomes.[187-189] PTMs associated with transcriptional activation, however, (H3K4me3, H3K36me) were shown to reduce PRC2 activity.[121, 131, 184, 190]

Given the complexity and intricate regulation of PRC2, further exploration into its recruitment mechanisms, interaction with PTMs, and function holds the promise of uncovering new layers of epigenetic regulation.

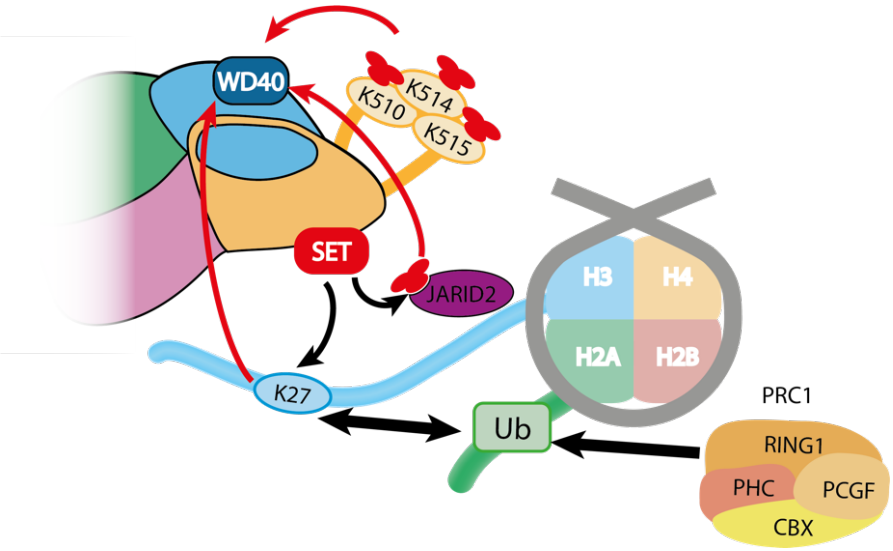

Figure 6:Mechanisms regulating PRC2 activtiy

PRC2 trimethylates H3K27 or JARID2 K116. (Black arrows). These trimethylated peptides target the aromatic cage within EED (Red arrows) and allosterically increase the activity of EZH2. Furthermore, PRC2 methylates three reisdues, K510, K514 and K515 on EZH2, which also increase activtiy in an unknown mechanism. PRC2 and PRC1 work synergistically to efficently spread heterochromatin.

6.2.4. PRC2 structure

Early structural studies of PRC2 subunits

PRC2 function is dictated by the regulation of its HMTase activity and its recruitment to chromatin. Understanding the architecture and interactions of the PRC2 core with its cofactors and chromatin is vital for unravelling the mechanisms of its chromatin-modifying function. Early studies laid the groundwork of our understanding of PRC2 function and regulation by investigating the structural properties of PRC2 subunits and their interactions.

EED has a ß-propeller structure consisting of seven WD40 repeats. A short helical region of EZH2, termed EED-binding domain (EBD) is bound by a binding groove on one face of the WD40 domain (Figure 7A).[191] Subsequent studies underscored the importance of EED in regulating PRC2 activity. Repressive marks (H3K9me3, H3K27me3) are bound by an aromatic cage (F97, Y148, Y365 and W364) at the center of the ß-propeller (Figure 7B). The residues at the −1 and +1 positions of the methyl-lysine are oriented away from EED, while those at the −2 and +2 positions form crucial interactions with two hydrophobic binding pockets. One pocket, which includes W364, Y308, and C324 and the other, consisting of I363, A412, and Q382, play a key role in guiding the specificity of methyl-lysine binding.[131] Furthermore, the residue in -4, -3 and particularly -1 were shown to be important for stimulating PRC2 activity but not bidning EED.[131, 149] This mechanism of trimethyl recognition on one hand, and binding the catalytic subunit EZH2 on the other hand pointed at a mechanism of allosteric activation of PRC2 by its enzymatic product.[131] RBBP4/RBBP7, like EED, also primarily consist of WD40 repeats and recognizes the N-terminus of unmodified H3. Additionally, it forms hydrophobic interactions on the side of the propeller with SUZ12.[121] SUZ12 harbours the C-terminal SUZ12^{VEFS} domain and Cys_2-His_2 zinc finger which are crucial for the structural integrity of PRC2, as its deletion impedes complex formation.[66, 90]

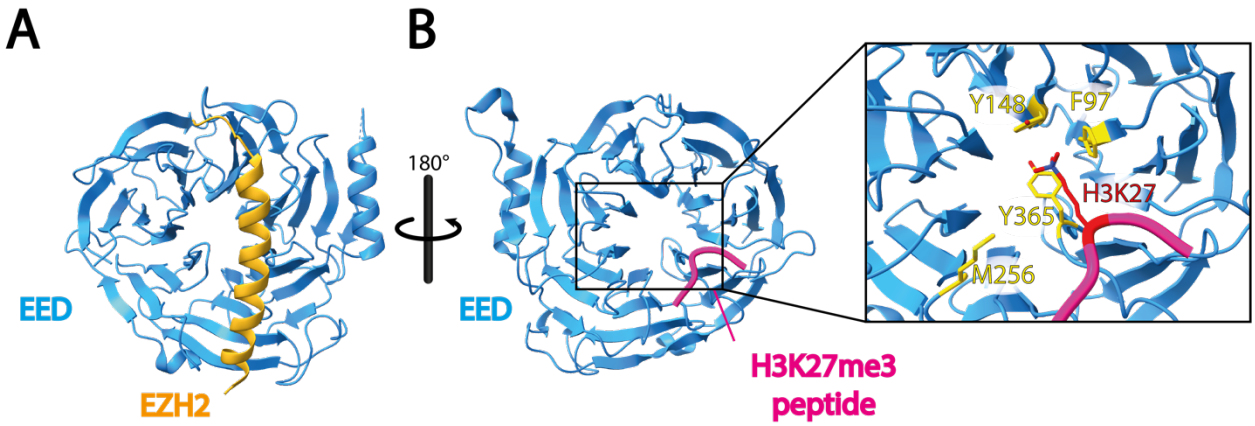

Figure 7: First structure showing EED interaction with EZH2 and H3K27me3

A. *Crystal structure of the front groove of EED (blue) bound by the EBD of EZH2 (orange) (PDB:2QXV)* ***B.*** *Crystal structure of the 'back' of EED with an H3K27me3 peptide (violet) engaging the aromatic cage. The inlet shows the aromatic cage consisting of F97, Y148, Y365 and W364 (yellow), which are central to recognizing H3K27. (PDB:3IIW)*

The core ternary complex of EZH2-EED-SUZ12

The initial structural characterization of the complete five-subunit PRC2-AEBP2 complex was achieved using negative-stain electron microscopy (EM) at a resolution limited to ~21 Å, in combination with genetic tagging and cross-linking mass spectrometry. [129] This study offered the first visualization of human PRC2 with its cofactor AEBP2, demonstrating that the complex can be divided into two distinct regions, termed the top and bottom lobes. In 2015, the first high-resolution structures were published, which showcased the organization of a ternary PRC2-like complex from *Chaetomium thermophilum*, consisting of EZH2, EED, and the SUZ12^{VEFS} domain (Figure 8A, B).[192] This complex corresponds to the top lobe of PRC2 and subsequent studies verified the structure of this complex in different species, including humans.[149, 193] Furthermore, these studies

identified two distinct states of PRC2: a 'stimulated' state, in which an H3K27me3 peptide was bound by EED, and a 'basal' state, in which no stimulating peptide was present. [149, 192]
The structure of these complexes is constituted by a SUZ12-EED dimer, which is wrapped around by an elongated part of EZH2. Because of this organization, EZH2 can be subdivided into an N-terminal regulatory region and a catalytic, C-terminal region (Figure 8B; left). The initial regulatory SANT1 binding domain (SBD) establishes a connection between the N-terminal regulatory domains by facilitating the binding of the downstream SANT1 domain. Subsequently, the EED binding domain (EBD), comprising a short helix and a flexible loop, binds to the surface groove of the β-propeller of EED, as previously described. [191] Following the EBD, the SET activation loop (SAL) extends away from EED, forming interactions with EZH2 including the SET domain and SUZ12^{VEFS}. These interactions are vital for the formation and maintenance of the stimulated active state of PRC2. [192] Following the SAL is the stimulation response motif (SRM), which was only observed in the presence of an activating H3K27me3 peptide bound to EED.

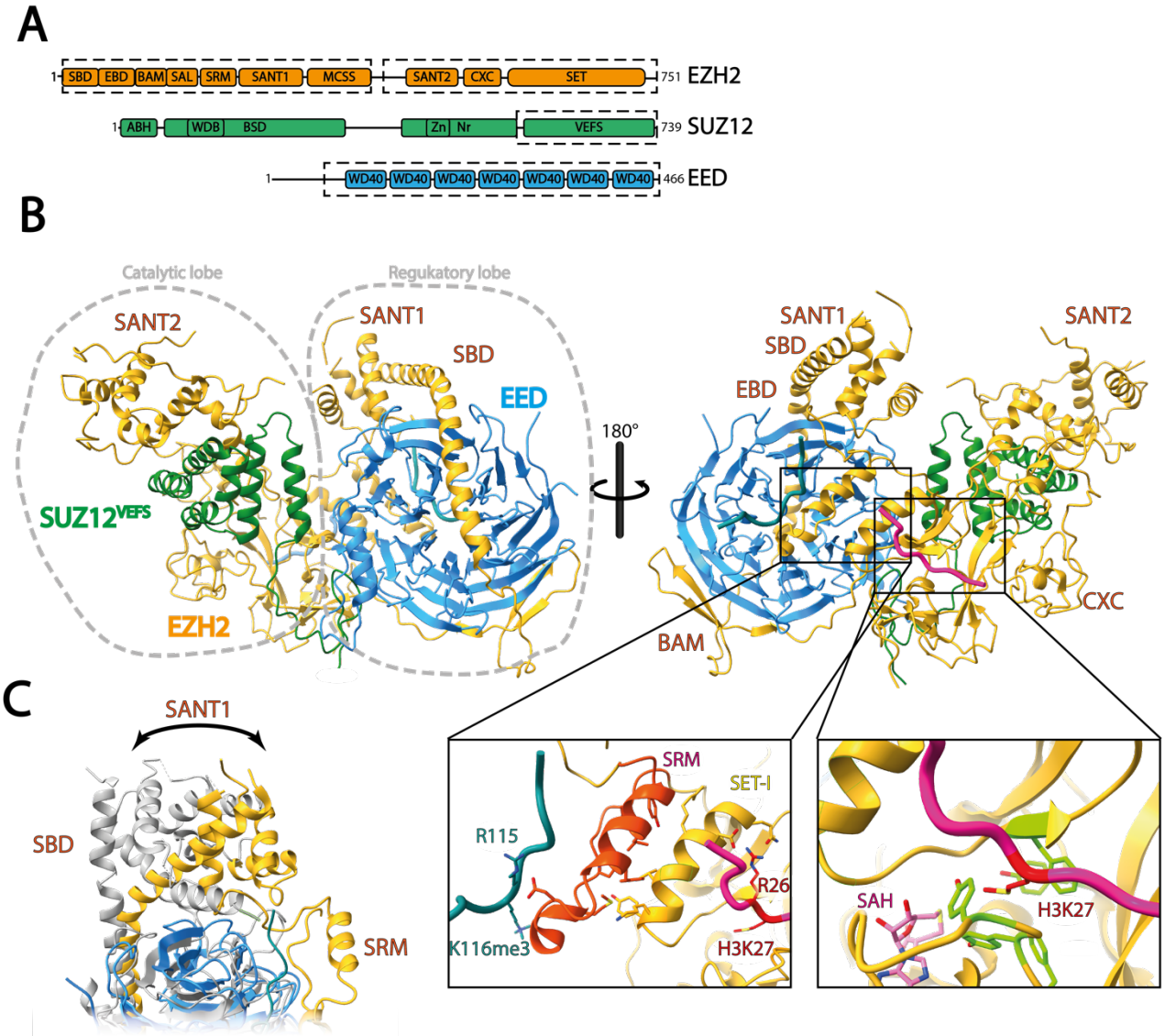

Figure 8:Structural insights of the ternary complex

A. *Schematic overview of the PRC2 subunits and their domains: EZH2 (yellow), SUZ12 (green) and EED (blue). The dotted lines show the regions used to generate the structure of the ternary complex.* ***B.*** *Overview of the crystal structure of the human ternary complex. (PDB:5HYN). The left inlet shows the SRM (orange) wedged between the SET-1 (yellow) and K116me3 of JARID2 bound by the EED β-propeller. The right inlet shows a zoomed view of the substrate-binding channel formed by a series of aromatic residus engaged to H3K27.* ***C.*** *Comparison of the crystal structure of the human (coloured, PDB:5HYN) and unstimulated chaetomium thermophilum ternary complex (grey, PDB:5CH2)*

The comparison of the two PRC2 states revealed that, when stimulated, the SRM consists of a mobile helix that wedges the peptide with the EED β-propeller. In the basal state, the SRM is flexible and/or disordered, rendering it unobservable. A similar mechanism was also shown for K116me3 of JARID2 (Figure 8B, left inlet).[148, 149] The arginine at the -1 position of the activating methyl lyines forms a salt bridge with acidic residues located on the turn between the SRM. The SRM is stabilized via JARID2 peptide binding through a series of backbone interaction with EED and the two aforementioned hydrophobic pockets.[131, 149] The proper folding of SRM and binding to the stimulating peptide result in the transmission of allosteric activation to the SET-1 helix of the catalytic centre.[149, 192] The loop of the SET-I form a series of hydrophobic interactions with the SRM positioning the SET-I helix against the SRM. The SET-I helix itself itself extends these hydrophobic interactions and further stabilizes the binding to via a salt bridge and hydrogen bonds. The SET-I in this stabilized conformation contributes many residues that interact with the substrate peptide.

Structural changes in a second region, the SANT1 module, are less compelling. In the stimulated state, the SBD helix is bent, whereas it remains straight when unstimulated (Figure 8C).[149, 192] However, this conformational change is not observed in fungal structures, even though the structuring of the SRM helix is evident.[194] Concluding the regulatory region of EZH2 is the SANT1-like (SANT1L) domain, which interacts with the SBD, thereby closing off the regulatory domains around EED, like a 'belt'.

The start of the catalytic region is formed by a motif connecting SANT1L and SANT2L (MCSS) which links the two SANT domains with a pair of bent α-helices. The SANT2 domain is located forming interactions with MCSS and $SUZ12^{VEFS}$. Subsequently, a highly conserved domain follows which harbours two zinc-sulfur clusters (Zn_3Cys_8His + Zn_3Cys_9/CXC). This CXC domain was suggested to play an important role in DNA binding, since in Drosophila it is responsible for the recruitment of the dosage compensation complex to the X-chromosome.[195] In the ternary complex, it forms interactions with $SUZ12^{VEFS}$, MCSS, SANT2L, and the SET domain.

The most C-terminal domain of EZH2 is the catalytic SET domain of PRC2. Before the resolution of the ternary complex, several studies had shown that the isolated SET domain is in an autoinhibitory state and EZH2 lacks noticeable activity in the absence of EED and SUZ12.[66, 126, 127, 196] In the activated ternary complex the SET domain opens a hydrophobic binding pocket for the H3 tail and SAM cofactor. Through the aforementioned contacts with SAL and SRM the active conformation is stabilized, enabling interaction with $SUZ12^{VEFS}$ and the WD40 propeller of EED to forward activating signals. Furthermore, a series of aromatic reisdues on the SET form a substrate-binding channel and the positioning of the SAH thioether directly opposite from the lysine ε-amino group suggests a state ready for catalytic activity (Figure 8B; right inlet).[54, 192]

This network of interactions within the ternary complex provides important insights into the mechanisms of core PRC2 function and regulation. The structures explain previous functional observations of PRC2 activation and the requirement of the minimal complex of EZH2, EED and SUZ12.

Cryo-EM studies of PRC2

While the study of the ternary complex provided important insights into the top lobe and the mechanisms of PRC2 function, it was limited by using a reduced complex and peptide substrates. This left unresolved questions about subunits such as full-length SUZ12, RBBP4/RBBP7, and cofactors such as AEBP2 and JARID2, as well as the engagement with the native nucleosome substrate. In recent years, these gaps have been filled by structures obtained by single-particle cryo-EM. By using the five-subunit PRC2-AEBP2 complex with a JARID2 fragment (aa106–450) in combination with bissulfosuccinimidyl suberate (BS3) cross-linking, high-resolution structures of the entire PRC2 complex were obtained.[128] They highlight the role of SUZ12 in stabilizing the full PRC2 complex by interacting with all other subunits. The previously enigmatic bottom lobe of PRC2 consists of RBBP4, the C-terminus of AEBP2 and a β-sheet-rich domain of SUZ12. The two lobes of PRC2 are connected by interactions between the SUZ12 zinc finger, AEBP2 and JARID2.

In the bottom lobe, the WD40 propeller of RBBP4 is enveloped by SUZ12, similar to EED and EZH2. RBBP4 recognizes residues K294 and R295 of the C-terminus of AEBP2, mimicking the previously described recognition of R2 and K4 of histone H3.[121, 130] Residues 263-283 of AEBP2 are involved in interactions with SUZ12 (aa426-548). The N-terminal region of AEBP2 is proximal to the SET domain, which creates structural and potentially functional link between RBAP48 and the SET domain.[128, 197] Utilizing the cofactor JARID2 the structures revealed that this cofactor binds PRC2 at two sites. On one hand, it targets the SET domain of EZH2 as a substrate for the HMTase activity. On the other hand, as an allosteric activator, where K116me3 binds EED similar to H3K27me3. Like in the ternary complex, PRC2 was observed in two distinct yet active conformational states. In the 'compact active state', the SRM domain forms a helix and the SBD bent. In the 'extended active' state the SRM helix is disordered, and the SBD is straight. This underpins the role of these two domains as hallmarks of PRC2 conformational states.

PRC2 on chromatin

While the previous structural studies of PRC2 provided invaluable insights into its mechanism of activity and regulation, they left unresolved the details of how PRC2 interacts with chromatin. This gap in understanding is significant, as the function of PRC2 is intrinsically tied to its ability to engage with its chromatin substrate and the broader chromatin environment. Recent advancements using cryo-EM have begun to address this, particularly through studies of the five-subunit PRC2 complex bound to chromatin substrates, including mononucleosomes with H2AK118Ub modifications and even dinucleosomes.[198-200] These high-resolution structures have illuminated the molecular basis of chromatin engagement and PRC2 interaction wwith specific nucleosomal features, providing a more comprehensive view of its functional dynamics.

The first structure of PRC2 engaged to a dinucleosome utilized one unmodified, substrate nucleosome and one stimulating nucleosome containing H3K27me3 (Figure 9A). The structure was resolved at an overall resolution of 6.2 Å and revealed the top lobe, the ternary complex of EZH2, EED and SUZ12 positioned between the two nucleosomes connected by 35 bp of linker DNA. The bottom lobe remained unresolved, likely due to denaturation at the water-air interface during sample preparation.[198, 200] Nonetheless, this structure revealed several key interactions with chromatin. On one hand, residues of the CXC domain (K563, Q565, K569, Q570) demonstrated a capacity to bind nucleosomal DNA in the vicinity of the substrate nucleosome (Figure 9A, left inlet). Additionally, the H3 tail was observed to extend from the nucleosome to the PRC2 active site, corroborating previous findings with peptides.[149, 200] On the other hand, the stimulating nucleosome is bound by positively charged patches on EED, the EBD domain and potentially the SANT1 domain, thereby elucidating the previously described mechanism of PRC2 activation (Figure 9A, right inlet). Importantly, the structure of PRC2 engaged to the dinucleosome showed that one PRC2 can bind two adjacent nucleosomes at the same time, giving mechanistic insights into H3K37me3 spreading.[131, 188, 189, 200]

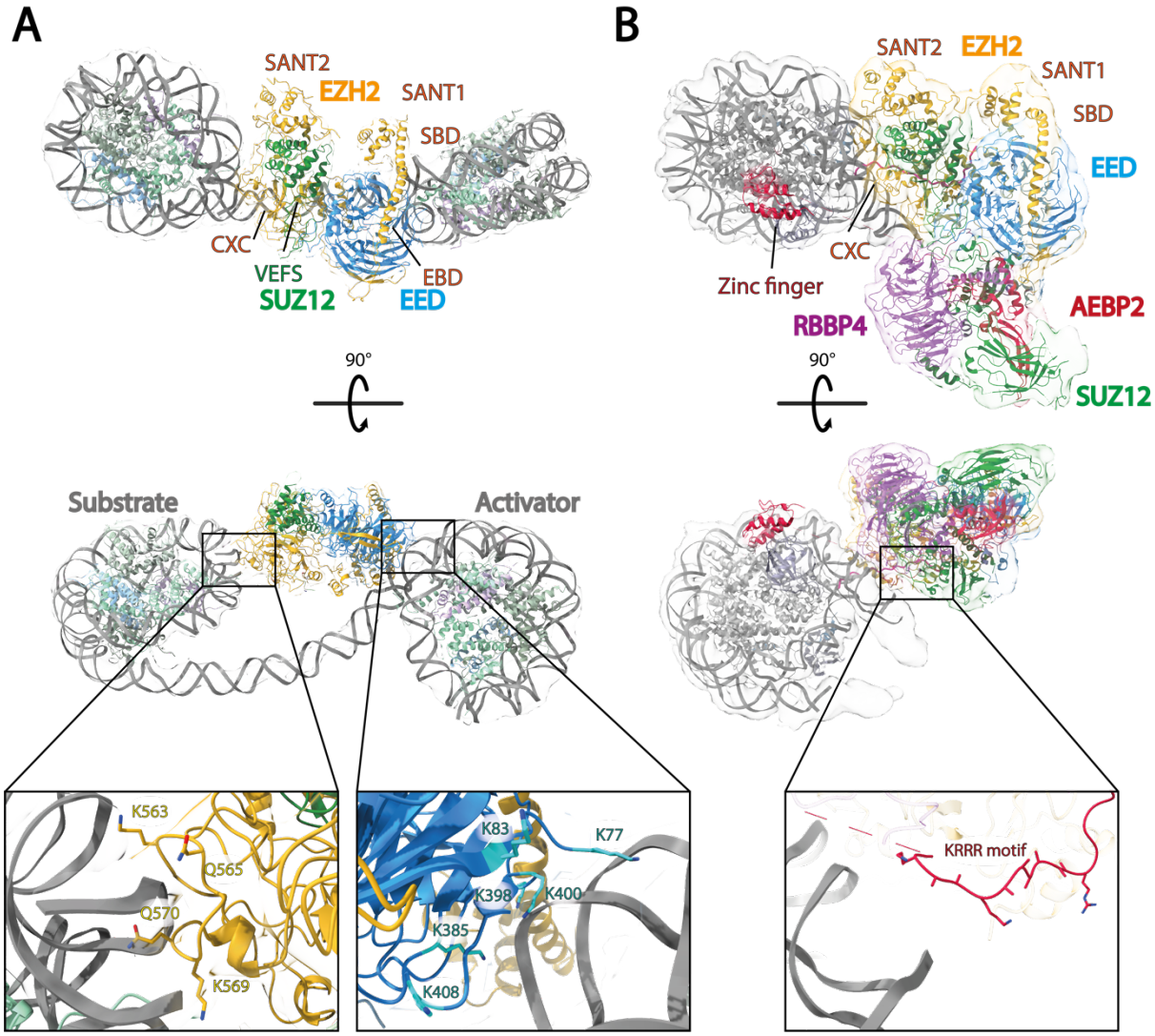

Figure 9:Cryo-EM structure of PRC2 engaged to chromatin

A. *Overview of PRC2 engaged to the dinucleosome. (EMDB:7306). The left inlet shows how charged residues on the CXC domain of EZH2 (K563, Q565, K569, Q570) engage with nucleosomeal DNA of the substrate. The right inlet show postively charged residues on the WD40-propeller of EED likely interacting with the DNA of the actvating nucleosome.* ***B.*** *Overview of the entire five subunit PRC2 engaged to the H2AK118Ub bearing mononucleosome (PDB:6WKR, EMDB:21707). The zoomed view shows the KRRR motif of AEBP2, which likely interacts with the DNA of the substrate nucleosome.*

Advancements in sample preparation have enabled the high-resolution visualization of the entire five-subunit PRC2-AEBP2 complex with a JARID2 fragment (aa1-450) bound to a mononucleosome bearing the H2AK119Ub modification.[199] This study on the one hand did not require cross-linking and, on the other hand, prevented denaturating of the bottom lobe on the water-air interface, thus painting a more complete picture. This structure confirmed the previous findings regarding the interaction of the SET and CXC domains of EZH2 with the H3 tail and revealed a lysine- and arginine-rich region in EZH2 (aa 480-515) that interacts with DNA.[198, 200] Upon binding to the nucleosome, this unstructured region undergoes a conformational change, forming an α-helix (aa497-511) that is positioned between the nucleosomal DNA, the SET domain, and the H3 tail, termed the bridge helix.[199] This region also includes the three lysines implicated in the automethylation-induced PRC2 activation.[185, 186]

Furthermore, the study corroborated that AEBP2 interacts with DNA through its KRRKLKNKRRR motif (aa171-181) and demonstrated that JARID2 and AEBP2 recognise the H2AK119Ub modification, which is deposited by PRC1, thereby providing stabilising interactions that support PRC2 recruitment to PRC1-modified nucleosomes (See: Polycomb: A historical perspective of the masterminds shaping cell fate).[135, 187, 199] A comprehensive understanding of PRC2 function and its is crucial for effectively addressing the potential dysregulation of this complex, which is implicated in a wide range of diseases.

6.2.5. PRC2 in disease

The significance of proper H3K27me3 regulation becomes evident in patients with pediatric diffuse intrinsic pontine gliomas, where H3K27 is frequently mutated to methionine (H3K27M). This mutation leads to a significant reduction in H3K27me3 levels and severe pathological consequences.[201, 202] Thus, given the crucial role that PRC2 plays in targeting H3K27 and gene regukation, it is unsurprising that its dysregulation is implicated in a range of diseases, particularly developmental disorders and cancers.[203, 204] Homozygous mutations in the core components EZH2, EED, and SUZ12 result in early embryonic death in mice.[108, 118-120, 205] Furthermore, heterozygous mutations in these subunits, especially EZH2, are associated with congenital overgrowth such as the Weaver or Cohen-Gibson syndrome.[206]

A key aspect of PRC2 in cancer is its tumor-type specificity. Both loss-of-function and gain-of-function mutations in PRC2 are associated with oncogenesis to a spectrum of cancer subtypes. [96, 102, 207-209] As the catalytic subunit, EZH2 is implicated in a variety of cancers, including lymphomas, prostate, and breast cancer, as well as many solid tumors.[209-213] In mouse models, extended loss of EZH2 has been shown to promote various cancers, such as breast, prostate, and pancreatic cancers.[209, 214-216] Functional loss of SUZ12 and EED is associated with highly aggressive tumor types, such as malignant peripheral nerve sheath tumors.[217-219] On the other hand, mutations leading to hyper trimethylation have been observed in subsets of human B-cell lymphoma and melanoma.[209, 220, 221]

Therefore, PRC2 has emerged as a potential therapeutic target for epigenetic drug development. Early studies have shown promising results in treating mice with gain-of-function mutations in EZH2 or EED, leading to FDA-approved drugs.[222-225] However, EZH2 inhibitors have demonstrated significant side effects and completely abolished PRC2 activity, suggesting that targeting the EED activation mechanism may be a more viable and targeted approach. Despite these advances, the high variability in PRC2-related pathogenesis underscores the need for a deeper understanding of PRC2 function to enable more precise therapeutic strategies.

CHAPTER II: STRUCTURAL ANALYSES OF MITOCHONDRIAL COMPLEX FORMATION OF APOPTOSIS-INDUCING FACTOR 1 (AIFM1)

6.1. Mitochondrion: Powerhouse of the cell

The mitochondrion is a vital organelle with a double membrane structure in eucaryotic cells, that is involved in playing a key role in numerous essential cellular processes. It is generally assumed that mitochondria originated from the endosymbiosis of proteobacteria, following their phagocytosis by an ancestral archaeon.[226-228] This hypothesis is supported by two main observations: the structural organization of mitochondria and the presence of a distinct mitochondrial genome. The mitochondrion consists of two membranes: The outer (OM) and inner membrane (IM). The IM further forms dynamic invaginations which are called cristae (Figure 10).[229]

The compartmentalization of the mitochondrion provides distinct environments, optimized for various biochemical processes, by segregating metabolic pathways and their intermediates. This spatial organization enhances the efficiency of for example energy production and regulation, while also facilitating precise control of ion gradients and protein transport across its membranes. Notable pathways include the integration of products from the tricarboxylic acid (TCA) cycle (also known as the Krebs cycle, citric acid cycle) and fatty acid oxidation in the mitochondrial matrix to the ATP production through oxidative phosphorylation at the intermembrane space (IMS).[230, 231]

Beyond energy metabolism, mitochondria play crucial roles in processes such as apoptosis, calcium homeostasis, metabolite generation, and the production of reactive oxygen species (ROS), with ongoing discoveries expanding the list of its functions. The complex involvement of mitochondria in these diverse cellular activities necessitates strict regulatory mechanisms to maintain cellular homeostasis.[232-234]

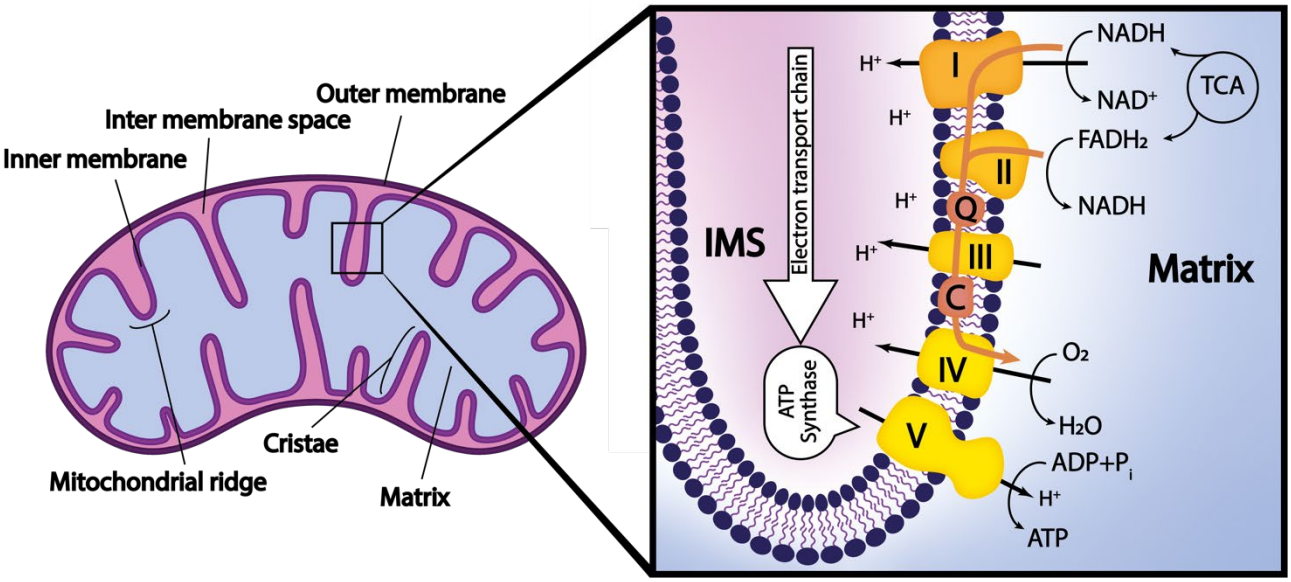

Figure 10: Mitochondrial structure and organization of OXPHOS proteins

Left: *Overview of the mitochondrial organization with its two membranes.* ***Right:*** *Protein complexes of the OXPHOS. Complexes I-IV with the electron carriers ubiquinone (Q) and cytochrome c (C) transfer electrons (orange arrow) from reduced NADH and $FADH_2$ to O_2 and pump protons into the IMS. The resulting electrochemical gradient drives ATP synthesis by the ATP synthase complex.*

6.1.1. Oxidative phosphorylation: Source of energy

The primary energy storage medium within cells is in the form of high-energy electron carrier molecules, such as nicotinamide adenine dinucleotide (NAD), flavin adenine dinucleotide (FAD) and adenosine triphosphate (ATP).[235, 236] Acetyl coenzyme A (acetyl-CoA), produced during glycolysis and fatty acid β-oxidation, enters the tricarboxylic acid (TCA) cycle, a central metabolic pathway responsible for energy production.[231, 237] The generated dinucleotide NADH and $FADH_2$ are subsequently utilized to produce ATP, the primary energy currency of the cell, through oxidative phosphorylation (OXPHOS).
OXPHOS involves two synergistic phases, carried out by mitochondrial protein complexes within the IMM: (1) The electron transport chain (ETC) is comprised of the four protein complexes - complex I (CI, NADH oxidoreductase), complex II (CII, succinate dehydrogenase), complex III (CIII, cytochrome bc1 oxidoreductase), and complex IV (CIV, cytochrome c oxidase) as well as two electron carriers, ubiquinone and cytochrome c (Cyt c).[238, 239] These transfer electrons from NADH and $FADH_2$ to oxygen, while simultaneously translocating protons (H^+) from the mitochondrial matrix to the IMS. (2) Due to the resulting electrochemical gradient across the IMM protons flow back into the matrix driving ATP synthase (complex V), catalyzing the conversion of ADP and phosphate into ATP.[235, 239-241]
Precise regulation of OXPHOS is critical for maintaining energy homeostasis, redox balance, and mitochondrial quality control, all of which are essential for cellular metabolism, adaptation to environmental stress and metabolic flexibility. Dysregulation of these processes is closely linked to various diseases and processes of ageing.[242-245]

6.1.2. Mitochondrial Protein Import: Through the eye of the needle

Mammalian mitochondria contain ~ 1000-1500 proteins, even though the mitochondrial genome encodes for just 13 proteins.[246] Therefore, the majority of mitochondrial proteins are nuclear-encoded and require import, proper folding and sorting within the organelle. Five different import pathways are coordinated by the multi-protein translocase complexes of the outer membrane (TOM), sorting and assembly machinery (SAM), mitochondrial import complex (MIM), translocase of the inner membrane 22 and 23 (TIM22, TIM23) and mitochondrial import and assembly (MIA) and presequence translocase-associated motor (PAM).[247, 248]
In the classical import pathway, termed the presequence pathway, mitochondrial proteins carry a cleavable amino-terminal presequence, which directs them to the target organelle.[248, 249] Proteins of the TOM complexes Tom20, Tom22 and Tom70 recognize these precursor proteins and transfer them to Tom40 for translocation to the IMS.[247, 248, 250, 251] Subsequently, TIM23 recognizes the preprotein and directs the transport to either the IM or the matrix, while the TIM22 complex facilitates the insertion of proteins without a classical presequence.[252] The transport to the matrix is facilitated by PAM in an ATP-driven manner, where the soluble form of its subunit mitochondrial heat-shock protein 70 (mtHsp70) functions as a chaperone.[253-255] Tim23 and Tim17 sort the protein to the IM while presequence translocase-associated motor (PAM) and TIM23 direct for import into the matrix. The presequence of both IM- and matrix-sorted and matrix-targeted precursor proteins are cleaved by matrix processing peptidases (MPP) (Figure 11).[256, 257]

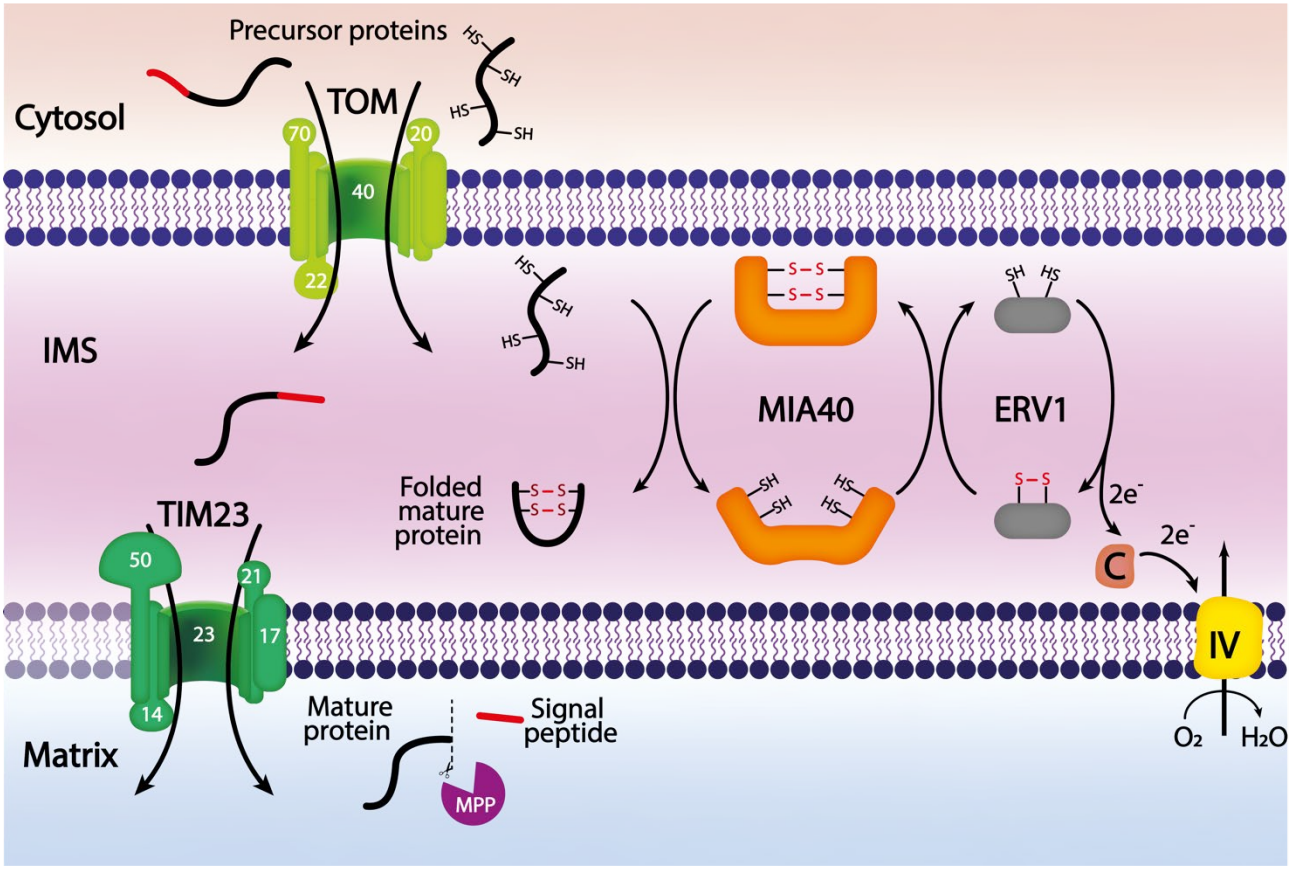

Figure 11: Mitochondrial presequence and MIA import pathways

In the presequence pathway, presequence-carrying precursor proteins are recognized and passed by the TOM complex at the OM. Thereafter they are transported via the TIM23 complex and PAM to the matrix, where the presequence is cleaved by MPP. Proteins of the IM are either directly integrated into the membrane or inserted after processing in the matrix. In the MIA pathway proteins containing specific cysteine motives are imported into the IMS and oxidized by MIA40. The reduced cysteines of MIA40 are reoxidized by ERV1, which regenerates its oxidized cysteine by shuttling its electrons to Cyt C and further into the respiratory chain.

Numerous proteins of the IMS with characteristic cysteine motifs require the coupling of import, proper folding and oxidation, establishing covalent modification and internal disulfide bonds in the process.[258, 259] This MIA import pathway or disulfide relay machinery, requires two major players: the oxidoreductase Mitochondrial intermembrane space import and assembly protein 40 (MIA40, in humans also CHCHD4) and the sulfhydryl oxidase essential for respiration and vegetative growth protein 1 (Erv1; in humans hERV1 or augmenter of liver regeneration, ALR,).[258-264]

In yeast, MIA40 is anchored to the IM via a hydrophobic N-terminus, while its human counterpart is a soluble protein in the IMS.[258, 259, 261, 265] This enzyme consist of six conserved cysteine residues, organized as one redox-sensitive CPC motif with two CX_9C motifs. The former functions by binding the substrate protein bearing CX_3C and CX_9C substrates via a hydrophobic cleft formed by two anti-parallel helices.[266, 267] The CX_9C bears redox-active cysteine pairs that accept electrons from the substrate, introducing disulphide bonds in a two-step reaction, switching from an oxidised state to reduced MIA40.[247, 258, 259, 266-271]

Erv1 re-oxidizes MIA40 and, subsequently, Cyt C accepts electrons from Erv1, recycling these enzymes.[260] Furthermore, this links the disulphide relay system directly to the respiratory chain since Cyt C is shuttled to complex IV (See Chapter 6.1.1).[272-274] Furthermore, MIA40 mediates the oxidative folding and import of OXPHOS proteins as substrates, such as structural subunits and assembly factors of CI, CIII, CIV and CV.[268, 275-277] Another substrate of MIA40 is adenylate kinase 2 (AK2) which catalyzes the reversible adenine nucleotide phosphoryl transfer in the reaction 2 ADP ↔ ATP + AMP in the IMS.[278-280]

Recent studies revealed that MIA40 itself interacts with the flavoprotein apoptosis-inducing factor mitochondrial (AIFM1), which on one hand facilitates its import to the IMS and on the other hand stabilises MIA40 by forming a complex. [278, 281-286]

6.2. Apoptosis-inducing Factor: A double-edged sword

6.2.1. AIFM1: Harbinger of death and guardian of life

The Apoptosis-Inducing Factor Mitochondrial 1 (AIFM1) is a highly conserved flavoprotein located in the IMS with common structural and functional characteristics across species.[287] In humans, AIFM1 is initially expressed as a 613 amino acid (aa) precursor protein with a molecular weight (MW) of 67 kDa, which is synthesized in the nucleus. This precursor contains one nuclear localization signal (NLS) and two N-terminal mitochondrial targeting sequences (MLS), which guide the protein through the classical presequence pathway (Chapter 6.1.2).[288] Upon the translocation and import of the protein into the mitochondrion, the MLS is cleaved by MPP at M53/A54, resulting in a 62 kDa protein (AIFM1$_{\Delta 1\text{-}54}$). An inner-membrane sorting signal then anchors the N-terminus of the mature AIFM1 into the IM leaving the C-terminus exposed in the IMS (Figure 12; green). As a result, AIFM1 functions as a type-I inner membrane protein.[289-291]

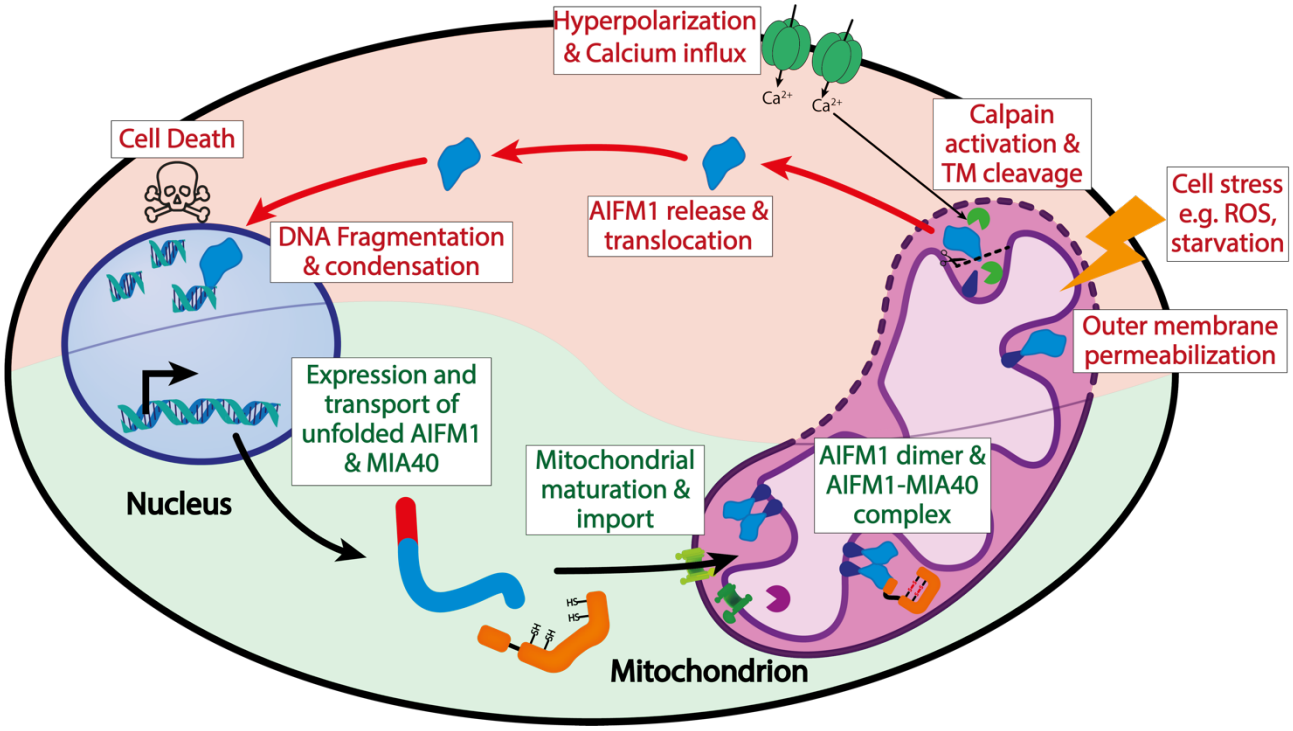

Figure 12: AIFM1 maturation and role in apoptosis

Bottom: *AIFM1 is synthesized as a 67 kDa protein and gets transported to the mitochondrion via the presequence pathway. In the mitochondrion, the presequence is cleaved and the enzyme folds into a mature protein of 62 kDa. Under physiological conditions, sufficient amounts of NADH drive AIFM1 dimerization, which acts as a binding platform for MIA40.* ***Top:*** *Upon apoptotic insult the OM permeabilizes the plasma membrane hyperpolarizes, causing an influx of Ca^{2+}. This leads to the activation of calpains which cleave the N-terminal TM releasing a 57 kDa pro-apoptotic protein. The protein translocates to the nucleus, where it induces chromatin condensation and DNA fragmentation.*

Originally, AIFM1 was described as being involved in caspase-independent apoptosis.[292, 293] This mitochondrial apoptotic pathway is triggered by intracellular stress stimuli, such as irreparable DNA damage and severe oxidative stress. Upon OM permeabilization and subsequent cleavage by calcium-activated μ-calpains, AIFM1 is first released into the cytosol as a soluble pro-apoptotic protein and interactions with either Heat shock 70 kDa protein (HSP70) prevents or with cyclophilin A promotes translocation to the nucleus.[289, 294-298] There it promotes DNA fragmentation and chromatin condensation, potentially through direct interactions with both DNA and DNases (Figure 12; red).[297, 299-303] Studies have shown that AIFM1 is involved in different forms of cell death and deficiencies in cellular systems result in resistance to apoptosis.[295, 304-307] The apoptotic mechanism is especially important in neurons and neuroendocrine cells. Consequently, defects in AIFM1 are associated with various neurological symptoms, neurodegenerative diseases, muscle weakness, and atrophy.[283, 308] Thus, the role of AIFM1 in apoptosis is critical for maintaining cellular function, particularly in tissues that are highly susceptible to apoptotic dysregulation.

Further studies across various species have shown that reduced AIFM1 activity leads to molecular defects in the respiratory chain, specifically downregulation of complexes I, III, and IV.[309-314] Although AIFM1 is not a respiratory chain subunit itself, its function is indirectly linked to the mitochondrial disulfide relay system, which is essential for proper oxidative folding and import of OXPHOS proteins (See Chapter 6.1.1). AIFM1 directly facilitates the import of MIA40 into the IMS.[281, 282, 315] Notably, AIFM1 and MIA40 form a stable complex and MIA40 overexpression can at least partially complement the respiratory chain defects caused by the loss of AIFM1.[285, 286]

This multifaceted function of AIFM1 in both apoptosis and mitochondrial maintenance emphasizes the complexity of regulation, prompting further exploration into its structural properties and emerging redox activity.

6.2.2. AIFM1: A structural perspective and the redox question

Early studies revealed that AIFM1 incorporates FAD and exhibits NAD(P)H redox activity toward small electron acceptors and cytochrome c.[288, 316] Typically, flavoenzymes form π-π charge–transfer interactions between the parallel-stacked isoalloxazine ring of FAD and the nicotinamide of NAD(P)H, resulting in a charge–transfer complex (CTC). These interactions promote the oxidation of NAD(P)H and the reduction of FAD.[317, 318]

$$FAD + NADH + H^+ <=> FADH_2 + 2\,NAD^+ + 2e^-$$

Once reduced, $FADH^-$ can transfer electrons to various electron acceptors, thereby facilitating substrate reduction[319]:

$$AIF(FADH_2) + Substrate(ox) <=> AIF(FAD) + Substrate(red)$$
$$FADH_2 + O2 <=> FAD + H_2O_2$$

AIFM1 shows a higher affinity for NADH compared to NADPH, effectively shuttling electrons from NADH to both one- and two-electron acceptors, albeit at a low turnover rate. Consequently, AIFM1 is classified as an oxidoreductase.[288, 316, 317] However, its precise catalytic function and specific enzymatic substrates remain unclear. One proposed role for AIFM1 is to function as an NADH sensor, potentially monitoring the redox state and overall health of mitochondria.[283, 320] To further elucidate the redox function, structural studies have provided critical insights into the protein architecture and functional implications.

The first structure resolved was that of the oxidized murine AIFM1, in which the transmembrane domain was deleted.[299] According to the structural features, the enzyme can be divided into three functional key regions: a FAD-binding domain (aa122–262 and aa400–477), an NADH-binding domain (aa263–399) and the C-terminal domain (aa478–610). The FAD- and NADH-binding domains exhibit a classical Rossmann fold, a super-secondary structure motif with a β-α-β core typically associated with nucleotide-binding proteins.[299, 321, 322] Meanwhile the C-terminal domain is composed of five antiparallel β-strands (aa 477–579) and two α-helices (aa 580–610). Since the initial characterisation, multiple structures paint a more comprehensive picture of the structural organization and subsequent functional implications of AIFM1 (Figure 13).[299, 317, 323, 324]

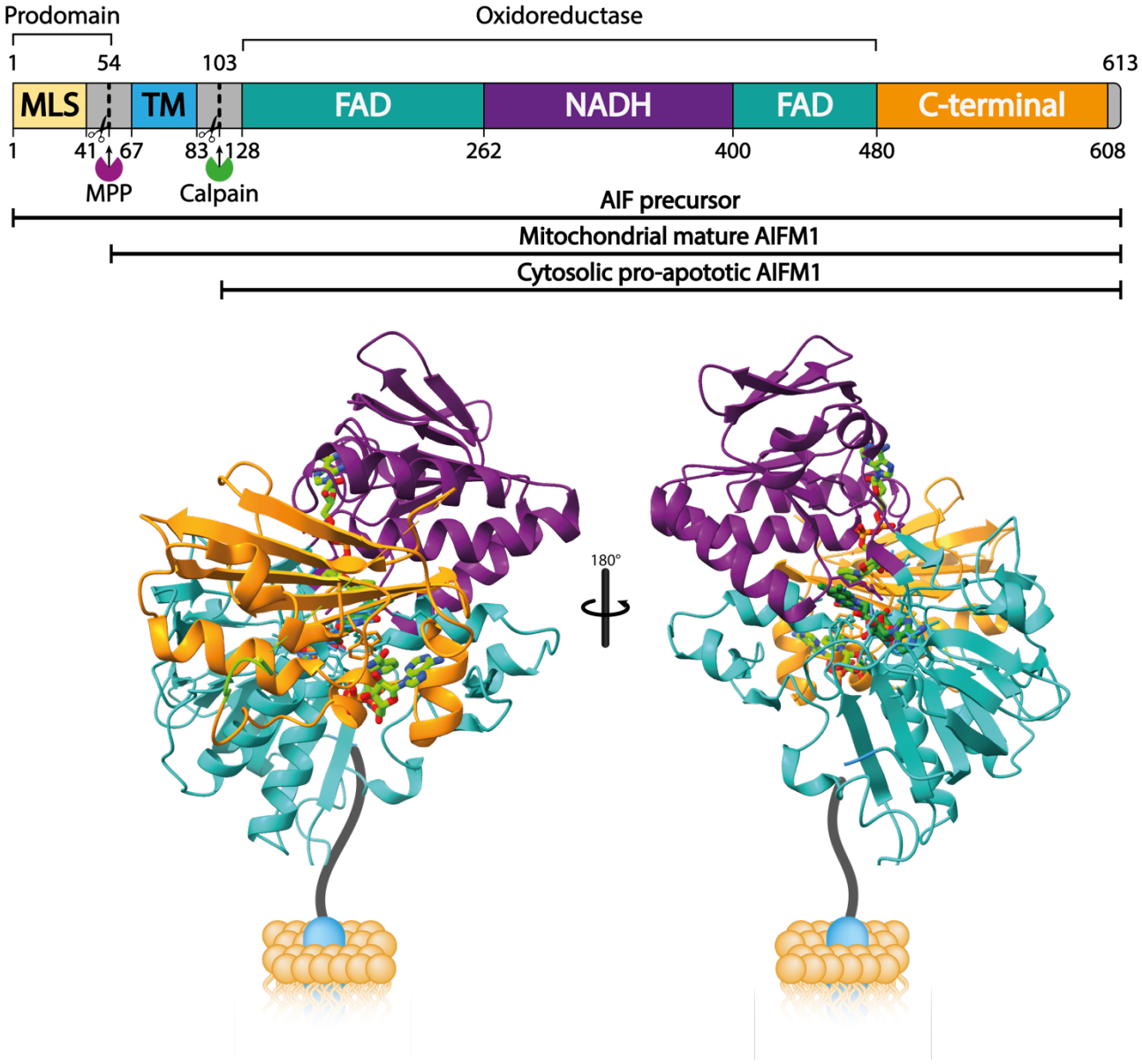

Figure 13: Structural organization of human AIFM1

Top: *Domain organisation of AIFM1, with the cleavage sites of MPP and calpains, resulting in protein maturation and apoptosis induction, respectively.* ***Bottom:*** *Crystal structure of the oxidized human AIFM1$_{\Delta 1–121}$ with the transmembrane truncated (PDB: 4BV6). Cartoon representation of the transmembrane domain in a memrane was added for visualization. The FAD-binding domain (turquoise) and the NAD-binding (violet) form the enzymatic oxidoreductase core of the enzyme. The cofactors NAD and FAD (green) are represented as ball sticks. The C-terminal domain (yellow) plays an important regulatory role.*

Upon binding of NADH, the complex undergoes a series of conformational changes, resulting in the formation of a long-lived, air-stable CTC.[299, 317, 323-325] This results in dimerization which is stabilized by hydrogen bonds and salt bridges between the two protomers (Figure 14A).[323, 324] A crucial conformational change for CTC formation is the release of a regulatory segment within the C-terminal domain, known as the "C-loop" (aa509–559), from contacts with the protein core and a β-hairpin (aa 190-207). This “Cβ-clasp” which connects the FAD and NADH domains, which in the oxdized state is particularly stabilized by W196 an R201(Figure 14C).[325] As a result of the release, key residues F310 and H454 reorient and engage the NADH cofactor and a central β-strand, that bridges the FAD-binding and C-terminal domain pivots at residue W483 (Figure 14B,C).[323, 325] Additionally, a rearrangement of a series of aromatic residues into an “aromatic tunnel” occurs wghich has been hypothesized to be involved in redox activity.[323]

The cofactors are bound by key residues that orient the nicotinamide of NADH for optimal parallel stacking between F310 and the isoalloxazine of FAD. Specifically, E314 forms hydrogen bonds with O4 of NAD and a salt bridge with K177, which in turn interacts with N5 of FAD. Meanwhile, H453 establishes a hydrogen bond with O7 of the nicotinamide (Figure 14B).[323, 324, 326] The cofactors are further stabilized by a hydrogen bond network involving of the NADH- and FAD-bidning domains.[323, 324] Notably, one crystal structure reported an additional NADH that parallel stacks on the opposite side of W483, which in turn stacks against the pyrimidine ring of FAD in a folded conformation, potentially blocking the reattachement of the Cβ-clasp (Figure 14B, bottom).[324]

It has been proposed that AIFM1 functions as an NADH sensor, potentially monitoring the redox state and overall health of mitochondria: Under non-stress conditions, sufficient amounts of NADH drive AIFM1 C-loop release and dimerization. In contrast, during stress conditions, such as starvation, reduced levels of NADH lead to a more prominent monomeric form of AIFM1.[285, 325, 327, 328] Furthermore, mutations affecting CTC formation are associated with neurodegenerative disease, highlighting the importance of this process.[329-333]

This transition between the dimeric and monomeric states, particularly the displacement of the C-loop, also plays a significant role in non-enzymatic functions. The interaction and import of MIA40 are primarily facilitated by the reduced dimer.[282, 285, 286, 334] Indeed, biochemical studies and a recent low-resolution crystal structure of AIFM1 in complex with a MIA40 peptide have identified an interaction between the N-terminal MIA40 β-hairpin (aa3-15) and the final β-strand of the AIFM1 C-terminus (aa491-510 and aa562-611).[282, 285, 334]

These structural studies of AIFM1 underscore its multifaceted role in cellular function, revealing critical interactions that facilitate non-enzymatic functions such as MIA40 import, while also suggesting the possibility of additional, as-yet-undiscovered interactions and regulatory mechanisms that may further illuminate AIFM1’s contributions to mitochondrial health and cellular homeostasis.

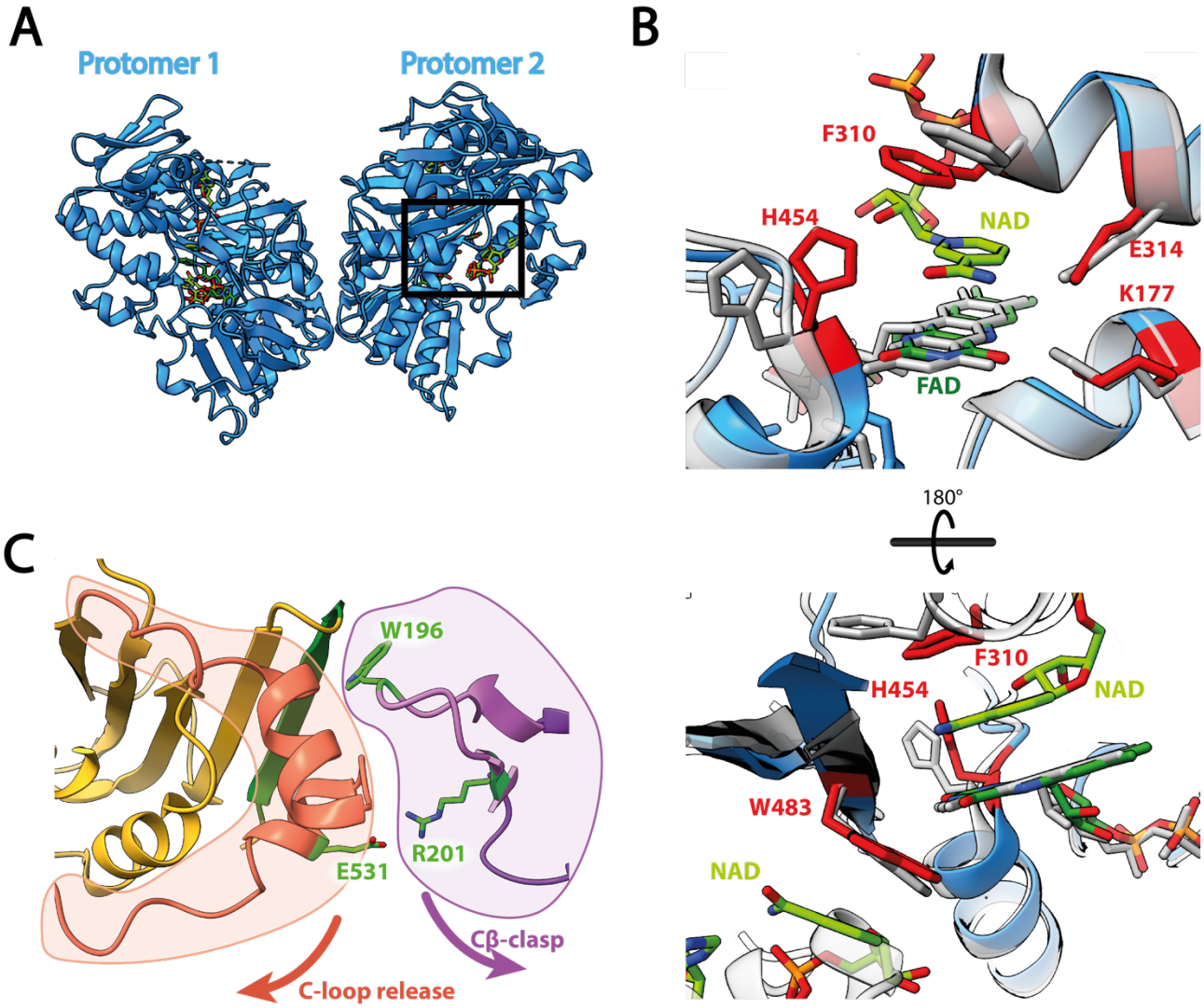

Figure 14: Active site and conformational changes upon NAD binding

A. *Upon biding of NAD AIFM1 forms a stable, dimeric CTC. (PDB:4BUR, blue). The rectangle shows the area of interest for B. and C..* ***B.*** *Overlay of the crystal structures of oxidized (PDB:4BV6, gray transparent) and reduced (PDB:4BUR, blue). NADH binding results in rearrangements and binding of key residues (red) positioning the cofactors for parllel stacking (red). H454, E314, K177 position the cofactors parallel to F310. The turned view shows that W483 parallel stacks with a reported second NAD.* ***C.*** *In oxidized AIFM1 the C-loop (orange) can be detected to bind the Cβ-clasp (purple). Upon reduction, the Cβ-clasp rearranges and releases the C-loop and the central β-strand pivots(dark green), eventually resulting in a dimeric CTC.*

7. RESEARCH QUESTIONS

7.1. Aim 1: Functional characterization of PRC2 dimerization on chromatin

Polycomb Repressive Complex 2 (PRC2) is the methyltransferase responsible for catalyzing the deposition of H3K27me1, H3K27me2 and H3K27me3. The latter is critical for transcriptional repression and chromatin organization. However, efficient deposition of H3K27me3 requires an allosteric activator to enhance activity of the catalytic subunit EZH2. Recent studies have shown that PRC2 undergoes automethylation on three lysines (K510, K514, and K515) of EZH2, leading to increased enzymatic activity. Structural insights obtained in collaboration with the Nogales Lab suggested a novel mechanism involving PRC2 dimerization on chromatin, with automethylation potentially targeting the EED-mediated activation pathway.
Based on this structural data, this study seeks to functionally explore the significance and interplay of dimerization and automethylation. By employing a combination of structural analyses, biochemical assays and transcriptomic approaches we aim to deepen our understanding of PRC2 activation and its biological implications, answering key questions:

1. Can PRC2 dimerization be connected to the stimulatory effect of automethylation?
2. What specific role do these mechanisms play in regulating PRC2 function and how do individual methylation sites (K510, K514, and K515) contribute to this process?
3. Is dimerization required for PRC2 activation *in vivo*, and does PRC2 automethylation and dimerization exert its regulatory effects during differentiation?

Through these questions, this thesis seeks to unravel the functional relevance of PRC2 dimerization and automethylation, advancing our understanding of its role as an epigentic regulator.

7.2. Aim 2: Structural analyses of mitochondrial AIFM1 interactions with binding partners MIA40 and AK2

The mitochondrial protein Apoptosis-Inducing Factor Mitochondrial 1 (AIFM1) is a multifunctional protein, fulfilling roles in apoptosis, protein import and exhibiting redox activity. Despite extensive research, the significance of AIFM1 catalytic oxidoreductase activity remains unclear. Recent studies have demonstrated that AIFM1 interacts with the Mitochondrial Intermembrane Space Import and Assembly Protein 40 (MIA40) facilitating its import and forming a stable complex. The Riemer group obtained a high-confidence interactome for AIFM1 in the IMS. This analysis re-affirmed the AIFM1-MIA40 interaction and unveiled a novel interaction partner: the long isoform of adenylate kinase 2 (AK2), AK2A.
In collaboration with the Riemer Lab, this study focuses on exploring the structural implications of AIFM1 interactions with MIA40 and AK2A. Using cryo-EM structural analyses and complementary biochemical approaches from the Riemer Lab we aim to address the following questions:

1. What are the are the interaction sites of MIA40 and AK2A with AIFM1?
2. What conformational changes occur upon binding of MIA40 and AK2A to AIFM1, and how does AIFM1 influence its binding partners?
3. How could these interactions modulate the structural stability and functional properties of AIFM1?

Through these objectives, the study aims to uncover the interactions of MIA40 and AK2A with AIFM1 on a molecular level and they impact the structure of AIFM1.

8. MATERIALS

8.1. Chemicals, peptides, and recombinant proteins

All common chemicals and materials used in this study were obtained from Sigma Aldrich or Roth unless specified otherwise.

Chemical	Source
ArgC Endopeptidase	Promega, Cat #V1881
Biotin	Sigma Aldrich, B4501-1G
EED inhibitor MAK683	Selleck Chem, Cat # S8983 / CAS: 1951408-58-4
EZH2_aa502-521	Genscript
EZH2_aa502-521_K510me3	Genscript
EZH2_aa502-521_K514me3	Genscript
EZH2_aa502-521_K515me3	Genscript
H3_aa17-38_K27me3	Genscript
KIT ECL PRIME DETECTION REAGENT	VWR, RPN2232
Midori Green Advance	NIPPON Genetics, 2082311
S-(5′-Adenosyl)-L-homocysteine	Sigma Aldrich, Cat # A9384 / CAS: 979-92-0
S-(5′-Adenosyl)-L-methionine chloride dihydrochloride	Sigma Aldrich, Cat #A7007 / CAS: 86867-01-8
Step-Tactin Superflow Plus	Qiagen, #30004
Strep-Tactin®XT 4Flow® resin	IBA Lifesciences, 2-5010-025
Streptavidin	New England Biolabs (NEB), Cat # N7021S
SUPERSIGNAL WEST FEMTO MAXIMUM	Pierce, 34094
SYBR™ Gold	Thermo Fisher, S11494

8.2. Buffers and Solutions

Buffers were prepared from the following stock solutions: 1 M HEPES, 1 M Tris, 500 mM EDTA, 2 M KCl, 2 M $MgCl_2$, 500 mM TCEP, 1 M DTT, 50% Glycerol

Buffer	Components	Use
10xSDS-Running Buffer	1.92 M glycine 333 mM Tris Base, pH 8.3 1% SDS	Protein gel, WB
10xTAE	2 M Tris base 1 M Acetic acid 50 mM EDTA 0.5M	Agarose gel
10xTransfer Buffer	250 mM Tris 1.92 M Glycine	WB
10xTris Buffered Saline (10x TBS)	200 mM Tris base 1.5 M NaCl	WB
10xTris/Borat/ (TAE) buffer	890 mM Tris 890 mM Boric acid 20 mM EDTA	Agarose gel
10xTris/Borat/EDTA (TBE) buffer	890 mM Tris Base 890 mM Boric Acid 20 mM EDTA (pH 8)	Native gel
1x TCS Buffer	20 mM Tris-HCl, pH7.5 1 mM EDTA 1 mM DTT	Nucleosome Reconstitution
2x YT medium	1.6% Tryptone 1% Yeast extract 0.5% NaCl 0.1% Glucose	Histone Expression

5% Native gel	300 µL 10x TBE 2.5 mL 30% Acrylamide (59:1) 12.2 mLH_2O 30 µL TEMED 90 µL APS 10%	EMSA
5xLaemmli Buffer (5x Loading Dye; 5xLD)	200 mM Tris-HCl, pH 6.8 8% SDS 50% Glycerol 0.4% Bromophenol blue 10% bME	Protein gel, WB
AIFM1 Freezing Buffer	100 mM NaCl 20 mM Tris/HCl pH 7.4 0.1 mM NADH	Cryo-EM sample preparation
Anion Exchange High Buffer	50 mM Tris, pH 7.5 2 M NaCl	Nucleosomal DNA purification
Blocking buffer	5 % Non-fat dry milk powder 1x TBS-T	WB
Coomassie Brilliant Blue (CBB) Solution	30 % (v/v) Ethanol 5 % (v/v) Acetic Acid 0.1 % Coomassie Brilliant Blue	Protein gel
Destaining solution	10 % (v/v) Ethanol 5 % (v/v) Acetic Acid	Protein gel
Histone Extraction buffer	7 M GuHCl 20 mM Tris pH 7.5 200 mM NaCl 1 mM EDTA 5 mM bME	Nucleosome purification
Histone Size Exclusion Buffer	7 M GuHCl 20 mM Na-acetate pH 5.2 1 M NaCl 1 mM EDTA 5 mM bME	Nucleosome purification
Histone Wash Buffer	20 mM Tris, pH 7.5 200 mM NaCl 1 mM EDTA 5 mM β-mercaptoethanol (BME)	Nucleosome purification
Lysis RIPA buffer	50 mM Tris-HCl pH 7.4 150 mM NaCl 1 mM EDTA 1 % NP-40 1% Na-deoxycholate 0.1 % SDS	Cell culture
PRC2 Activity Assay (AA) Buffer	25 mM HEPES pH 7.9 50 mM NaCl 2.5 mM MgCl2 0.25 mM EDTA 5% Glycerol 1 mM DTT 80 µM SAM	Activity assay
PRC2 Binding Buffer	25 mM HEPES pH 7.9 50 mM NaCl 1 mM DTT 100 µM SAH	Native gel (EMSA)
PRC2 Elution Buffer	25 mM HEPES 150 mM NaCl 2% Glycerol 0.5 mM TCEP 50 mM Biotin	Protein purification

PRC2 High Salt Buffer	25 mM HEPES 1 M NaCl 2% Glycerol 0.5 mM TCEP 0.1% NP-40	Protein purification
PRC2 Low Salt Buffer	25 mM HEPES 150 mM NaCl 2% Glycerol 0.5 mM TCEP	Protein purification
PRC2 Lysis Buffer	25 mM HEPES 150 mM NaCl 2% Glycerol 0.5 mM TCEP 0.1% NP-40 1x PIC Benzonase	Protein purification
RB High Buffer	10 mM Tris-HCl, pH7.5 2 M KCl 1 mM EDTA 1 mM DTT	Nucleosome Reconstitution
RB Low Buffer	10 mM Tris-HCl, pH7.5 250 mM KCl 1 mM EDTA 1 mM DTT	Nucleosome Reconstitution
Refolding Buffer	10 mM Tris-HCl, pH 7.5 2 M NaCl, 1 mM EDTA 5 mM bME	Octamer Refolding
TBS-T buffer	20 mM Tris 150 mM NaCl 0.1 % Tween 20	WB
Unfolding Buffer	6 M GuHCl 20 mM Tris-HCl, pH7.5 5 mM DTT	Octamer Refolding

8.3. Bacterial Strains and Cell Lines

Name	Organism	Use	Source
BL21 (DE3) pLysS	*E. coli*		Novagen, Cat #70236
DH10EMBacY	*E. coli*	Bacmid generation	Geneva Biotech, DH10EMBacY
EZH1/2 dKO mESCs	*Mus Musculus*	Rescue experiments	Lavarone et al., 2019[335]
EZH1/2 dKO, EV control cells	*Mus Musculus*	Rescue experiments	This thesis
EZH1/2 dKO, EZH2amKR rescue cells	*Mus Musculus*	Rescue experiments	This thesis
EZH1/2 dKO, WT EZH2 rescue cells	*Mus Musculus*	Rescue experiments	This thesis
Sf9	*Spodoptera frugiperda*	Baculovirus generation	Expression Systems, IPLB-Sf-21-AE
SUZ12 KO mESCs	*Mus Musculus*	Rescue experiments	Pasini et al., 2007[336]
SUZ12 KO mESCs, EV control cells	*Mus Musculus*	Rescue experiments	This thesis
SUZ12 KO mESCs, SUZ12deltadim rescue cells	*Mus Musculus*	Rescue experiments	This thesis
SUZ12 KO mESCs, WT SUZ12 rescue cells	*Mus Musculus*	Rescue experiments	This thesis
Tni, High Five (H5)	*Trichoplusia ni*	Protein expression	Expression Systems, 94-002F

8.4. Molecular Weight markers and enzymes

Name	Use	Source
100bp DNA Ladder	DNA Ladder	SM0242
1kb DNA Ladder	DNA Ladder	SM0311
BsaI	Golden Bac	New England Biolabs, R3733S
Fast Digest DPNI EA	Site-directed mutagenesis PCR	Life Technologies, FD1704
Fast Digest MssI	Restriction enzyme	Life Technologies, FD1344
Fast Digest PvuI	Restriction enzyme	Life Technologies, FD0624
FastDigest EcoRV	Restriction enzyme	Life Technologies, FD0303
FastDigest XbaI	Restriction enzyme	Life Technologies, FD0684
GoTaq® DNA Polymerase	Polymerase, nucleosmal DNA	Promega, M8298
In-Fusion® Snap Assembly Master Mix	Golden Bac	Takara, 638949
Phusion Flash High-Fidelity PCR Master Mix	Polymerase	Thermo Scientific, F548L
PHUSION HOT START II HIGH-FIDELITY	Polymerase	Life Technologies, F549L
Plasmid-Safe DNase	Restriction enzyme	Lucigen, 161010
Precision Plus Protein Dual Color Standards	Protein Marker	Bio Rad, 1610374
Precision Plus Protein Unstained Protein Standards	Plasmid isolation	Bio Rad, 1610396
T4 DNA Ligase	Golden Bac	Life Technologies, EL0014

8.5. Plasmids

Construct	Vector	Affinity tag	Resistance	Species	Source
CpG, 601	pUC	-	Amp	-	This thesis
EV	pPB	-	Amp, Puro	-	This thesis
EZH2	pPB	-	Amp, Puro	H. s.	This thesis
EZH2^{amKR}	pPB	-	Amp, Puro	H. s.	This thesis
H2A	pET	-	Amp	X. l.	Dyer et al., 2004
H2B	pET	-	Amp	X. l.	Dyer et al., 2004
H3	pET	-	Amp	X. l.	Dyer et al., 2004
H4	pET	-	Amp	X. l.	Dyer et al., 2004
PRC2	pGB	Strep	Gent	H. s.	This thesis
PRC2$^{\Delta dim}$	pGB	Strep	Gent	H. s.	This thesis
PRC2^{amKR}	pGB	Strep	Gent	H. s.	This thesis
PRC2$^{amKR/Y365A}$	pGB	Strep	Gent	H. s.	This thesis
PRC2^{CXC}	pGB	Strep	Gent	H. s.	This thesis
PRC2$^{CXC/\Delta dim}$	pGB	Strep	Gent	H. s.	This thesis
PRC2$^{CXC/amKR}$	pGB	Strep	Gent	H. s.	This thesis
Suptertransposase	pUC	-	Amp	-	System Biosciences, Cet#PB200PA-1
SUZ12	pPB	-	Amp, Puro	H. s.	This thesis
SUZ12$^{\Delta dim}$	pPB	-	Amp, Puro	H. s.	This thesis

8.6. Antibodies

Antibody	Dilution	Species	Source
Ezh2 (AC22) Mouse mAb	1:1000	Mouse	Cell Signaling, Cat #3147S
Monoclonal Anti-beta-Actin	1:2000	Mouse	Sigma-Aldrich, A5441-.2M
Mouse monoclonal Histone H4 (L64C1) antibody	1:2000	Mouse	Cell Signaling, Cat #2935
Rabbit monoclonal Di-Methyl-Histone H3 (Lys27)	1:1000	Rabbit	Cell Signaling, Cat #9728
Rabbit polyclonal Histone H3K27me3 antibody (pAb)	1:1000	Rabbit	Active Motif, Cat #39155
SUZ12 (D39F6) XP® Rabbit mAb	1:1000	Rabbit	Cell Signaling, Cat #3737S

8.7. Cell culture growth media and bacterial media

Media	Supplements	Use
EMBacY Plates	LB Agar 50 µg/ml Kanamycin 7 µg/ml Gentamycin 10 µg/ml Tetracycline 40 µg/ml IPTG 100 µg/ml Xgal	Blue-White Screening
MESC media	GMEM 20% ES-grade FBS 2 mM Glutamine 100 U/ml Penicillin 0.1 mg/ml Streptomycin 0.1 mM NE-AA 1 mM Sodium pyruvate 50 µM ß-mercaptoethanol 1000 U/ml LIF GSK3β inhibitors MEK 1/2 inhibitors	MESC cultivation
Insect Cell medium	ESF 921 Insect Cell Culture Medium Protein Free 5 % Pen Strep	Insect Cell cultivation
EMBacY Plates medium	LB medium 50 µg/ml Kanamycin 7 µg/ml Gentamycin 10 µg/mL Tetracyline	Transposition
MESC Diferentiation medium	GMEM 20% ES-grade FBS 2 mM Glutamine 100 U/ml Penicillin 0.1 mg/ml Streptomycin 0.1 mM NE-AA 1 mM Sodium pyruvate 50 µM ß-mercaptoethanol 0.1 µM Retinoic acid	MESC cultivation differentiation

8.7.1. Cell culture growth media and bacterial media supplements

Supplement	Use	Source
0.1% Gelatin in Sterile Water	MESC Culture	Merck, ES-006-B
0.25% Trypsin	Cell detachment	Life Technologies, 25200056
Ampicillin	Selection antibiotic	Carl Roth, K029.2
Chloramphenicol	Selection antibiotic	Sigma Aldrich, 56-75-7
ES-grade FBS	MESC Culture	Gibco, 16141002
ESF 921 Insect Cell Culture Medium	Insect culture	96-001-01, Expression Systems
ESGRO® Recombinant Mouse LIF Protein	MESC Culture	Sigma Aldrich, ESG1107
Gentamicin	Selection antibiotic	Fisher Scientific, J62834.06
Glutamine	MESC Culture	Gibco, 25030081
Glycogen synthase kinase GSK-3 inhibitor	MESC Culture	Axon Medchem, AXON 1386 / CHIR99021 / CT99021 / CAS: 252917-06-9
GMEM	MESC Culture	Gibco, 11710035
IPTG	Induction	VWR, 437144NP
Kanamycin	Selection antibiotic	Life Technologies, 11815024
LIF	MESC Culture	Sigma Aldrich, ESG1107
Lipofectamine 2000	Transfection	Life Technologies, 11668030
MEK 1/2 Inhibitor Mirdametinib PD0325901	MESC Culture	Axon Medchem, AXON 1408 / PD0325901 / CAS: 391210-10-9
Non-essential amino acid (NE-AA)	MESC Culture	Gibco, 11140035
PBS	-	Life Technologies, 10010023
Penicillin/ streptomycin	MESC Culture	Gibco, 15140130
Retinoic acid	MESC Differentiation	VWR, R2625-50MG
Sodium pyruvate	MESC Culture	Gibco, 11360039
ß-mercaptoethanol	MESC Culture	Gibco, 21985023
Tetracycin	Selection antibiotic	Sigma Aldrich, T3383-25G
TRANSIT®-Insect TRANSFECTION REAGENT	Transfection	Mirus, 731-0697
X-gal	Blue-White screen	VWR, 730-1498

8.8. Kits

Name	Use	Source
NucleoSpin Gel and PCR Clean-up Kit	DNA isolation	Macherey Nagel, 740609.250
NovaSeq 6000 SP Reagent Kit v1.5	RNA seq	Illumina, 20028401
NucleoBond Xtra Midi EF, Midi Kit	Plasmid isolation	Macherey Nagel, 740420.5
NucleoSpin Plasmid, Mini kit	Plasmid isolation	Macherey Nagel, 740588.250
NucleoSpin RNA Kit	RNA isolation	MACHEREY NAGEL, 740955
Pierce™ Rapid Gold BCA Protein-Assay-Kit	Protein quantification	Thermo Fisher Scientific
QIAGEN Plasmid Mini Kit (25)	Plasmid isolation	Quiagen, 12123
QuantSeq 3’ mRNA Seq Library Prep Kit FWD with Unique Dual Indices for Illumina	RNA seq	Lexogen 115.384

8.9. Equipment

Name	Use	Identifier
4-20% Mini-PROTEAN TGX Stain-Free Protein Gels, 10 well	Protein gels	Bio-Rad, 4568096
4-20% Mini-PROTEAN TGX Stain-Free Protein Gels, 15-well,	Protein gels	Bio-Rad, 7885007
ChemiDoc MP	Signal visualization	Bio Rad, 12003026, 12003028
Eve plus	Cell Counter	Nanoentek, 734-3333
Faclon III	Cryo-EM	Thermo Fisher Scientific
Falcon 4i	Cryo-EM	Thermo Fisher Scientific
HiPrep Sephacryl S-200 HR 26/60	Histone purifcation	Cytiva,17-1195-01
HiTrap Q HP	DNA purifcation	Cytiva,17-1153-01
Mini Trans Blot Cell Bio Rad	Western blot	Bio Rad, M1703910
Model 491 Prep Cell	Nucleosome assembly	BioRad, #1702928
Poros HS 20 resin	Histone purifaction	Thermo Scientific, 1332212
PVDF blotting membranes 0.2 µm	Western Blot	VWR, 10600021
Selectris energy filter	Cryo-EM	Thermo Fisher Scientific
Superdex200 10/300	Size Exclusion	Cytiva, 28-9909-44
Superose 6 10/300	Size Exclusion	Cytiva, 29-0915-96DE
Talos L120C	Negative stain EM	Thermo Fisher Scientific
TC20 Automated Cell Counter	Cell Counter	Bio Rad, 1450102
Titan Krios G3i	Cryo-EM	Thermo Fisher Scientific
Titan Krios G4i	Cryo-EM	Thermo Fisher Scientific
UltrAuFoil® R 1.2/1.3 grid	Cryo-EM	Quantifoil

8.10. Software

Software	Version	Use	Source
Adobe Illustrator	2024/2025	Figure creation	Adobe
ChatGPT	2 (Date 20.11.2024)	Spell checking	OpenAI
Coot	0.9.8.7	Model Building	Emsley et al.[337]
CryoSparc	4.4	Cryo-EM data processing	Structura Biotechnology
Endnote	20	Citation	Clarivate
EPU	-	Cryo-EM data acquisition	Thermo Fisher Scientific
Grammarly	(Date 20.11.2024)	Spell checking	Grammarly
GraphPad PRISM	10	Data analysis	GraphPad Software
Image Lab Software	6.1.0	Densitometric analysis	Bio Rad
Phenix	1.21-5207	Model Refinement	Liebschner et al.[338]
SnapGene	7.2	Sequence management	SnapGene
Topaz	CryoSparc	Cryo-EM particle picking	Bepler et al.[339]
UCSF ChimeraX	1.7.1	Model representation	Meng et al.[340]

9. METHODS

9.1. Molecular Biology

9.1.1. PCR applications

Multiple PCR variations, with different polymerases and different programs were required, depending on the application. The two most common applications were site-directed mutagenesis PCR and generation constructs for In-fusion assembly. For site-directed mutagenesis primers were designed and generated (Integrated DNA Technologies, Inc.) containing the desired mutations flanked by 10-15 bp of complementing DNA. Primer design was assisted by the GeneArt Primer and Construct Design Tool (Thermo Fisher). For generating inserts for In-fuion cloning, primers with 15-20 bp of identical bases to the backbone plasmid were chosen, such that the melting temperature was above 58°C. Primer design was assisted by the In-Fusion Cloning Primer Design Tool (Takara Bio Inc.). Phusion Flash High-Fidelity PCR Master Mix was utilized as standard polymerase according to the manufacturer's instruction and indicated in Table 2.

Table 2: Standard Conditions for Phusion Flash High-Fidelity PCR Master Mix

Step	T [°C]	t [s]	
1	98	10	
2	98	1	30x
3	60	5	
4	72	15s/kb	
5	72	60	
6	4	∞	

Volume [µL]	Component
10	2x Master mix
1	Template DNA (1 ng/µL)
1	Forward primer
1	Reverse primer
7	H_20
20	Total

9.1.2. Agarose gel electrophoresis

An appropriate mass of agarose (1-2%) was added to 1xTAE buffer and carefully melted in a microwave. The mixture was swirled every 30 s until the agarose was dissolved, subsequently stained Midori green (NIPPON Genetics) and cast in an appropriate tray. Samples were supplemented with 6xLoading dye and electrophoresis was carried out at room temperature with 110 V for 30 min. Afterwards the DNA was visualized with UV light and correct bands excised. DNA was extracted from gel slices according to the manufacturer's instructions for the NucleoSpin Gel and PCR Clean-up Kit.

9.1.3. In-Fusion assembly

The Golden Bac system was utilized to express multiple subunit protein complexes in insect cells. [341] This system allows the cloning of 16 different inserts into plasmids with unique overhangs upon BsaI cleavage. The subsequent Golden Gate assembly would combine the insert into one expression vector for transposition.
The In-Fusion system was mainly used to introduce inserts into these plasmids in a ligation independent manner. Firstly, primer pairs were designed with 15-20 bp identical overhang between insert and destination vector, and a melting temperature above 58°C. Initial primers were generated with the Takara Primer Design Tool as inidicated in the manufacturers instructions. The insert and vector DNA was linearized and amplified via PCR, separated via agarose gel electorphoresis and extracted. The reaction mixture was prepared as indicated in Table 3. Afterwards bacteria were transformed with 2.5 µL of the In-fusion mixture.

Table 3: In-Fusion Reaction mixture

Step	T [°C]	t [min]
1	50	15/30
2	4	∞

Volume [µL]	Component
1 µL	5x Enzyme Premix
x	Linearized Vector (50-200 ng)
x	Linearized Insert (10-200 ng)
Ad 5 µL	ddH_2O

9.1.4. Transformation

Competent *E. coli* bacteria of the strand XL-1 Blue,Stellar or DH10β were utilized for heat shock transformation. After 30 min thaw on ice, 100 ng of plasmid DNA or 2.5 µL of In-fusion product were added to the bacteria and incubated for 5 min on ice. Subsequently, they were heat shocked at 42°C for 1 min and recovered on ice for 5 min. Bacteria were then suspended in 500 µL LB-Media and incubated (1h/37°C/750xg). The suspension was centrifuged (1000xg/5min/RT) and 300 µL of the supernatant aspirated. Bacteria were resuspended and plated on agar plates with the respective antibiotic.

9.1.5. Plasmid isolation from *E. coli* culture

For plasmid isolation, 4 mL of LB medium supplemented with the appropriate antibiotic was inoculated with a single bacterial colony. The cultures were incubated overnight at 37°C with agitation at 750 rpm. Following incubation, the cultures were centrifuged at 1000 × g for 5 minutes at 4 °C, and the supernatant was discarded.
The NucleoSpin Plasmid, Mini kit (Macherey Nagel) was used according to the manufacturer's instructions. Briefly, the pelleted bacterial cells were resuspended in 250 µL of Resuspension Solution (Buffer A1) and vortexed. Subsequently, 250 µL of Lysis Solution (Buffer A2) was added, and the mixture was inverted six times to ensure thorough mixing. After 5 min incubation 300 µL of Neutralization Buffer (Buffer A3) was added, and the mixture was inverted six times. The sample was centrifuged (12,000xg/5 m/ 4°C) to pellet the debris, and the supernatant was transferred to a NucleoSpin Plasmid column. The column was centrifuged at (12,000xg/ 1 min/4°C), followed by two washes with 600 µL of Washing Solution (Buffer A4). After each wash, the column was centrifuged (12,000xg/ 1 min/4 °C) and the flow-through discarded. Thereafter, the column was centrifuged (12,000xg/ 1 min/4 °C) and for elution transferred to a fresh collection tube. The column was incubated with 50 µL of ddH_2O at 70°C for 5 minutes, and centrifuged (12,000 x g/ 1 min/4 °C) The concentration of the eluted DNA was measured using a Nanodrop and purified plasmid DNA was subsequently sent for Sanger sequencing, which was performed by Microsynth.

9.1.6. Golden Bac assembly

Golden Gate cloning was used to construct multi-gene expression systems compatible with baculovirus expression systems, as described by Neuhold et al..[341] This so-called Golden Bac system utilizes a set of 16 vectors with unique 4 bp overhangs upon BsaI digest, enabling modular assembly of multi-gene constructs. The pGB vectors have BsaI sites flanking promoter and terminator regions, allowing the insertion of single genes into these insert vectors. The destination vector, pGBdest, features terminal overhangs "01" and "16" for assembling these inserts. Genes of interest are cloned into individual pGB vectors with matching overhangs. The first module must start with "01," the last must end with "16," and intermediate modules must align via compatible overhangs. Empty positions are filled with dummy modules containing appropriate overhangs. To prevent unspecific assembly the genes of interest have to be checked for BsaI digest sites and if present substituted with silent mutations. For the assembly equimolar amounts of all inserts with a concentration of 0.05 pmol and 0.025 pmol of pGBdest were prepared as indicated in Table 4. The longer program with 50 cycles was only tried if the initial assembly yielded no result.

Table 4: Golden Gate assembly program and recipe

Step	T [°C]	t [min]	
1	37	5	11/50x
2	16	5	
3	37	30	
4	50	4	
5	80	20	
6	4	∞	

Volume [µL]	Component
x	pGB inserts
x	pGBdest
2	BSA (2mg/ml)
2	10 x Ligase Buffer
1,2	T4 Ligase
1	BsaI-HF®v2
Ad 20	H2O

Afterwards the mixture was incubated with a nuclease to remove intermediate and not fully ligated products as indicated in Table 5. Afterwards bacteria were transformed with 3-5 µL of the product and successful assembly was verified via Sanger sequencing performed by Microsynth.

Table 5: Plamid Safe digest program

Step	T [°C]	t [min]
1	37	60
2	70	30
3	4	∞

Volume [µL]	Component
0.85	ATP
1	Plasmid Safe Nuclease

9.1.7. Histone expression

Plasmids containing the four canonical histones were transformed into BL21 RIL as previously described and incubated on agar plates with the respective antibiotic at 37°C ON. Subsequently, a 50 mL culture was inoculated and incubated for 1-2 h at 37°C under agitation. Afterwards, 3-4 L cultures were prepared with the 50 mL pre-culture and allowed to grow at 37°C under agitation until reaching the bacterial log phase (OD: 0.5). Thereafter, histone expression was induced with 0.2 mM IPTG for 3-4 h, whereafter cells were harvested by centrifugation (1000xg, 10 min, 4°C). Cell pellets were flash-frozen and stored at -80°C.

9.1.8. Electrophoretic mobility shift assay (EMSA)

EMSAs were performed using a 5% Native TBE gel in 0.2x TBE buffer with a total volume of 15 µL reactions of 50 nM nucleosome and increasing concentrations of PRC2 in triplicates in PRC2 Binding Buffer. The reaction mixture was incubated at room temperature for 30 minutes and supplemented with sucrose to a final concentration of 5%. The gels were run at 150 V for 1 h and then stained with SYBR™ Gold (Thermo Fisher) according to the manufacturer's instructions. The stained gels were imaged using a ChemiDoc MP (BioRad) imager, and densitometric analysis was performed using Image Lab Software version 6.1.0 (BioRad). The bands of the shifted (bound) and free nucleosomes (unbound) were identified and boxed out. After background correction, the bound signal was divided by the sum of both signals to determine the bound fraction.

9.1.9. RNA isolation and RNA seq

Total RNA was isolated from cells using the NucleoSpin RNA Kit according to the manufacturer's instructions. RNAseq was performed by the AG Hänsel-Hertsch. Briefly, libraries for RNA seq were generated using QuantSeq 3' mRNA Seq Library Prep Kit FWD with Unique Dual Indices for Illumina. Sequencing was performed on an Illumina NovaSeq 6000 platform with NovaSeq 6000 SP Reagent Kit v1.5 100 cycles. RNA seq experiments were conducted with three independent biological replicates.

9.2. Cell culture

9.2.1. General insect cell cultivation

Sf 9 cells were used for transduction and virus generation while High Five were used for protein expression. Both cell lines were cultivated as suspension cultures in Insect Cell Medium at 28˚C with 120 rpm in glass Erlenmeyer flasks. Sf9 cells were passaged at a density of 6-8 x 10^6 cells/ml to 0.5 x 10^6 cells /ml while Tni cells were passaged at a density of 6-7x 10^6 cells /ml to 0.2 x 10^6 cells /ml. Cell density, viability and diameter were verified with an Eve plus cell counter (Nanoentek). Juliane Renn of the Poepsel Lab performed most of the maintenance of the insect cells.

9.2.2. Transposition

In this project, chemically competent DH10EMBacY bacteria were used to generate bacmids for virus generation. First, 100 ng of DNA was incubated with 100 µL of bacteria and incubated on ice for 30 min. Thereafter, heat shock was performed at 42°C for 15 s and cells were incubated on ice for 5 min. Thereafter, cells were suspended in 800 µL of LB medium and allowed to recover for 3-5 h. Subsequently, 50-100 µL of the cells were plated on EMBacY Plates medium and incubated for 48 h. After the blue-white screen, white colonies were inoculated into 4 mL of EMBacY Medium and incubated over night (ON/37°C/ 150 rpm)be.

9.2.3. Bacmid DNA purification

After the blue-white screen, several white colonies were inoculated into 4 mL of EMBacY Medium and incubated ON/37°C/ 150 rpm. Subsequently, the cell suspension was pelleted (500xg/3 min/RT) and lysed according to the manufacturer's instructions for the Plasmid Mini Kit (Quiagen) for the following steps: Cells were resuspended in 250 µL of A1 Buffer. After the addition of 250 µL of buffer A2, 10x gentle inversion cells were lysed for 5 min at RT. Afterwards, 350 µL of Buffer A3 was added for neutralization and following 10x gentle inversion and subsequent centrifugation (21000xg/10 min/4°C).
Subsequently, 700 µL of the supernatant was combined with 700 µL of ice-cold isopropanol, mixed vigorously and incubated at -80°C for 30 min. After a centrifugation (21000xg/30 min/4°C) the supernatant was aspirated, and the pellet was carefully washed with 800 µL of 70% EtOH. After another centrifugation (21000xg/30 min/RT) the supernatant was aspirated, and the pellet air-dried at RT for 5 min and resuspended in 100 mL of ddH_2O. The DNA concentration was determined with a nanodrop.

9.2.4. Transfection of Sf9 cells

Firstly, Sf9 cells were seeded in 2 mL of Insect Cell Medium in 6-well plates at a density of $1x10^6$ cells/mL and left to attach for at least 1 h. Meanwhile, one transfection mix per well was prepared according to the manufacturer's instructions by diluting 2.5 µg of bacmid DNA in 250 µl serum-free medium and supplementing with 5 µl TransIT reagent. After gently mixing by pipetting and an incubation of 30 min the transfection mix was added carefully drop-wise to the respective well. After 2-3 days transfection could be checked for YFP expression in the cells, because the EmBacY cells have a YFP reporter that is expressed upon successful expression. After 5-6 days, the supernatant of wells with cells that showed a strong YFP signal, and a cytopathic effect of swelling and clumping was harvested. The supernatant is the first virus stock V0 and could be stored at 4°C.

9.2.5. Virus amplification

For protein expression, a larger amount of virus is required. Thus, the V0 stock was amplified by infecting a 50 mL Sf9 suspension cell culture at a density of $1x10^6$ cells/mL with the entirety of 2 mL V0. After incubation of 4-5 days, the infection efficiency was verified by checking the YFP expression. Subsequently, the cells were pelleted (700xg/3 min/RT) and the supernatant, the second virus stock V1, could be stored at 4°C. For most expressions a V1 stock was sufficient. If additional viruses were required a V2 stock could be generated by infection 50 mL Sf9 suspension cell culture at a density of $1x10^6$ cells/mL with 1% of V1 stock and harvesting after 4 days.

9.2.6. Protein expression

Generally, subunits of multi-protein complexes were expressed using one virus stock from one plasmid, utilizing the GoldenBac system.[341] However, it is possible to achieve the same expression by mixing virus stocks expressing the respective subunits. To evaluate protein virus stock quality and subsequent protein expression efficiency, an initial test expression of 50 mL Tni cells at a density of $1x10^6$ cells/mL was infected with 1.5% of V1. After 3 days, cells were harvested and 500 µL of the cell suspension was centrifuged (700xg/3 min/RT) and the supernatant aspirated. The pellet was resuspended in 1xLD and syringe-sheared with 21g syringes. Expression was evaluated by SDS-gel against a non-transfected Tni control.
Larger expressions were generally performed at 400 mL and infected as previously described. After 3 days, cells were harvested by pelleting (700xg/3 min/RT), aspirating the supernatant and subsequent flash-freezing. Cell pellets were stored at -80°C

9.2.7. General mouse embryonic stem cell (mESC) cultivation

The EZH1/2 dKO and SUZ12 KO mESCs (N/A Strain of origin 129P2/Ola) used were kindly provided by the Pasini lab and previously characterized.[120, 335] The cells were cultured on 0.1% gelatin-coated dishes in mESC media supplemented with fresh GSK3β and MEK 1/2 inhibitors (Axon Medchem BV) to a final concentration of 3 µM and 1 µM, respectively. For maintenance, cells were passaged at a confluency of between 70 and 80% every 2–3 days by washing twice with phosphate-buffered saline (PBS) and dissociation with 0.25% Trypsin for 3 min at 37°C. The reaction was stopped with an excess of mESC media and the cells were gently suspended, centrifuged and resuspended in a fresh medium. Subsequently, cells were seeded in a 1:8 dilution.

9.2.8. Generation and differentiation of stable mESC cells

For transfection, EZH2 wild type, SUZ12 wild, EZH2amKR and SIU12Δdim were cloned into a pPB_PGK plasmid and co-transfected with a piggyback transposase at a ratio of 1:2.5 respectively using Lipofectamine 2000 following the manufacturer's instructions and were selected with puromycin (1 µg/ml) for two weeks. Successful transfection was verified with Western blot.
For differentiation, mESCs were seeded at a density of 10500 cells/cm^2 in mESC media lacking LIF, GSK3β, and MEK 1/2 for 12 hours to allow for cell attachment. The media was then exchanged and supplemented with 0.1 µM all-trans-retinoic acid, and subsequently changed every 48 hours. Cells were harvested as previously described.

9.3. Protein Biochemistry

9.3.1. PRC2 purification

The PRC2 in this project utilized AEBP2 (Q6ZN18-3) with an N-terminal Twin-Strep-tag. Initially, frozen cell pellets were resuspended in PRC2 Lysis Buffer, whereas the NP-40 and Benzonase were added freshly after resuspension. The suspension was incubated for 30 min on ice and subsequently sonicated with (50% amplitude, 15s on, 45s off, and 6 min total). The cell lysate was centrifuged (21,000xg/30 min/4°C) and the supernatant was collected. In the meantime, an appropriate column volume (CV) of usually 2 mL per 400 mL expression volume of Strep-Tactin®XT 4Flow® resin was prepared for batch binding by three steps of centrifuging (700xg/5min/4°C) and washing with PRC2 Lysis buffer. Subsequently, the resin was resuspended in the supernatant and incubated ON/4°C with slight agitation. Afterwards, the resin was sedimented in a Streptactin column and washed first with 10xCV of PRC2 Low Salt Buffer, then 10xCV of PRC2 High Salt Buffer and eventually again with 10xCV of PRC2 Low Salt Buffer. Proteins were eluted with PRC2 Elution Buffer in 0.6 CV as elution fraction 1 (E1), then 1.6 CV (E2), 1 CV (E3) and 0.8 CV (E4, E5). At this stage, the quality of the affinity chromatography was evaluated via sodium dodecyl sulfate – poly acrylamide gel electrophoresis (SDS-PAGE). Fractions with successfully eluted protein were combined and digested with in-house purified TEV protease. Subsequently, the eluate was concentrated following the manufacturer's instruction to a volume of 250-500 µL. In a final step, the concentrate was further purified via SEC using a pre-equilibrated Superdex200 10/300 in PRC2 Low Salt Buffer. Successful purification was evaluated via SDS-PAGE and suitable protein fractions were concentrated, flash-frozen and stored at -80°C.

9.3.2. Protein extraction from mESCs

Protein extraction was performed by resuspending and incubating the harvested cell pellet in ice-cold RIPA buffer supplemented with a protease inhibitor cocktail and 1 µg/mL Benzonase (produced in-house) on ice for 30 minutes. Subsequently, the cells were sonicated (30s on, 30s off, 5 min total) and the lysate was centrifuged (23.000xg/30 min/4 °C). Protein concentration was determined with Pierce™ Rapid Gold BCA Protein-Assay-Kit and normalized to 60 µg before being supplemented with 5xLD buffer. Protein lysates were separated via SDS-PAGE and transferred to the PVDF membrane at 90V for 120 minutes. Membranes were probed with primary antibodies ON at 4°C and washed three times with TBS-T. Afterwards, secondary antibodies were incubated at RT for 1 h and washed three times with TBS-T and once with TBS. The protein signals were detected on a ChemiDoc MP.

9.3.3. Nucleosome reconstitutions

9.3.3.1. Generation of nucleosomal DNA

The nucleosome reconstituion follows closely the protocol published by Luger et al. and Dyer et al..[342, 343] For easy generation of nucleosomal DNA, a pUC plasmid (Materials 8.5) was generated with 601 widom DNA with a CpG linker.[344] We amplified sufficient quantities of this plasmid as template DNA and subsequently performed large-scale PCR in 96-Well plates as indicated in Table 6. PCRs were verified sporadically via agarose gel electrophoresis and pooled. The volume of 6 96-wells was thereafter loaded on HiTrap Q HP for anion exchange. Exchange chromatography was subsequently performed with Anion Exchange Low Buffer with a fast-increasing gradient to 50 % and a slowly increasing gradient to 100 % of Anion Exchange High Buffer. The eluted fractions were pooled and acidified with 1/10th of the volume of 3 M sodium acetate (pH 5.2). The mixture was combined with two volumes of 100% EtOH and mixed vigorously. After incubation at -80°C for 30 min, the sample was centrifuged (23.000xg/30 min/4 °C) and the supernatant was aspirated. The precipitated DNA pellet was washed with ice-cold 70% EtOH and centrifuged (23.000xg/30 min/4 °C). After removing the supernatant, the pellet was dried at RT for 15 min and resuspended in RB High Buffer. The concentration was determined with nanodrop spectrophotometry.

Table 6: PCR settings and reaction for generating cPG DNA

Step	T [°C]	t [s]
1	94	180
2	94	30
3	58	15
4	72	30
5	72	120
6	4	∞

Volume [µL]	Component
980	5x Buffer
196	dNTPs
245	cPG_fwd
245	cPG_rev
392	25 mM $MgCl_2$
98	5 ng/µL template
2, 720	H_2O
24.5	GoTaq
4,900.5	Total

9.3.3.2. Inclusion body purification

The day before protein expression, BL21 RIL cells were transformed and plated on LB agar plates containing chloramphenicol and ampicillin. The plates were incubated at 37°C for 16-20 hours. Cells were cultivated in 2x YT supplemented with 0.1% glucose and half the standard concentration of Cm and slightly lower than the normal concentration of Amp. Several 2-3 mL cultures were inoculated from a few colonies each and grown for 3 hours until cultures became turbid. These small cultures were then used to inoculate larger cultures of 50-100 mL each, which were grown until the optical density (OD) reached approximately 0.5. These cultures were centrifuged at 4,000 rpm for 10 minutes, resuspended in fresh medium, and used to inoculate larger cultures, typically 2-3 liters. Once the OD reached around 0.4-0.5, protein expression was induced with 0.2 mM IPTG. Expression was allowed to proceed for 3 hours at 37°C. Afterwards, cells were centrifuged at (3,000 rpm/10 minutes) and the resulting pellet resuspended in approximately 20 mL of Histone Wash Buffer per 2-3 liters of culture. The cells were freeze-thawed two times in liquid nitrogen and a waterbath and subsequently supplemented with 1 tablet of PIC and 2.5µL of benozonase. Cells were lysed on ice via sonication (amplitude 60 %, on: 10 sec, off: 15 sec, total: 8 min) and thereafter centrifuged. (23,000xg, 4˚C, 20 min) whereafter the supernatant was discarded. The pellet with inclusion bodies was resuspended with Histone Wash Buffer supplemented with 1% Triton X-100, PIC and benzonase and centrifuge (12,000xg, 4˚C, 10 min). This washing step was repeated once and subseqently twice without Triton X-100 supplementatation. Eventually the pellet with washed inclusion bodies could be stored at -20°C.

9.3.3.3. Histone extraction

The pellet with inclusion bodies was suspended in 300 µL DMSO, minced with a spatula and soaked on ice for 30 min. Thereafter, Extraction buffer was added slowly, while the pellet was stirred vigorously, suspended with a pipetous and incubated for 1 h. After a second resuspension step the sample was centrifuged (23,000xg, 20˚C, 10 min) and the supernatant collected for size exclusion. The extracted histones were loaded on an equilibrated GE HiPrep Sephacryl S-200 HR 26/60, fractions verified via SDS PAGE and pooled for cation exchange. The sample was diluted with Cation Exchange Buffer without NaCl to a concentration approximately 100 mM NaCl. Cation exchange was performed on a 10 mL self packed column with Poros HS 20 resin by running a gradient from 0 mM NaCl to 1M NaCl Cation exchange buffer. Eluted fractions were verified with SDS PAGE pooled and dialized three times against 3 L of H_2O with 2 mM bME at 4°C. Concentration was determined via nanodrop and the histones were lyophilized in aliquots of approximately 1-2 mg for later octamer refolding.

9.3.3.4. Octamer Refolding and purification

Of each histone, 2 mg of protein was suspended in 1 mL Unfolding Buffer and incubated on ice for 30 min, with concentrations determined by nanodrop spectrophotometry. Equimolar amounts of histones were calculated with an additional 10% excess of H2A and H2B, then combined and diluted to a final concentration of 1 mg/mL octamer. The octamer solution was dialyzed twice overnight and once for 6 h against the Refolding Buffer. After dialysis, the refolded octamers were centrifuged /21,000 xg/10 min/4°C) and purified by size exclusion chromatography on a Superdex200 10/300 column. The SEC fractions were analyzed by SDS-PAGE and the octamer-containing fractions were pooled, concentrated and stored on ice at 4°C until further use.

9.3.3.5. Nucleosome assembly and purification

Due to a certain possibility of variability during nucleosome reconstruction, different ratios of DNA to octamer were tested at a smaller scale. Octamer to DNA ratios from 0.8:1 to 1.2:1 at a constant concentration of 4 µM DNA were tested. Therefore, the DNA was diluted in a 20 µL reaction with RB High buffer and subsequently, the octamer was added. Afterwards, the solution was dialyzed ON at 4°C against 400 mL of RB High buffer, which was gradually replaced with 1600 mL of RB Low buffer at a flow rate of 1.2 mL/min. Subsequently, the reaction was dialyzed against 400 mL of RB Low buffer for 1h/ON/4°C. The samples were evaluated via EMSA as described in method section 0.

Before large-scale reconstitution, a Model 491 Prep Cell was prepared with a 7.5 cm column of native gel. For large-scale nucleosome assembly, a reaction of 1.5 mL was dialyzed as previously described and additionally dialyzed against 1xTCS buffer buffer for 2h/4°C. Subsequently, the Model 491 Prep Cell was assembled according to the manufacturer's instructions and chambers filled with 0.2xTBE and 1xTCS as indicated in Figure 15. The bottom chamber was also filled with 0.2xTBE and the outlet ran through an ice slurry to ensure sufficient cooling of the native gel. The flow rate of the fractionator was adjusted to ~1ml/min and subsequently, the native gel was prerun at run at 10 W for 1.5 h. Thereafter, the sample was supplemented with sucrose to a final concentration of 5 % loaded on the native gel and ran at 10W constant. Elution was collected and analyzed via EMSA as described in method section 0.. The nucleosome is usually eluted after 1h.

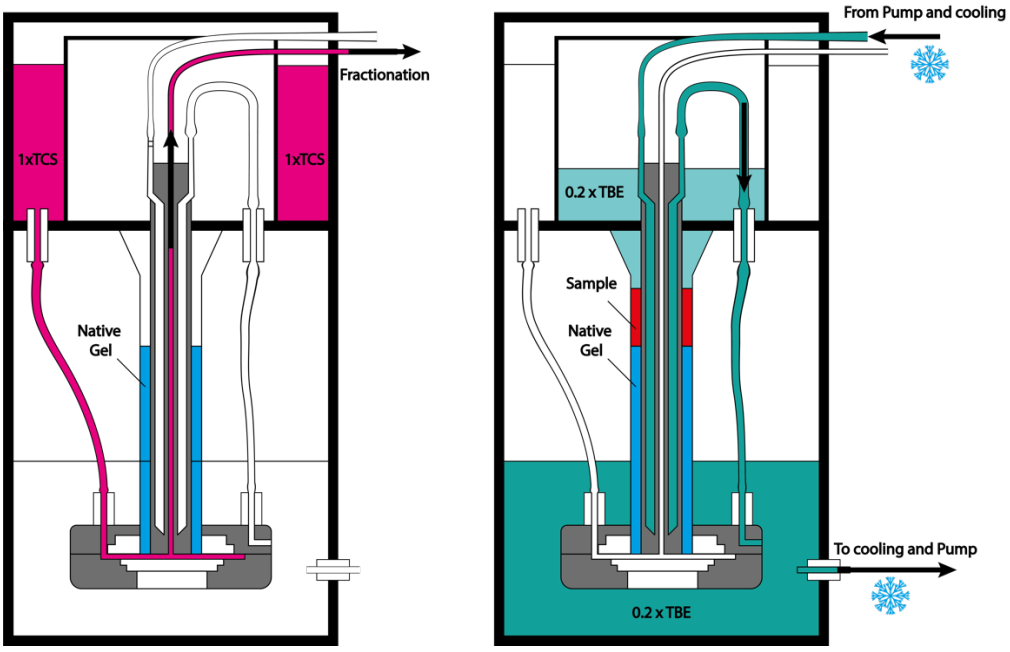

Figure 15: Nucleosome reconstitution in a prep cell

The 491 prep cell has two different buffer chambers. Left: The outer chamber was filled with 1xTCS and would elute reconstituted nucleosome for fractionation. Right: The inner chamber contained the native gel, that would separate the sample and was filled with 0.2xTBE. The bottom chamber was also filled with 0.2xTBE and the tubing was running through an ice slurry to ensure cooling of the native gel.

9.3.4. Histone methyltransferase assay of PRC2

HMTase reactions were carried out in a total volume of 12 µL containing 200 nM nucleosome and 400 nM PRC2 in the PRC2 Activity Assay. Before adding the nucleosome, the reaction mix with PRC2 was preincubated at room temperature for 1 hour to allow for automethylation.
The reaction was incubated at room temperature for 90 minutes and subsequently quenched by adding 5x loading buffer and heat inactivating at 95°C for 5 minutes. In the case of peptide stimulation, the peptides were added last, immediately after the nucleosome. Gel electrophoresis was performed with 4–20% Mini-PROTEAN® TGX™ precast protein gels and the stain-free signal was detected according to the manufacturer's instructions. Proteins were subsequently transferred to a 0.2 µM PVDF membrane at 90V for 10 min and 60V for 30 min. Membranes were probed with primary antibodies ON at 4°C and washed three times with TBS-T. Subsequently, membranes were incubated with secondary antibodies at RT for 1 h and washed three times with TBS-T and once with TBS. Reactions were performed in multiplets and detected on a ChemiDoc MP. Densitometric analysis was performed using the Image Lab Software version 6.1.0 (BioRad) by background-correcting the signal to the negative control and normalizing it against the WT signal. GraphPad Prism was used for visualization.

9.3.5. Mass spectrometry analyses of methylation

Mass spectrometry was performed by Farnusch Kaschani at the Department of Chemical Biology at the University of Duisburg-Essen.
Sample preparation for LC/MS/MS is based on the SP3 protocol (REF Hughes, 2019). 15 µg protein extracts were taken up in 100 µL 1× SP3 lysis buffer (final concentrations: 1% (wt/vol) SDS, 10 mM TCEP, 200 µL 40 mM chloracetamide, 250 mM HEPES pH 8) and heated for 5 min at 90 °C. Since the samples were purified proteins the Benzonase treatment was skipped. Next samples were mixed with 75 µg hydrophobic (#65152105050250) and 75 µg hydrophilic (#45152105050250) SeraMag Speed Beads (Cytiva) (bead to protein ratio 10 to 1) and gently mixed. Then 100 µL 100% vol/vol Ethanol (EtOH) was added before incubation for 20 min at 24°C shaking vigorously. The beads were

collected on a magnet and the supernatant was aspirated. The beads were then washed 4 times with 180 µL 80 % EtOH (collection time on the magnet minimum of 4 min). The beads were finally taken up in Arg-C incubation buffer (50 mM Tris-HCl (pH 7.6-7.9), 5 mM $CaCl_2$, 2 mM EDTA) containing 150 ng ArgC (Promega V1881; activated in Arg-C activation buffer (50 mM Tris-HCl (pH 7.6-7.9), 50 mM DTT, 2 mM EDTA). To help bead dissociation, samples were incubated for 5 min in a sonification bath (preheated to 37°C). Samples were incubated overnight, shaking vigorously (1300 rpm). The next day samples were acidified with formic acid (FA, final 1% vol/vol) before collection on a magnet. The supernatants were transferred to a fresh Eppendorf tube, before removing trace beads using a magnet for 5 min. The tryptic digests were then desalted on homemade C18 StageTips as described (REF Rappsilber, 2007 #12724). Briefly, peptides were immobilized and washed on a homemade 2-disc C18 StageTip. Samples were then dried using a vacuum concentrator (Eppendorf) and the peptides were taken up in 0.1% formic acid solution (10 µL) and directly used for LC-MS/MS experiments.

LC-MS/MS experiments were performed on an Orbitrap Fusion Lumos (Thermo) that was coupled to a Vanquish Neo-liquid chromatography (LC) system (Thermo). The LC was operated in the one-column mode. The analytical column was a fused silica capillary (75 µm × 28 cm) with an integrated frit emitter (CoAnn Technologies) packed in-house with Kinetex C18-XB core-shell 1.7 µm resin (Phenomenex). The analytical column was encased by a column oven (Sonation) and attached to a nanospray flex ion source (Thermo). The column oven temperature was adjusted to 50 °C during data acquisition. The LC was equipped with two mobile phases: solvent A (0.2% formic acid, FA, 99.9% H_2O) and solvent B (0.2% formic acid, FA, 80% Acetonitrile, ACN, 19.8% H_2O). All solvents were of UPLC grade (Honeywell). Peptides were directly loaded onto the analytical column with a maximum flow rate that would not exceed the set pressure limit of 950 bar (usually around 0.5 µL/min). Peptides were subsequently separated on the analytical column by running a 105 min gradient of solvent A and solvent B (start with 8% B; gradient 8% to 80% B for 80:00 min; gradient 80% to 100% B for 19:00 min and 100% B for 6:00 min) at a flow rate of 250 nl/min. The mass spectrometer was operated using Tune v3.5.3881.18. The mass spectrometer was set in the positive ion mode. Precursor ion scanning was performed in the Orbitrap analyzer (FTMS; Fourier Transform Mass Spectrometry) in the scan range of m/z 380-1800 and at a resolution of 120000 with the internal lock mass option turned on (lock mass was 445.120025 m/z, polysiloxane) (REF Olsen 2005). Product ion spectra were recorded in a data dependent fashion in the FTMS at a resolution of 30000. The ionization potential (spray voltage) was set to 2.3 kV and ion transfer capillary temperature was set to 270 °C. RF-lens was set to 40% to facilitate the transition of larger peptides. Peptides were analyzed using a repeating cycle (cycle time max 3 sec) consisting of a full precursor ion scan (AGC standard; acquisition time “auto”) followed by a variable number of product ion scans (AGC 200% and acquisition time 70 ms) where peptides are isolated based on their intensity in the full survey scan (threshold of 50000 counts) for tandem mass spectrum (MS2) generation that permits peptide sequencing and identification. Fragmentation was achieved by stepped Higher Energy Collision Dissociation (sHCD) (NCE 25, 02, 40). During MS2 data acquisition dynamic ion exclusion was set to 30 seconds and a repeat count of one. Ion injection time prediction, preview mode for the FTMS, monoisotopic precursor selection and charge state screening were enabled. Only charge states between +3 and +10 were considered for fragmentation.

Data analysis. RAW spectra were analysed in Proteome Discoverer (v2.5.0.400) using Sequest HT and MS Amanda 2.0 Nodes. The MS/MS spectra data were searched against a project-specific database containing the 5 sequences of the investigated protein complex (ACE_0861_SOI_v01.fasta; 5 entries). All searches also included a contaminants database search (contaminants. fasta, 245 entries). The contaminants database contains known MS contaminants and was included to estimate the level of contamination. The searches allowed the oxidation of methionine residues (16 Da), Monomethylation (14)/ Dimethylation (28 Da)/ Trimethylation (42 Da) on Lysin as variable modifications. Carbamidomethylation on Cystein (57) was selected as static modification. Enzyme specificity was set to “Trypsin_R (full)” (which is the specificity of “ArgC”. The precursor mass tolerance was set to ±10 ppm. The MS/MS match tolerance was set to ±0.02 Da. The PSM validation

was done using the Percolator Node (target FDR strict 0.01 and relaxed 0.05 based on the target-decoy approach). Feature detection was done using the Minora Node (default settings). In the consensus workflow, the Feature Mapper node was set to align retention times (max window 10 min). The "precursor ion quantification" node was set to do ion quantification based on intensity. The calculated abundances for the combined EP01 ($PRC2^{CXC}$) and EP02 ($PRC2^{CXC/\Delta dim}$) runs were extracted from the peptide groups output together with the coefficients of variation of the variation. All values were transferred to the log2(x) scale and used to generate the bar diagram.

9.3.6. SDS polyacrylamide gel electrophoresis

SDS-PAGE was conducted using either 4-20% gradient MP TGX Stain-Free Gels (Bio-Rad) or self-cast gels. For self-cast gels, the separating gel mixture was poured into a cassette and topped with isopropanol for polymerization. Isopropanol was then removed and the stacking gel added with a comb to form wells. Protein samples were diluted to equal concentrations with water and 5x Laemmli buffer, then boiled at 95°C for 10 minutes to denature the proteins. Samples, along with a size marker, were loaded onto the gel. Electrophoresis was performed at 110 V for 30 minutes, followed by 130 V until bromophenol blue reached the end of the gel. Gels were visualized with Stain-Free, stained with Coomassie Brilliant Blue (CBB) or processed for Western blotting.
For Stain-Free imaging, the trihalo compound in the gels was photoactivated for either 45 s or 5 min. For CBB staining, gels were washed with ddH_2O, boiled in CBB solution, and incubated for 10 min at room temperature. They were then washed twice with ddH_2O, boiled in Destaining solution and incubated for 30 min at room temperature. Protein detection was carried out using the ChemiDoc MP (BioRad) imager.

9.3.7. Western Blot

Proteins were transferred from SDS gels to Immobilon®-FL PVDF membranes (Merck Millipore) using a Mini Trans Blot Cell (Bio-Rad). The blotting sandwich was assembled according to the manufacturer's instructions, utilizing two pieces of Whatman paper as filter paper. The transfer was conducted on ice in the cold room with a constant voltage of 90 V for 120 min.
Following electrophoretic transfer, the PVDF membrane was incubated with 5 mL of blocking buffer for 1 hour at room temperature, then washed twice with TBS-T. The membrane was incubated overnight at 4°C with primary antibodies. Unbound primary antibodies were removed by washing three times with TBS-T. The membrane was then incubated for 1 hour at room temperature with secondary antibodies diluted 1:10,000 in TBS-T. Afterwards, the membrane was washed five times for 10 minutes with TBS-T and once with TBS. Immunoreactive bands were visualized using the ChemiDoc MP (BioRad) imager.

9.4. Structural Biology

9.4.1. Negative stain EM

Negative-stain analysis of PRC2 was performed by Dr. Simon Poepsel as described before.[200] Briefly, 4 µL of 200 nM PRC2 was applied to a continuous carbon grid and incubated for 45 seconds. This was followed by five sequential short incubation steps with 2% (w/v) uranyl formate stain. Excess stain was blotted from the grid edges using filter paper, and the grids were air-dried.
Screening and data collection were conducted on a Talos L120C microscope (Thermo Fisher) using EPU for automated data acquisition. Data were acquired at an electron dose of 25 $e^-/Å^2$ with a nominal pixel size of 2.44 Å/px.

9.4.2. Negative stain EM data processing

Data processing was carried out by Dr. Simon Poepsel using cryoSPARC, [345] with contrast transfer function (CTF) estimation performed via CTFFIND4[346] and particle picking using the blob picker. For $PRC2^{WT}$, $PRC2^{amKR}$ and $PRC2^{\Delta dim}$, a total of 117,434, 248,000, and 176,329 particle images, respectively, were extracted from initial picks based on 242, 398, and 286 manually curated micrographs. Several rounds of 2D classification were conducted, resulting in subsets of particle classes exhibiting the typical structural features of PRC2. These structural features were found to be generally consistent across $PRC2^{WT}$ and variants. Representative views of intact PRC2 were selected and orientation-adjusted for further analysis.

9.4.3. Cryo-EM sample and grid preparation

Prior to cryo-EM, sample quality was evaluated using negative staining electron microscopy as previously described (Chapter 9.4.1, data not shown). For cryo-grid preparation, 3 µL of purified protein was applied to glow-discharged UltrAuFoil® R 1.2/1.3 grids (Quantifoil), which had been treated for 1 minute and 45 seconds, no more than 15 minutes prior to use. Grids were blotted for 4 seconds under conditions of 100% humidity, 8°C and 0 blot force, then plunged into liquid ethane cooled by liquid nitrogen using a Vitrobot Mark IV (Thermo Fisher Scientific). Prepared grids were stored in liquid nitrogen until further use.

9.4.4. Cryo-EM data collection

Cryo-EM data for AIFM1-MIA40 were collected using a Titan Krios G3i (Thermo Fisher Scientific), while data for the AIFM1 dimer and AIFM1-AK2A complex were acquired on a Titan Krios G4 (Thermo Fisher Scientific), all operated at 300 kV with a 35° tilt to overcome preferred orientation using EPU (Thermo Fisher Scientific).
Two datasets were collected for the AIFM1-MIA40 complex, consisting of 1,907 and 2,084 raw movies, respectively, using a Falcon III direct electron detector with a pixel size of 0.654 Å/pixel, which was calibrated with apoferritin. The total electron dose was 50.82 $e^-/Å^2$ for the first dataset and 50.57 $e^-/Å^2$ for the second, each distributed across 48 frames, with a defocus range of −0.6 to −2.6 µm.
For the AIFM1 dimer, 15,440 raw movies were recorded at a pixel size of 0.46 Å/pixel, and for the AIFM1-AK2A complex, 4,542 movies were collected at a pixel size of 0.58 Å/pixel. These datasets were obtained with a Falcon 4i detector equipped with a Selectris energy filter (Thermo Fisher Scientific) and were stored in electron-event representation (EER) format. Each dataset received a total electron dose of 50 $e^-/Å^2$, distributed over 468 frames, with a defocus range of −0.7 to −1.7 µm.

9.4.5. Cryo-EM data processing

All datasets were processed using cryoSPARC (v4.4).[345] Detailed workflows are provided in Supplementary Figure 1 for the AIFM1 dimer, Supplementary Figure 2 for AIFM1-MIA40 and Supplementary Figure 3 for AIFM1 AK2A. Briefly, the movies underwent patch-based motion correction and CTF estimation during preprocessing. Initial particle identification was performed via blob picking and 2D classification to isolate classes with distinct features, which were subsequently used to train the TOPAZ particle picker.[339] After an additional 2D classification, particles were split into high- and low-defocus groups and each set was used for further TOPAZ training. Iterative cycles of TOPAZ picking, 2D classification, and ab initio reconstruction yielded good results which led to homogeneous or non-uniform refinement of high-quality reconstructions.
For the AIFM1 dimer, two initial models comprising 149,783 and 188,760 particles, respectively, were pooled and classified via *ab initio* classification and subsequently refined using non-uniform refinement. For the AIFM1-AK2A complex (229,483 particles) and the AIFM1-MIA40 complex (310,098 particles), additional rounds of TOPAZ training, 2D classification, and ab initio reconstruction were conducted, followed by either homogeneous or non-uniform refinement.
Particle extraction was performed with box sizes of 420 pixels for AIFM1-MIA40 and 416 pixels for the AIFM1 dimer and AIFM1-AK2A. Final refinements included Reference Motion correction, yielding resolutions of 2.8 Å for the AIFM1 dimer (277,866 particles), 2.4 Å for AIFM1-MIA40 (291,656 particles), and 2.6 Å for AIFM1-AK2A (307,496 particles).

9.4.6. Cryo-EM data fitting, modelling and refinement

For all AIFM1 structures generated in this study, initial models were obtained using AlphaFold2 and cross-referenced with previously published human and mouse AIFM1 structures (PDB: 4BUR and PDB: 3GD4). Residue adjustments were performed in Coot [337] while iterative refinement and optimization was conducted using PHENIX (v1.21). [338] Maps were processed using DeepEMhancer to enhance visualization during initial model construction.[347] Structural maps and models were visualized and analyzed with ChimeraX. [340, 348] Data collection statistics and validation reports were generated automatically via MolProbity within PHENIX and are collected in Table 7. [349]

9.5. Data Analysis

9.5.1. RNA seq data analysis

The data analysis of the RNAseq data was performed by Dr. Pascal Hunold of the Hänsel-Hertsch group. Upon quality trimming using bbduk[350] (k=13 ktrim=r useshortkmers=t mink=5 qtrim=t trimq=10 minlength=20), fastq files were aligned with STAR[351] v2.7.3a to the *mm10* mouse reference genome. BAM files were down-sampled to 8 million reads with samtools[352] v1.13 and counted by HTSeq[353] v2.0.1 (-m union -s no -t exon). Differential expression analysis was performed using DESeq2 [354] v1.38.3. Expression of marker genes during RA-driven differentiation was extracted from DESeq2 (counts(dds, normalization = TRUE)) and plotted with Prism v9.2.0. PCA with mean log-transformed DESeq2 (rlogTransformation(dds, blind = FALSE)) was plotted with the ggplot2 v3.4.2. PCA mean top 10000 most variable genes were plotted with the ggplot2 v3.4.2. Variant stabilisation transformed counts were plotted for the top 50 most differentially expressed genes with the pheatmap v1.0.12 package.

CHAPTER I: FUNCTIONAL CHARACTERIZATION OF PRC2 DIMERIZATION ON CHROMATIN

10. RESULTS

The Polycomb Repressive Complex 2 (PRC2) is an epigenetic regulator that acts as a methyltransferase for H3K27. However, it requires an allosteric activator for efficient catalytic activity. Recent studies revealed that PRC2 can methylate three lysines on its own catalytic subunit EZH2, which enhances its enzymatic activity — a process known as automethylation.
In collaboration with the Nogales Lab, we obtained structural data on a PRC2 dimer on chromatin, suggesting a possible mechanism of automethylation-mediated stimulation of PRC2 activity. This study aims to elucidate the relevance of PRC2 automethylation and subsequent dimerization on chromatin, both *in vitro* and in a cellular model.

10.1. Production of recombinant protein for biochemical studies

10.1.1. Generating PRC2 variants for expression in insect cells

We decided to purify a five-subunit PRC2 complex, consisting of full-length EZH2, SUZ12, EED, RBBP4 and embryonic AEBP2 (Isoform: Q6ZN18-3). This specific complex was selected because it represents the core components of PRC2 required for catalytic activity and chromatin association, as well as AEBP2, which is known to enhance enzymatic activity and contribute to chromatin targeting. The AEBP2 isoform used is predominantly expressed during embryonic development and was fused with an N-terminal Twin-Strep-tag for affinity purification of a complex that consistently includes this accessory subunit. Importantly, this five-subunit variant has been extensively studied both structurally and functionally, providing a foundation for our experiments and ensuring compatibility with existing structural data.[199, 200]
The cryo-EM structure, provided by our collaboration partner Dr. Paul Viktor Sauer from the Nogales group, guided our decision to clone various PRC2 variants for loss-of-function and separation-of-function studies. The proteins of interest were cloned into the GoldenBac system, allowing for a fast and versatile combination of PRC2 subunits.[341] All generated plasmids were verified via Sanger sequencing.

10.1.2. Expression and Purification of recombinant five subunit PRC2

The method for purifying the five-subunit PRC2 complex involved the co-expression of all subunits in a baculoviral expression system, which ensures proper folding and functional complex formation.[86] This system enabled us to produce PRC2 complexes with full-length subunits
Briefly, we generated and purified the bacmid constructs from DH10EMBacY *E. coli* to produce large baculovirus stocks in Sf9 insect cells. Subsequent infection of Tni cells was performed, and expression was verified via YFP signal and SDS-PAGE, as detailed in the methods section. In an example purification of WT PRC2, the initial purification step, utilizing the Twin-Strep-tag, indicates that some protein remained in the cell pellet post-lysis and especially on the resin after elution (Figure 16A). Nonetheless, the yield from the elutions was deemed sufficient for size-exclusion chromatography (SEC). The SEC purification was performed using a Superdex 200 Increase 10/300 GL column (Cytiva), which is optimized for separating proteins within the molecular weight range of 10–600 kDa. As shown in Figure 16B, PRC2 eluted as a monomer at approximately 10 mL and as a dimer at ~8.5 mL, consistent with previously published SEC curves.[142, 167] Notably, the elution profile for $PRC^{CXC/amKR}$ and $PRC2^{CXC/\Delta dim}$, two PRC2 variants with mutations that interfere with the dimerization and the engagement of nucleosomal DNA studied in this thesis (See Chapter: 10.3),

showed a markedly reduced dimer elution. This observation suggests that these mutations may disrupt the formation of the dimer described during purification.[142, 167]
The fractions corresponding to monomeric PRC2 yielded a homogeneous complex of high purity with all five subunits as indicated in the SDS gel in Figure 16B (bottom panel). PRC2 variant purifications showed elution volumes consistent with wild-type complex, suggesting correct complex assembly (Figure 16C). The final samples yielded on average 5-7 mg/mL in ~500 µL and were stored with 10% glycerol at −80 °C as single-use aliquots, which were thawed just before use, followed by centrifugation (21,000xg/10 min/4°C).

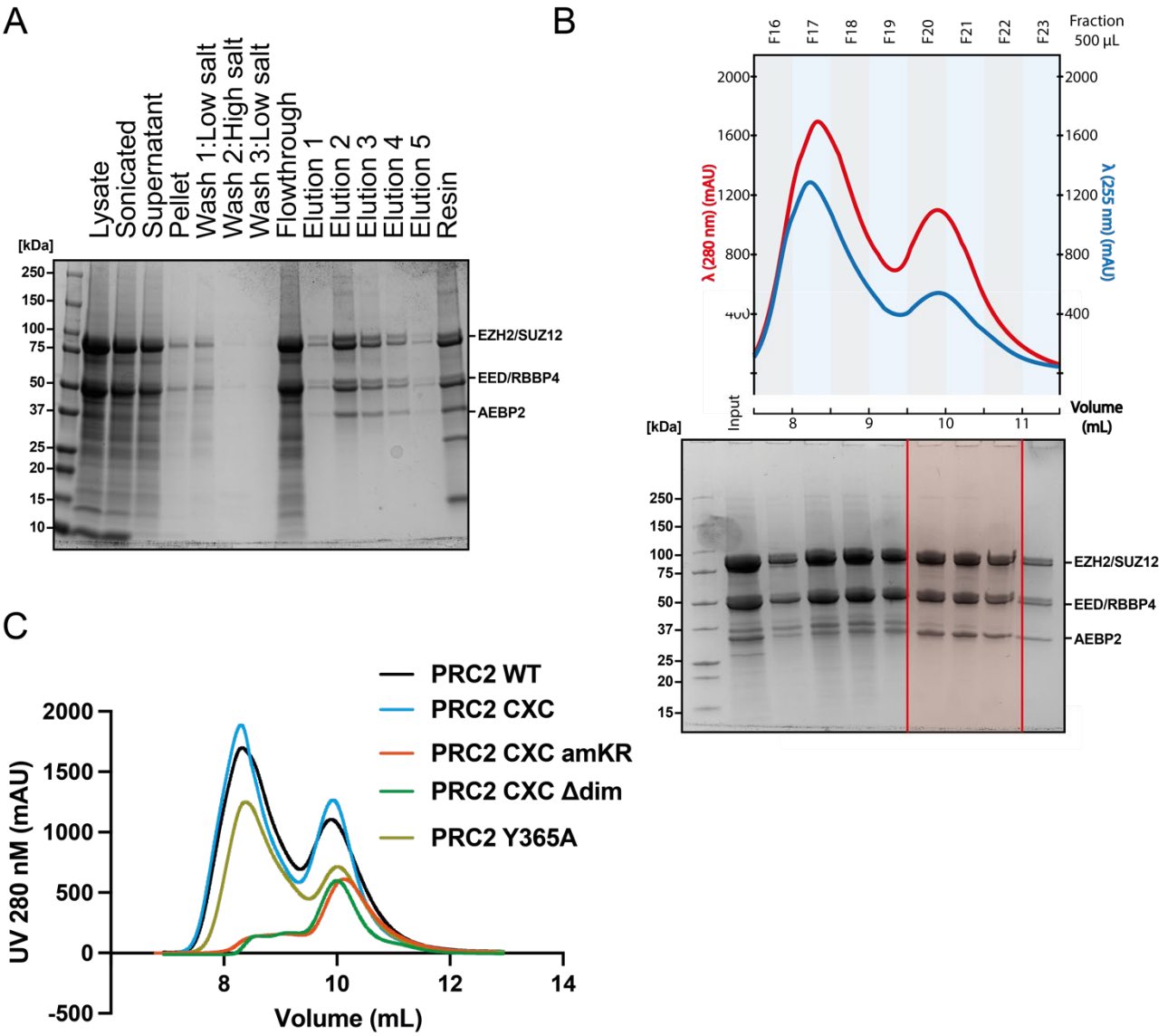

Figure 16: PRC2 Purification

A. *Initial purification of the PRC2 complex using streptactin affinity chromatography with the Strep-Tactin®XT 4Flow® resin (IBA Lifesciences). Despite some protein retention in the cell pellet post-lysis, especially on the resin after elution, sufficient protein is eluted. (The Precision Plus Protein™ Unstained Protein Standard (Bio-Rad) was used as molecular weight markers)* ***B.*** *SEC purification with a Superdex 200 Increase 10/300 GL column (Cytiva) and 400 µL fraction size shows two peaks at 8.5 mL and 10 mL. Fractions of the PRC2 monomer peak at 10 mL (red) represent the monomer and were collected. (The Precision Plus Protein™ Unstained Protein Standard (Bio-Rad) was used as molecular weight markers)* ***C.*** *SEC profiles at UV=280 nM of exemplary PRC2 purifications reveal elution at the same volume as the wild-type complex, confirming that PRC2 variants form correctly assembled complexes.*

10.1.3. Purification of recombinant nucleosomes

For the structural and biochemical characterization of PRC2 function on its nucleosome substrate, we followed a well-established protocol for purifying and reassembling nucleosomes using the histone octamer from *Xenopus laevis*.[15] Briefly, we expressed and purified the four canonical histones from *E. coli* and subsequently assembled them into octamers. We cloned 601 widom DNA with a CpG linker into a pUC plasmid. The 601 Widom sequence is a well-known DNA sequence with high affinity to the histone octamers, which positions the GC-rich CpG linkers symmetrically at each end of the nucleosome.[165] After cloning, we amplified the recombinant plasmid using large-scale PCR to produce sufficient quantities of the DNA fragment for reconstitution.
To reconstitute nucleosomes, we tested octamer-to-DNA ratios between 0.8:1 and 1.2:1 (at 4 µM DNA). This range of ratios was tested to optimize the conditions for efficient nucleosome assembly. Due to the minimal size difference between the histone octamer and the H3-H4 tetramer, the latter is co-purified with the former. Thus, the optimal ratio needed to maximize DNA binding to histone octamers while minimizing the formation of incomplete or off-target bound complexes, such as hexasomes or free DNA, had to be determined. In general, a 1:1 ratio was found to yield the best results, producing a nucleosome-rich product after native polyacrylamide gel purification using a Model 491 Prep Cell (Bio-Rad). During this purification, the sample began to elute after approximately 1 hour, with the majority of unbound DNA and hexasomes formed during reconstitution eluting first. The fractions containing nucleosomes eluted after approximately 90 minutes and were then verified via EMSA and collected (Figure 17). The final samples were concentrated, yielding an average of ~600 µg/mL in ~500 µL volume and were stored on ice at 4°C.
.

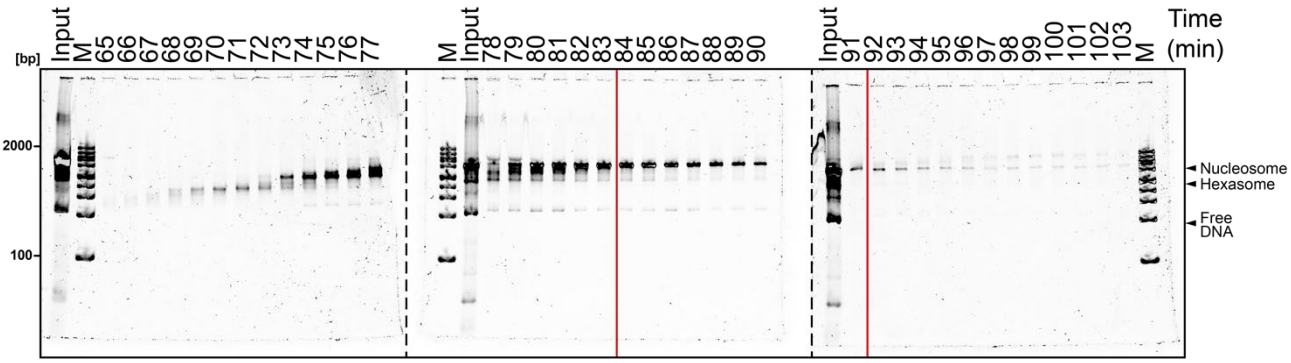

Figure 17: Nucleosome purification

Exemplary elution of a large-scale nucleosome purification, shows a shift from free DNA to hexasomes and eventually nucleosomes. The fraction containing the nucleosome from 84 to 91 min (red) were collected. (The 100 bp DNA-Ladder (Invitrogen) was used as a DNA ladder to analyse migrating behaviour)

10.2. Cryo-EM study of PRC2 on chromatin

The structural data generated by Dr. Paul Viktor Sauer forms the basis for the functional studies of this thesis. Our collaborative goal was to describe and characterize the role of PRC2 automethylation. Therefore, a cryo-EM structure of PRC2 bound to its mononucleosome substrate was resolved in the absence of its known activators H3K27me3 and methylated JARID2.
The cryo-EM analysis revealed two distinct populations of PRC2 complexes interacting with the nucleosome: The first population showed a single PRC2 engaged with a nucleosome, consistent with previous studies.[199] The second population revealed two PRC2 complexes bound to a single nucleosome. In the latter, these two PRC2 interact asymmetrically with the nucleosome: one, termed $PRC2^{prox}$ (Figure 18A, blue), contacts the nucleosome in a configuration primed for histone methylation, while the other, $PRC2^{dist}$ (Figure 18A, orange), interacts with $PRC2^{prox}$ and is distal to the nucleosome substrate. All five subunits could be fitted into the cryo-EM densities of the two PRC2 complexes in the dimer (Figure 18B).

The characterization of engagement with the nucleosome revealed that PRC2^{prox} binds the DNA through its CXC domain, including the structured bridge helix, at DNA Binding Site 1 (DBS1), as previously described (Figure 18C, Chapter 6.2.4). [197, 200, 355] Meanwhile, the dimer is stabilized by two PRC2 ^{dist}-DNA interactions. On one hand, PRC2^{dist} binds one linker DNA via the lateral surface of EED at DBS2, which has been previously shown to bind nucleosomal DNA in the dinucleosome context (Figure 18C).[200] On the other hand, the opposite linker DNA is bound by a loop (aa 481-485) and adjacent positively charged residues of SUZ12 (DBS3) (Figure 18C). These three DNA binding sites position and stabilize the PRC2 dimer on the nucleosome substrate.

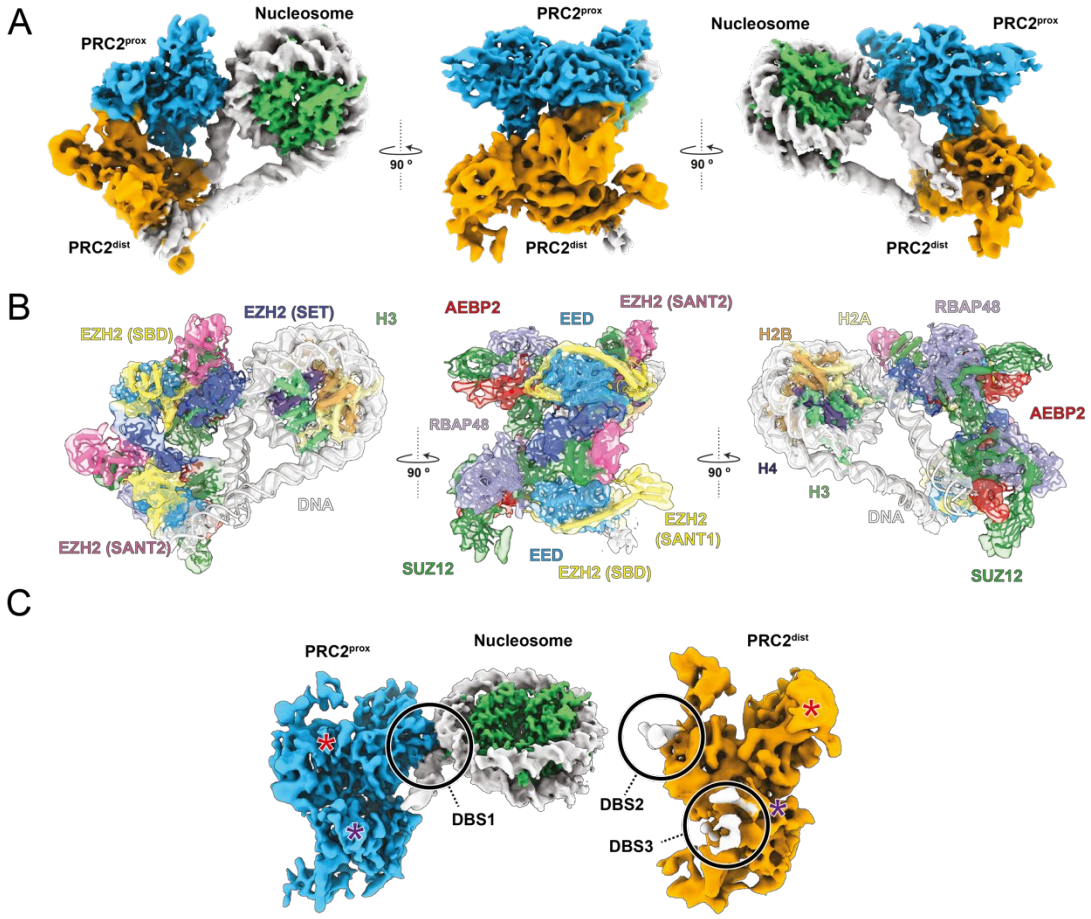

Figure 18: Structural characterization of nucleosome-bound assymetric PRC2 dimer

A. *In the PRC2 dimer, PRC2^{prox} (blue) is engaged to the nucleosome for catalytic activity, while a second PRC2^{dist} (orange) is distal from the nucleosome substrate.* ***B.*** *All subunits of PRC2 could be fit into the map.* ***C.*** *The structure in A has been rotated and aligned to show both PRC2s in the same general orientation. DNA binding sites (DBS) are labeled by black circles, while asterisks mark the dimer interfaces between EED^{prox} and EZH2^{dist} (red) and between SUZ12^{prox} and SUZ12^{dist} (purple).*[356]

The two PRC2 complexes interact using two distinct interaction surfaces (Figure 19). First, SUZ12 aa481-485 of PRC2^{prox}, the same loop that binds linker DNA in the case of PRC2^{dis} (DBS3), together with SUZ12 L426 and R427 form a SUZ12-SUZ12 interaction interface with a negatively charged helix on SUZ12^{dist} (aa 542-548) (Figure 19A, left). Second, an interaction of EZH2^{dist} with EED^{prox} involves critical functional regions. Notably, the bridge helix of EZH2^{dist} could not be resolved, suggesting that the loop containing the automethylated lysines K510, K514 and K515 (am-loop) is unfolded. However, the SET domain of EZH2^{dist} is positioned near EED^{prox}, allowing the automethylated lysines on the unfolded am-loop of EZH2^{dist} to reach into the binding pocket of the aromatic cage off EED^{prox} (Figure 19A, right). Local refinement further confirmed the presence of a density at the allosteric site of EED^{prox}, which we propose corresponds to the methylated am-loop of EZH2^{dist}, acting as an allosteric activator similar to H3K27me3 and JARID2.[128, 199, 200]

Following these observations, the two PRC2 complexes exhibit different conformational states. PRC2^{prox} displays an observable SRM helix and bent SBD domain, characteristics of EED-mediated activation (Figure 19Figure 19B, top). In contrast, PRC2^{dist} shows an unobservable and thus unstructured or flexible SRM and an extended SBD helix (Figure 19Figure 19B, bottom) and therefore is not in an activated conformation.

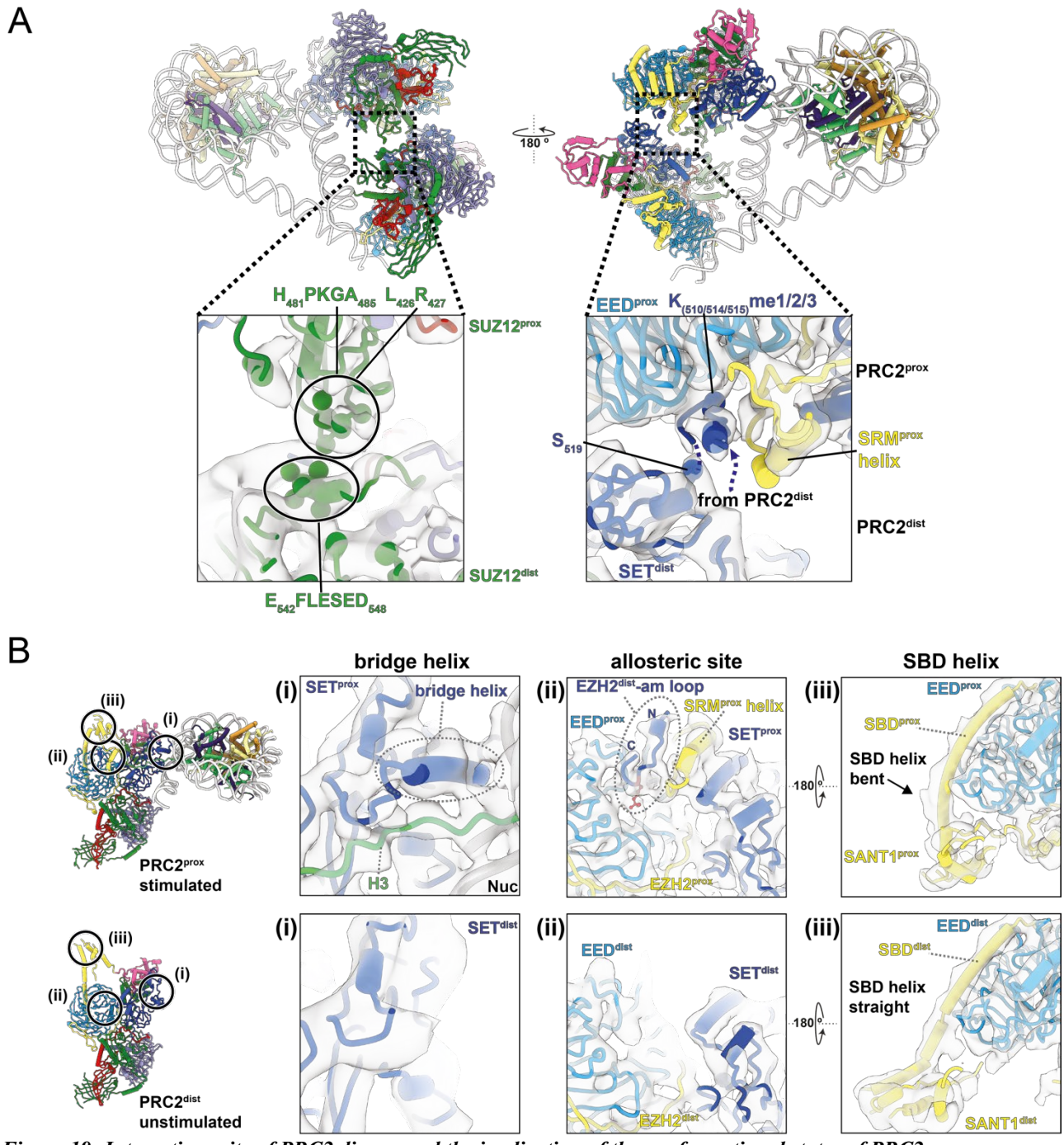

Figure 19: Interactions site of PRC2 dimers and the implication of the conformational states of PRC2

A. *Detailed view of the two interaction sites between PRC2^{prox} and PRC2^{dist}. On the left side, the SUZ12-SUZ12 interaction is depicted, while on the right site, EZH2^{dist}-EED^{prox} contacts reveal key residues and the potential role of automethylated lysines as an allosteric activator.* ***B.*** *The conformational difference between the two PRC2s indicates different functional states. On the top the structured SRM helix and a bent SBD domain of PRC2^{prox} indicate an active state, whereas PRC2^{dist} on the bottom lacks these features, suggesting a basal, non-activated state.*[356]

The structural data provides a detailed understanding of a novel regulatory mechanism for PRC2, revealing that the complex dimerizes on its chromatin substrate. Notably, both PRC2 complexes exhibit distinct conformational states: $PRC2^{prox}$ displays all the hallmarks of an activated state upon engagement with the nucleosomal substrate, whereas these features are absent in $PRC2^{dist}$. These findings lay the foundation for further exploration into the significance of PRC2 dimerization and its functional relevance, particularly in relation to the role of automethylation in modulating enzymatic activity.

To validate these observations, several key questions must be addressed. First, it is crucial to determine whether the two interaction interfaces, $SUZ12^{dist}$-$SUZ12^{prox}$ and $EZH2^{dist}$-EED^{prox}, are indeed responsible for facilitating PRC2 dimerization. Second, beyond confirming dimerization under physiological conditions (i.e. outside of cryo-EM), the functional consequences of these interactions must be carefully examined. Specifically, the impact of automethylation on dimerization and vice versa and the effect on PRC2 chromatin binding and histone methylation activity must be explored in more detail.

While the structural data offers compelling insights into a potentially new mechanism of PRC2 regulation, it is crucial to establish its biological relevance. Therefore, the primary aim of this thesis is not only to verify these structural observations but also to expand upon them through functional studies to gain a deeper understanding of how dimerization and automethylation regulate PRC2 activity in the chromatin context.

10.3. Biochemical studies of PRC dimerization

10.3.1. Characterization of PRC2 variants

The structural data indicates that an automethylated PRC2 can function as an allosteric activator of a substrate-bound PRC2, thereby inducing the characteristic structural features associated with allosterically activated EZH2 in $PRC2^{dist}$. Therefore, we initially generated loss-of-function mutations targeting the two interaction sites of PRC2 dimerization: The automethylation mutant PRC2amKR substitutes the three automethylation lysines K510, K514 and K515 with arginine, eliminating potential automethylation and the dimerization variant $PRC2^{\Delta dim}$ deletes the loop involved in dimerization (aa542-548).

After purification, we confirmed that these PRC2 variants do not affect PRC2 structure and function globally, independent of automethylation. Multiple studies have characterized the structural organization of the PRC2 complex. Therefore, we utilized negative-stain EM to evaluate the overall structural integrity and rule out a global impact of the mutations on PRC2 structure. We deemed that 2D classification is sufficient since the 2D class averages obtained of the PRC^{WT}, $PRC2^{\Delta dim}$ and $PRC2^{amKR}$ are practically indistinguishable, indicating that the mutations do not affect global complex integrity (Figure 20A).

Further, we utilized EMSAs to evaluate the binding affinity of the PRC2 variants to the nucleosome substrate. An increasing amount of PRC2 with a two-fold titration ranging from 25–800 nM was incubated with 50 nM nucleosome (Figure 20C). As seen in the mock control without PRC2, we can identify three bands: the lowest of free DNA, a faint hexasome and a nucleosome band. With the addition of PRC2, the nucleosome bands shift to slower migrating species. The comparison of the variants to the wild-type control did not exhibit any significant differences. This indicates that the mutations do not interfere with nucleosome engagement.

Since the structural data indicated that automethylation-driven activation targets EED, we verified that the introduced mutations do not affect this mechanism. Therefore, we performed western blot analyses of PRC2 activity with H3K27me3 peptide stimulation (Figure 20D). Both PRC2 variants behaved like wt PRC2 and were stimulated by an increasing amount of the peptide.

These results indicate that the mutations did not impair PRC2 function, particularly the allosteric activation via EED, confirming that neither automethylation nor dimerization directly affects this activation mechanism. However, since the mutations are expected to impact automethylation and

dimerization, it is crucial to investigate further how these changes affect PRC2. Given these assumptions, the precise roles of automethylation and dimerization must be carefully dissected to understand their impact on PRC2 regulation.

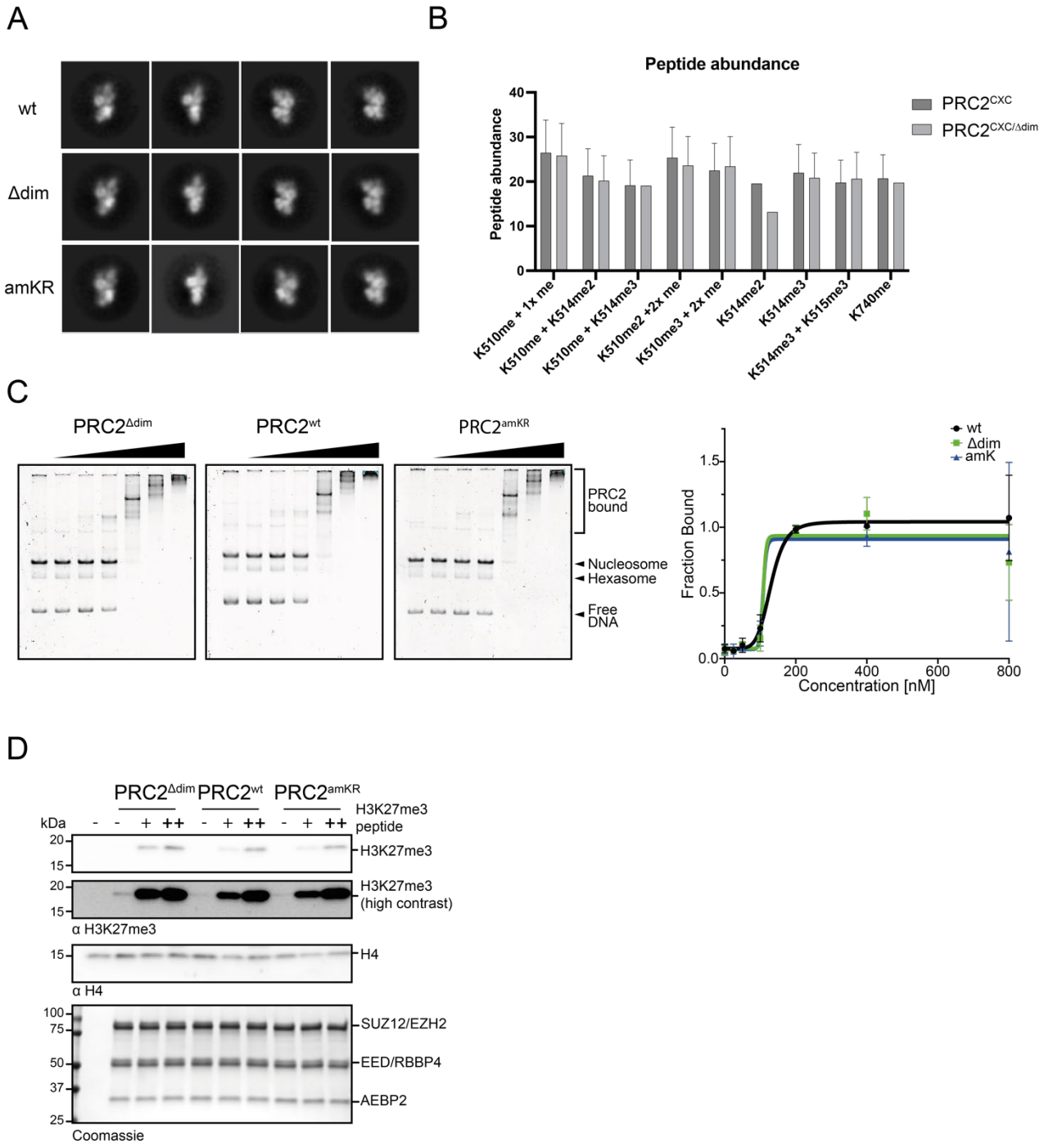

Figure 20: Functional characterization of PRC2 variants

A. *Structural integrity of PRC2 variants PRC2$^{\Delta dim}$ and PRC2^{amKR} was confirmed through negative stain EM and 2D classification. These show that both mutants are structurally indistinguishable from PRC2^{WT}, indicating no disruption of the overall complex architecture. Pierre Rodewald and Dr. Simon Pöpsel performed the grid preparation and processing.* ***B.*** *Mass spectrometry analysis of the PRC2^{CXC} variant reveals retained automethylation capability despite the mutation disrupting DNA binding with the nucleosome and thus catalytic inactivation.* ***C.*** *Electrophoretic Mobility Shift Assay (EMSA) results indicate that the PRC2 variants maintain binding affinity to nucleosome substrates similar to the wild-type complex. Nucleosome bands shift to slower migrating species upon PRC2 binding, demonstrating that mutations do not interfere with nucleosome engagement. (n=3-6)* ***D.*** *Western blot analysis of PRC2 activity assays with H3K27me3 peptide stimulation shows that PRC2$^{\Delta dim}$ and PRC2^{amKR} respond similarly to PRC2^{WT}, confirming that mutants can be allosterically activated via EED.(n=3)*

10.3.2. Automethylation affects HMTase activity in *trans*

The activity assays shown in Figure 21D, along with additional HMTase assays not included in this thesis, revealed that the analysis of allosteric activation via automethylation is often obscured by the stimulation caused by the accumulation of the H3K27me3 product of the reaction. To address this, we modified our experimental setup by introducing separation-of-function mutations, combining the previously published PRC2^{CXC} mutation with our automethylation mutations. A graphical overview of the experimental setup is provided in Figure 21A and detailed in section 9.3.4 of the methods.[198] The mutations are designed to isolate distinct aspects of PRC2 function, allowing us to assess how automethylation and dimerization contribute to allosteric activation and catalytic activity. The PRC2^{CXC} mutation contains four residue substitutions in EZH2 (K568A/Q570A/K574A/Q575A), which disrupt the ability of the complex to bind the DNA of the nucleosome substrate, effectively rendering the enzyme catalytically inactive. This prevents PRC2^{CXC} from occupying the proximal position and enables it to only act as an allosteric activator from a distal position, decoupling its automethylation from its catalytic activity. Mass spectrometry confirmed that PRC2^{CXC} retains its automethylation capability, ensuring it can fulfill its role as a distal activator (Figure 20B).
Conversely, the PRC2^{amKR} mutation substitutes lysines K510, K514, and K515 with arginines, specifically abolishing automethylation while preserving the ability to bind nucleosomes and deposit H3K27 methylation (Characterized in detail in chapter 10.3.1). These mutations therefore render PRC2^{amKR} incapable of functioning as an allosteric activator in the distal position but retain the ability to be activated and enzymatically active in the proximal position. By utilizing PRC2^{CXC} and PRC2^{amKR}, we distinctly define the roles and positions of the two PRC2 complexes within a dimer, allowing us to dissect the contributions of dimerization and automethylation to allosteric activation.
To further investigate these mechanisms within a dimeric context, we combined PRC2^{CXC} with the previously characterized dimerization mutation PRC2$^{\Delta dim}$, which disrupts dimerization by deleting the SUZ12 loop (aa 542–548) and the automethylation variant PRC2^{amKR}. This combination allowed us to systematically explore how dimerization and automethylation contribute to PRC2 activation and function.
Firstly, we observed that both PRC^{amKR} and PRC2^{CXC} exhibited low or barely detectable basal activity, confirming that these PRC2 variants don't display appreciable HMTase activity by themselves and don't contribute to the H3K27me3 detected in the assay. Upon adding PRC^{CXC} to PRC2^{amkR}, we observed a ~50% increase in generated H3K27me3 (Figure 21B). The combination of PRC2^{CXC} with the Δdim amKR mutations, which disrupt dimerization and automethylation, respectively, abrogated the increased generation of H3K27me3 to only ~25% and basal level, respectively (Figure 21B). These functional assays support our structural model, suggesting that upon dimerization, the methylated am-loop of PRC2^{dist} activates PRC2^{prox} through a *trans* mechanism.

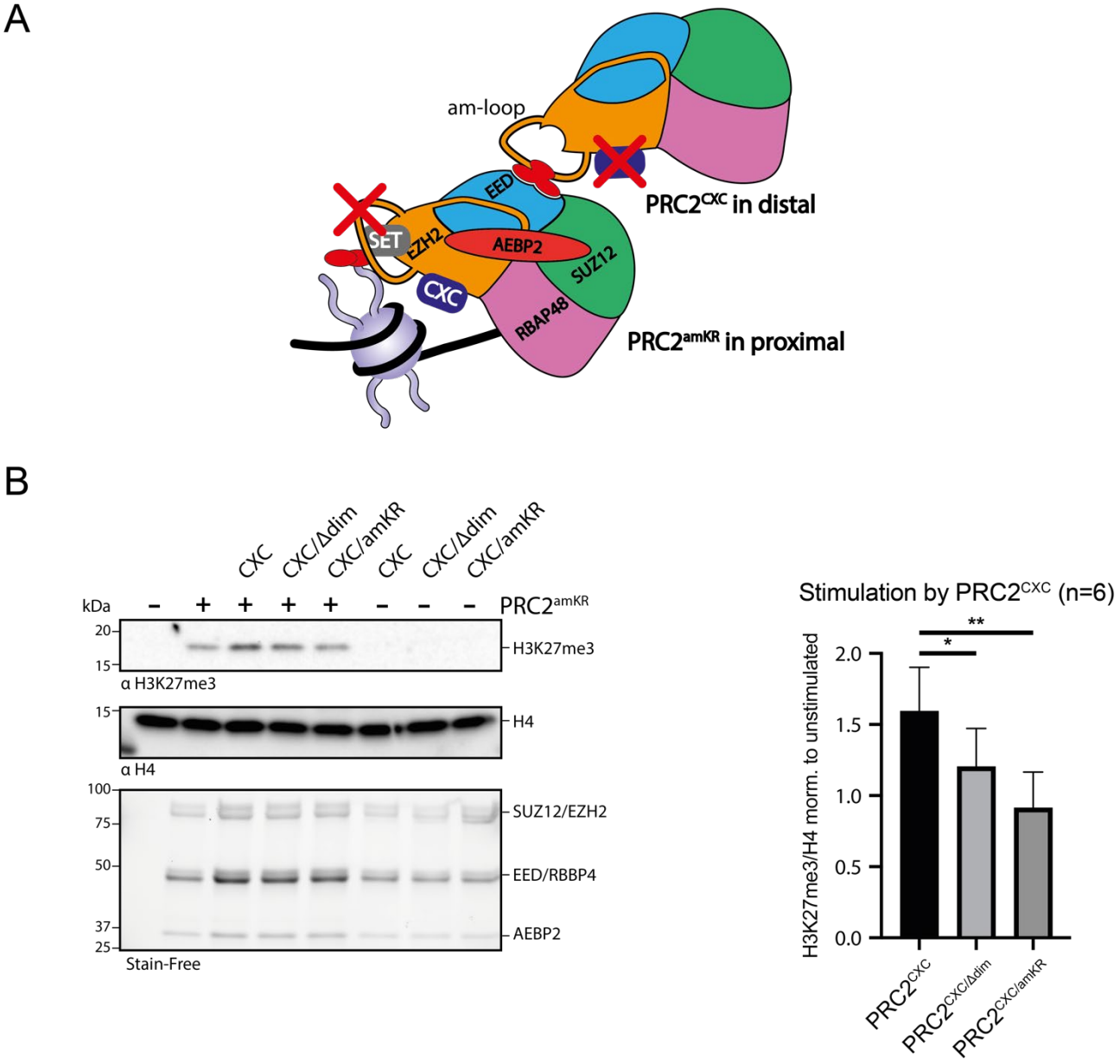

Figure 21: Allosteric activation with separation-of-function variants PRC2^{amKR} with PRC2^{CXC}

A. *Schematic representation of separation-of-function PRC2 variants and their respective positions within a PRC2 dimer to dissect PRC2 allosteric activation via separation-of-function mutations. The PRC2^{CXC} variant contains specific residue substitutions in the CXC domain (K568A/Q570A/K574A/Q575A) that impair its ability to bind DNA at the nucleosomal substrate while retaining automethylation capability, allowing it to serve as a potential distal activator. In contrast, the PRC2^{amKR} variant substitutes lysines K510, K514, and K515 with arginines, abolishing automethylation while preserving catalytic activity and the ability to be stimulated. While PRC2amKR can occupy both proximal and distal positions within the dimer, it is incapable of functioning as an allosteric activator in the distal position.* ***B.*** *Western blot of the HMTase assay described in A with the bar graph analyzing H3K27me3 H3K27me3 generation. The assay reveals that adding PRC2^{CXC} as an allosteric activator to PRC2^{amKR} increases H3K27 trimethylation by approximately 50%. The introduction of additional mutations in PRC2$^{CXC/Δdim}$ or PRC2$^{CXC/amKR,}$ respectively, reduced H3K27me3 generation to ~25% and basal levels. These results highlight the necessity of dimerization and automethylation for effective PRC2 activation. (n=6*

10.3.3. *Trans* activation is mediated by EED

Our structural and functional data demonstrated that PRC2 dimerization is required for allosteric activation via automethylation, further suggesting that this activation is mediated by EED. To validate this observation functionally, we employed two distinct approaches: first, we used the previously described Y365A mutation in the aromatic cage of EED, and second, we applied the EED inhibitor MAK683, which both reportedly disrupted the activation mechanism.[131, 357] In both cases, H3K27me3 generation was significantly diminished, even when $PRC2^{CXC}$ was added as an allosteric activator (Figure 22). By disrupting the EED-mediated activation, we confirmed that activation via automethylation indeed follows this mechanism.
Further, we observed that H3K27me2 levels were unaffected by either $PRC2^{CXC}$ stimulation or EED disruption and instead depended solely on the total amount of PRC2 (Figure 22B). This is according to the literature, which indicates that H3K27me1 and H3K27me2 are not reliant on allosteric activation, with activation only required for the rate-limiting step of H3K27me3.[220, 358] Taken together, we confirmed that stimulation via automethylation only affects the rate-limiting deposition of the third methyl group and functions in an EED-mediated manner.

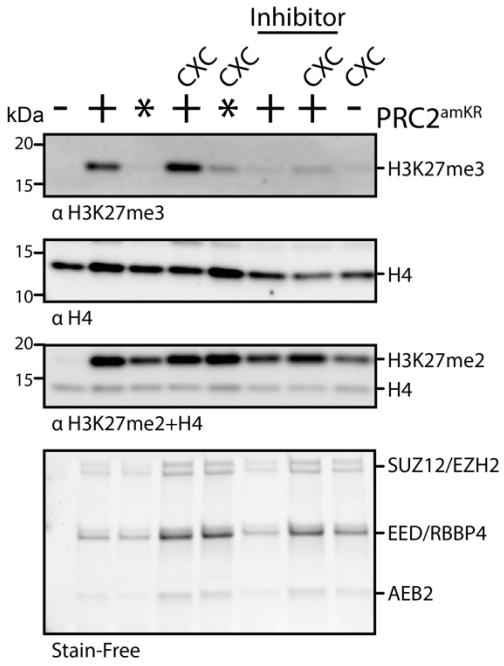

Figure 22: HMTase assay with allosteric activation in the dimerization context with inhibited EED activation
$PRC2^{CXC}$ can allosterically activate $PRC2^{amKR}$. The Y365A mutation in the aromatic cage of EED (marked by an asterisk) and the EED inhibitor MAK683 prevent activation via EED. Disruption of EED-mediated allosteric activation thus significantly reduces H3K27me3 levels. H3K27me2 levels remain unchanged by $PRC2^{CXC}$ stimulation or EED disruption, mainly relying on the total PRC2 concentration.

Previous studies were unable to determine which of the potentially automethylated lysines of the am-loop contributes to PRC2 activation. To address this, we investigated the effect of synthetic am-loop peptides (EZH2:aa 502-521) containing trimethylated K510, K514, or K515. We observed that only K510me3 resulted in an increased activity (Figure 23A). Sequence alignment of known allosteric activators of PRC2 via EED shows that they share an arginine at the -1 position relative to the methyl-lysine.[131, 149] The PRC2 am-loop sequence analysis showed that only K510 follows an arginine (Figure 23B). Moreover, analyses of cancer databases revealed mutations not only in the dimerization site of SUZ12 but also in both R509 and K510 of EZH2, further underscoring the critical roles of these residues (Figure 23C).
In summary, our results show that PRC2 activation via automethylation, specifically at K510, occurs upon dimerization via the known EED-mediated mechanism.

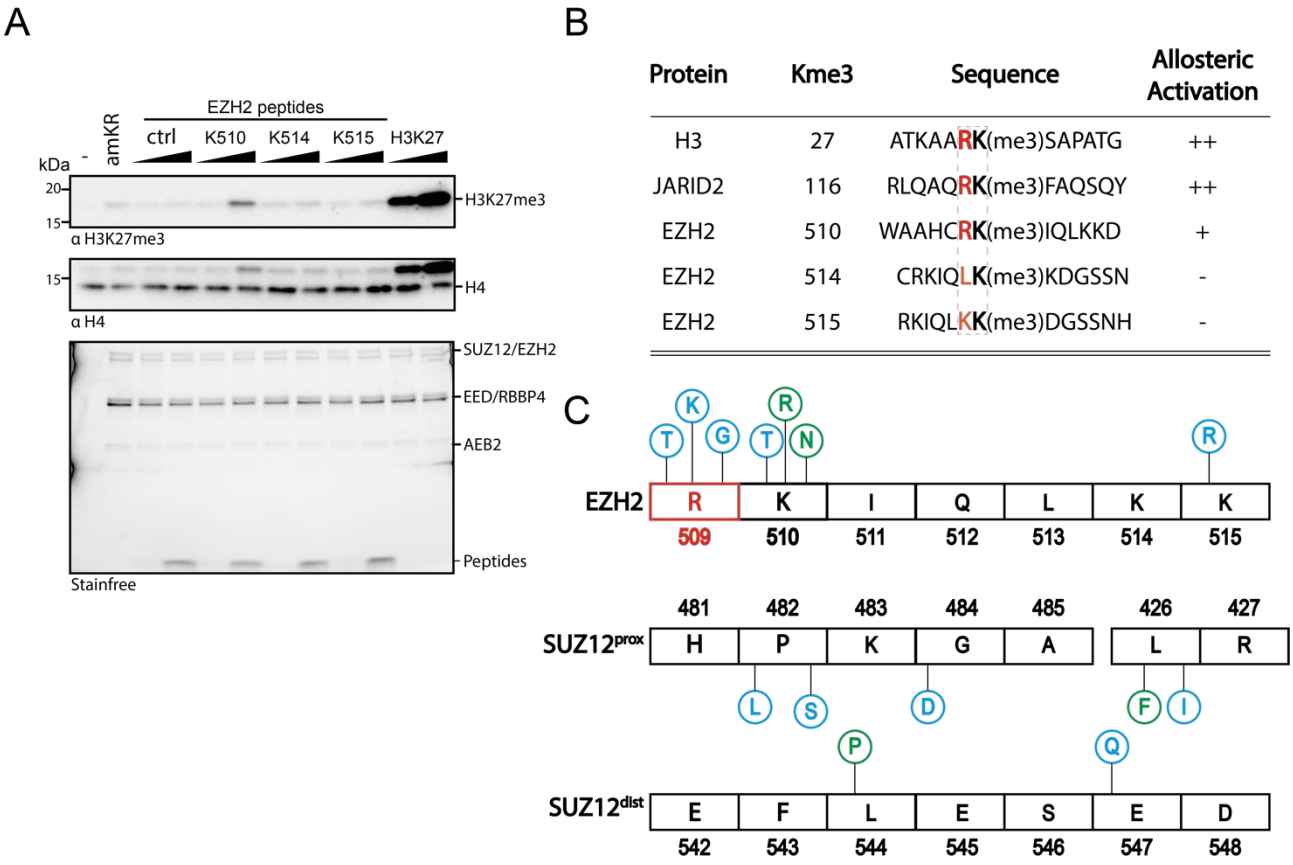

Figure 23: Characterization of automethylation lysines on activity

A. *To identify which lysine is responsible for PRC2 stimulation via automethylation, am-loop peptides with trimethylated K510, K514, or K515 were tested. Only K510me3 significantly increased PRC2 activity. (n=3)* ***B.*** *Sequence alignment of known PRC2 allosteric activators via EED shows a shared arginine at the -1 position relative to the trimethyl-lysine in peptides with a stimulating effect. Analysis of the am-loop sequence shows that only K510 follows R509, supporting its role in allosteric activation.* ***C.*** *Substitution mutations obtained from cancer databases COSMIC (blue)[359] and NCI Genomic Data Commons (green)[360, 361] show that mutations of both R509 and K510 were reported in cancer as well as on the dimerization interaction site of SUZ12.*

10.4. Cellular studies of PRC2 automethylation and dimerization

10.4.1. Generation of mouse embryonic stem cells

The structural and functional results have revealed a novel mechanism by which PRC2 activity is regulated by automethylation and dimerization on a recombinant nucleosome substrate. Based on these findings, we hypothesized that these regulatory mechanisms could also play a role in a biological context. Given the importance of PRC in gene silencing, we further speculated that these mechanisms might be particularly relevant in a chromatin context, especially where other allosteric activators of PRC2 may not always be present. Thus, the goal of the cellular experiments was to investigate how the characterized mutations that impair dimerization or automethylation affect PRC2 function in a cellular environment.

Mouse embryonic stem cells (mESCs) were selected as the model system due to their well-documented utility in elucidating mechanisms and biological roles of PRC2. The deposition of H3K27me3 by PRC2 is essential for silencing developmental genes, enabling mESCs to maintain their self-renewal and pluripotency while orchestrating precise transcriptional programs during differentiation.[97, 123, 180, 336] Studies in mESCs have shown that PRC2 is indispensable for regulating differentiation pathways, with impaired PRC2 gene silencing leading to a loss of lineage fidelity and inappropriate expression of lineage-specific genes during differentiation.[102, 362, 363] Given the central

role of PRC2 in these processes, we sought to use mESCs to investigate whether the defects in automethylation and dimerization observed *in vitro* would manifest *in vivo*. Specifically, we aimed to determine how these impairments affect the ability of PRC2 to maintain gene silencing and proper function during differentiation.

The Pasini Lab had previously generated and characterized EZH1/2 double knock-out (dKO)[335] and SUZ12 KO [336] and kindly provided them to us. We performed rescue experiments by introducing $EZH2^{wt}$ or $EZH2^{amKR}$, $SUZ12^{wt}$ or $SUZ12^{\Delta dim}$ as well as an empty vector (EV) control into the respective cell lines (Figure 24A). Western blot analyses revealed that within each cell line, the wild type and respective PRC2 variants reached comparable bulk levels of the PRC2 subunits and H3K27me3. This follows the literature, where stable expression of wt and automethylation mutants restored comparable levels of H3K27me3 (Figure 24B).[186]

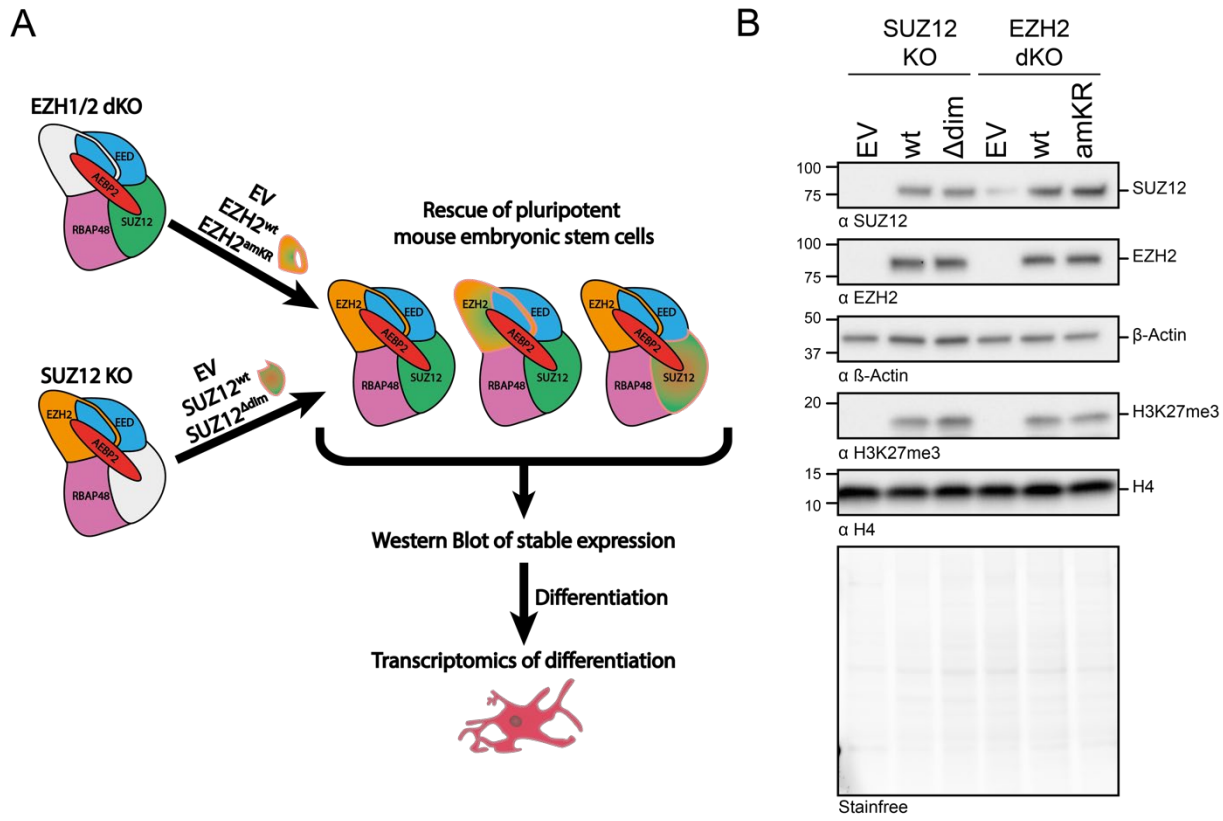

Figure 24: Generation of mESCs stably expressing PRC2 variants

A. *Schematic overview of the mESC experiments performed. Knockout (KO) mESCs were stably transfected with constructs expressing PRC2 subunits—either wild-type or variant—or an empty vector (EV) control. Expression of the introduced subunits was verified by Western blot. The pluripotent mESCs were then differentiated using retinoic acid (RA) treatment and RNA-seq was conducted at multiple time points to analyze transcriptional changes during differentiation. (n=3)* ***B.*** *Western blots show the restoration of PRC2 subunits and H3K27me3 levels in cells expressing the respective wild-type or mutant constructs compared to the EV controls. This confirms the reconstitution of functional PRC2 complexes at comparable levels in all rescued cell lines.*

10.4.2. Investigating the role of automethylation in PRC2 gene silencing

We sought to characterize the effect of impaired automethylation and dimerization on PRC2 function in cells. Therefore, we subjected the mESC to differentiation-inducing conditions with retinoic acid (RA), a known inducer of neural differentiation that drives the pluripotent mESCs toward a neuronal lineage. RA treatment has been shown to trigger the downregulation of pluripotency markers and promote the expression of neuronal-specific genes, facilitating the transition from a pluripotent to a differentiated state.[364] Subsequently, we analyzed their transcriptome at different time points via RNA-seq.

Successful differentiation was confirmed by monitoring changes in the transcription of key pluripotency markers, such as SRY (sex determining region Y)-box 2 (SOX2), Nanog homeobox (Nanog), and POU domain, class 5, transcription factor 1 (POU5F1, also known as Oct4), which were downregulated, as well as differentiation markers, including neuronal ectodermal markers like paired box 6 (Pax6), the neuronal progenitor marker nestin (Nes), and neuron-specific tubulin beta-3 chain (Tubb3), which were upregulated (Figure 25A,B).[365]. Importantly, we observed no significant deviation in these expression patterns between the various cell lines, suggesting that all lines successfully underwent differentiation. Notably, previous studies have shown that differentiation of PRC2 KO cells eventually leads to cell death; this outcome was not observed in our experimental condition, possibly due to a short differentiation protocol.[101, 335, 336, 362]

However, an analysis of Differentially Expressed Genes (DEGs), comparing the KOs and variants ($PRC2^{\Delta dim}$ and $PRC2^{amKR}$) to the WT rescues, revealed important differences. Particularly on day 4, when differentiation is most advanced, both the rescued variants and the KO cell line exhibited most DEGs compared to the wild-type (WT) line. As expected, the knockout of the core PRC2 subunits, SUZ12 and EZH2, resulted in a much higher number of DEGs than the variants (Figure 25C, D). This suggests that while $PRC2^{\Delta dim}$ and $PRC2^{amKR}$ mutants can partially rescue PRC2 function during differentiation, they still fail to fully restore PRC2 function, as evidenced by the significant changes in gene expression. These results imply that defects in dimerization and automethylation may affect PRC2 transcriptional regulation during differentiation.

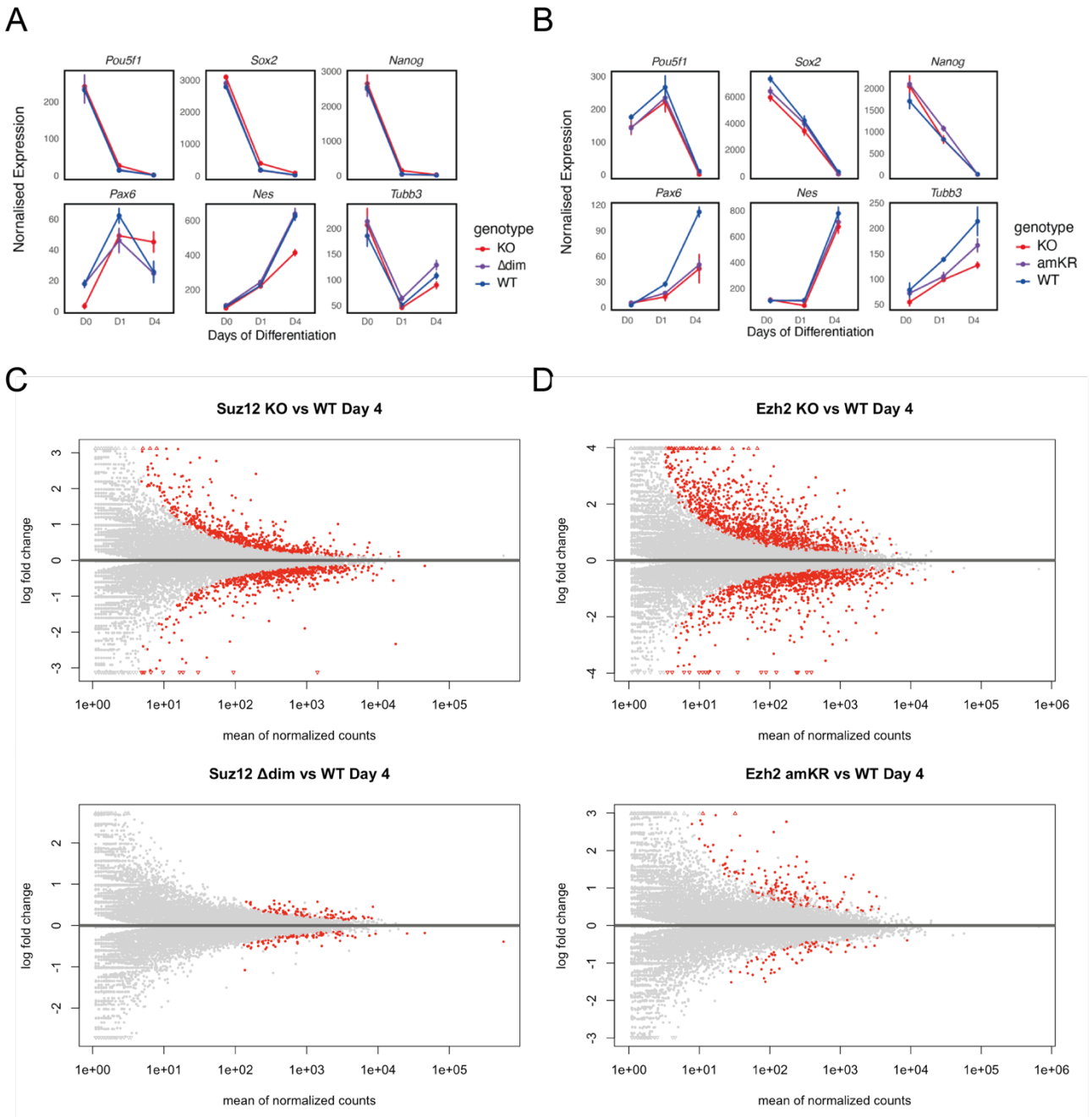

Figure 25: Transcriptome analyses of RA-driven differentiation in mESCs

A. *Gene expression profiles in SUZ12 rescue experiments of pluripotency markers (top) and neural trajectory markers (bottom) during RA-driven differentiation* ***B.*** *Gene expression profiles in EZH2 rescue experiments of pluripotency markers (top) and neural trajectory markers (bottom) during RA-driven differentiation* ***C.*** *MA Plots showing the relationship between average log2 fold change (y-axis) and average expression (x-axis) for differentially expressed genes (DEGs) in SUZ12 KO (top) and SUZ12Δdim (bottom) relative to WT SUZ12 cells. To assess DEGs in SUZ12 KO (top) and SUZ12$^{\Delta dim}$ (bottom) relative to WT SUZ12 cells. Significant DEGs are highlighted in red. The plots show a more significant number of DEGs in the SUZ12 KO than in SUZ12 $^{\Delta dim}$ when compared to the WT SUZ12.* ***D.*** *MA Plots show the same as in C to assess DEGs in EZH2 KO (top) and EZH2^{amKR} (bottom) relative to WT EZH2 cells. Significant DEGs are highlighted in red. The EZH2^{amKR} is more similar to the EZH2 WT than the EZH2 KO.*

To analyze the potential effect of an impaired automethylation mechanism in detail, we performed Gene Set Enrichment Analyses (GSEA), which allows us to evaluate groups of related genes to see if they are upregulated or downregulated when compared to the respective wild-type cell line (Figure 26). Of these gene sets, the EZH1/2 dKO and EZH2^{amKR} cells share 21 out of the respective total 29 or 28 enriched pathways and three out of 8 or 4 depleted pathways, implying that the impaired automethylation of the EZH2^{amKR} mutant functionally overlaps with the complete loss of PRC2 function to some degree (Figure 26A, Supplementary Figure 4, 5). This functional overlap suggests

that although the EZH2^{amKR} mutant does not fully replicate the loss of PRC2 function, it leads to a gene expression profile that resembles the complete PRC2 knockout. The enriched pathways, for instance, were those of inflammatory and stress response, while pathways for cell division and checkpoint progression were depleted, which is expected due to differentiation-induced cell stress.[366-368]

The SUZ12 KO and SUZ12$^{\Delta dim}$ rescue exhibited no shared enriched pathways. However, they shared 8 depleted pathways out of the respective total 24 or 11 depleted pathways, which indicates that the impaired dimerization of the SUZ12$^{\Delta dim}$ affects PRC2 function less severely than disrupted automethylation (Figure 26B, Supplementary Figure 6, 7). The affected pathways shared between the SUZ12 KO and SUZ12$^{\Delta dim}$ included the stress response and pre-oncogenic pathway. This suggests that disruption of dimerization and especially automethylation also influences the transcriptional response compared to normal PRC2 function and that the affected pathways partially overlap with the loss of PRC2. Notably, the comparison of GSEA results also suggests that differentiation itself imposes a certain level of cellular stress that impacts the transcriptome across all cell lines. These effects may complicate the interpretation of PRC2-specific pathways and could potentially be mitigated by optimizing the differentiation protocol to minimize stress-induced transcriptional responses.

The comparison between all the cell lines revealed two shared depleted pathways for E2F targets and G2M checkpoint control (Figure 26C). These pathways have been reported to be regulated by retinoblastoma protein (RB) and PRC2, underscoring a critical convergence in biological processes related to cell cycle regulation.[369, 370] This overlap between EZH2^{amK} and SUZ12$^{\Delta dim}$ mutants highlights the interconnected roles of automethylation and dimerization in PRC2 function and provides compelling evidence for a cooperative mechanism. Moreover, this shared depletion also reveals a nuanced impact of automethylation and dimerization defects, suggesting that combined these mechanisms regulate gene expression in specific chromatin environments.

In summary, our findings suggest that automethylation and dimerization defects exert context-specific effects on PRC2 function. While PRC2 activity appears to be broadly preserved in the KO under these experimental conditions, the shared depletion of gene sets between impaired automethylation and dimerization supports a cooperative role for these mechanisms, potentially in chromatin environments requiring *de-novo* H3K27me3 deposition, especially in the absence of other allosteric activators. Together, these results support a model in which automethylation and dimerization fine-tune PRC2 activity to meet specific transcriptional and epigenetic demands.

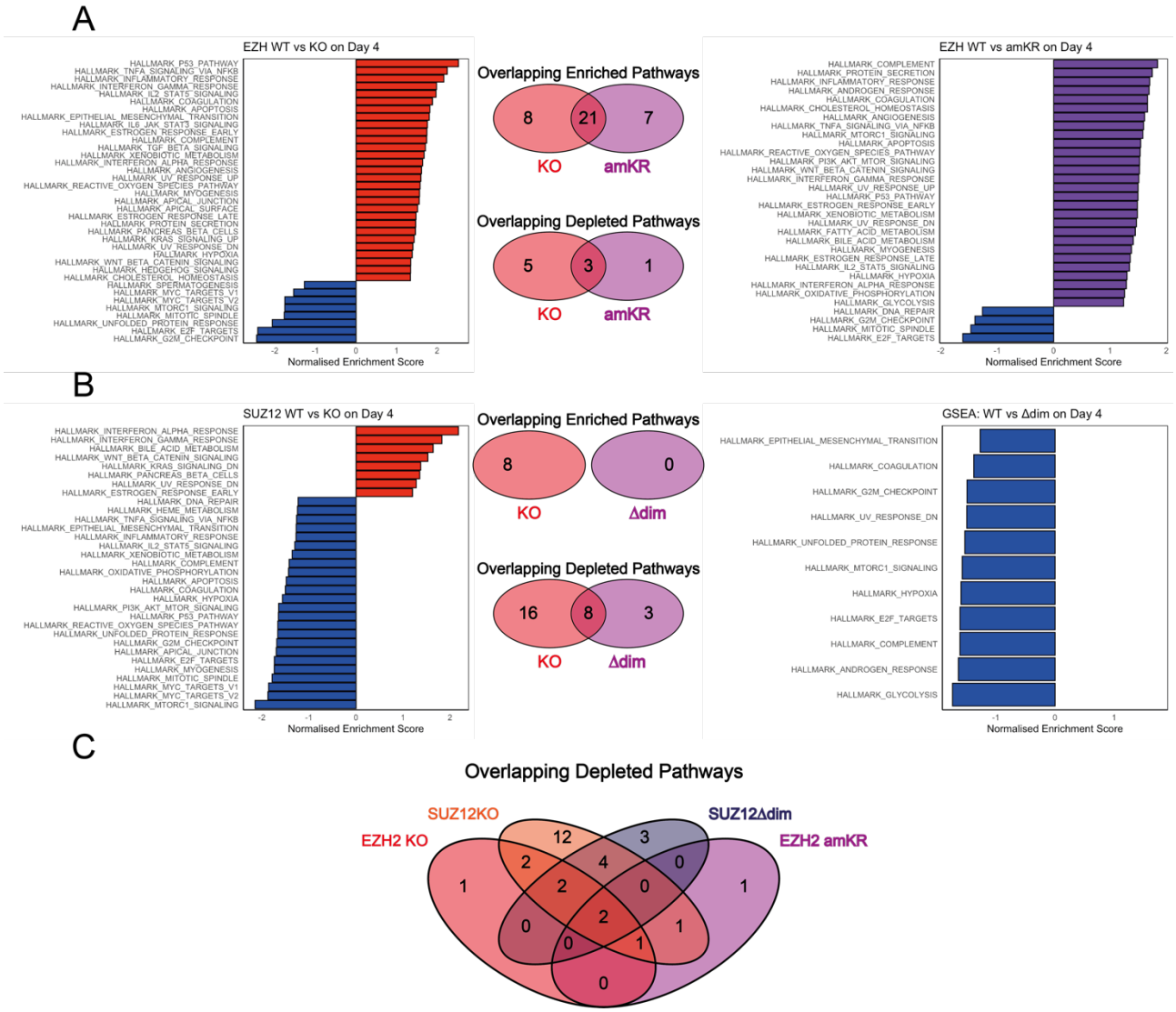

Figure 26: Gene Set Enrichment Analysis (GSEA) of impaired PRC2 variants

A. *GSEA of EZH1/2 KO (left) and EZH2^{amKR} (right) compared to the WT cells reveals a substantial functional overlap (middle), with 21 shared enriched pathways (e.g., inflammatory and stress response) and three depleted pathways (e.g., cell division and checkpoint progression), indicating that EZH2 automethylation impairment partially mimics PRC2 loss.* ***B.*** *Comparison GSEA of SUZ12 KO and SUZ12$^{\Delta dim}$ rescue cells shows no common enriched pathways but eight shared depleted pathways related to stress response and pre-oncogenic signalling.* ***C.*** *Across both PRC2 variants and both KO cell lines, two depleted pathways for E2F targets and G2M checkpoint control are shared.*

11. DISCUSSION

11.1. PRC2 dimerization a new layer of PRC2 regulation

Multiple studies have characterized how PRC2 engages with its nucleosome substrate and described mechanisms regulating its enzymatic function in detail.[128, 149, 199, 200, 371] Recent work demonstrated that PRC2 can automethylate three lysine residues on EZH2 in a *cis* manner, and that automethylation has a stimulatory effect on its HMTase activity.[185, 186] However, the mechanism behind this activation have remained unclear.

Through a collaboration with structural studies from the Nogales Lab, we addressed these questions, proposing a model where PRC2 activation occurs through dimerization. Structural analyses in Chapter 10.2 reveal that a subset of PRC2 molecules dimerize on nucleosomes, exhibiting two functionally distinct complexes: The substrate histone octamer engaging $PRC2^{prox}$ and the substrate-distal $PRC2^{dist}$. These two complexes exist in different conformational and functional states: 1. $PRC2^{prox}$ exhibits features of an activated state, including a folded SRM, bridge helix, and a bent SBD helix - characteristics that prime the complex for catalytic activity as previously described.[199, 200] 2. In contrast, $PRC2^{dist}$ lacks these structural hallmarks. Our analyses also identified two interaction sites - between $SUZ12^{prox}$-$SUZ12^{dist}$ and $EZH2^{prox}$-EED^{dist}. Notably, the SET domain positioning enables automethylated lysines in the unfolded am-loop of $EZH2^{dist}$ to reach into the binding pocket of the aromatic cage of EED^{prox}, where an undefined density was observed.
These findings led us to hypothesize a novel mechanism of PRC2 regulation: While PRC2 automethylates in *cis*, activation occurs in *trans* through chromatin-mediated dimerization (Figure 27).

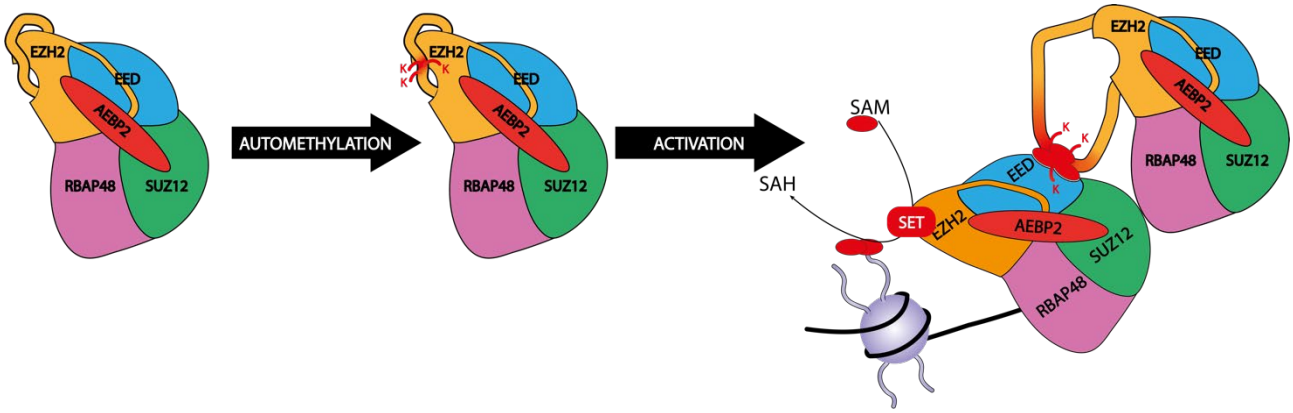

Figure 27: Mechanism of PRC2 avitvation by automethylation and dimerization
PRC2 methylates itself on three lysines on EZH2: K510,K514 and K515. The methylated K510 of EZH^{dist} targets the aromatic cage of EED^{prox} as an allosteric activator, thereby leveraging the well-studied EED-mediated stimulation mechanism, similar to that of trimethylated peptides of H3K27me3 and JARID2 K116me3.

11.1.1. Functional separation confirms *trans* activation

Our experimental design using separation-of-function variants provided insights into this regulatory mechanism of PRC2, but we faced several challenges requiring a complex experimental setup. A key challenge was controlling the methylation state of PRC2, as the complex undergoes partial methylation during expression. Due to the close proximity of the automethylation lysines, mass spectrometry primarily reports the overall methylation state of the peptide, allowing for various combinations of mono-, di-, and trimethylation between the lysines without distinguishing specific modifications. Ideally, controlling or abolishing the methylation state of these lysines would provide optimal experimental conditions; however, this remained unattainable. To approximate a highly methylated state, we preincubated PRC2 with an excess of SAM prior to the activity assay, which was confirmed via mass spectrometry.[356]

Another obstacle was determining optimal enzyme and substrate concentrations. High nucleosome concentrations, as used in previous studies, saturated the enzyme, masking subtle effects from automethylation.[198] To mitigate this, we reduced substrate concentration, which brought us close to the detection limits of Western blot. Nevertheless, Western blot offered a critical advantage over other activity assays, such as those measuring the SAM conversion to SAH or autoradiography, by allowing the use of specific antibodies to distinguish between methylation states. The rate-limiting H3K27me3 deposition relies on allosteric activation and employing this method ensured that our assay was sensitive to this key reaction.[220, 358]

Addressing these challenges required careful optimization of PRC2 and nucleosome concentrations, reaction times and Western blot conditions. Despite these efforts, initial Western blot analyses yielded inconclusive results due to rapid H3K27me3 production outcompeting dimerization-driven EED activation. These challenges highlighted the need for a refined experimental approach.

By introducing mutations that disrupted various aspects of PRC2 function – the catalytic engagement of the nucleosome via the CXC domain and mutations preventing either dimerization or automethylation – we successfully characterized the allosteric effects of automethylation and dimerization.[198] Consistent with our hypothesis, $PRC2^{CXC}$ can act as an allosteric activator, with impaired dimerization reducing and impaired automethylation effectively abolishing this effect.

This experimental approach, while logically sound and based on structural insights, assumes that the Δdim mutation adequately interferes with dimerization. However, this disruption should ideally be verified independently. We attempted multiple methods to establish a reliable dimerization assay or stabilize the dimer, but faced significant challenges due to the low abundance of PRC2 dimers, estimated at only ~10% compared to monomers, as previously observed in the cryo-EM studies conducted by Dr. Paul Sauer.[356] It is important to note that this estimation does not represent a realistic quantification, but highlights the difficulties of capturing the dimeric form of PRC2.

When we attempted to use cross-linking mass spectrometry, we were unable to detect cross-links specific to the dimer, likely due to its low abundance. We also explored tagging PRC2 with Halo Tags or Förster resonance energy transfer (FRET) biosensors based on our structural results for detection via bulk fluorescence spectroscopy. However, this approach required extensive optimization, and we were ultimately unable to detect dimerization, possibly due to low abundance of PRC2 dimers, the transient nature of dimerization and limitations in assay sensitivity. If successful, this method could open new avenues for studying dimerization dynamics. One promising yet complex approach for further optimization could involve immobilizing nucleosomes on a surface and incubating them with PRC2 afterward. This would allow for the detection of dimeric FRET signals at the single-molecule level and reduce background interference from monomeric PRC2. Given the abundance levels seen in cryo-EM, this method could enable the quantification of reduced dimerization more accurately.[372] One such approach could involve using biotinylated DNA on nucleosomes as was used to analyse PRC2 residence on nucleosome arrays via total internal reflection fluorescence (TIRF).[159]

Additionally, we began working on establishing GFP complementation assays using Split-GFP to study dimer formation. However, due to the complexity of the dimer and the challenges in assay optimization, this approach could not be pursued further. If successfully completed, the complemented GFP tags could be used not only to visualize dimer formation but also to enrich dimeric PRC2. For example, the complemented GFP could be purified using antibody-coupled affinity chromatography.[373] Alternatively, the Split-GFP could be modified with additional tags.[374, 375] This methodology would also open new possibilites to characterize dimerization in a cellular context and and potentially identify interacting partners. For instance, the complemented GFP could be targeted for epigenetic assays such as CUT&RUN, provided an antibody specifically recognizing the complemented GFP is available. Furthermore, the Split-GF can be coupled with proximity labeling methods which could be applied to investigate which proteins interact specifically with the dimer in a cellular context.[376, 377] These methods would allow for investigations into the occurrence and context of dimerization on chromatin, such as identifying specific gene loci environments where PRC2 dimers form.

Previous studies by Lee et al. and Wang et al., suggested that automethylation functions via a *cis*-autoinhibition mechanism, according to which the unmethylated am-loop sterically blocks the active site of PRC2. Complete methylation would promote the release of the am-loop, making the active site accessible to substrates.[186] A similar conformational switch corresponding to such a mechanism was described for Clr4 H3K9 methyltransferase in *Schizosaccharomyces pombe*.[378] While steric effects on the active site of PRC2 cannot be excluded, an increase in activity would be expected for the automethylation mutant. As described in the previous studies, arginines mimic a lysine with a positively charged state that cannot be neutralized by methylation, which thus would simulate the released state.[185, 186] Not only was the opposite observed by us, but the activation via $PRC2^{CXC}$ suggests that the stimulatory effect is mainly driven by dimerization in *trans*. An interesting observation by Wang et al. described a significant increase of K510 methylation by incubating recombinant proteins with SAM and H3 substrate compared to only SAM.[186] They hypothesized that due to the location of the automethylation lysines on a disordered loop (aa 480-515) of EZH2, this steric-driven mechanism could influence the release of the am-loop. However, more recent structures revealed that this region forms an α-helix when bound to a substrate nucleosome, that is positioned between the nucleosomal DNA, the EZH2-SET domain and the H3 tail.[199, 200] Automethylation could directly influence the bridge helix conformation and thereby indirectly affect nucleosome engagement and catalytic efficiency, which was not observed in our experiments. Indeed, comparable mechanisms were described for kinases where conformational changes occur upon phosphorylation which increase substrate binding.[379-381]

We further identified K510me3 as the lysine primarily responsible for the stimulatory effect, showing sequence similarities with H3K27me3 and JARID2 K116me3, where an arginine at the -1 position enhances EED binding affinity.[131, 149] This aligns with *in vitro* findings showing that K514A/K515A double mutations do not significantly impact the stimulatory effect of automethylation.[186] While K514me3 or K515me3 did not play a notable role in our experiments, K510/K514 double mutations reduced the stimulatory effect compared to individual single mutations.[185] On that note, an additional regulatory layer may involve the initial methylation of the automethylation lysines. While previous studies have shown that PRC2 methylates itself in *cis* and our results suggest that only K510me3 results in an increased activity, K514 and K515 are also methylated.[185, 186] The proximity of the three lysines complicates the identification of each residue's methylation state, however, our mass spectrometry analyses suggest K514 methylation may be more abundant than K510 methylation, as was also observed by Lee et al. and Wang et al..[185, 186, 356] Interestingly, the most commonly observed methylations were mono- and di- methylation which raises the question of whether additional processes occur to reach the trimethylated state proposed for the stimulatory effect. For example, PRC2 deposits H3K27me1/2/3, but only trimethylation requires allosteric activation.[220] Furthermore, point mutation studies showed that mutations of K510A and K510R minimally impacted methylation levels of EZH2. In contrast, K514 and K515 substitutions with alanine and arginine resulted in a dramatic overall decrease of EZH2 automethylation.[186] As such, these two

lysines may not affect the stimulatory mechanism but the initial methylation deposition. Thus, K514 and K515 may regulate methylation levels upstream of the dimerization described here.

11.1.2. Automethylation fine-tunes PRC2 regulation in an environment-specific context

In mammalian systems, the mechanisms by which PRC2 is recruited to establish H3K27me3 remain poorly understood. PRC2 recruitment may be caused by H2AK119ub, which directly interacts with JARID2 and in turn, recruits PRC2 to target loci.[124, 134, 171, 182, 199, 362, 382] However, the complex mechanisms of PRC2 recruitment remain inconclusive and a topic of debate.[383] Our transcriptomic analyses in mESCs indicate that disrupting either dimerization or automethylation affects specific transcriptional programs, including E2F target genes and the G2M checkpoint during later differentiation stages. These disruptions point at context-dependent deregulation of pathways that overlap between the automethylation and dimerization mutants, without impairing global PRC2 functionality, as evidenced by the restoration of bulk H3K27me3 levels.

This finding aligns with previous studies demonstrating that PRC2 function globally remains intact despite disrupted automethylation.[185, 186] Moreover, this context-dependent activity challenges the proposed *cis*-autoinhibition model of EZH2 automethylation, which would predict a more widespread impairment of PRC2 function independently of genomic context. Indeed, the absence of a global effect is further supported by Lee et al., who observed that automethylation mutants did not alter chromatin engagement or genome-wide occupancy of PRC2.[185] Together, these results emphasize the context-specific regulatory role of automethylation and suggest that PRC2 activity adapts to environmental or chromatin context variations rather than being broadly compromised.

One limitation in our experimental system is that differentiation was not strongly affected across all cell lines, including the EZH1/2 and SUZ12 KO cells, raising concerns about the robustness of the differentiation protocol. Prior studies suggest that PRC2 KO cells lose viability during differentiation.[120, 336] . Thus, the differentiation observed in our system may reflect compensatory mechanisms or PRC2-independent pathways specific to this lineage. Future studies should utilize differentiation models more reliant on PRC2 function, such as neuromesodermal progenitors, to reveal a more pronounced impact of impaired automethylation.[384] Further analyses, including ATAC-seq and epigenomic approaches such as ChIP-Seq or CUT&Tag to map the genome-wide distribution of H3K27me3 and PRC2 occupancy are essential to elucidate how these mechanisms affect chromatin features at distinct genomic loci. Despite these limitations, our findings establish a foundation for understanding the nuanced role of automethylation in transcriptional fine-tuning, distinct from global PRC2 activity.

We propose that automethylation and dimerization may activate PRC2 in environments lacking other activators, thereby representing a possible nucleation point on chromatin to initiate H3K27me3 deposition. This mechanism may require a high local PRC2 concentration, as two PRC2 molecules are necessary for dimerization. Additionally, PRC2 may interact with transcription factors and non-histone substrates, where automethylation could play unique regulatory roles. On the one hand, these substrates may recruit PRC2 to loci for dimerization, while on the other hand, they may act as non-histone substrates of EZH2, necessitating automethylation.[385-388] Future research should investigate whether other methyltransferases or demethylases target PRC2 automethylation sites, potentially adding another layer of regulation

Furthermore, the composition of PRC2 itself may fine-tune this mechanism. The am-loop is conserved between EZH1 and EZH2, and while EZH1 exhibits lower activity, automethylation could enhance PRC2-EZH1 activity.[114, 115, 187] Since we used the defined five-subunit PRC2 complex, certain accessory subunits may not support dimerization (See: Chapter 6.2.2). Indeed, structural studies by Paul Sauer and others indicate that PRC2 dimerization cannot occur in certain chromatin contexts, such as when JARID2 is bound to the complex or in the presence of dinucleosomes.[356] JARID2 recruitment to chromatin is guided via mechanisms such as engagement with mono-ubiquitinated H2AK119ub to specific regions for *de-novo* H3K27 trimethylation.[173, 199] The

structural comparison revealed that JARID2 sterically blocks PRC2 dimerization by obstructing the SUZ12-SUZ12 interface and may inhibit $PRC2^{dist}$ linker DNA binding. This inhibition occurs even in the absence of K116me3, emphasizing that JARID2 structurally competes with $PRC2^{dist}$ binding to EED.[199, 356] Similarly, dinucleosome engagement, in which a H3K27me3-bearing nucleosome activates PRC2 to methylate an adjacent nucleosome, is sterically incompatible with dimerization, as the methylated nucleosome would clash with the SANT2 domain of $PRC2^{dist}$.[200, 356] Collectively, these findings suggest PRC2 activation via dimerization represents an alternative, rather than a complementary, mechanism to JARID2- or H3K27me3-driven activation.

Exploring the newly discovered regulatory mechanisms of the PRC2 complex opens therapeutic possibilities, especially given its association with various cancers types. Drugs targeting epigenetic regulators often lack specificity, risking disruption of essential cellular processes. The broad activity of these proteins across various cell types makes selective targeting particularly difficult, underscoring the importance of understanding their regulatory mechanisms to improve specificity.[389] Emerging technologies like proteolysis-targeting chimeras (PROTACs) offer promising avenues by enabling the selective degradation of specific protein targets, potentially increasing precision and minimizing off-target effects in cancer therapies.[390, 391] EED and EZH2 inhibitors have already demonstrated promising results, underscoring the potential of PRC2 as a therapeutic target.[96, 102, 207-209] However, a deeper understanding of automethylation and dimerization could inform new therapeutic strategies aimed at selectively targeting these regulatory mechanisms selectively. PROTAC compounds targeting PRC2 are under development and could be optimized to exploit these insights.[392, 393] For these approaches to be viable, therapeutic strategies must be highly specific, targeting these regulatory steps without affecting other processes and minimizing toxicity, thus ensuring efficacy.

Just as a symphony orchestra operates through layers of precisely timed and coordinated instrumental contributions, PRC2 utilizes dimerization and automethylation to fine-tune its regulatory function. This intricate composition reveals the depth of regulatory nuances of PRC2 and uncovers new “notes” in the regulatory landscape.

CHAPTER II: STRUCTURAL ANALYSES OF MITOCHONDRIAL COMPLEX FORMATION OF APOPTOSIS-INDUCING FACTOR 1 (AIFM1)

12. RESULTS

The mitochondrial protein AIFM1 is associated with a plethora of different functions. However, despite extensive studies on AIFM1, its intrinsic catalytic activity and detailed mechanistic role remain insufficiently characterized. Recent findings have demonstrated that AIFM1 facilitates the import of the Mitochondrial Intermembrane Space Import and Assembly Protein 40 (MIA40) and directly forms a stable complex with the protein.
The group of Jan Riemer at the University of Cologne obtained a high-confidence interactome for AIFM1 in the IMS.[394] This analysis reaffirmed the AIFM1-MIA40 interaction and unveiled a novel interaction partner: AK2A, the longer isoform of adenylate kinase 2 (AK2). In collaboration with the group of Jan Riemer, the primary goal of this study was to investigate the structural details of AIFM1 interactions with MIA40 and AK2A and to elucidate the mechanistic basis that underly the functional consequences of these interactions.

12.1. Cryo-EM study of mitochondrial AIFM1 interaction with MIA40 and AK2

12.1.1. Sample preparation of AIFM1

To characterize the impact of AK2A and MIA40 on the AIFM1 structure, Alex Rothemann from the Riemer group provided us with reconstituted, recombinant protein complexes to perform cryo-EM. We were interested in the structural determinants of AK2 and MIA40 interactions with AIFM1 and their structural implications. Therefore, this study aimed to solve three structures of human AIFM1 to evaluate structural differences and potential functional implications: 1. the dimer of soluble AIFM1 in the absence of an interaction partner (termed ‘AIFM1 dimer’ here; aa 103-613) 2. AIFM1 bound to AK2A (termed ‘AIFM1-AK2A’) 3. AIFM1 bound to MIA40 (termed ‘AIFM-MIA40’). After preliminary testing, the optimal buffer conditions for AIFM1 freezing were determined to be the same as those used in the protein purification process, ensuring stability and consistency for high-resolution data acquisition.

12.1.2. Cryo-EM data analysis

The initial cryo-EM analysis of AIFM1 complexes showed a good particle distribution and quantity, allowing for effective 2D classification (Figure 28A). The resulting 2D classes showed well-defined structural features and symmetrical elements, which reflect the good quality of both the sample and the imaging process. However, the analyses also revealed challenges as the limited number of distinguishable 2D classes indicated preferred particle orientation, which significantly affected the quality of the overall reconstructions. Specifically, angular distribution analysis showed a pronounced bias in particle views, with the data dominated by a subset of orientations that appeared more frequently than others (Figure 28B). Although local resolution analysis revealed particularly poor resolution in flexible regions such as the C-terminal domain and peripheral edges, the issue extended across the entire map. The overall resolution of 4.6 Å was likely an overestimation, as the preferred orientations limited our ability to produce a reasonable 3D reconstruction (Figure 28C).

To address these challenges, we modified the data acquisition strategy by introducing a 35° stage tilt during imaging, as described in Methods Section 9.4.3. This adjustment reduced the orientation bias and provided a broader set of particle views, enabling the generation of higher-quality maps and improving the overall reconstruction quality for all three complexes.

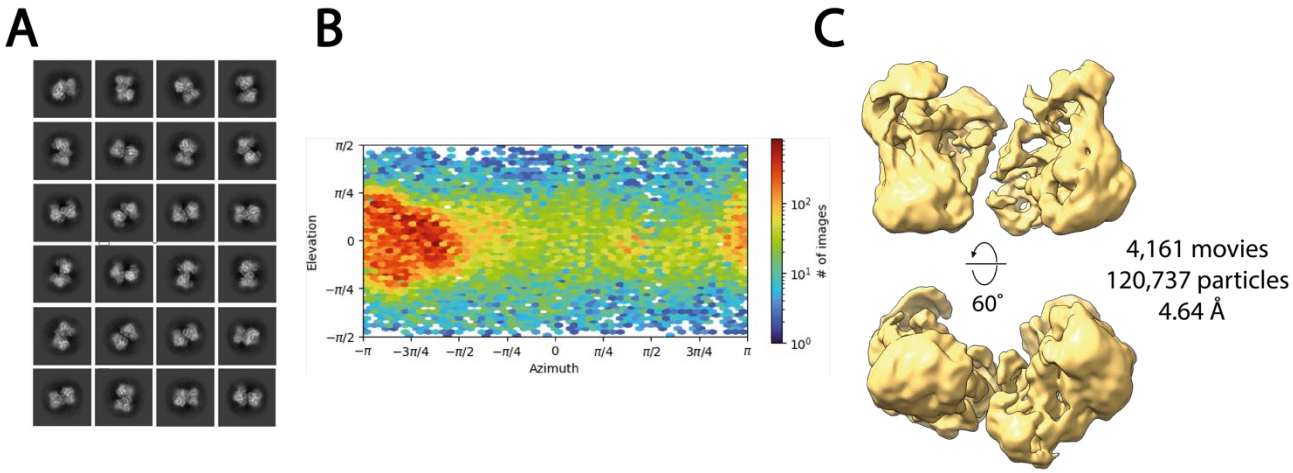

Figure 28: Initial cryo-EM processing without tilted data acquisition

A. *Exemplary 2D classification of the AIFM1-MIA40 complex dataset without tilt. This classification highlights the preferred particle orientation, with clusters of particles predominantly aligned in similar orientations. These 2D classes were then used in subsequent refinement steps.* ***B.*** *Angular distribution plot of the reconstruction, showing gaps in views due to preferred orientation. This lack of complete angular coverage led to missing information for certain parts of the structure.* ***C.*** *Initial reconstruction from this dataset shows good resolution in core areas; however, visual inspection reveals missing densities and reduced quality in the more flexible regions.*

We successfully obtained reconstructions for the AIFM1 dimer, AIFM1-AK2A and AIFM-MIA40 complexes with a global resolution of 2.8 Å, 2.6 Å and 2.4 Å, respectively. Interestingly, the AIFM1-AK2A complex yielded a higher-quality map with less data (15,440 movies, 307,496 particles) compared to the AIFM1 dimer (3,991 movies, 277,866 particles). The AIFM1-MIA40 (4,542 movies, 291,656 particles) complexes resulted in the best resolution, even though all samples underwent identical preparation. However it is important to note that the AIFM1-MIA40 data were collected under different imaging conditions, using a different detector, dose and pixel size, which could have significantly impacted the data quality and subsequently reconstruction.

The comparison of local resolution maps of the three complexes shows that AIFM1-MIA40 and dimer show higher variability in the local resolution, which could be a hint towards conformational variability in these complexes. Both the AIFM1-MIA40 and AIFM1 dimer complexes show higher variability in local resolution as compared to AIFM1-AK2A, possibly due to conformational flexibility. In contrast, this variability was less pronounced in the AIFM1-AK2A complex, where the resolution was more uniform across the map contributing to its high-quality reconstruction.

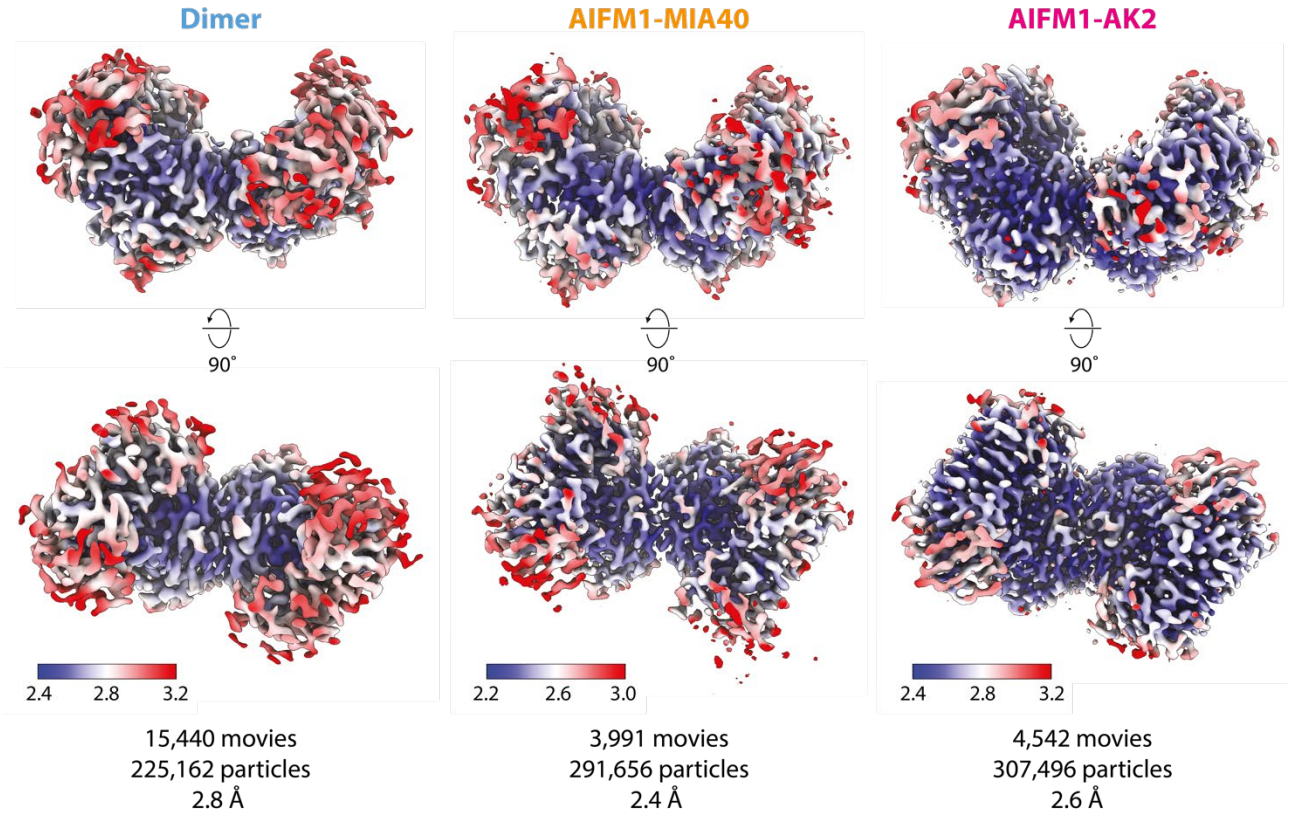

Figure 29: Local resolution maps of the three AIFM complex reconstructions

The local resolution maps across the three reconstructions with the respective global resolution and data required to obtain the maps. The AIFM1-AK2A complex demonstrates more consistent resolution throughout whereas the AIFM1-MIA40 and AIFM1 dimer complexes display areas of variable resolution, highlighting regions of potential conformational flexibility.

12.1.3. Structural characterization of the three AIFM1 complexes

The high-resolution cryo-EM maps allowed us to build atomic models for AIFM1 (aa 128–611), MIA40 (aa 2–20), and AK2A (aa 232–239) in each respective complex. For all AIFM1 structures analyzed in this study, an initial model was generated using AlphaFold2. This model was then cross-referenced with previously published human and mouse AIFM1 structures (PDB: 4BUR and PDB: 3GD4) and residues were adjusted using Coot and the models iteratively refined using Phenix.[337, 338] To enhance visualization during initial model building, maps were processed using DeepEMhancer.[347]

All three complexes were resolved as dimers, containing both FAD and NADH cofactors, in line with previously published structures of reduced AIFM1.[324] In agreement with the structures obtained for reduced AIFM1 by X-ray crystallography, we did not obtain density for the C-terminal region (aa 511–557 for AIFM1 dimer and AIFM1-MIA40, aa 511-549) likely due to its inherent flexibility. Additionally, only the sections of MIA40 and AK2A directly interacting with AIFM1 could be resolved, while the remaining parts were undetectable, likely owing to high flexibility in these regions (Figure 30A).

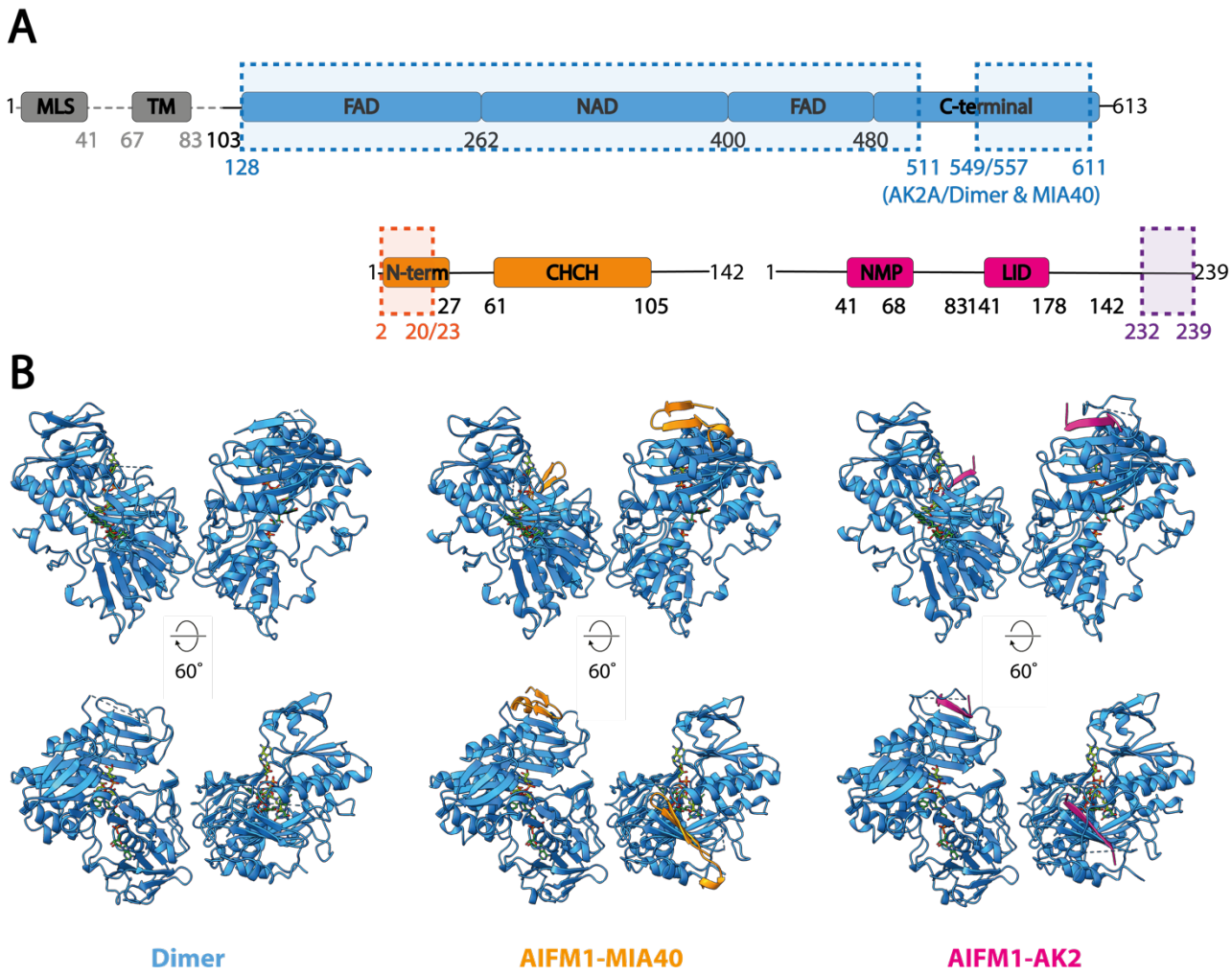

Figure 30: Refined atomic models of the three AIFM complexes

A. *The schematic overview shows the proteins and their respective domains. AK2A (violet, aa 1-239) and MIA40 (orange, aa 1-142) were expressed as full-length proteins while for AIFM1 aa(103-613) was the transmembrane domain was truncated. The dashed boxes mark the regions resolved in the final structure. For AK2A an additional region (aa 549-557) of the C-terminal domain was resolved* ***B.*** *Overview depiction of the refined atomic models of the three AIFM1 complexes the AIFM1 dimer (left), AIFM1-AK2A (middle), and AIFM1-MIA40 (right). AIFM1 (blue) was resolved in all models as a dimer with both cofactors, resembling reduced AIFM1. Two β-strands of MIA40 (orange) and one of AK2A (violet) could be built into the map..*

Both AK2A and MIA40 were found to share the same binding site on AIFM1, extending the five β-strands of the C-terminal domain. Each partner contributes β-strands to this site in a parallel manner, with AK2A and MIA40 complementing the β-sheet of AIFM1 with one and two additional β-strands, respectively (Figure 31A). This binding mode is consistent with the low-resolution crystal structure of MIA40-bound oxidized AIFM1.[334] Interestingly, this binding region was shown to be occupied by an AIFM1 β-strand in previously reported murine and human AIFM1 dimer crystal structures, where residues 538–544 in murine and 510–515 in human AIFM1 form the sixth β-strand.[320, 323, 324] Our cryo-EM dimer structure corroborates this observation. However, the local density did not allow for unambiguous interpretation. In contrast to these previously published structures, the AIFM1-dimer EM density indicated a possible AIFM1 β-strand on both protomers, instead of only one.
In our reconstruction, we could clearly identify the side chains of F14 of MIA40 and F238 of AK2A. These allowed us to unambiguously determine the β-strand from these proteins on both AIFM1 protomers (Figure 31B, C). Modelling of the complexes further suggests that each AIFM1 dimer can bind two molecules of either AK2A or MIA40, with both binding sites occupied simultaneously. Notably, no observed reconstructions showed occupancy of only one of the binding sites per AIFM1 dimer, indicating that the formation of the heterotetramer by either AK2A or MIA40 may stabilize

the AIFM1 dimer, thereby favoring fully bound complexes and yielding the highest resolution reconstructions.

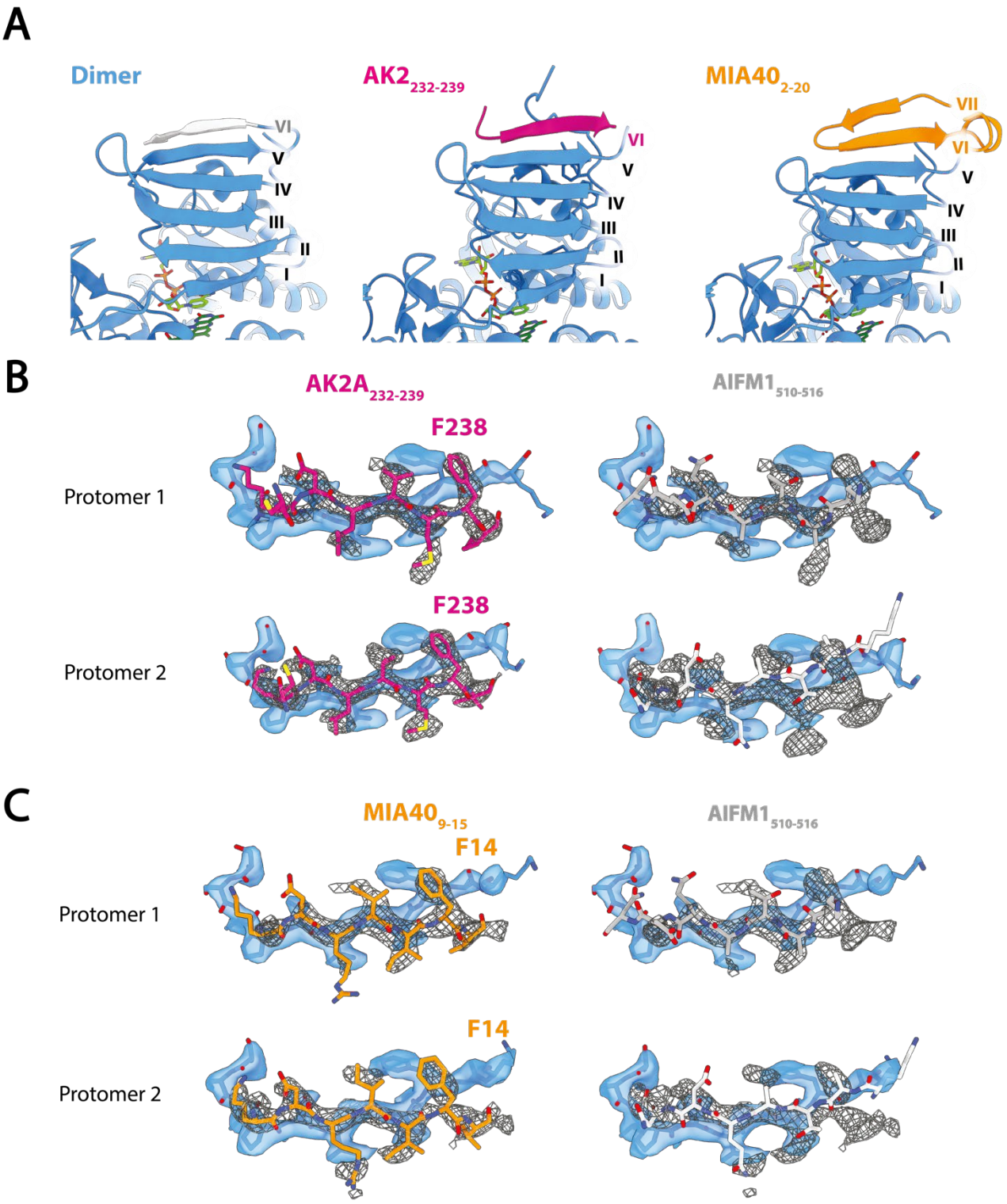

Figure 31: Binding interfaces and β-strand complementation of AK2A and MIA40 on AIFM1

A. *Both AK2A (violet) and MIA40 (orange) engage in β-strand complementation at the five C-terminal β-strands of AIFM1 (blue). MIA40 extends the structure with two β-strands, while AK2A contributes only one. Additionally, the AIFM1 dimer forms a sixth β-strand (white), consistent with previously published structures.* ***B.*** *Comparison of the AK2A-complemented β-strand (left) with the possible sixth β-strand of AIFM1 (right) reveals that only AK2A can occupy the density on both protomers, particularly at F238.* ***C.*** *The complemented β-strand of MIA40 fit into the map (left) compared to the possible sixth β-strand of AIFM1 (right) demonstrating that only MIA40 can occupy the density on both protomers, especially at F14.*

Although AK2A and MIA40 share a common binding site, their interaction with AIFM1 differs in specific ways (Figure 32A,B). In both complexes, hydrophobic interactions are formed between V505 and V507 of AIFM1 with either I13 of MIA40 or L235 and M237 of AK2A. Opposite this region, a hydrophobic patch on AIFM1 formed by Y347, F508, and Y560 interacts with residues I12 and F14 of MIA40, or V236 and F238 of AK2A. This interaction is further strengthened by the additional aromatic residue F3 on the second β-strand of MIA40, which stacks with F14, adding stability to the interaction. Lysine and aspartate residues at the C-terminal end of the complementing β-strand further contribute to binding stability. In AK2A, K233 and D234 potentially form hydrogen bonds with S500, the backbone carbonyl of L502, and the side chain of T504 in AIFM1(Figure 32B, bottom). Similarly, K9 and D10 in MIA40 may also participate in hydrogen bonding at this site, anchoring the entire interaction (Figure 32A, bottom).

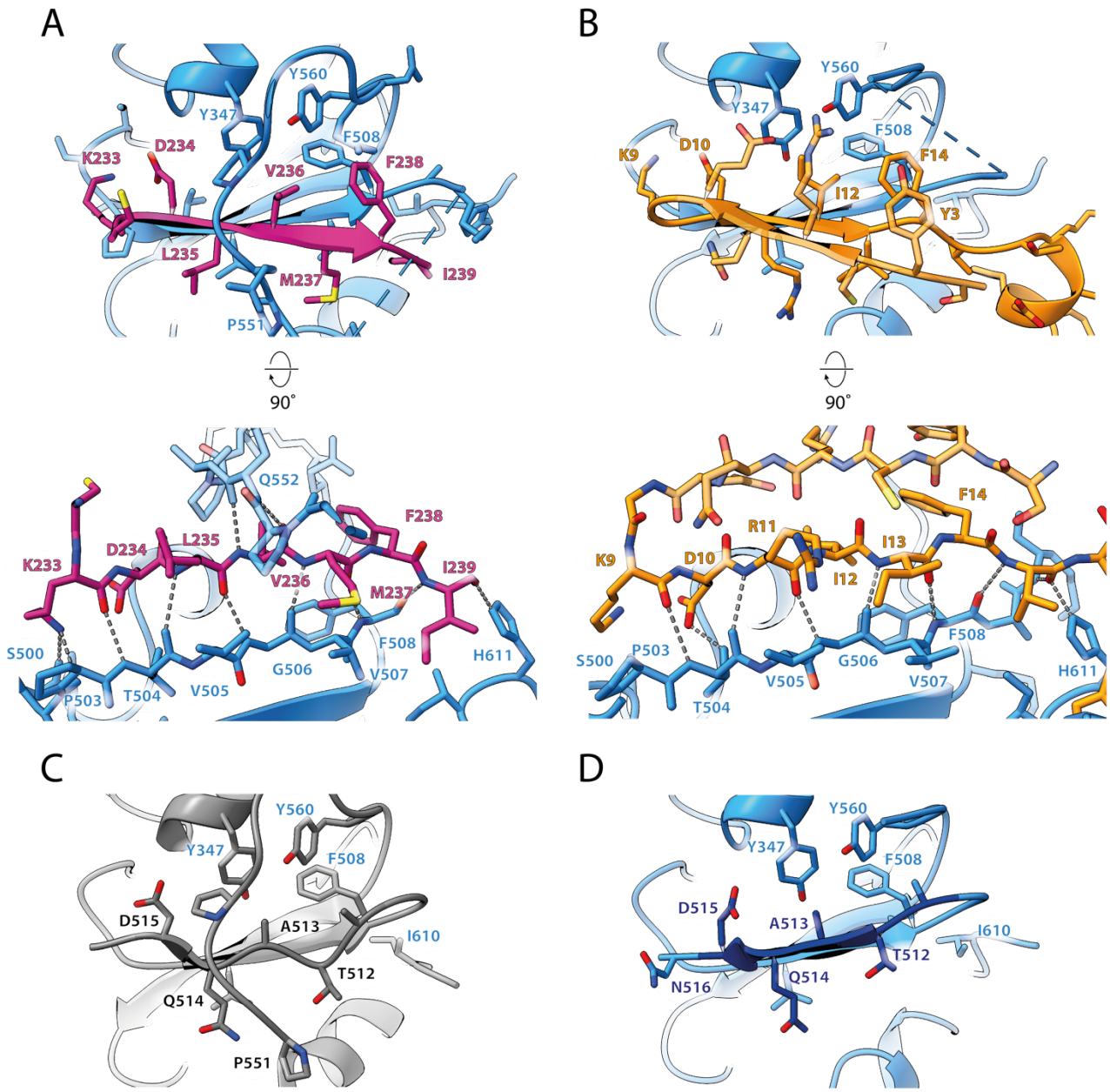

Figure 32: Interacting residues involved in the β-strand complementation

A. *Zoomed view of the interaction interface between AIFM1(blue) with AK2A (violet). The second turned view shows the residues likely forming hydrogen bonds facilitating the interaction between AIFM1 and AK2A. The additionally resolved region of the C-loop (549-557) may stabilize AK2A bidning, particularly through interactions with Q552.* ***B.*** *Specific residues at the interaction interface between AIFM1 (blue) with MIA40 (orange). The second view shows the residues liekely facilitating the interaction between AIFM1 and MIA40.* ***C.*** *The crystal structure of the reduced AIFM (PDB:4BUR, Gray) shows that the additional C-loop (aa 550–558) resolved in the AK2A interaction interface was previously described*

to bind the sixth β-strand of AIFM1. ***D.*** *The additional β-strand of AIFM1 (dark blue) that was fit into the resolved AIFM1 dimer structures.*

Interestingly, possibly due to the lack of a second β-strand in the AIFM1-AK2A structure, an additional part of the otherwise flexible C-loop (aa 549–557) was resolved. This segment traverses the β-strand of AK2A, potentially forming hydrogen bonds between the backbone carbonyl of Q552 in AIFM1 and the backbone amine of V236 in AK2A (Figure 32A, bottom). Even though we could not observe the additional section of the C-terminal region, this engagement was observed for the additional β-strand (residues 510–515) of the previously described human crystal structure(Figure 32C,D).[324]
In conclusion, while AK2A and MIA40 bind to the same site on AIFM1 and involve key conserved residues, the structural interactions differ subtly. These distinctions provide insights into diverging binding mechanisms and stabilizing effects of β-strand complementation in these complexes.

12.1.4. Characterization of the structural variability of the complexes

To assess the structural impact of AK2A and MIA40 binding on AIFM1, we first compared the structural differences of AIFM1 protomers within each complex (Figure 33). Afterwards, we analyzed the differences in the bound forms relative to the free AIFM1 dimer (Figure 34). The well-resolved N-terminal domain near the dimerization site (aa 232–257, 404–434 and 440–450) was selected as a stable reference region for alignment. Afterwards, the root mean square deviation (r.m.s.d. or rmsd) of the Cα backbone was calculated to quantify structural differences.
Analysis of the AIFM1 dimer revealed notable differences within the complex, suggesting an inherent asymmetry between the two protomers. This effect was even more pronounced in the AIFM1-MIA40 complex, especially in the NAD binding and C-terminal domains, hinting that MIA40 binding introduces or accentuates structural variability between protomers. In contrast, the AIFM1-AK2A complex displayed a high degree of structural similarity between the protomers, suggesting that AK2A binding stabilizes a conformation of AIFM1 in both protomers.

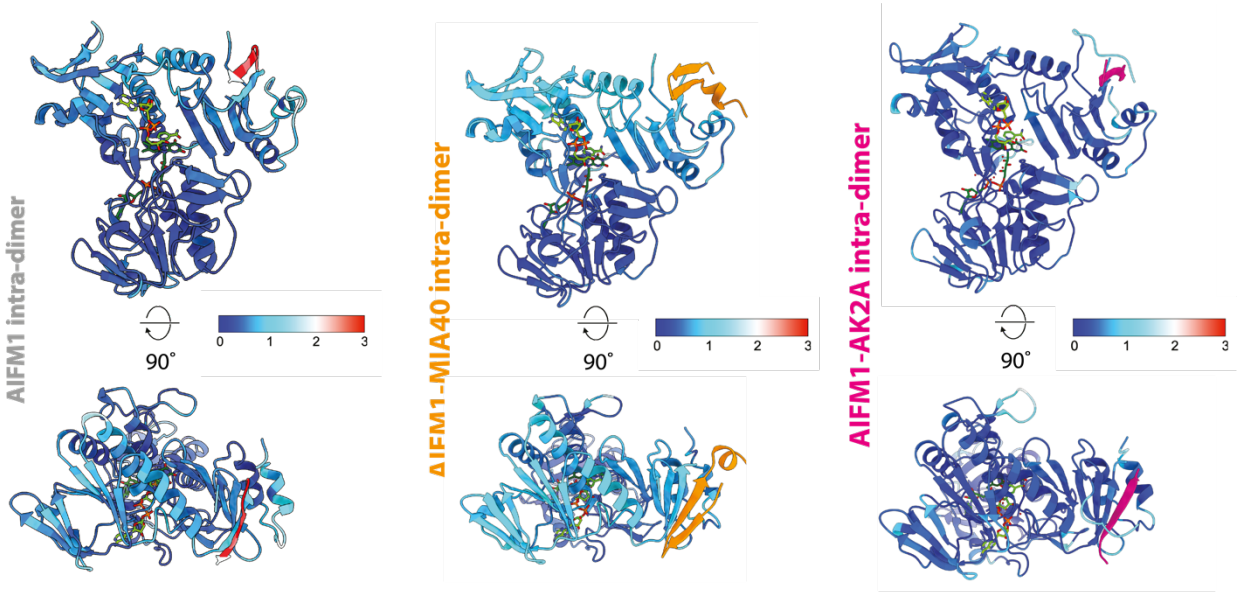

Figure 33: Analyses of the structural variability of AIFM1 protomers within one diemr complex
Illustration of the RMSD differences between AIFM1 protomers within one complex. The dimer (left) and AIFM1-MIA40 (middle) exhibit greater structural differences as indicated by the light blue parts of the model as compared to the relatively consistent conformation induced by AK2A (right) binding that appear dark blue in this representation.

When comparing the bound protomers to the AIFM1 dimer, we observed that the AIFM1-AK2A complex closely resembles one of the protomers of the free AIFM1 dimer. This finding suggests that

AK2A binding stabilizes AIFM1 in one conformation and reduces structural variability. In contrast, the AIFM1-MIA40 complex showed RMSD differences of up to 3 Å in comparison to the AIFM1 dimer, particularly in the NAD binding domain and an α-helix near the C-terminal domain (aa 345–359). MIA40 binding induced compaction in AIFM1 that affected cofactors. The distance between the nicotinamide and isoalloxazine rings was reduced by approximately 0.2 Å in the AIFM1-MIA40 complex and the position of the adenine ring of NADH shifted by more than 2 Å relative to its position in the unbound AIFM1 dimer.
These shifts indicate that while AK2A binding stabilizes one AIFM1 conformation, MIA40 binding induces structural rearrangements that may influence the catalytic function through modifications in the NAD binding domain.

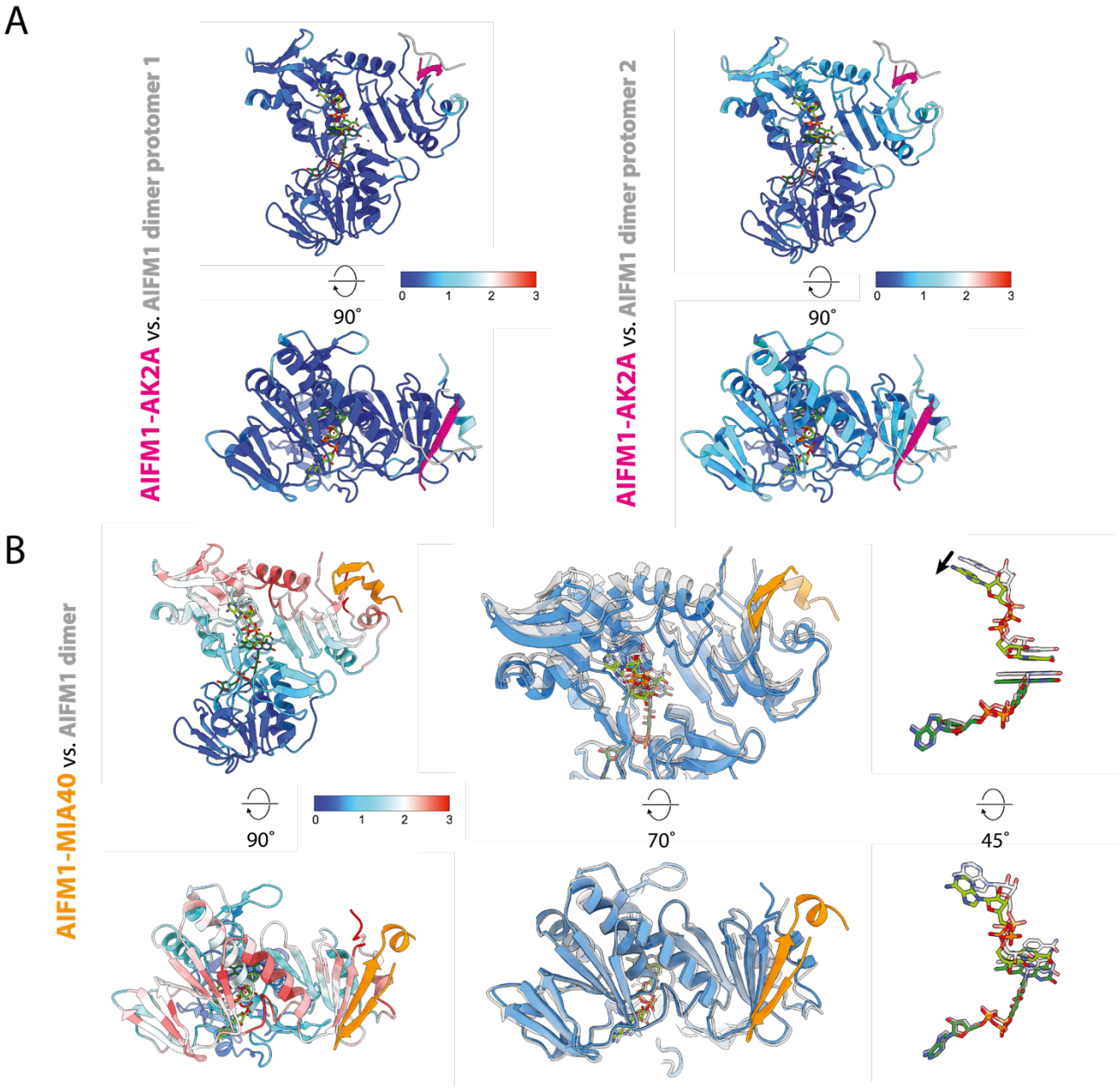

Figure 34: Analyses of the structural variability of bound AIFM1 protomers towards the AIFM1 dimer
A. *Illustration of the RMSD differences between AIFM1-AK2A compared to the AIFM1 dimer protomers. AIFM1-AK2A closely resembles one of the protomers of the AIFM1 dimer.* ***B.*** *The left panel shows the RMSD difference between AIFM1-MIA40 compared to one AIFM1 dimer. The NAD binding domain shows prominent displacement. The middle view shows an enlarged view of these overlayed monomer (AIFM1-MIA40: blue, Dimer: transparent) after alignment and the NAD binding domain seems to move towards the dimer interface. On the right the isolated view of NADH and FAD of both*

monomers (AIFM1-MIA40: green, Dimer: transparent) shows that this difference is mirrored on the cofactos. The direction of the displacement is visualized by the arrow.

12.1.5. Impact of MIA40 binding on cofactor interactions

In our structural models, the FAD and NAD cofactors were well-resolved, allowing us to examine their interactions with AIFM1. Across all three complexes, the residues involved in cofactor binding were consistent with those identified in previous studies. Notably, E314 formed hydrogen bonds with the O4 atoms of NAD and established a salt bridge with K177, which then interacted with the N5 atom of FAD. Additionally, H454 formed a hydrogen bond with the O7 atom of the nicotinamide, aligning it for optimal parallel stacking between F310 and the isoalloxazine ring of FAD. [323, 324, 326]

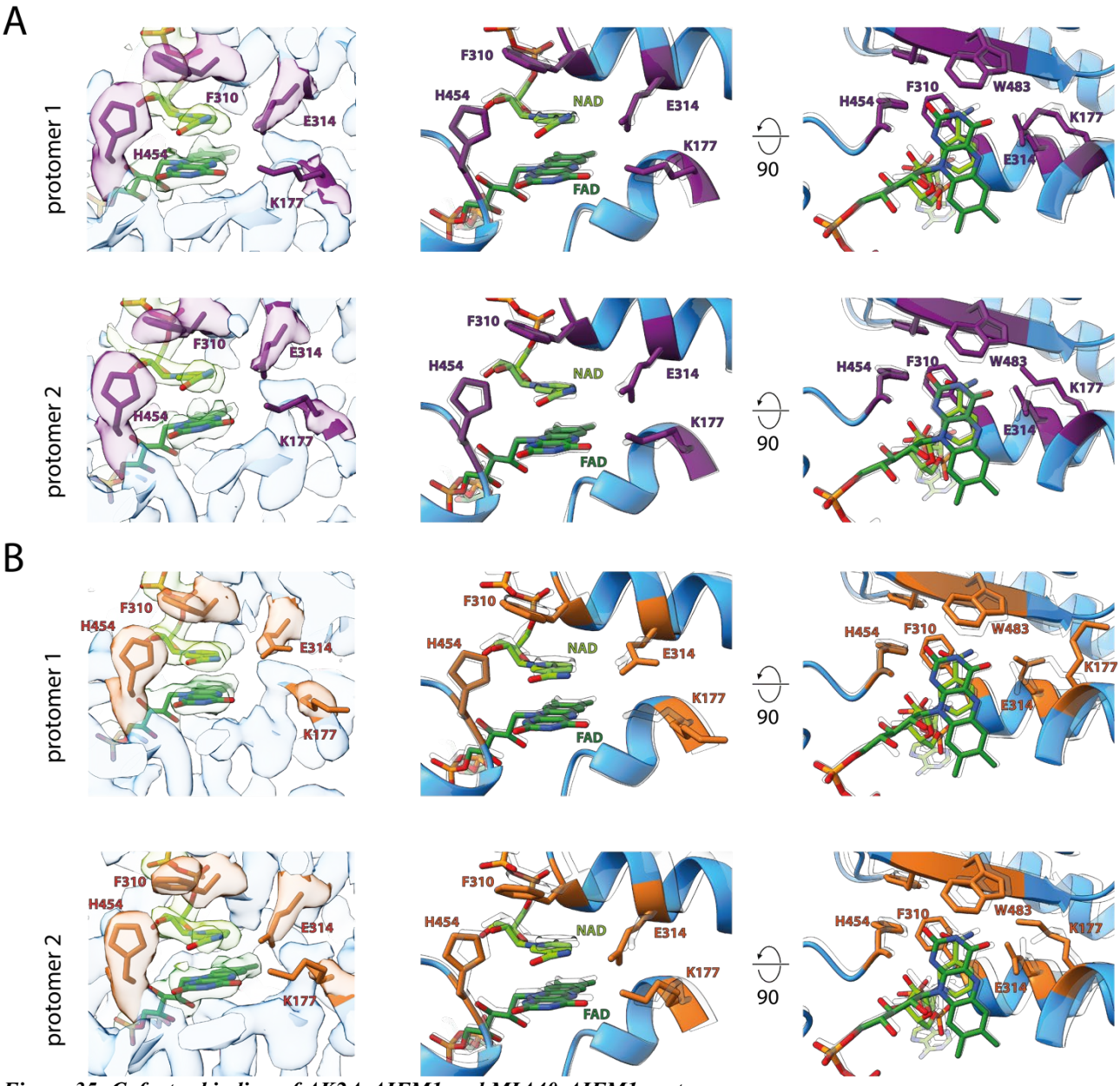

Figure 35: Cofactor binding of AK2A-AIFM1 and MIA40-AIFM1 protomers

A. *On the left, the residues (violet) of AIFM1-AK2 binding the cofactors (green) are represented in the transparent and colored EM density. On the right, the respective residues were aligned to the monomer of the AIFM1-dimer (transparent) which AIFM1-AK2A resemble.* ***B.*** *On the left, the residues (orange) binding the cofactors (green) are represented in the map. On the right, the respective area and residues were overlayed to tge monomer of the AIFM1-dimer (transparent). Especially the α-helix bearing F310 and E314 show noticeable differences when compared to the AIFM1 dimer.*

In the AIFM1-MIA40 complex, we observed a minor shift in the α-helix (residues 310-326), which moved closer to the cofactors by 0.2-0.6 Å. This adjustment decreased the distance between the Cα atoms of F310, E314, and K177 in the AIFM1-MIA40 complex compared to the AIFM1 dimer and AIFM1-AK2A. However, in one protomer of the AIFM1-MIA40 complex, K177 exhibited variability, with one conformation engaging with FAD and E314 while the other pointed away. Interstingly, K177 was less well-resolved, likely due to variability or beam-induced damage, which usually affects aspartate and glutamate. Therefore, it is surprising that E314 remained relatively well-resolved, possibly due to the stabilizing salt bridge it forms with K177.
Variability in K177 suggests flexibility in this region, which may be critical for accommodating different cofactor configurations. Furthermore, these conformational changes impacted other residues in the MIA40-bound protomers, particularly F310 and H454, which adopted slightly changed positions compared to other AIFM1 protomers. This structural variability indicates that MIA40 binding influences the conformation of AIFM1's active site, potentially altering its cofactor interactions and by extension, modulating its activity.

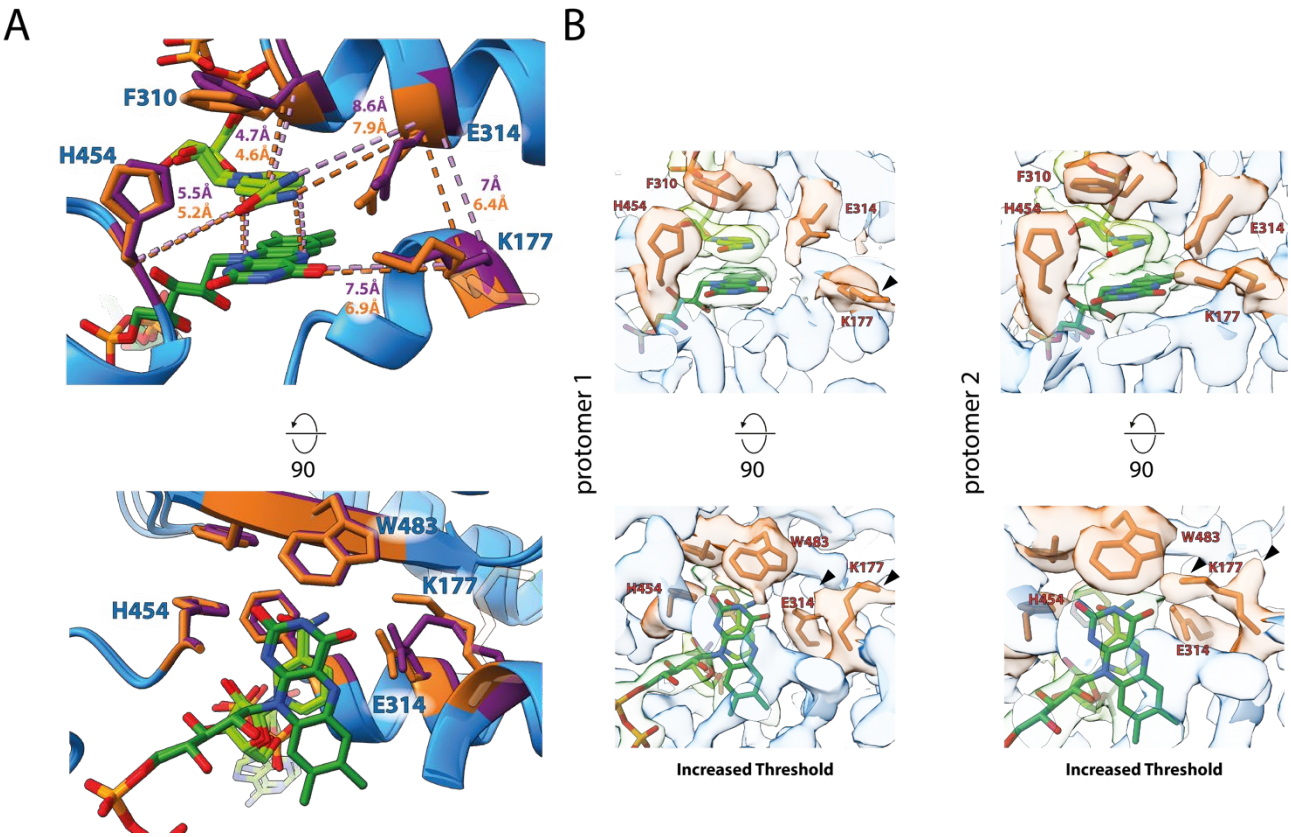

Figure 36: Comparison of cofactor binding in AIFM1-MIA40 and AIFM1-AK2A

A. *Detailed view of AIFM1 interactions with cofactors in the AIFM1-AK2A and AIFM1-MIA40 complexes. Residues stabilizing the cofactors are shown in stick representation, with those from the AK2A complex highlighted in purple and those from the MIA40 complex in orange. The two structures were overlaid, and dashed lines represent the distances between the Cα atoms of the respective residues or cofactor atoms. Distance labels are color-coded to match the respective binding partner.* ***B.*** *Close-up view of the residues involved in cofactor stabilization, shown within their respective density maps at an increased threshold. The key residue K177 is observed in two potential conformations: one oriented toward the cofactors and another facing away.*

12.1.6. The aromatic tunnel: Electron transfer or conformational lock?

Our reconstructions capture AIFM1 in its reduced, dimeric state, offering insights into the impact of AK2A and MIA40 on the conformational changes that occur between oxidized and reduced states. Previous studies identified two major structural shifts when AIFM1 transitions into the reduced CTC: remodelling of the C-loop and the formation of an aromatic tunnel.

In the oxidized state, the C-terminal domain of AIFM1 is stabilized by a β-strand (residues 483-485) that links the FAD-binding and C-terminal domains. This β-strand interacts with a β-hairpin (residues 190-202) that connects the FAD and NADH-binding regions. Upon reduction, this central β-strand releases W198, causing the C-loop to disengage and exposing the surface for potential interactions with electron acceptors or a second NADH molecule. Although previous models suggested the possibility of a second NADH binding in this state, we observed no density corresponding to a second NADH in any of our structures.[324, 325]

The second conformational change upon reduction involves the reorientation of several aromatic residues (F310, Y347, W351, F482, Y492, F508, Y560, and W579) into an 'aromatic tunnel' that has been hypothesized to facilitate redox activity by linking the central cofactors to the C-terminal domain.[323, 325] Both the AIFM1-AK2A and AIFM1-MIA40 complexes extend this aromatic tunnel, with AK2A adding one aromatic residue (F238) and MIA40 contributing two (F14 and Y3) (Figure 37A). However, the specific arrangement of aromatic residues in this region, especially the presence of phenylalanine - which can disrupt charge transfer - suggests that the tunnel is unlikely to participate in redox function as it has been suggested.

Instead, we propose that AK2A and MIA40 serve as conformational locks, stabilizing AIFM1 by securing key residues in place. In particular, their binding would prevent the rearrangement of Y560, which in turn stabilizes W579 and Y492, locking the aromatic tunnel and maintaining the reduced CTC state, thus preventing the reattachment of the C-loop.

This structural hypothesis is supported by functional experiments performed by Alex Rothemann of the AG Riemer that showed that removing excess NADH from a stable CTC state resulted in a half-life of the AIFM1 dimer of approximately four hours. However, when either AK2A or MIA40, or their respective interacting peptides (aa 2-30: SYSRQEGKDRIIFVTKEDHETPSSAELVA for MIA40, and aa 230-239: ATSKDLVMFI for AK2A), were added, the half-life of the dimer extended beyond seven hours (Figure 37B,C). Furthermore, he obtained enzymatic data from a reduction assay with the artificial electron acceptor 2,6-dichlorophenolindophenol (DCIP) (Figure 37D). Adding MIA40 interacting peptides to AIFM1 decreased the K_M and increased k_{cat}, significantly increasing AIFM1 redox activity. Meanwhile, the AK2A peptide exhibited a less prominent activating effect with K_M mostly remaining similar to the negative control and increased k_{cat}. The mutation of aromatic residues in the peptides (MIA40-Y3I, AK2-F238L) diminished or abolished these activating effects, as represented by the unchanged K_M and k_{cat} compared to the negative control(Figure 37E). These findings suggest that AK2A and MIA40 not only enhance the stability of the dimeric state of AIFM1 by preserving its reduced state through structural stabilization but also exhibit an activating function for the otherwise low oxidoreductase activity of AIFM1.

In conclusion, this study reveals that MIA40 and AK2A stabilize AIFM1 through distinct structural interactions that modulate conformation and enhance redox activity. Both partners act as conformational locks at the shared binding site, stabilising the aromatic and effectively extending the functional half-life of reduced dimeric AIFM1. These findings provide valuable insights into the regulatory role of MIA40 and AK2A, highlighting how specific binding interactions can finely tune enzyme stability and activity in cellular redox pathways.

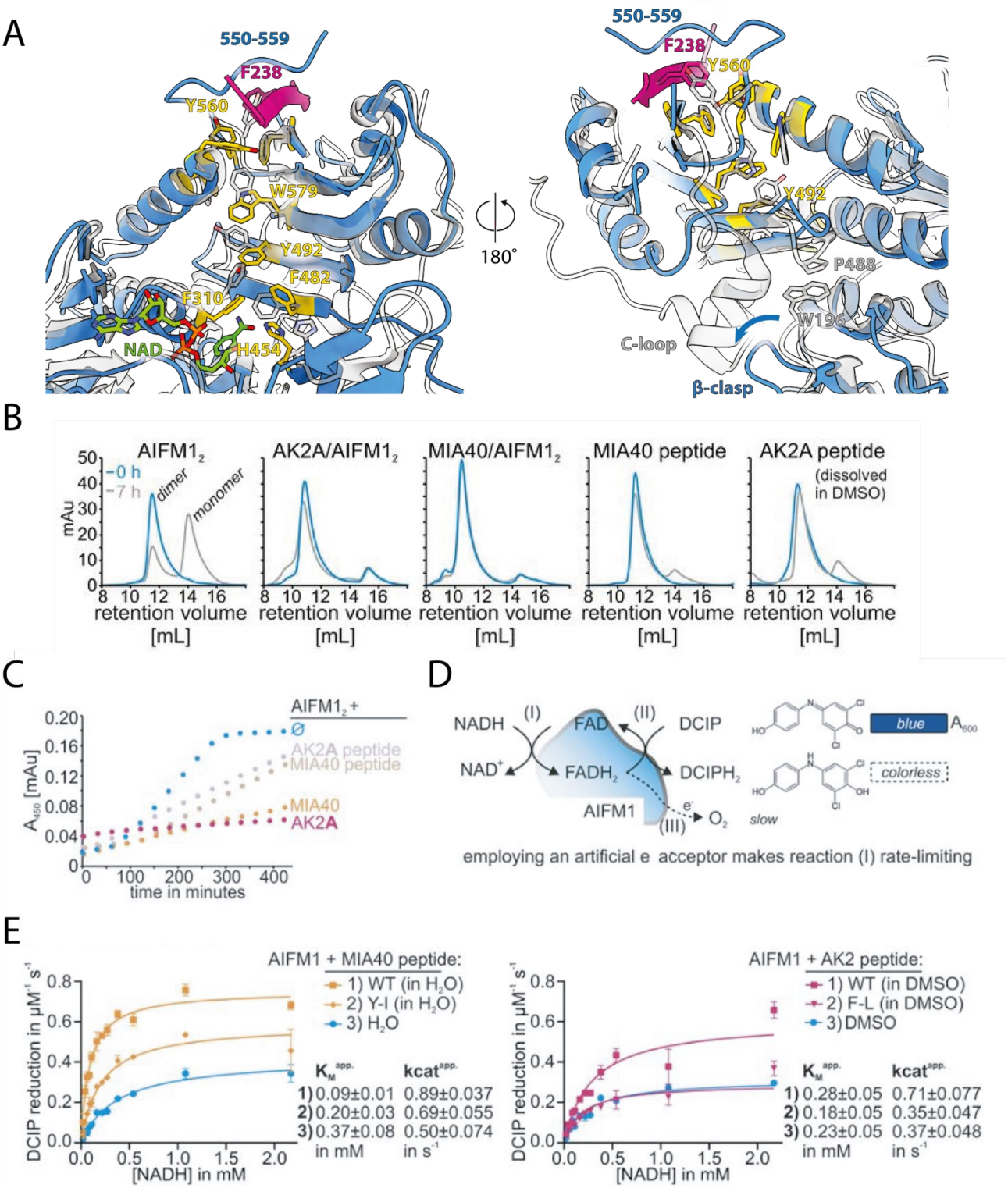

Figure 37: AK2A and MIA40 stabilize AIFM1 by locking the aromatic tunnel

A. *Structural comparison of residues involved in the aromatic tunnel (yellow), showing oxidized AIFM1 (PDB: 4BV6, transparent) overlaid with AK2A-bound AIFM1 (blue).* ***B.*** *Stability of the AIFM1 dimer, AIFM1-AK2A and AIFM1-MIA40 complexes upon NADH removal, analyzed by gel filtration. This experiment performed by Alex Rothemann assessed whether the binding of either MIA40 or AK2A, as well as their respective peptides, stabilizes the dimeric state.* ***C.*** *Stability of the reduced AIFM1 dimer, AIFM1-AK2A and AIFM1-MIA40 complexes after NADH removal, analyzed by absorbance. This assay performed by Alex Rothemann tracked the reoxidation of FADH2 to FAD over time, with slower reoxidation indicating stabilization of the reduced state. Binding of AK2A, MIA40 or their respective peptides significantly reduced FADH2 reoxidation.* ***D.*** *Strategy for measuring the NADH oxidoreductase activity of AIFM1 using the artificial electron acceptor DCIP. This experiment monitored the reduction of DCIP as a proxy for AIFM1 activity.* ***E.*** *These experiments performed by Alex Rothemann show that the MIA40-binding site peptide significantly enhances the redox activity of AIFM1, while the AK2A-binding peptide shows a milder activation effect. Mutations in the key aromatic residues within the peptides (MIA40-Y3I and AK2-F238L) reduce or abolish these effects.*[394]

13. DISCUSSION

AFIM1 has long been associated with caspase-independent apoptosis.[292, 293] Structural and biochemical analyses have identified its NADH-dependent redox functionality, which led to the hypothesis that AIFM1 may play a role as an NADH sensor within the IMS. More recent studies also link AIFM1 to the mitochondrial disulfide relay import pathway, where it facilitates import and serves as a binding platform for MIA40.[283, 320] AK2, previously identified as a substrate of the disulfide relay import pathway was characterized by the AG Riemer as a direct interaction partner of AIFM1.[278] However, the specific mechanisms and functional implications of these interactions remain to be fully elucidated.

The Riemer group successfully purified and isolated AIFM1 complexes with both MIA40 and the AK2A isoform, enabling structural investigation via cryo-EM.[394] Initial reconstructions indicated that the AIFM1 complexes were stable but displayed preferred orientations. Through optimization and tilted acquisition techniques, we obtained cryo-EM reconstructions for the AIFM1 dimer, the AIFM1-AK2A complex and the AIFM1-MIA40 complex. All three structures aligned with previously published crystal structures of reduced AIFM1, showing that both AK2A and MIA40 target the same C-terminal domain of AIFM1.[323, 324, 334] They each contribute additional β-strands—MIA40 using its N-terminal β-hairpin and AK2A using its last seven amino acids—to this binding site.

This binding site was previously characterized as a region that harbours the sixth β-strand of the C-terminal region. In humans, it was proposed that upon reduction, the proximal loop (residues 510–516) adopts this β-strand configuration, whereas, in murine AIFM1, a more distal region of the C-loop (residues 536–543) is thought to form the strand on one protomer within a dimer.[323, 324] Notably, differences in crystallization conditions—e.g. anaerobic for human AIFM1 and aerobic for murine AIFM1—may explain observed structural variations in β-strand formation. Given the sensitivity of protein conformation to redox states and environmental factors, it is plausible that these conditions influenced the structural configurations observed in the two systems.[323, 324] Our cryo-EM analysis of the AIFM1 dimer indicated the presence of a sixth β-strand resembling the human configuration, though local resolution limitations did not allow exact modeling.

We observed density resembling the β-strand, along with AK2A and MIA40 binding at both protomers in each of the three complexes. This contrasts with the ITC data from the Riemer group, which indicated a 2:1 stoichiometry for both AIFM1:MIA40 and AIFM1:AK2A complexes. [323, 324, 394] Our findings, however, align with small-angle X-ray scattering (SAXS) data, suggesting the existence of a heterotetrameric AIFM1-MIA40 complex.[334] Notably, both cryo-EM and ITC were performed under the same experimental conditions, meaning they should theoretically yield similar stoichiometries. The divergence in results likely stems from differences between the techniques. ITC requires precise control over protein purity and concentration, as the technique measures the heat released or absorbed during molecular interactions in solution, which can be influenced by conformational changes. This approach reflects average binding behaviors, but may not capture the full range of stoichiometric variability that exists in a population of molecules, particularly if there are deviations in protein concentration or purity, which can lead to inaccurate stoichiometric determination.

In contrast, cryo-EM captures a broader range of conformational states of by the possibility to visualize of individual species with potentially varying binding stoichiometries, including higher-order complexes. Cryo-EM has the possibility to capture these variations, showing that not all binding sites may be occupied uniformly, whereas ITC might average out these variations in solution, leading to a lower reported stoichiometry. Cryo-EM also allows for the distinction of different complexes within a sample during data processing, using techniques such as 3D classification, as demonstrated with the PRC2 dimer (Chapter 10.2).[356] However, in our case, the presence of two seemingly equivalent binding sites in AIFM1 presents a particular challenge. In ITC, it is difficult to determine

whether one binding site or the other is targeted, as it does not resolve the dynamics of the individual monomers. Moreover, the small size of the resolved regions for MIA40 and AK2A complicates 3D classification. It is possible that either monomer is bound, but during processing these species are combined into a data set, where both binding sites appear to be occupied. This would be represented in a poorer local resolution of these regions. Nevertheless, we were able to unambiguously model the amino acids in these regions, and the lower resolution at the edges is common for cryo-EM density maps. Therfore we can not unambigously conclude whether AIFM1 is bound by one ore two binding partners. This overlaying of species could also explain why the density of K177 exhibits two possible conformations.

Notably, a concurrent study by Schildhauer et al. still under peer-review also resolved a structure of AIFM1-AK2.[395] This structure used a different processing approach by utilizing Relion for inital particle picking and subsequent 3D-classification in cryoSPARC, which revealed additional regions of AK2A.[396] This approach is in agreement with the AK2A binding site on AIFM1 identified in our study. Additionally, their structure suggests that the initial binding of one AK2A would sterically block the binding of a second, resulting in a 2:1 stochiometry for AIFM1:AK2A.

A key question arising from the observed discrepancies is whether there is any preference for the two binding sites. Alignment of the AIFM1 dimer protomers reveals a small but notable asymmetry. Homodimers often display internal asymmetries due to functional roles or for the recruitment of additional proteins.[397] These differences between monomers in AIFM1 are also reflected in the crystal structures, where the sixth β-strand is observed in only one monomer, suggesting an inherent asymmetry that can be targeted by a binding partner.[323, 324, 394] In the case of AIFM1-MIA40, this asymmetry is further amplified, as MIA40 binding likely induces conformational changes that enhance differences between the protomers. These changes included movement of the NADH-binding domain and adenine of NAD. Additionally, the distance between the FAD and NAD is reduced by 0.2 Å.. In contrast, binding of AIFM1-AK2A appears to reduce this asymmetry, stabilizing the dimer into a more symmetrical conformation. Despite these differences, binding of both partners increased the stability of the reduced AIFM1 complex and enhanced its activity toward the artificial electron acceptor DCIP. The binding of MIA40 and AK2A stabilizes the C-loop and aromatic tunnel, key to maintaining AIFM1 in its NAD-bound state.

Since the C-loop undergoes additional conformational changes on top of forming the additional β-strand, the binding site of AK2A and MIA40 is of special interest. Specifically, the release of W198 from the Cβ-clasp destabilizes and releases the C-loop, enabling NADH binding and making the interaction site accessible for β-strand complementation.[325] Alongside the aromatic tunnel is formed, which in our structures gets extended by both AK2A (F238) and MIA40 (F14, Y3), functioning as a conformational lock.[323, 325] This mechanism stabilizes the aromatic tunnel in its NAD-bound state and prevents C-loop reattachment, which may explain why AK2A and MIA40 binding significantly reduces NADH reoxidation rates and subsequently inhibit dimer dissociation, as shown in the functional studies by Alex Rothemann. Specifically, AK2A binds and stabilizes an additional region of the C-loop (aa 550-558) while MIA40, on the other hand, impacts the CTC and cofactor binding site. These different effect may result in the varying impact on the redox activity of AIFM1.

Based on these findings, we propose a model where oxidized AIFM1 is reduced and dimerizes, with MIA40 and AK2A binding to stabilize this reduced state (Figure 38).

.

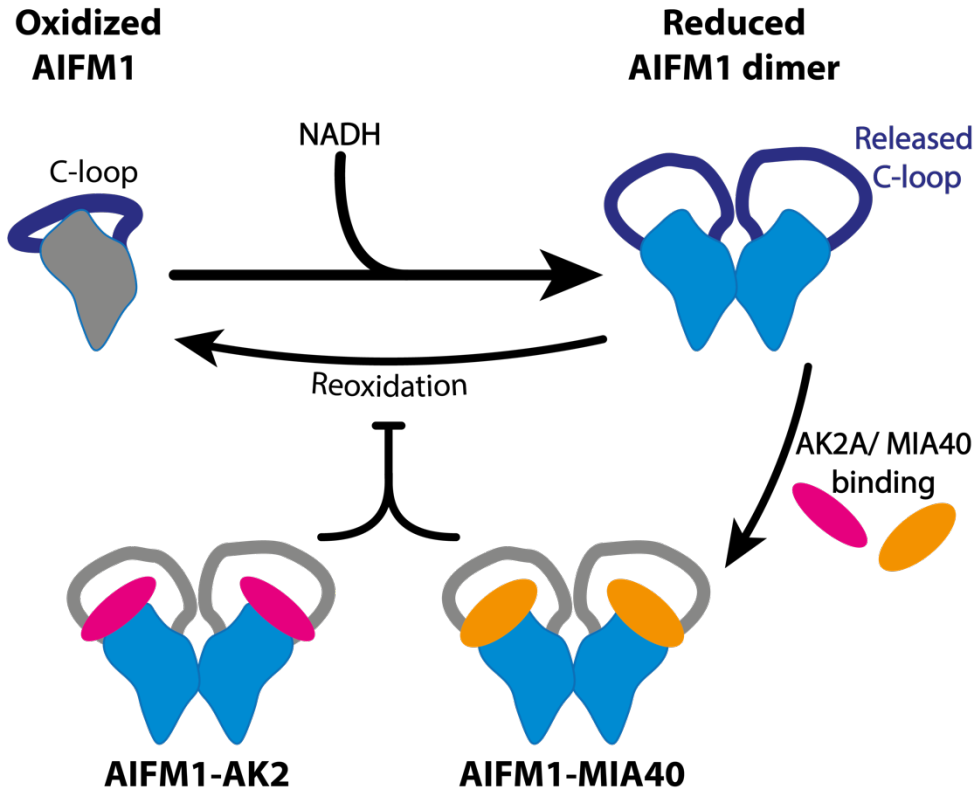

Figure 38: MIA40 and AK2A binding stabilize the AIFM1 dimer

Oxidized AIFM1 dimerizes and undergoes conformational changes, such as the release of the C-loop, upon reduction with NADH. This generally air-stable complex oxidizes over time but gets stabilized by AK2A and MIA40 binding, which prevents the rebinding of the C-loop.

Notably, the concurrent study by Schildhauer et al. arrived at a similar conclusion.[395] The molecular dynamics simulation performed in their study further highlighted that the C-loop (aa509-533) without NADH and AK2 showed little flexibility. The flexibility in the entirety of the C-loop increased upon the addition of NADH (aa 512-559) and was reduced upon the addition of AK2A (aa 509-512 and 546-559). This indicates that AK2A binding prevents C-loop reattachment, keeping the electron acceptor site accessible. The stabilized, bound state of AIFM1 may promote its hypothesized role as an NADH sensor, where interactions with binding partners modulate redox activity, monitoring the mitochondrion. In this context, since MIA40 exclusively binds the AIFM1 dimer, the stabilization of reduced AIFM1 may support its function in the disulphide relay system. In the case of AK2, the AFIM1 may position the protein in the IMS close to the IMM in proximity to ADP/ATP translocases, thus supporting ADP-ATP exchange.[394] Therefore, AIFM1 is indirectly involved in the OXPHOS via the disulphide relay system and in the ATP housekeeping via AK2A interaction.
The intricate interplay between AIFM1 and its binding partners, MIA40 and AK2A, underscores its critical role in cellular stress responses and mitochondrial function.

14. LITERATURE

1. Crick, F., *Central Dogma of Molecular Biology.* Nature, 1970. **227**(5258): p. 561-563.
2. Haldane, J.B.S., *Organisers and Genes.* Nature, 1940. **146**(3700): p. 413-413.
3. Deichmann, U., *Epigenetics: The origins and evolution of a fashionable topic.* Dev Biol, 2016. **416**(1): p. 249-254.
4. Kornberg, R.D., *Chromatin structure: a repeating unit of histones and DNA.* Science, 1974. **184**(4139): p. 868-71.
5. Presman, D.M., et al., *Chromatin structure and dynamics: one nucleosome at a time.* Histochemistry and Cell Biology, 2024. **162**(1): p. 79-90.
6. Finn, E.H. and T. Misteli, *Molecular basis and biological function of variability in spatial genome organization.* Science, 2019. **365**(6457): p. eaaw9498.
7. Watson, J.D. and F.H.C. Crick, *Molecular Structure of Nucleic Acids: A Structure for Deoxyribose Nucleic Acid.* Nature, 1953. **171**(4356): p. 737-738.
8. Wilkins, M.H.F., A.R. Stokes, and H.R. Wilson, *Molecular Structure of Nucleic Acids: Molecular Structure of Deoxypentose Nucleic Acids.* Nature, 1953. **171**(4356): p. 738-740.
9. Franklin, R.E. and R.G. Gosling, *Molecular Configuration in Sodium Thymonucleate.* Nature, 1953. **171**(4356): p. 740-741.
10. Olins, D.E. and A.L. Olins, *Chromatin history: our view from the bridge.* Nature Reviews Molecular Cell Biology, 2003. **4**(10): p. 809-814.
11. Olins, A.L. and D.E. Olins, *Spheroid chromatin units (v bodies).* Science, 1974. **183**(4122): p. 330-2.
12. Woodcock, C.L., J.P. Safer, and J.E. Stanchfield, *Structural repeating units in chromatin. I. Evidence for their general occurrence.* Exp Cell Res, 1976. **97**: p. 101-10.
13. Kornberg, R.D. and J.O. Thomas, *Chromatin structure; oligomers of the histones.* Science, 1974. **184**(4139): p. 865-8.
14. Oudet, P., M. Gross-Bellard, and P. Chambon, *Electron microscopic and biochemical evidence that chromatin structure is a repeating unit.* Cell, 1975. **4**(4): p. 281-300.
15. Luger, K., et al., *Crystal structure of the nucleosome core particle at 2.8 Å resolution.* Nature, 1997. **389**(6648): p. 251-260.
16. Richmond, T.J. and C.A. Davey, *The structure of DNA in the nucleosome core.* Nature, 2003. **423**(6936): p. 145-150.
17. Jenuwein, T. and C.D. Allis, *Translating the histone code.* Science, 2001. **293**(5532): p. 1074-80.
18. Arents, G., et al., *The nucleosomal core histone octamer at 3.1 A resolution: a tripartite protein assembly and a left-handed superhelix.* Proc Natl Acad Sci U S A, 1991. **88**(22): p. 10148-52.
19. Arents, G. and E.N. Moudrianakis, *Topography of the histone octamer surface: repeating structural motifs utilized in the docking of nucleosomal DNA.* Proc Natl Acad Sci U S A, 1993. **90**(22): p. 10489-93.
20. Cutter, A.R. and J.J. Hayes, *A brief review of nucleosome structure.* FEBS Lett, 2015. **589**(20 Pt A): p. 2914-22.
21. Wang, D., N.B. Ulyanov, and V.B. Zhurkin, *Sequence-dependent Kink-and-Slide deformations of nucleosomal DNA facilitated by histone arginines bound in the minor groove.* J Biomol Struct Dyn, 2010. **27**(6): p. 843-59.
22. Hergeth, S.P. and R. Schneider, *The H1 linker histones: multifunctional proteins beyond the nucleosomal core particle.* EMBO Rep, 2015. **16**(11): p. 1439-53.
23. Martire, S. and L.A. Banaszynski, *The roles of histone variants in fine-tuning chromatin organization and function.* Nat Rev Mol Cell Biol, 2020. **21**(9): p. 522-541.
24. Ahmad, K. and S. Henikoff, *The histone variant H3.3 marks active chromatin by replication-independent nucleosome assembly.* Mol Cell, 2002. **9**(6): p. 1191-200.

25. Zhang, T., S. Cooper, and N. Brockdorff, *The interplay of histone modifications - writers that read.* EMBO Rep, 2015. **16**(11): p. 1467-81.
26. Hansen, J.C., C. Tse, and A.P. Wolffe, *Structure and function of the core histone N-termini: more than meets the eye.* Biochemistry, 1998. **37**(51): p. 17637-41.
27. Wolffe, A.P. and J.J. Hayes, *Chromatin disruption and modification.* Nucleic Acids Res, 1999. **27**(3): p. 711-20.
28. Tessarz, P. and T. Kouzarides, *Histone core modifications regulating nucleosome structure and dynamics.* Nature Reviews Molecular Cell Biology, 2014. **15**(11): p. 703-708.
29. Grunstein, M., *Histone acetylation in chromatin structure and transcription.* Nature, 1997. **389**(6649): p. 349-52.
30. Sterner, D.E. and S.L. Berger, *Acetylation of histones and transcription-related factors.* Microbiol Mol Biol Rev, 2000. **64**(2): p. 435-59.
31. Zhang, Y. and D. Reinberg, *Transcription regulation by histone methylation: interplay between different covalent modifications of the core histone tails.* Genes Dev, 2001. **15**(18): p. 2343-60.
32. Bannister, A.J. and T. Kouzarides, *Regulation of chromatin by histone modifications.* Cell Res, 2011. **21**(3): p. 381-95.
33. Nowak, S.J. and V.G. Corces, *Phosphorylation of histone H3: a balancing act between chromosome condensation and transcriptional activation.* Trends Genet, 2004. **20**(4): p. 214-20.
34. Rossetto, D., N. Avvakumov, and J. Côté, *Histone phosphorylation: a chromatin modification involved in diverse nuclear events.* Epigenetics, 2012. **7**(10): p. 1098-108.
35. Davie, J.R. and L.C. Murphy, *Level of ubiquitinated histone H2B in chromatin is coupled to ongoing transcription.* Biochemistry, 1990. **29**(20): p. 4752-7.
36. Strahl, B.D. and C.D. Allis, *The language of covalent histone modifications.* Nature, 2000. **403**(6765): p. 41-5.
37. Tordera, V., R. Sendra, and J.E. Pérez-Ortín, *The role of histones and their modifications in the informative content of chromatin.* Experientia, 1993. **49**(9): p. 780-8.
38. López-Rodas, G., et al., *Histone deacetylase. A key enzyme for the binding of regulatory proteins to chromatin.* FEBS Lett, 1993. **317**(3): p. 175-80.
39. Loidl, P., *Histone acetylation: facts and questions.* Chromosoma, 1994. **103**(7): p. 441-9.
40. Turner, B.M., *Decoding the nucleosome.* Cell, 1993. **75**(1): p. 5-8.
41. Mizzen, C., et al., *Signaling to chromatin through histone modifications: how clear is the signal?* Cold Spring Harb Symp Quant Biol, 1998. **63**: p. 469-81.
42. Bassett, A., et al., *The folding and unfolding of eukaryotic chromatin.* Curr Opin Genet Dev, 2009. **19**(2): p. 159-65.
43. Millán-Zambrano, G., et al., *Histone post-translational modifications — cause and consequence of genome function.* Nature Reviews Genetics, 2022. **23**(9): p. 563-580.
44. Biswas, S. and C.M. Rao, *Epigenetic tools (The Writers, The Readers and The Erasers) and their implications in cancer therapy.* European Journal of Pharmacology, 2018. **837**: p. 8-24.
45. Turner, B.M., *Cellular Memory and the Histone Code.* Cell, 2002. **111**(3): p. 285-291.
46. Ramazi, S., A. Allahverdi, and J. Zahiri, *Evaluation of post-translational modifications in histone proteins: A review on histone modification defects in developmental and neurological disorders.* Journal of Biosciences, 2020. **45**(1): p. 135.
47. Cosgrove, M.S., J.D. Boeke, and C. Wolberger, *Regulated nucleosome mobility and the histone code.* Nat Struct Mol Biol, 2004. **11**(11): p. 1037-43.
48. Neumann, H., et al., *A method for genetically installing site-specific acetylation in recombinant histones defines the effects of H3 K56 acetylation.* Mol Cell, 2009. **36**(1): p. 153-63.
49. Verdin, E. and M. Ott, *50 years of protein acetylation: from gene regulation to epigenetics, metabolism and beyond.* Nat Rev Mol Cell Biol, 2015. **16**(4): p. 258-64.

50. Lee, K.K. and J.L. Workman, *Histone acetyltransferase complexes: one size doesn't fit all.* Nature Reviews Molecular Cell Biology, 2007. **8**(4): p. 284-295.
51. Weaver, I.C.G., et al., *Stress and the Emerging Roles of Chromatin Remodeling in Signal Integration and Stable Transmission of Reversible Phenotypes.* Frontiers in Behavioral Neuroscience, 2017. **11**.
52. Jeanmougin, F., et al., *The bromodomain revisited.* Trends Biochem Sci, 1997. **22**(5): p. 151-3.
53. Winston, F. and C.D. Allis, *The bromodomain: a chromatin-targeting module?* Nat Struct Biol, 1999. **6**(7): p. 601-4.
54. Dhalluin, C., et al., *Structure and ligand of a histone acetyltransferase bromodomain.* Nature, 1999. **399**(6735): p. 491-496.
55. Owen, D.J., et al., *The structural basis for the recognition of acetylated histone H4 by the bromodomain of histone acetyltransferase gcn5p.* Embo j, 2000. **19**(22): p. 6141-9.
56. Cheng, X., R.E. Collins, and X. Zhang, *Structural and sequence motifs of protein (histone) methylation enzymes.* Annu Rev Biophys Biomol Struct, 2005. **34**: p. 267-94.
57. Schubert, H.L., R.M. Blumenthal, and X. Cheng, *Many paths to methyltransfer: a chronicle of convergence.* Trends Biochem Sci, 2003. **28**(6): p. 329-35.
58. Jones, D.O., I.G. Cowell, and P.B. Singh, *Mammalian chromodomain proteins: their role in genome organisation and expression.* Bioessays, 2000. **22**(2): p. 124-37.
59. Paro, R. and D.S. Hogness, *The Polycomb protein shares a homologous domain with a heterochromatin-associated protein of Drosophila.* Proc Natl Acad Sci U S A, 1991. **88**(1): p. 263-7.
60. Kouzarides, T., *Chromatin modifications and their function.* Cell, 2007. **128**(4): p. 693-705.
61. Dimitrova, E., A.H. Turberfield, and R.J. Klose, *Histone demethylases in chromatin biology and beyond.* EMBO Rep, 2015. **16**(12): p. 1620-39.
62. Cloos, P.A., et al., *Erasing the methyl mark: histone demethylases at the center of cellular differentiation and disease.* Genes Dev, 2008. **22**(9): p. 1115-40.
63. Kizer, K.O., et al., *A novel domain in Set2 mediates RNA polymerase II interaction and couples histone H3 K36 methylation with transcript elongation.* Mol Cell Biol, 2005. **25**(8): p. 3305-16.
64. Pavlenko, E., et al., *Functions and Interactions of Mammalian KDM5 Demethylases.* Front Genet, 2022. **13**: p. 906662.
65. Piunti, A. and A. Shilatifard, *The roles of Polycomb repressive complexes in mammalian development and cancer.* Nat Rev Mol Cell Biol, 2021. **22**(5): p. 326-345.
66. Müller, J., et al., *Histone methyltransferase activity of a Drosophila Polycomb group repressor complex.* Cell, 2002. **111**(2): p. 197-208.
67. Rea, S., et al., *Regulation of chromatin structure by site-specific histone H3 methyltransferases.* Nature, 2000. **406**(6796): p. 593-599.
68. Saksouk, N., E. Simboeck, and J. Déjardin, *Constitutive heterochromatin formation and transcription in mammals.* Epigenetics Chromatin, 2015. **8**: p. 3.
69. Padeken, J., S.P. Methot, and S.M. Gasser, *Establishment of H3K9-methylated heterochromatin and its functions in tissue differentiation and maintenance.* Nature Reviews Molecular Cell Biology, 2022. **23**(9): p. 623-640.
70. Trojer, P. and D. Reinberg, *Facultative heterochromatin: is there a distinctive molecular signature?* Mol Cell, 2007. **28**(1): p. 1-13.
71. Morrison, O. and J. Thakur, *Molecular Complexes at Euchromatin, Heterochromatin and Centromeric Chromatin.* Int J Mol Sci, 2021. **22**(13).
72. Nicetto, D. and K.S. Zaret, *Role of H3K9me3 heterochromatin in cell identity establishment and maintenance.* Curr Opin Genet Dev, 2019. **55**: p. 1-10.
73. Laugesen, A., J.W. Højfeldt, and K. Helin, *Molecular Mechanisms Directing PRC2 Recruitment and H3K27 Methylation.* Mol Cell, 2019. **74**(1): p. 8-18.

74. Voigt, P., W.W. Tee, and D. Reinberg, *A double take on bivalent promoters.* Genes Dev, 2013. **27**(12): p. 1318-38.
75. Bernstein, B.E., et al., *A bivalent chromatin structure marks key developmental genes in embryonic stem cells.* Cell, 2006. **125**(2): p. 315-26.
76. Lewis, E.B., *A gene complex controlling segmentation in Drosophila.* Nature, 1978. **276**(5688): p. 565-70.
77. Lewis, P. and R. Mislove, *New mutants report.* Drosoph. Inf. Serv, 1947. **21**: p. 69.
78. Jürgens, G., *A group of genes controlling the spatial expression of the bithorax complex in Drosophila.* Nature, 1985. **316**(6024): p. 153-155.
79. Simon, J., A. Chiang, and W. Bender, *Ten different Polycomb group genes are required for spatial control of the abdA and AbdB homeotic products.* Development, 1992. **114**(2): p. 493-505.
80. Kassis, J.A., J.A. Kennison, and J.W. Tamkun, *Polycomb and Trithorax Group Genes in Drosophila.* Genetics, 2017. **206**(4): p. 1699-1725.
81. McKeon, J. and H.W. Brock, *Interactions of thePolycomb group of genes with homeotic loci ofDrosophila.* Rouxs Arch Dev Biol, 1991. **199**(7): p. 387-396.
82. Ingham, P.W., *Trithorax: A new homoeotic mutation ofDrosophila melanogaster : II. The role oftrx (+) after embryogenesis.* Wilehm Roux Arch Dev Biol, 1981. **190**(6): p. 365-369.
83. Struhl, G. and M. Akam, *Altered distributions of Ultrabithorax transcripts in extra sex combs mutant embryos of Drosophila.* Embo j, 1985. **4**(12): p. 3259-64.
84. Schuettengruber, B., et al., *Genome regulation by polycomb and trithorax proteins.* Cell, 2007. **128**(4): p. 735-45.
85. Bracken, A.P., et al., *Genome-wide mapping of Polycomb target genes unravels their roles in cell fate transitions.* Genes Dev, 2006. **20**(9): p. 1123-36.
86. Cao, R. and Y. Zhang, *SUZ12 is required for both the histone methyltransferase activity and the silencing function of the EED-EZH2 complex.* Mol Cell, 2004. **15**(1): p. 57-67.
87. Francis, N.J., R.E. Kingston, and C.L. Woodcock, *Chromatin Compaction by a Polycomb Group Protein Complex.* Science, 2004. **306**(5701): p. 1574-1577.
88. Francis, N.J. and R.E. Kingston, *Mechanisms of transcriptional memory.* Nature Reviews Molecular Cell Biology, 2001. **2**(6): p. 409-421.
89. Grossniklaus, U. and R. Paro, *Transcriptional silencing by polycomb-group proteins.* Cold Spring Harb Perspect Biol, 2014. **6**(11): p. a019331.
90. Kuzmichev, A., et al., *Histone methyltransferase activity associated with a human multiprotein complex containing the Enhancer of Zeste protein.* Genes Dev, 2002. **16**(22): p. 2893-905.
91. Scheuermann, J.C., et al., *Histone H2A deubiquitinase activity of the Polycomb repressive complex PR-DUB.* Nature, 2010. **465**(7295): p. 243-7.
92. Klymenko, T., et al., *A Polycomb group protein complex with sequence-specific DNA-binding and selective methyl-lysine-binding activities.* Genes Dev, 2006. **20**(9): p. 1110-22.
93. Schuettengruber, B., et al., *Genome Regulation by Polycomb and Trithorax: 70 Years and Counting.* Cell, 2017. **171**(1): p. 34-57.
94. Wang, H., et al., *Role of histone H2A ubiquitination in Polycomb silencing.* Nature, 2004. **431**(7010): p. 873-878.
95. Pengelly, A.R., et al., *Transcriptional repression by PRC1 in the absence of H2A monoubiquitylation.* Genes Dev, 2015. **29**(14): p. 1487-92.
96. Yu, J.R., et al., *PRC2 is high maintenance.* Genes Dev, 2019. **33**(15-16): p. 903-935.
97. Margueron, R. and D. Reinberg, *The Polycomb complex PRC2 and its mark in life.* Nature, 2011. **469**(7330): p. 343-9.
98. Masui, O., et al., *Polycomb repressive complexes 1 and 2 are each essential for maintenance of X inactivation in extra-embryonic lineages.* Nature Cell Biology, 2023. **25**(1): p. 134-144.
99. Brockdorff, N., *Polycomb complexes in X chromosome inactivation.* Philos Trans R Soc Lond B Biol Sci, 2017. **372**(1733).

100. Bousard, A., et al., *The role of Xist-mediated Polycomb recruitment in the initiation of X-chromosome inactivation.* EMBO Rep, 2019. **20**(10): p. e48019.
101. Glancy, E., et al., *PRC2.1- and PRC2.2-specific accessory proteins drive recruitment of different forms of canonical PRC1.* Mol Cell, 2023. **83**(9): p. 1393-1411.e7.
102. Laugesen, A., J.W. Højfeldt, and K. Helin, *Role of the Polycomb Repressive Complex 2 (PRC2) in Transcriptional Regulation and Cancer.* Cold Spring Harb Perspect Med, 2016. **6**(9).
103. Fischer, S., L.M. Weber, and R. Liefke, *Evolutionary adaptation of the Polycomb repressive complex 2.* Epigenetics & Chromatin, 2022. **15**(1): p. 7.
104. Czermin, B., et al., *Drosophila enhancer of Zeste/ESC complexes have a histone H3 methyltransferase activity that marks chromosomal Polycomb sites.* Cell, 2002. **111**(2): p. 185-96.
105. Cao, R., et al., *Role of Histone H3 Lysine 27 Methylation in Polycomb-Group Silencing.* Science, 2002. **298**(5595): p. 1039-1043.
106. Ferrari, K.J., et al., *Polycomb-dependent H3K27me1 and H3K27me2 regulate active transcription and enhancer fidelity.* Mol Cell, 2014. **53**(1): p. 49-62.
107. Lee, H.G., et al., *Genome-wide activities of Polycomb complexes control pervasive transcription.* Genome Res, 2015. **25**(8): p. 1170-81.
108. Højfeldt, J.W., et al., *Accurate H3K27 methylation can be established de novo by SUZ12-directed PRC2.* Nat Struct Mol Biol, 2018. **25**(3): p. 225-232.
109. Jung, H.R., et al., *Quantitative Mass Spectrometry of Histones H3.2 and H3.3 in Suz12-deficient Mouse Embryonic Stem Cells Reveals Distinct, Dynamic Post-translational Modifications at Lys-27 and Lys-36*.* Molecular & Cellular Proteomics, 2010. **9**(5): p. 838-850.
110. Juan, A.H., et al., *Roles of H3K27me2 and H3K27me3 Examined during Fate Specification of Embryonic Stem Cells.* Cell Rep, 2016. **17**(5): p. 1369-1382.
111. Cui, K., et al., *Chromatin signatures in multipotent human hematopoietic stem cells indicate the fate of bivalent genes during differentiation.* Cell Stem Cell, 2009. **4**(1): p. 80-93.
112. Steiner, L.A., et al., *Patterns of histone H3 lysine 27 monomethylation and erythroid cell type-specific gene expression.* J Biol Chem, 2011. **286**(45): p. 39457-65.
113. Vakoc, C.R., et al., *Profile of histone lysine methylation across transcribed mammalian chromatin.* Mol Cell Biol, 2006. **26**(24): p. 9185-95.
114. Margueron, R., et al., *Ezh1 and Ezh2 maintain repressive chromatin through different mechanisms.* Mol Cell, 2008. **32**(4): p. 503-18.
115. Shen, X., et al., *EZH1 mediates methylation on histone H3 lysine 27 and complements EZH2 in maintaining stem cell identity and executing pluripotency.* Mol Cell, 2008. **32**(4): p. 491-502.
116. Birve, A., et al., *Su(z)12, a novel Drosophila Polycomb group gene that is conserved in vertebrates and plants.* Development, 2001. **128**(17): p. 3371-9.
117. Jones, R.S. and W.M. Gelbart, *Genetic analysis of the enhancer of zeste locus and its role in gene regulation in Drosophila melanogaster.* Genetics, 1990. **126**(1): p. 185-99.
118. Faust, C., et al., *The Polycomb-group gene eed is required for normal morphogenetic movements during gastrulation in the mouse embryo.* Development, 1998. **125**(22): p. 4495-506.
119. O'Carroll, D., et al., *The polycomb-group gene Ezh2 is required for early mouse development.* Mol Cell Biol, 2001. **21**(13): p. 4330-6.
120. Pasini, D., et al., *Suz12 is essential for mouse development and for EZH2 histone methyltransferase activity.* Embo j, 2004. **23**(20): p. 4061-71.
121. Schmitges, F.W., et al., *Histone methylation by PRC2 is inhibited by active chromatin marks.* Mol Cell, 2011. **42**(3): p. 330-41.
122. Peng, J.C., et al., *Jarid2/Jumonji Coordinates Control of PRC2 Enzymatic Activity and Target Gene Occupancy in Pluripotent Cells.* Cell, 2009. **139**(7): p. 1290-1302.

123. Li, G., et al., *Jarid2 and PRC2, partners in regulating gene expression.* Genes Dev, 2010. **24**(4): p. 368-80.
124. Healy, E., et al., *PRC2.1 and PRC2.2 Synergize to Coordinate H3K27 Trimethylation.* Mol Cell, 2019. **76**(3): p. 437-452.e6.
125. Trievel, R.C., et al., *Structure and catalytic mechanism of a SET domain protein methyltransferase.* Cell, 2002. **111**(1): p. 91-103.
126. Wu, H., et al., *Structure of the catalytic domain of EZH2 reveals conformational plasticity in cofactor and substrate binding sites and explains oncogenic mutations.* PLoS One, 2013. **8**(12): p. e83737.
127. Antonysamy, S., et al., *Structural context of disease-associated mutations and putative mechanism of autoinhibition revealed by X-ray crystallographic analysis of the EZH2-SET domain.* PLoS One, 2013. **8**(12): p. e84147.
128. Kasinath, V., et al., *Structures of human PRC2 with its cofactors AEBP2 and JARID2.* Science, 2018. **359**(6378): p. 940-944.
129. Ciferri, C., et al., *Molecular architecture of human polycomb repressive complex 2.* Elife, 2012. **1**: p. e00005.
130. Chen, S., et al., *Unique Structural Platforms of Suz12 Dictate Distinct Classes of PRC2 for Chromatin Binding.* Mol Cell, 2018. **69**(5): p. 840-852.e5.
131. Margueron, R., et al., *Role of the polycomb protein EED in the propagation of repressive histone marks.* Nature, 2009. **461**(7265): p. 762-767.
132. Oksuz, O., et al., *Capturing the Onset of PRC2-Mediated Repressive Domain Formation.* Mol Cell, 2018. **70**(6): p. 1149-1162.e5.
133. Perino, M., et al., *MTF2 recruits Polycomb Repressive Complex 2 by helical-shape-selective DNA binding.* Nature Genetics, 2018. **50**(7): p. 1002-1010.
134. Holoch, D. and R. Margueron, *Mechanisms Regulating PRC2 Recruitment and Enzymatic Activity.* Trends in Biochemical Sciences, 2017. **42**(7): p. 531-542.
135. Grijzenhout, A., et al., *Functional analysis of AEBP2, a PRC2 Polycomb protein, reveals a Trithorax phenotype in embryonic development and in ESCs.* Development, 2016. **143**(15): p. 2716-23.
136. Hauri, S., et al., *A High-Density Map for Navigating the Human Polycomb Complexome.* Cell Reports, 2016. **17**(2): p. 583-595.
137. Chen, S., et al., *A Dimeric Structural Scaffold for PRC2-PCL Targeting to CpG Island Chromatin.* Mol Cell, 2020. **77**(6): p. 1265-1278.e7.
138. Conway, E., et al., *A Family of Vertebrate-Specific Polycombs Encoded by the LCOR/LCORL Genes Balance PRC2 Subtype Activities.* Mol Cell, 2018. **70**(3): p. 408-421.e8.
139. Alekseyenko, A.A., et al., *Reciprocal interactions of human C10orf12 and C17orf96 with PRC2 revealed by BioTAP-XL cross-linking and affinity purification.* Proc Natl Acad Sci U S A, 2014. **111**(7): p. 2488-93.
140. Beringer, M., et al., *EPOP Functionally Links Elongin and Polycomb in Pluripotent Stem Cells.* Mol Cell, 2016. **64**(4): p. 645-658.
141. Liefke, R. and Y. Shi, *The PRC2-associated factor C17orf96 is a novel CpG island regulator in mouse ES cells.* Cell Discovery, 2015. **1**(1): p. 15008.
142. Youmans, D.T., et al., *Competition between PRC2.1 and 2.2 subcomplexes regulates PRC2 chromatin occupancy in human stem cells.* Mol Cell, 2021. **81**(3): p. 488-501.e9.
143. Smits, A.H., et al., *Stoichiometry of chromatin-associated protein complexes revealed by label-free quantitative mass spectrometry-based proteomics.* Nucleic Acids Research, 2012. **41**(1): p. e28-e28.
144. Kloet, S.L., et al., *The dynamic interactome and genomic targets of Polycomb complexes during stem-cell differentiation.* Nature Structural & Molecular Biology, 2016. **23**(7): p. 682-690.
145. Kim, H., K. Kang, and J. Kim, *AEBP2 as a potential targeting protein for Polycomb Repression Complex PRC2.* Nucleic Acids Research, 2009. **37**(9): p. 2940-2950.

146. Kim, H., et al., *AEBP2 as a transcriptional activator and its role in cell migration.* Genomics, 2015. **105**(2): p. 108-115.
147. Son, J., et al., *Nucleosome-binding activities within JARID2 and EZH1 regulate the function of PRC2 on chromatin.* Genes Dev, 2013. **27**(24): p. 2663-77.
148. Sanulli, S., et al., *Jarid2 Methylation via the PRC2 Complex Regulates H3K27me3 Deposition during Cell Differentiation.* Mol Cell, 2015. **57**(5): p. 769-783.
149. Justin, N., et al., *Structural basis of oncogenic histone H3K27M inhibition of human polycomb repressive complex 2.* Nat Commun, 2016. **7**: p. 11316.
150. Schwartz, Y.B., *Chapter 6 - Cooperative Recruitment of Polycomb Complexes by Polycomb Response Elements*, in *Polycomb Group Proteins*, V. Pirrotta, Editor. 2017, Academic Press. p. 111-129.
151. Müller, J. and J.A. Kassis, *Polycomb response elements and targeting of Polycomb group proteins in Drosophila.* Current Opinion in Genetics & Development, 2006. **16**(5): p. 476-484.
152. Laprell, F., K. Finkl, and J. Müller, *Propagation of Polycomb-repressed chromatin requires sequence-specific recruitment to DNA.* Science, 2017. **356**(6333): p. 85-88.
153. Schwartz, Y.B., et al., *Alternative epigenetic chromatin states of polycomb target genes.* PLoS Genet, 2010. **6**(1): p. e1000805.
154. Brown, J.L., et al., *The Drosophila Polycomb group gene pleiohomeotic encodes a DNA binding protein with homology to the transcription factor YY1.* Mol Cell, 1998. **1**(7): p. 1057-64.
155. Coleman, R.T. and G. Struhl, *Causal role for inheritance of H3K27me3 in maintaining the OFF state of a Drosophila HOX gene.* Science, 2017. **356**(6333): p. eaai8236.
156. Dietrich, N., et al., *REST–Mediated Recruitment of Polycomb Repressor Complexes in Mammalian Cells.* PLOS Genetics, 2012. **8**(3): p. e1002494.
157. Herranz, N., et al., *Polycomb Complex 2 Is Required for E-cadherin Repression by the Snail1 Transcription Factor.* Molecular and Cellular Biology, 2008. **28**(15): p. 4772-4781.
158. Arnold, P., et al., *Modeling of epigenome dynamics identifies transcription factors that mediate Polycomb targeting.* Genome Research, 2013. **23**(1): p. 60-73.
159. Choi, J., et al., *DNA binding by PHF1 prolongs PRC2 residence time on chromatin and thereby promotes H3K27 methylation.* Nat Struct Mol Biol, 2017. **24**(12): p. 1039-1047.
160. Li, H., et al., *Polycomb-like proteins link the PRC2 complex to CpG islands.* Nature, 2017. **549**(7671): p. 287-291.
161. Bauer, M., J. Trupke, and L. Ringrose, *The quest for mammalian Polycomb response elements: are we there yet?* Chromosoma, 2016. **125**(3): p. 471-96.
162. Bartke, T., et al., *Nucleosome-interacting proteins regulated by DNA and histone methylation.* Cell, 2010. **143**(3): p. 470-84.
163. Lynch, M.D., et al., *An interspecies analysis reveals a key role for unmethylated CpG dinucleotides in vertebrate Polycomb complex recruitment.* Embo j, 2012. **31**(2): p. 317-29.
164. King, A.D., et al., *Reversible Regulation of Promoter and Enhancer Histone Landscape by DNA Methylation in Mouse Embryonic Stem Cells.* Cell Rep, 2016. **17**(1): p. 289-302.
165. Wang, X., et al., *Molecular analysis of PRC2 recruitment to DNA in chromatin and its inhibition by RNA.* Nature Structural & Molecular Biology, 2017. **24**(12): p. 1028-1038.
166. Davidovich, C., et al., *Promiscuous RNA binding by Polycomb repressive complex 2.* Nat Struct Mol Biol, 2013. **20**(11): p. 1250-7.
167. Davidovich, C., et al., *A dimeric state for PRC2.* Nucleic Acids Res, 2014. **42**(14): p. 9236-48.
168. Kaneko, S., et al., *PRC2 binds active promoters and contacts nascent RNAs in embryonic stem cells.* Nat Struct Mol Biol, 2013. **20**(11): p. 1258-64.
169. Rinn, J.L., et al., *Functional Demarcation of Active and Silent Chromatin Domains in Human HOX Loci by Noncoding RNAs.* Cell, 2007. **129**(7): p. 1311-1323.

170. Zhao, J., et al., *Polycomb proteins targeted by a short repeat RNA to the mouse X chromosome.* Science, 2008. **322**(5902): p. 750-6.
171. da Rocha, S.T., et al., *Jarid2 Is Implicated in the Initial Xist-Induced Targeting of PRC2 to the Inactive X Chromosome.* Mol Cell, 2014. **53**(2): p. 301-16.
172. Beltran, M., et al., *The interaction of PRC2 with RNA or chromatin is mutually antagonistic.* Genome Res, 2016. **26**(7): p. 896-907.
173. Kaneko, S., et al., *Nascent RNA interaction keeps PRC2 activity poised and in check.* Genes Dev, 2014. **28**(18): p. 1983-8.
174. Cifuentes-Rojas, C., et al., *Regulatory Interactions between RNA and Polycomb Repressive Complex 2.* Molecular Cell, 2014. **55**(2): p. 171-185.
175. Gail, E.H., et al., *Inseparable RNA binding and chromatin modification activities of a nucleosome-interacting surface in EZH2.* Nature Genetics, 2024. **56**(6): p. 1193-1202.
176. Fischle, W., et al., *Molecular basis for the discrimination of repressive methyl-lysine marks in histone H3 by Polycomb and HP1 chromodomains.* Genes Dev, 2003. **17**(15): p. 1870-81.
177. Min, J., Y. Zhang, and R.M. Xu, *Structural basis for specific binding of Polycomb chromodomain to histone H3 methylated at Lys 27.* Genes Dev, 2003. **17**(15): p. 1823-8.
178. Blackledge, N.P., N.R. Rose, and R.J. Klose, *Targeting Polycomb systems to regulate gene expression: modifications to a complex story.* Nature Reviews Molecular Cell Biology, 2015. **16**(11): p. 643-649.
179. Tavares, L., et al., *RYBP-PRC1 Complexes Mediate H2A Ubiquitylation at Polycomb Target Sites Independently of PRC2 and H3K27me3.* Cell, 2012. **148**(4): p. 664-678.
180. Blackledge, N.P., et al., *Variant PRC1 complex-dependent H2A ubiquitylation drives PRC2 recruitment and polycomb domain formation.* Cell, 2014. **157**(6): p. 1445-1459.
181. Kalb, R., et al., *Histone H2A monoubiquitination promotes histone H3 methylation in Polycomb repression.* Nature Structural & Molecular Biology, 2014. **21**(6): p. 569-571.
182. Cooper, S., et al., *Jarid2 binds mono-ubiquitylated H2A lysine 119 to mediate crosstalk between Polycomb complexes PRC1 and PRC2.* Nat Commun, 2016. **7**: p. 13661.
183. Cao, Q., et al., *The central role of EED in the orchestration of polycomb group complexes.* Nature Communications, 2014. **5**(1): p. 3127.
184. Xu, C., et al., *Binding of different histone marks differentially regulates the activity and specificity of polycomb repressive complex 2 (PRC2).* Proceedings of the National Academy of Sciences, 2010. **107**(45): p. 19266-19271.
185. Lee, C.H., et al., *Automethylation of PRC2 promotes H3K27 methylation and is impaired in H3K27M pediatric glioma.* Genes Dev, 2019. **33**(19-20): p. 1428-1440.
186. Wang, X., et al., *Regulation of histone methylation by automethylation of PRC2.* Genes Dev, 2019. **33**(19-20): p. 1416-1427.
187. Lee, C.-H., et al., *Distinct Stimulatory Mechanisms Regulate the Catalytic Activity of Polycomb Repressive Complex 2.* Molecular Cell, 2018. **70**(3): p. 435-448.e5.
188. Yuan, W., et al., *Dense chromatin activates Polycomb repressive complex 2 to regulate H3 lysine 27 methylation.* Science, 2012. **337**(6097): p. 971-5.
189. Ge, E.J., et al., *Nucleation and Propagation of Heterochromatin by the Histone Methyltransferase PRC2: Geometric Constraints and Impact of the Regulatory Subunit JARID2.* J Am Chem Soc, 2019. **141**(38): p. 15029-15039.
190. Yuan, W., et al., *H3K36 methylation antagonizes PRC2-mediated H3K27 methylation.* J Biol Chem, 2011. **286**(10): p. 7983-7989.
191. Han, Z., et al., *Structural Basis of EZH2 Recognition by EED.* Structure, 2007. **15**(10): p. 1306-1315.
192. Jiao, L. and X. Liu, *Structural basis of histone H3K27 trimethylation by an active polycomb repressive complex 2.* Science, 2015. **350**(6258): p. aac4383.
193. Brooun, A., et al., *Polycomb repressive complex 2 structure with inhibitor reveals a mechanism of activation and drug resistance.* Nature Communications, 2016. **7**(1): p. 11384.

194. Bratkowski, M., X. Yang, and X. Liu, *Polycomb repressive complex 2 in an autoinhibited state.* J Biol Chem, 2017. **292**(32): p. 13323-13332.
195. Zheng, S., et al., *Solution Structure of MSL2 CXC Domain Reveals an Unusual Zn3Cys9 Cluster and Similarity to Pre-SET Domains of Histone Lysine Methyltransferases.* PLOS ONE, 2012. **7**(9): p. e45437.
196. Ketel, C.S., et al., *Subunit contributions to histone methyltransferase activities of fly and worm polycomb group complexes.* Mol Cell Biol, 2005. **25**(16): p. 6857-68.
197. Kasinath, V., S. Poepsel, and E. Nogales, *Recent Structural Insights into Polycomb Repressive Complex 2 Regulation and Substrate Binding.* Biochemistry, 2019. **58**(5): p. 346-354.
198. Finogenova, K., et al., *Structural basis for PRC2 decoding of active histone methylation marks H3K36me2/3.* Elife, 2020. **9**.
199. Kasinath, V., et al., *JARID2 and AEBP2 regulate PRC2 in the presence of H2AK119ub1 and other histone modifications.* Science, 2021. **371**(6527).
200. Poepsel, S., V. Kasinath, and E. Nogales, *Cryo-EM structures of PRC2 simultaneously engaged with two functionally distinct nucleosomes.* Nature Structural & Molecular Biology, 2018. **25**(2): p. 154-+.
201. Lewis, P.W., et al., *Inhibition of PRC2 Activity by a Gain-of-Function H3 Mutation Found in Pediatric Glioblastoma.* Science, 2013. **340**(6134): p. 857-861.
202. Schwartzentruber, J., et al., *Driver mutations in histone H3.3 and chromatin remodelling genes in paediatric glioblastoma.* Nature, 2012. **482**(7384): p. 226-231.
203. Liu, X. and X. Liu, *PRC2, Chromatin Regulation, and Human Disease: Insights From Molecular Structure and Function.* Front Oncol, 2022. **12**: p. 894585.
204. Højfeldt, J.W., et al., *Non-core Subunits of the PRC2 Complex Are Collectively Required for Its Target-Site Specificity.* Mol Cell, 2019. **76**(3): p. 423-436.e3.
205. Montgomery, N.D., et al., *The murine polycomb group protein Eed is required for global histone H3 lysine-27 methylation.* Curr Biol, 2005. **15**(10): p. 942-7.
206. Cyrus, S., et al., *PRC2-complex related dysfunction in overgrowth syndromes: A review of EZH2, EED, and SUZ12 and their syndromic phenotypes.* American Journal of Medical Genetics Part C: Seminars in Medical Genetics, 2019. **181**(4): p. 519-531.
207. Comet, I., et al., *Maintaining cell identity: PRC2-mediated regulation of transcription and cancer.* Nat Rev Cancer, 2016. **16**(12): p. 803-810.
208. Erokhin, M., et al., *Clinical Correlations of Polycomb Repressive Complex 2 in Different Tumor Types.* Cancers (Basel), 2021. **13**(13).
209. Wassef, M. and R. Margueron, *The Multiple Facets of PRC2 Alterations in Cancers.* J Mol Biol, 2017. **429**(13): p. 1978-1993.
210. Simon, J.A. and C.A. Lange, *Roles of the EZH2 histone methyltransferase in cancer epigenetics.* Mutation Research/Fundamental and Molecular Mechanisms of Mutagenesis, 2008. **647**(1): p. 21-29.
211. Raaphorst, F.M., et al., *Coexpression of BMI-1 and EZH2 Polycomb Group Genes in Reed-Sternberg Cells of Hodgkin’s Disease.* The American Journal of Pathology, 2000. **157**(3): p. 709-715.
212. Kleer, C.G., et al., *EZH2 is a marker of aggressive breast cancer and promotes neoplastic transformation of breast epithelial cells.* Proceedings of the National Academy of Sciences, 2003. **100**(20): p. 11606-11611.
213. Varambally, S., et al., *The polycomb group protein EZH2 is involved in progression of prostate cancer.* Nature, 2002. **419**(6907): p. 624-629.
214. Bae, W.K., et al., *The methyltransferase EZH2 is not required for mammary cancer development, although high EZH2 and low H3K27me3 correlate with poor prognosis of ER-positive breast cancers.* Molecular Carcinogenesis, 2015. **54**(10): p. 1172-1180.
215. Wassef, M., et al., *Impaired PRC2 activity promotes transcriptional instability and favors breast tumorigenesis.* Genes Dev, 2015. **29**(24): p. 2547-62.

216. Mallen-St Clair, J., et al., *EZH2 couples pancreatic regeneration to neoplastic progression.* Genes Dev, 2012. **26**(5): p. 439-44.
217. De Raedt, T., et al., *PRC2 loss amplifies Ras-driven transcription and confers sensitivity to BRD4-based therapies.* Nature, 2014. **514**(7521): p. 247-251.
218. Lee, W., et al., *PRC2 is recurrently inactivated through EED or SUZ12 loss in malignant peripheral nerve sheath tumors.* Nature Genetics, 2014. **46**(11): p. 1227-1232.
219. Zhang, M., et al., *Somatic mutations of SUZ12 in malignant peripheral nerve sheath tumors.* Nature Genetics, 2014. **46**(11): p. 1170-1172.
220. Sneeringer, C.J., et al., *Coordinated activities of wild-type plus mutant EZH2 drive tumor-associated hypertrimethylation of lysine 27 on histone H3 (H3K27) in human B-cell lymphomas.* Proc Natl Acad Sci U S A, 2010. **107**(49): p. 20980-5.
221. Morin, R.D., et al., *Somatic mutations altering EZH2 (Tyr641) in follicular and diffuse large B-cell lymphomas of germinal-center origin.* Nat Genet, 2010. **42**(2): p. 181-5.
222. Liu, K.L., K. Zhu, and H. Zhang, *An overview of the development of EED inhibitors to disable the PRC2 function.* RSC Med Chem, 2022. **13**(1): p. 39-53.
223. He, Y., et al., *The EED protein-protein interaction inhibitor A-395 inactivates the PRC2 complex.* Nat Chem Biol, 2017. **13**(4): p. 389-395.
224. McCabe, M.T. and C.L. Creasy, *EZH2 as a potential target in cancer therapy.* Epigenomics, 2014. **6**(3): p. 341-51.
225. Liu, Y. and Q. Yang, *The roles of EZH2 in cancer and its inhibitors.* Med Oncol, 2023. **40**(6): p. 167.
226. Margulis, L., *Symbiosis in cell evolution: Life and its environment on the early earth.* 1981.
227. Gray, M.W., *Lynn Margulis and the endosymbiont hypothesis: 50 years later.* Mol Biol Cell, 2017. **28**(10): p. 1285-1287.
228. Raval, P.K., W.F. Martin, and S.B. Gould, *Mitochondrial evolution: Gene shuffling, endosymbiosis, and signaling.* Sci Adv, 2023. **9**(32): p. eadj4493.
229. Kühlbrandt, W., *Structure and function of mitochondrial membrane protein complexes.* BMC Biology, 2015. **13**(1): p. 89.
230. Spinelli, J.B. and M.C. Haigis, *The multifaceted contributions of mitochondria to cellular metabolism.* Nature Cell Biology, 2018. **20**(7): p. 745-754.
231. Alberts, B., et al., *Molecular biology of the cell*. Sixth edition ed. 2015, New York, NY: Garland Science, Taylor and Francis Group.
232. Pagliarini, D.J. and J. Rutter, *Hallmarks of a new era in mitochondrial biochemistry.* Genes Dev, 2013. **27**(24): p. 2615-27.
233. Shen, K., et al., *Mitochondria as Cellular and Organismal Signaling Hubs.* Annu Rev Cell Dev Biol, 2022. **38**: p. 179-218.
234. Benard, G., et al., *Multi-site control and regulation of mitochondrial energy production.* Biochimica et Biophysica Acta (BBA) - Bioenergetics, 2010. **1797**(6): p. 698-709.
235. Walsh, C.T., B.P. Tu, and Y. Tang, *Eight Kinetically Stable but Thermodynamically Activated Molecules that Power Cell Metabolism.* Chemical Reviews, 2018. **118**(4): p. 1460-1494.
236. Xie, N., et al., *NAD+ metabolism: pathophysiologic mechanisms and therapeutic potential.* Signal Transduction and Targeted Therapy, 2020. **5**(1): p. 227.
237. Krebs, H.A. and W.A. Johnson, *The role of citric acid in intermediate metabolism in animal tissues.* FEBS Letters, 1980. **117**: p. K2-K10.
238. Letts, J.A. and L.A. Sazanov, *Clarifying the supercomplex: the higher-order organization of the mitochondrial electron transport chain.* Nature Structural & Molecular Biology, 2017. **24**(10): p. 800-808.
239. Vercellino, I. and L.A. Sazanov, *The assembly, regulation and function of the mitochondrial respiratory chain.* Nature Reviews Molecular Cell Biology, 2022. **23**(2): p. 141-161.
240. Mitchell, P., *Coupling of Phosphorylation to Electron and Hydrogen Transfer by a Chemi-Osmotic type of Mechanism.* Nature, 1961. **191**(4784): p. 144-148.

241. Bennett, C.F., P. Latorre-Muro, and P. Puigserver, *Mechanisms of mitochondrial respiratory adaptation.* Nature Reviews Molecular Cell Biology, 2022. **23**(12): p. 817-835.
242. Protasoni, M. and M. Zeviani, *Mitochondrial Structure and Bioenergetics in Normal and Disease Conditions.* Int J Mol Sci, 2021. **22**(2).
243. Bandy, B. and A.J. Davison, *Mitochondrial mutations may increase oxidative stress: implications for carcinogenesis and aging?* Free Radic Biol Med, 1990. **8**(6): p. 523-39.
244. Russell, O.M., et al., *Mitochondrial Diseases: Hope for the Future.* Cell, 2020. **181**(1): p. 168-188.
245. Frazier, A.E., D.R. Thorburn, and A.G. Compton, *Mitochondrial energy generation disorders: genes, mechanisms, and clues to pathology.* J Biol Chem, 2019. **294**(14): p. 5386-5395.
246. Calvo, S.E. and V.K. Mootha, *The mitochondrial proteome and human disease.* Annu Rev Genomics Hum Genet, 2010. **11**: p. 25-44.
247. Chacinska, A., et al., *Importing mitochondrial proteins: machineries and mechanisms.* Cell, 2009. **138**(4): p. 628-44.
248. Wiedemann, N. and N. Pfanner, *Mitochondrial Machineries for Protein Import and Assembly.* Annu Rev Biochem, 2017. **86**: p. 685-714.
249. Vögtle, F.N., et al., *Global analysis of the mitochondrial N-proteome identifies a processing peptidase critical for protein stability.* Cell, 2009. **139**(2): p. 428-39.
250. Abe, Y., et al., *Structural basis of presequence recognition by the mitochondrial protein import receptor Tom20.* Cell, 2000. **100**(5): p. 551-60.
251. Yamano, K., et al., *Tom20 and Tom22 share the common signal recognition pathway in mitochondrial protein import.* J Biol Chem, 2008. **283**(7): p. 3799-807.
252. Schulz, C., A. Schendzielorz, and P. Rehling, *Unlocking the presequence import pathway.* Trends in Cell Biology, 2015. **25**(5): p. 265-275.
253. van der Laan, M., et al., *Motor-free mitochondrial presequence translocase drives membrane integration of preproteins.* Nat Cell Biol, 2007. **9**(10): p. 1152-9.
254. Kang, P.J., et al., *Requirement for hsp70 in the mitochondrial matrix for translocation and folding of precursor proteins.* Nature, 1990. **348**(6297): p. 137-43.
255. Horst, M., et al., *Sequential action of two hsp70 complexes during protein import into mitochondria.* Embo j, 1997. **16**(8): p. 1842-9.
256. Hawlitschek, G., et al., *Mitochondrial protein import: identification of processing peptidase and of PEP, a processing enhancing protein.* Cell, 1988. **53**(5): p. 795-806.
257. Gakh, O., P. Cavadini, and G. Isaya, *Mitochondrial processing peptidases.* Biochimica et Biophysica Acta (BBA) - Molecular Cell Research, 2002. **1592**(1): p. 63-77.
258. Chacinska, A., et al., *Essential role of Mia40 in import and assembly of mitochondrial intermembrane space proteins.* Embo j, 2004. **23**(19): p. 3735-46.
259. Naoé, M., et al., *Identification of Tim40 that mediates protein sorting to the mitochondrial intermembrane space.* J Biol Chem, 2004. **279**(46): p. 47815-21.
260. Mesecke, N., et al., *A Disulfide Relay System in the Intermembrane Space of Mitochondria that Mediates Protein Import.* Cell, 2005. **121**(7): p. 1059-1069.
261. Terziyska, N., et al., *Mia40, a novel factor for protein import into the intermembrane space of mitochondria is able to bind metal ions.* FEBS Lett, 2005. **579**(1): p. 179-84.
262. Allen, S., et al., *Erv1 mediates the Mia40-dependent protein import pathway and provides a functional link to the respiratory chain by shuttling electrons to cytochrome c.* J Mol Biol, 2005. **353**(5): p. 937-44.
263. Rissler, M., et al., *The essential mitochondrial protein Erv1 cooperates with Mia40 in biogenesis of intermembrane space proteins.* J Mol Biol, 2005. **353**(3): p. 485-92.
264. Mordas, A. and K. Tokatlidis, *The MIA Pathway: A Key Regulator of Mitochondrial Oxidative Protein Folding and Biogenesis.* Accounts of Chemical Research, 2015. **48**(8): p. 2191-2199.

265. Terziyska, N., et al., *Structural and functional roles of the conserved cysteine residues of the redox-regulated import receptor Mia40 in the intermembrane space of mitochondria.* J Biol Chem, 2009. **284**(3): p. 1353-63.
266. Banci, L., et al., *MIA40 is an oxidoreductase that catalyzes oxidative protein folding in mitochondria.* Nat Struct Mol Biol, 2009. **16**(2): p. 198-206.
267. Kawano, S., et al., *Structural basis of yeast Tim40/Mia40 as an oxidative translocator in the mitochondrial intermembrane space.* Proc Natl Acad Sci U S A, 2009. **106**(34): p. 14403-7.
268. Al-Habib, H. and M. Ashcroft, *CHCHD4 (MIA40) and the mitochondrial disulfide relay system.* Biochem Soc Trans, 2021. **49**(1): p. 17-27.
269. Sideris, D.P., et al., *A novel intermembrane space-targeting signal docks cysteines onto Mia40 during mitochondrial oxidative folding.* J Cell Biol, 2009. **187**(7): p. 1007-22.
270. Sideris, D.P. and K. Tokatlidis, *Oxidative folding of small Tims is mediated by site-specific docking onto Mia40 in the mitochondrial intermembrane space.* Mol Microbiol, 2007. **65**(5): p. 1360-73.
271. Milenkovic, D., et al., *Biogenesis of the Essential Tim9–Tim10 Chaperone Complex of Mitochondria: SITE-SPECIFIC RECOGNITION OF CYSTEINE RESIDUES BY THE INTERMEMBRANE SPACE RECEPTOR Mia40*.* Journal of Biological Chemistry, 2007. **282**(31): p. 22472-22480.
272. Bihlmaier, K., et al., *The disulfide relay system of mitochondria is connected to the respiratory chain.* J Cell Biol, 2007. **179**(3): p. 389-95.
273. Peker, E., et al., *Erv1 and Cytochrome c Mediate Rapid Electron Transfer via A Collision-Type Interaction.* Journal of Molecular Biology, 2021. **433**(15): p. 167045.
274. Hell, K., *The Erv1–Mia40 disulfide relay system in the intermembrane space of mitochondria.* Biochimica et Biophysica Acta (BBA) - Molecular Cell Research, 2008. **1783**(4): p. 601-609.
275. Zarges, C. and J. Riemer, *Oxidative protein folding in the intermembrane space of human mitochondria.* FEBS Open Bio. **n/a**(n/a).
276. Geldon, S., E. Fernández-Vizarra, and K. Tokatlidis, *Redox-Mediated Regulation of Mitochondrial Biogenesis, Dynamics, and Respiratory Chain Assembly in Yeast and Human Cells.* Frontiers in Cell and Developmental Biology, 2021. **9**.
277. Stojanovski, D., P. Bragoszewski, and A. Chacinska, *The MIA pathway: A tight bond between protein transport and oxidative folding in mitochondria.* Biochimica et Biophysica Acta (BBA) - Molecular Cell Research, 2012. **1823**(7): p. 1142-1150.
278. Finger, Y., et al., *Proteasomal degradation induced by DPP9 ‐ mediated processing competes with mitochondrial protein import.* The EMBO Journal, 2020. **39**(19): p. e103889.
279. Burkart, A., et al., *Adenylate Kinase 2 Links Mitochondrial Energy Metabolism to the Induction of the Unfolded Protein Response *.* Journal of Biological Chemistry, 2011. **286**(6): p. 4081-4089.
280. Klepinin, A., et al., *Adenylate Kinase and Metabolic Signaling in Cancer Cells.* Front Oncol, 2020. **10**: p. 660.
281. Meyer, K., et al., *Loss of apoptosis-inducing factor critically affects MIA40 function.* Cell Death Dis, 2015. **6**(7): p. e1814.
282. Hangen, E., et al., *Interaction between AIF and CHCHD4 Regulates Respiratory Chain Biogenesis.* Mol Cell, 2015. **58**(6): p. 1001-14.
283. Wischhof, L., et al., *AIFM1 beyond cell death: An overview of this OXPHOS-inducing factor in mitochondrial diseases.* EBioMedicine, 2022. **83**: p. 104231.
284. Reinhardt, C., et al., *AIF meets the CHCHD4/Mia40-dependent mitochondrial import pathway.* Biochimica et Biophysica Acta (BBA) - Molecular Basis of Disease, 2020. **1866**(6): p. 165746.
285. Salscheider, S.L., et al., *AIFM1 is a component of the mitochondrial disulfide relay that drives complex I assembly through efficient import of NDUFS5.* Embo j, 2022. **41**(17): p. e110784.
286. Murschall, L.M., et al., *The C-terminal region of the oxidoreductase MIA40 stabilizes its cytosolic precursor during mitochondrial import.* BMC Biology, 2020. **18**(1): p. 96.

287. Lorenzo, H.K. and S.A. Susin, *Mitochondrial effectors in caspase-independent cell death.* FEBS Lett, 2004. **557**(1-3): p. 14-20.
288. Susin, S.A., et al., *Molecular characterization of mitochondrial apoptosis-inducing factor.* Nature, 1999. **397**(6718): p. 441-446.
289. Otera, H., et al., *Export of mitochondrial AIF in response to proapoptotic stimuli depends on processing at the intermembrane space.* The EMBO Journal, 2005. **24**(7): p. 1375-1386-1386.
290. Yu, S.W., et al., *Outer mitochondrial membrane localization of apoptosis-inducing factor: mechanistic implications for release.* ASN Neuro, 2009. **1**(5).
291. Cao, G., et al., *Critical role of calpain I in mitochondrial release of apoptosis-inducing factor in ischemic neuronal injury.* J Neurosci, 2007. **27**(35): p. 9278-93.
292. Susin, S.A., et al., *Bcl-2 inhibits the mitochondrial release of an apoptogenic protease.* J Exp Med, 1996. **184**(4): p. 1331-41.
293. Zamzami, N., et al., *Mitochondrial control of nuclear apoptosis.* J Exp Med, 1996. **183**(4): p. 1533-44.
294. Polster, B.M., et al., *Calpain I induces cleavage and release of apoptosis-inducing factor from isolated mitochondria.* J Biol Chem, 2005. **280**(8): p. 6447-54.
295. Wang, Y., V.L. Dawson, and T.M. Dawson, *Poly(ADP-ribose) signals to mitochondrial AIF: a key event in parthanatos.* Exp Neurol, 2009. **218**(2): p. 193-202.
296. Hangen, E., et al., *Life with or without AIF.* Trends Biochem Sci, 2010. **35**(5): p. 278-87.
297. Lui, J.C.-K. and S.-K. Kong, *Heat shock protein 70 inhibits the nuclear import of apoptosis-inducing factor to avoid DNA fragmentation in TF-1 cells during erythropoiesis.* FEBS Letters, 2007. **581**(1): p. 109-117.
298. Shelar, S.B., et al., *Thioredoxin-dependent regulation of AIF-mediated DNA damage.* Free Radical Biology and Medicine, 2015. **87**: p. 125-136.
299. Maté, M.J., et al., *The crystal structure of the mouse apoptosis-inducing factor AIF.* Nat Struct Biol, 2002. **9**(6): p. 442-6.
300. Ye, H., et al., *DNA binding is required for the apoptogenic action of apoptosis inducing factor.* Nat Struct Biol, 2002. **9**(9): p. 680-4.
301. Parrish, J.Z. and D. Xue, *Functional genomic analysis of apoptotic DNA degradation in C. elegans.* Mol Cell, 2003. **11**(4): p. 987-96.
302. Candé, C., et al., *AIF and cyclophilin A cooperate in apoptosis-associated chromatinolysis.* Oncogene, 2004. **23**(8): p. 1514-21.
303. Artus, C., et al., *AIF promotes chromatinolysis and caspase-independent programmed necrosis by interacting with histone H2AX.* Embo j, 2010. **29**(9): p. 1585-99.
304. Joza, N., et al., *Essential role of the mitochondrial apoptosis-inducing factor in programmed cell death.* Nature, 2001. **410**(6828): p. 549-54.
305. Feraud, O., et al., *Cavitation of embryoid bodies requires optimal oxidative phosphorylation and AIF.* Cell Death & Differentiation, 2007. **14**(2): p. 385-387.
306. Qi, Y., et al., *Bnip3 and AIF cooperate to induce apoptosis and cavitation during epithelial morphogenesis.* J Cell Biol, 2012. **198**(1): p. 103-14.
307. Cheung, E.C.C., et al., *Dissociating the dual roles of apoptosis‐inducing factor in maintaining mitochondrial structure and apoptosis.* The EMBO Journal, 2006. **25**(17): p. 4061-4073-4073.
308. Norberg, E., S. Orrenius, and B. Zhivotovsky, *Mitochondrial regulation of cell death: processing of apoptosis-inducing factor (AIF).* Biochem Biophys Res Commun, 2010. **396**(1): p. 95-100.
309. Bénit, P., et al., *The variability of the harlequin mouse phenotype resembles that of human mitochondrial-complex I-deficiency syndromes.* PLoS One, 2008. **3**(9): p. e3208.
310. Brown, D., et al., *Loss of Aif function causes cell death in the mouse embryo, but the temporal progression of patterning is normal.* Proc Natl Acad Sci U S A, 2006. **103**(26): p. 9918-23.
311. Pospisilik, J.A., et al., *Targeted deletion of AIF decreases mitochondrial oxidative phosphorylation and protects from obesity and diabetes.* Cell, 2007. **131**(3): p. 476-91.

312. Vahsen, N., et al., *AIF deficiency compromises oxidative phosphorylation.* Embo j, 2004. **23**(23): p. 4679-89.
313. Bertan, F., et al., *Comparative analysis of CI- and CIV-containing respiratory supercomplexes at single-cell resolution.* Cell Reports Methods, 2021. **1**(1): p. 100002.
314. Klein, J.A., et al., *The harlequin mouse mutation downregulates apoptosis-inducing factor.* Nature, 2002. **419**(6905): p. 367-74.
315. Petrungaro, C., et al., *The Ca(2+)-Dependent Release of the Mia40-Induced MICU1-MICU2 Dimer from MCU Regulates Mitochondrial Ca(2+) Uptake.* Cell Metab, 2015. **22**(4): p. 721-33.
316. Miramar, M.D., et al., *NADH oxidase activity of mitochondrial apoptosis-inducing factor.* J Biol Chem, 2001. **276**(19): p. 16391-8.
317. Churbanova, I.Y. and I.F. Sevrioukova, *Redox-dependent changes in molecular properties of mitochondrial apoptosis-inducing factor.* J Biol Chem, 2008. **283**(9): p. 5622-31.
318. Romero, E., et al., *Same Substrate, Many Reactions: Oxygen Activation in Flavoenzymes.* Chemical Reviews, 2018. **118**(4): p. 1742-1769.
319. Massey, V., *Activation of molecular oxygen by flavins and flavoproteins.* Journal of Biological Chemistry, 1994. **269**(36): p. 22459-22462.
320. Sevrioukova, I.F., *Apoptosis-inducing factor: structure, function, and redox regulation.* Antioxid Redox Signal, 2011. **14**(12): p. 2545-79.
321. Medvedev, K.E., et al., *Functional analysis of Rossmann-like domains reveals convergent evolution of topology and reaction pathways.* PLoS Comput Biol, 2019. **15**(12): p. e1007569.
322. Rossmann, M.G. and P. Argos, *The taxonomy of binding sites in proteins.* Molecular and Cellular Biochemistry, 1978. **21**(3): p. 161-182.
323. Sevrioukova, I.F., *Redox-linked conformational dynamics in apoptosis-inducing factor.* J Mol Biol, 2009. **390**(5): p. 924-38.
324. Ferreira, P., et al., *Structural insights into the coenzyme mediated monomer-dimer transition of the pro-apoptotic apoptosis inducing factor.* Biochemistry, 2014. **53**(25): p. 4204-15.
325. Brosey, Chris A., et al., *Defining NADH-Driven Allostery Regulating Apoptosis-Inducing Factor.* Structure, 2016. **24**(12): p. 2067-2079.
326. Sorrentino, L., et al., *Key Role of the Adenylate Moiety and Integrity of the Adenylate-Binding Site for the NAD(+)/H Binding to Mitochondrial Apoptosis-Inducing Factor.* Biochemistry, 2015. **54**(47): p. 6996-7009.
327. Herrmann, J.M. and J. Riemer, *Apoptosis inducing factor and mitochondrial NADH dehydrogenases: redox-controlled gear boxes to switch between mitochondrial biogenesis and cell death.* 2021. **402**(3): p. 289-297.
328. Ferreira, P., et al., *Apoptosis-Inducing Factor 1, Mitochondrial*, in *Encyclopedia of Signaling Molecules*, S. Choi, Editor. 2016, Springer New York: New York, NY. p. 1-7.
329. Rinaldi, C., et al., *Cowchock Syndrome Is Associated with a Mutation in Apoptosis-Inducing Factor.* The American Journal of Human Genetics, 2012. **91**(6): p. 1095-1102.
330. Ghezzi, D., et al., *Severe X-linked mitochondrial encephalomyopathy associated with a mutation in apoptosis-inducing factor.* Am J Hum Genet, 2010. **86**(4): p. 639-49.
331. Berger, I., et al., *Early prenatal ventriculomegaly due to an AIFM1 mutation identified by linkage analysis and whole exome sequencing.* Mol Genet Metab, 2011. **104**(4): p. 517-20.
332. Zong, L., et al., *Mutations in apoptosis-inducing factor cause X-linked recessive auditory neuropathy spectrum disorder.* J Med Genet, 2015. **52**(8): p. 523-31.
333. Diodato, D., et al., *A novel AIFM1 mutation expands the phenotype to an infantile motor neuron disease.* Eur J Hum Genet, 2016. **24**(3): p. 463-6.
334. Fagnani, E., et al., *CHCHD4 binding affects the active site of apoptosis inducing factor (AIF): Structural determinants for allosteric regulation.* Structure, 2024. **32**(5): p. 594-602.e4.
335. Lavarone, E., C.M. Barbieri, and D. Pasini, *Dissecting the role of H3K27 acetylation and methylation in PRC2 mediated control of cellular identity.* Nature Communications, 2019. **10**(1): p. 1679.

336. Pasini, D., et al., *The polycomb group protein Suz12 is required for embryonic stem cell differentiation.* Mol Cell Biol, 2007. **27**(10): p. 3769-79.
337. Emsley, P., et al., *Features and development of Coot.* Acta Crystallogr D Biol Crystallogr, 2010. **66**(Pt 4): p. 486-501.
338. Liebschner, D., et al., *Macromolecular structure determination using X-rays, neutrons and electrons: recent developments in Phenix.* Acta Crystallogr D Struct Biol, 2019. **75**(Pt 10): p. 861-877.
339. Bepler, T., et al., *Positive-unlabeled convolutional neural networks for particle picking in cryo-electron micrographs.* Nat Methods, 2019. **16**(11): p. 1153-1160.
340. Meng, E.C., et al., *UCSF ChimeraX: Tools for structure building and analysis.* Protein Science, 2023. **32**(11): p. e4792.
341. Neuhold, J., et al., *GoldenBac: a simple, highly efficient, and widely applicable system for construction of multi-gene expression vectors for use with the baculovirus expression vector system.* BMC Biotechnol, 2020. **20**(1): p. 26.
342. Dyer, P.N., et al., *Reconstitution of nucleosome core particles from recombinant histones and DNA.* Methods Enzymol, 2004. **375**: p. 23-44.
343. Luger, K., T.J. Rechsteiner, and T.J. Richmond, *Preparation of nucleosome core particle from recombinant histones.* Methods Enzymol, 1999. **304**: p. 3-19.
344. Lowary, P.T. and J. Widom, *New DNA sequence rules for high affinity binding to histone octamer and sequence-directed nucleosome positioning.* J Mol Biol, 1998. **276**(1): p. 19-42.
345. Punjani, A., et al., *cryoSPARC: algorithms for rapid unsupervised cryo-EM structure determination.* Nature Methods, 2017. **14**(3): p. 290-+.
346. Rohou, A. and N. Grigorieff, *CTFFIND4: Fast and accurate defocus estimation from electron micrographs.* Journal of Structural Biology, 2015. **192**(2): p. 216-221.
347. Sanchez-Garcia, R., et al., *DeepEMhancer: a deep learning solution for cryo-EM volume post-processing.* Communications Biology, 2021. **4**(1): p. 874.
348. Goddard, T.D., et al., *UCSF ChimeraX: Meeting modern challenges in visualization and analysis.* Protein Sci, 2018. **27**(1): p. 14-25.
349. Williams, C.J., et al., *MolProbity: More and better reference data for improved all-atom structure validation.* Protein Sci, 2018. **27**(1): p. 293-315.
350. Bushnell, B., J. Rood, and E. Singer, *BBMerge - Accurate paired shotgun read merging via overlap.* Plos One, 2017. **12**(10).
351. Dobin, A., et al., *STAR: ultrafast universal RNA-seq aligner.* Bioinformatics, 2013. **29**(1): p. 15-21.
352. Li, H., et al., *The Sequence Alignment/Map format and SAMtools.* Bioinformatics, 2009. **25**(16): p. 2078-2079.
353. Anders, S., P.T. Pyl, and W. Huber, *HTSeq-a Python framework to work with high-throughput sequencing data.* Bioinformatics, 2015. **31**(2): p. 166-169.
354. Love, M.I., W. Huber, and S. Anders, *Moderated estimation of fold change and dispersion for RNA-seq data with DESeq2.* Genome Biology, 2014. **15**(12).
355. Grau, D., et al., *Structures of monomeric and dimeric PRC2:EZH1 reveal flexible modules involved in chromatin compaction.* Nature Communications, 2021. **12**(1).
356. Sauer, P.V., et al., *Activation of automethylated PRC2 by dimerization on chromatin.* Molecular Cell, 2024. **84**(20): p. 3885-3898.e8.
357. Huang, Y., et al., *Discovery of the Clinical Candidate MAK683: An EED-Directed, Allosteric, and Selective PRC2 Inhibitor for the Treatment of Advanced Malignancies.* Journal of Medicinal Chemistry, 2022. **65**(7): p. 5317-5333.
358. Qi, W., et al., *An allosteric PRC2 inhibitor targeting the H3K27me3 binding pocket of EED.* Nature Chemical Biology, 2017. **13**(4): p. 381-388.
359. Tate, J.G., et al., *COSMIC: the Catalogue Of Somatic Mutations In Cancer.* Nucleic Acids Research, 2018. **47**(D1): p. D941-D947.

360. Grossman, R.L., et al., *Toward a Shared Vision for Cancer Genomic Data.* N Engl J Med, 2016. **375**(12): p. 1109-12.
361. Yan, K.S., et al., *EZH2 in Cancer Progression and Potential Application in Cancer Therapy: A Friend or Foe?* Int J Mol Sci, 2017. **18**(6).
362. Pasini, D., et al., *JARID2 regulates binding of the Polycomb repressive complex 2 to target genes in ES cells.* Nature, 2010. **464**(7286): p. 306-10.
363. Leeb, M., et al., *Polycomb complexes act redundantly to repress genomic repeats and genes.* Genes Dev, 2010. **24**(3): p. 265-76.
364. Zhang, J., et al., *Retinoic Acid Induces Embryonic Stem Cell Differentiation by Altering Both Encoding RNA and microRNA Expression.* PLoS One, 2015. **10**(7): p. e0132566.
365. Li, Y., et al., *An optimized method for neuronal differentiation of embryonic stem cells in vitro.* Journal of Neuroscience Methods, 2020. **330**: p. 108486.
366. Rochette-Egly, C., *Retinoic acid signaling and mouse embryonic stem cell differentiation: Cross talk between genomic and non-genomic effects of RA.* Biochimica et Biophysica Acta (BBA) - Molecular and Cell Biology of Lipids, 2015. **1851**(1): p. 66-75.
367. Sutula, G.I., et al., *Inducible Ulk1 expression activates the p53 protein in mouse embryonic stem cells.* Biochemical and Biophysical Research Communications, 2020. **532**(2): p. 280-284.
368. Delacroix, L., et al., *Cell-Specific Interaction of Retinoic Acid Receptors with Target Genes in Mouse Embryonic Fibroblasts and Embryonic Stem Cells.* Molecular and Cellular Biology, 2010. **30**(1): p. 231-244.
369. Gil, J. and G. Peters, *Regulation of the INK4b-ARF-INK4a tumour suppressor locus: all for one or one for all.* Nat Rev Mol Cell Biol, 2006. **7**(9): p. 667-77.
370. Adhikari, A. and J.K. Davie, *The PRC2 complex directly regulates the cell cycle and controls proliferation in skeletal muscle.* Cell Cycle, 2020. **19**(18): p. 2373-2394.
371. Cookis, T., et al., *Structural basis for the inhibition of PRC2 by active transcription histone posttranslational modifications.* bioRxiv, 2024.
372. Lamichhane, R., et al., *Single-molecule FRET of protein-nucleic acid and protein-protein complexes: surface passivation and immobilization.* Methods, 2010. **52**(2): p. 192-200.
373. Zhuang, R., et al., *Purification of GFP fusion proteins with high purity and yield by monoclonal antibody-coupled affinity column chromatography.* Protein Expr Purif, 2008. **59**(1): p. 138-43.
374. Murayama, T. and T. Kobayashi, *Purification of Recombinant Proteins with a Multifunctional GFP Tag*, in *Protein Affinity Tags: Methods and Protocols*, R.J. Giannone and A.B. Dykstra, Editors. 2014, Springer New York: New York, NY. p. 151-161.
375. Bignon, C., A. Gruet, and S. Longhi, *Split-GFP Reassembly Assay: Strengths and Caveats from a Multiparametric Analysis.* Int J Mol Sci, 2022. **23**(21).
376. Koidl, S. and H.T.M. Timmers, *greenCUT&RUN: Efficient Genomic Profiling of GFP-Tagged Transcription Factors and Chromatin Regulators.* Curr Protoc, 2021. **1**(10): p. e266.
377. Fujimoto, S., S. Tashiro, and Y. Tamura, *Complementation Assay Using Fusion of Split-GFP and TurboID (CsFiND) Enables Simultaneous Visualization and Proximity Labeling of Organelle Contact Sites in Yeast.* Contact (Thousand Oaks), 2023. **6**: p. 25152564231153621.
378. Iglesias, N., et al., *Automethylation-induced conformational switch in Clr4 (Suv39h) maintains epigenetic stability.* Nature, 2018. **560**(7719): p. 504-508.
379. Newcombe, E.A., et al., *How phosphorylation impacts intrinsically disordered proteins and their function.* Essays Biochem, 2022. **66**(7): p. 901-913.
380. Nolen, B., S. Taylor, and G. Ghosh, *Regulation of Protein Kinases: Controlling Activity through Activation Segment Conformation.* Molecular Cell, 2004. **15**(5): p. 661-675.
381. Huse, M. and J. Kuriyan, *The Conformational Plasticity of Protein Kinases.* Cell, 2002. **109**(3): p. 275-282.

382. Landeira, D., et al., *Jarid2 is a PRC2 component in embryonic stem cells required for multi-lineage differentiation and recruitment of PRC1 and RNA Polymerase II to developmental regulators.* Nat Cell Biol, 2010. **12**(6): p. 618-24.
383. Chan, H.L. and L. Morey, *Emerging Roles for Polycomb-Group Proteins in Stem Cells and Cancer.* Trends in Biochemical Sciences, 2019. **44**(8): p. 688-700.
384. Cruz-Molina, S., et al., *PRC2 Facilitates the Regulatory Topology Required for Poised Enhancer Function during Pluripotent Stem Cell Differentiation.* Cell Stem Cell, 2017. **20**(5): p. 689-705.e9.
385. Xu, K., et al., *EZH2 oncogenic activity in castration-resistant prostate cancer cells is Polycomb-independent.* Science, 2012. **338**(6113): p. 1465-9.
386. Shi, B., et al., *Integration of estrogen and Wnt signaling circuits by the polycomb group protein EZH2 in breast cancer cells.* Mol Cell Biol, 2007. **27**(14): p. 5105-19.
387. Jung, H.Y., et al., *PAF and EZH2 induce Wnt/β-catenin signaling hyperactivation.* Mol Cell, 2013. **52**(2): p. 193-205.
388. Li, J., et al., *TRIM28 interacts with EZH2 and SWI/SNF to activate genes that promote mammosphere formation.* Oncogene, 2017. **36**(21): p. 2991-3001.
389. Miranda Furtado, C.L., et al., *Epidrugs: targeting epigenetic marks in cancer treatment.* Epigenetics, 2019. **14**(12): p. 1164-1176.
390. Schwalm, M.P., et al., *Tracking the PROTAC degradation pathway in living cells highlights the importance of ternary complex measurement for PROTAC optimization.* Cell Chem Biol, 2023. **30**(7): p. 753-765.e8.
391. Peng, X., et al., *Overview of epigenetic degraders based on PROTAC, molecular glue, and hydrophobic tagging technologies.* Acta Pharm Sin B, 2024. **14**(2): p. 533-578.
392. Bashore, F.M., et al., *PROTAC Linkerology Leads to an Optimized Bivalent Chemical Degrader of Polycomb Repressive Complex 2 (PRC2) Components.* ACS Chem Biol, 2023. **18**(3): p. 494-507.
393. Liu, Z., et al., *Design and Synthesis of EZH2-Based PROTACs to Degrade the PRC2 Complex for Targeting the Noncatalytic Activity of EZH2.* J Med Chem, 2021. **64**(5): p. 2829-2848.
394. Rothemann, R.A., et al., *Interaction with AK2A links AIFM1 to cellular energy metabolism.* bioRxiv, 2024: p. 2024.09.09.611957.
395. Schildhauer, F., et al., *An NADH-controlled gatekeeper of ATP synthase.* bioRxiv, 2024: p. 2024.08.22.609182.
396. Zivanov, J., et al., *New tools for automated high-resolution cryo-EM structure determination in RELION-3.* eLife, 2018. **7**: p. e42166.
397. Swapna, L.S., K. Srikeerthana, and N. Srinivasan, *Extent of structural asymmetry in homodimeric proteins: prevalence and relevance.* PLoS One, 2012. **7**(5): p. e36688.

15. APPENDIX

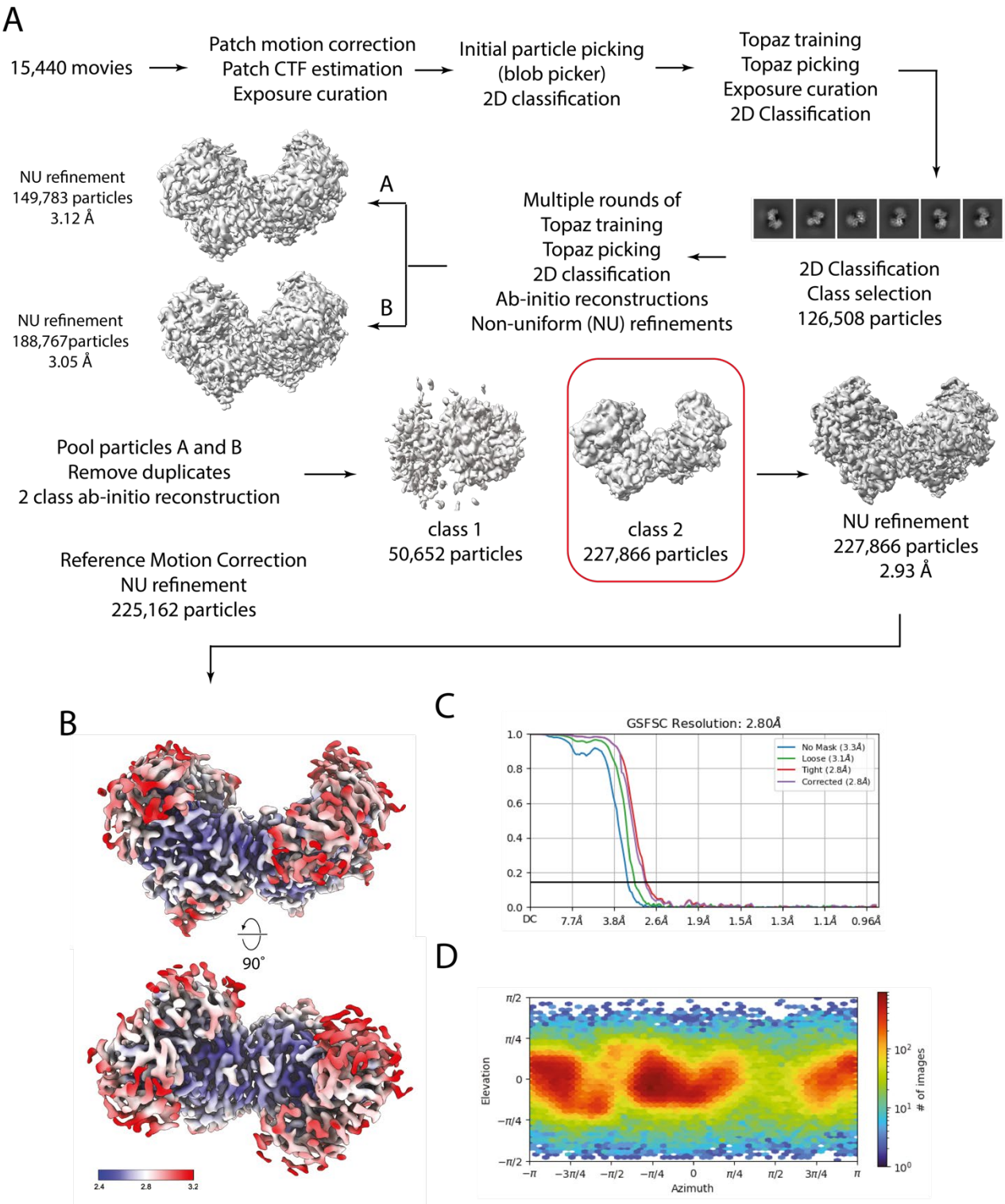

Supplementary Figure 1: Cryo-EM data processing workflow used to obtain the AIFM1 dimer

A. *For preprocessing the movies were subjected to patch-based motion correction and CTF estimation. Initial particles were selected via blob picking, subjected to 2D classification and suitable 2D classes used for TOPAZ training. Particles were further refined by splitting into high- and low-defocus groups for additional TOPAZ training. Particles from two resulting 3D refinements were pooled and subjected to iterative cycles of TOPAZ picking, 2D classification, and ab initio reconstruction resulting in high-quality reconstructions, followed by non-uniform refinement.* ***B.*** *Local resolution map of the AIFM1 dimer ranging from 2.4-3.2 Å.* ***C.*** *Global resolution of 2.8 Å was determined by FSC cut-off at 0.143.* ***D.*** *Euler angle distribution of the AIFM1 dimer.*

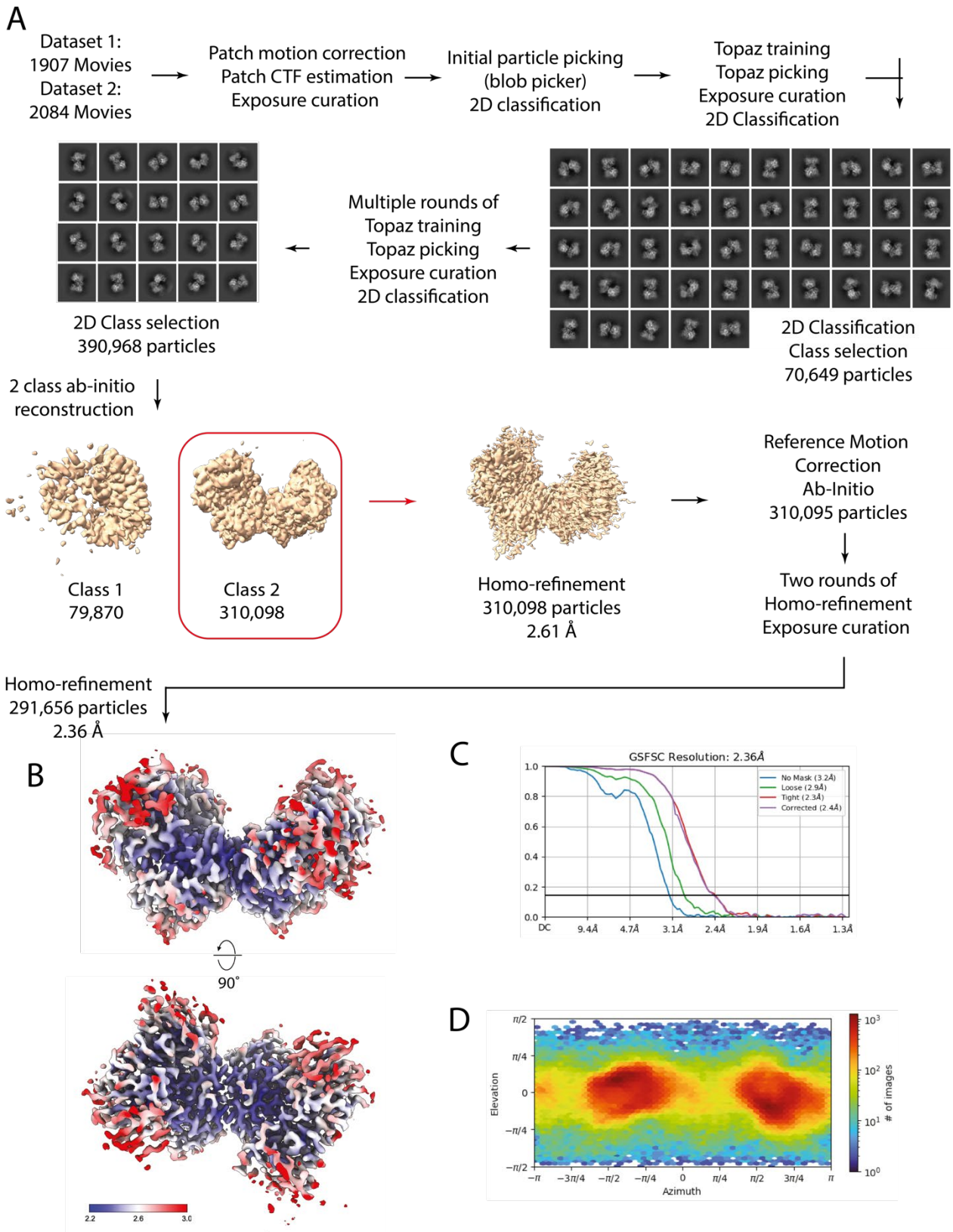

Supplementary Figure 2: Cryo-EM data processing workflow used to obtain AIFM1-MiA40

A. *For preprocessing the movies were subjected to patch-based motion correction and CTF estimation. Initial particles were obtained via blob picking, subjected to 2D classification and suitable 2D classes used for TOPAZ training. Particles were further refined by splitting into high- and low-defocus groups for additional TOPAZ training. Iterative cycles of TOPAZ picking, 2D classification, and ab initio reconstruction resulted in high-quality reconstructions, followed by homogenous refinement.* ***B.*** *Local resolution map of the AIFM1-MIA40 complex ranging from 2.2-3.0 Å.* ***C.*** *Global resolution of 2.8 Å was determined by FSC cut-off at 0.143.* ***D.*** *Euler angle distribution of the AIFM1-MIA40 complex.*

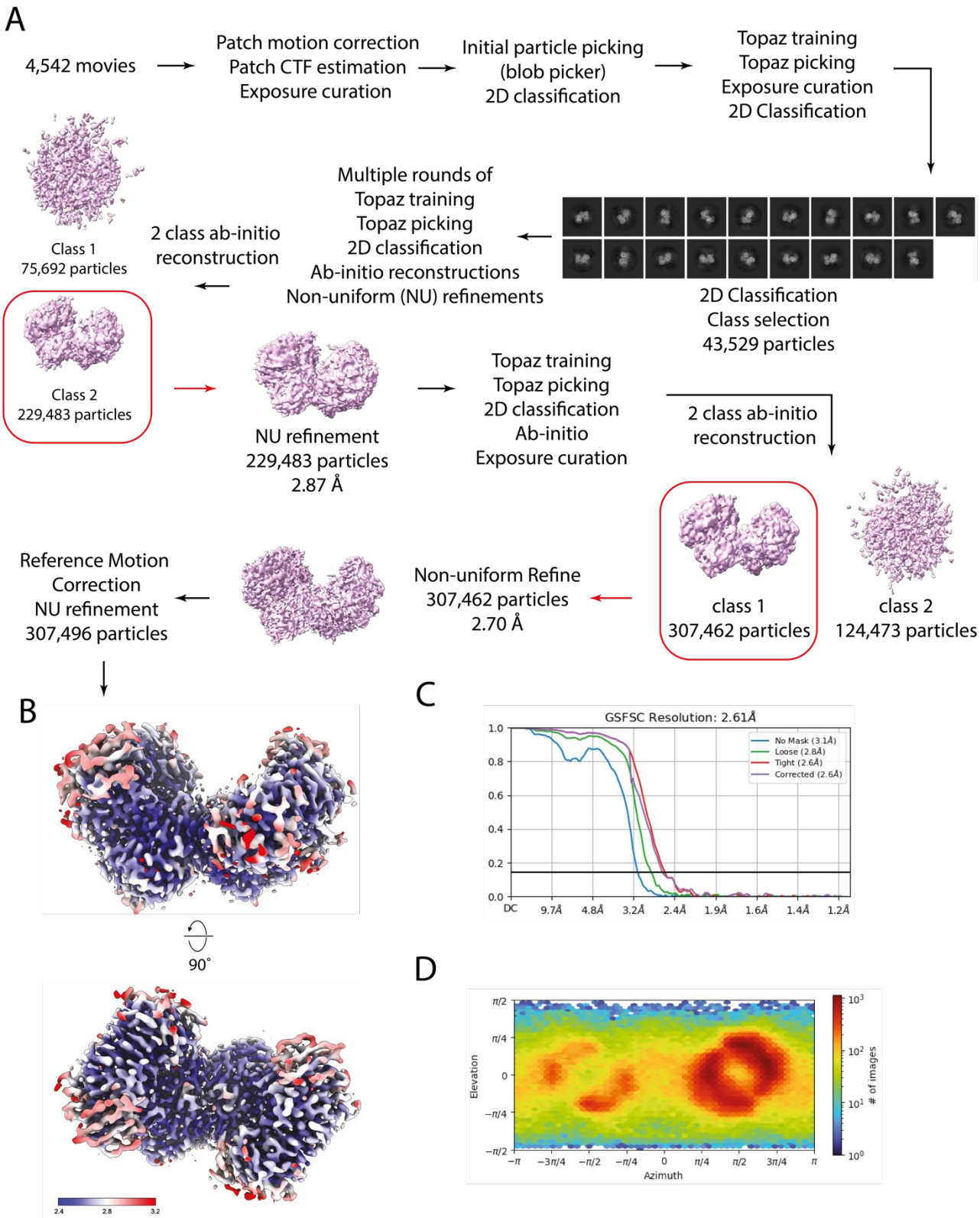

Supplementary Figure 3: Cryo-EM data processing workflow used to obtain AIFM1-AK2A

A. *For preprocessing the movies were subjected to patch-based motion correction and CTF estimation. Initial particles were obtained via blob picking, subjected to 2D classification and suitable 2D classes used for TOPAZ training. Particles were further refined by splitting into high- and low-defocus groups for additional TOPAZ training. Iterative cycles of TOPAZ picking, 2D classification, and ab initio reconstruction resulted in high-quality reconstructions, followed by non-uniform refinement.* ***B.*** *Local resolution map of the AIFM1-AK2A complex ranging from 2.4-3.3 Å.* ***C.*** *Global resolution of 2.8 Å was determined by FSC cut-off at 0.143.* ***D.*** *Euler angle distribution of the AIFM1-AK2A complex.*

Table 7: Data collection and validation reports of the AIFM1 complexes

	AIFM1 dimer	**AIFM-AK2**	**AIFM1-MIA40**
Data Collection and Processing			
Microscope	Titan Krios G4i	Titan Krios G4i	Titan Krios G3i
Voltage (keV)	300	300	300
Magnification	120,000	120,000	120,000
Pixel size at detector (Å/pixel)	0.46	0.58	0.654
Total electron exposure (e^{-} /Å^2)	50	50	50.82/50.57
Number of frames	468	468	48
Defocus range (μm)	0.7-1.7	0.7-1.7	0.6-2.6
Automation software	EPU	EPU	EPU
Energy filter	Selectris	Selectris	-
Micrographs collected (no.)	15,440	4542	1907/2084
For each reconstruction:			
Final particles (no.)	227,866	307,496	291,656
Space group	P1	P1	P1
Map sharpening B factor (Å2)	124.9	97.7	88.2
Resolution (global, Å)			
FSC 0.5 (unmasked/masked)	3.1/2.91	2.87/2.72	2.98/2.68
FSC 0.143 (unmasked/masked)	2.79/2.75	2.6/2.56	2.37/2.34
FSC 0 (unmasked/masked)	2.76/2.72	2.57/2.54	2.34/2.3
Model composition			
Chains	5	7	7
Atoms	7068 (Hydrogens: 0)	7224 (Hydrogens: 0)	7336 (Hydrogens: 0)
Residues	Protein: 887 Nucleotide: 0	Protein: 905 Nucleotide: 0	Protein: 915 Nucleotide: 0
Water	12	24	17
Ligands	FAD: 2	FAD: 2	FAD: 2
	NAD: 2	NAD: 2	NAD: 2

Model Refinement			
Bonds (RMSD)			
Length (Å) (# > 4σ)	0.005 (0)	0.003 (0)	0.002 (0)
Angles (°) (# > 4σ)	0.591 (0)	0.527 (0)	0.499 (0)
MolProbity score	1.50	1.48	1.61
Clash score	4.39	4.30	6.35
Ramachandran plot (%)			
Outliers	0.00	0.00	0.00
Allowed	4.10	3.92	3.88
Favored	95.90	96.08	96.12
Rama-Z (Ramachandran plot Z-score RMSD)			
whole (N = 893)	-0.40 (0.28)	-0.17 (0.28)	0.40 (0.28)
helix (N = 247)	1.35 (0.35)	1.16 (0.35)	1.78 (0.34)
sheet (N = 214)	-0.33 (0.36)	0.63 (0.35)	0.09 (0.34)
loop (N = 432)	-1.00 (0.29)	-1.30 (0.27)	-0.42 (0.30)
Rotamer outliers (%)	0.28	0.00	0.00
Cβ outliers (%)	NA	NA	NA
Peptide plane (%)			
Cis proline/general	0.0/0.0	0.0/0.0	0.0/0.0
Twisted proline/general	0.0/0.0	0.0/0.0	0.0/0.0
CaBLAM outliers (%)	2.18	1.70	2.02
ADP (B-factors)			
Iso/Aniso (#)	7068/0	7224/0	7336/0
min/max/mean			
Protein	9.09/132.73/63.11	6.14/105.04/36.33	22.79/135.12/64.32
Nucleotide	---	---	---
Ligand	18.37/80.80/37.07	8.74/40.20/21.01	31.78/68.66/46.21
Water	18.05/53.20/30.17	12.12/31.41/19.63	30.22/58.08/46.41
Occupancy			
Mean	1.00	1.00	1.00
occ = 1 (%)	100.00	100.00	100.00
0 < occ < 1 (%)	0.00	0.00	0.00
occ > 1 (%)	0.00	0.00	0.00

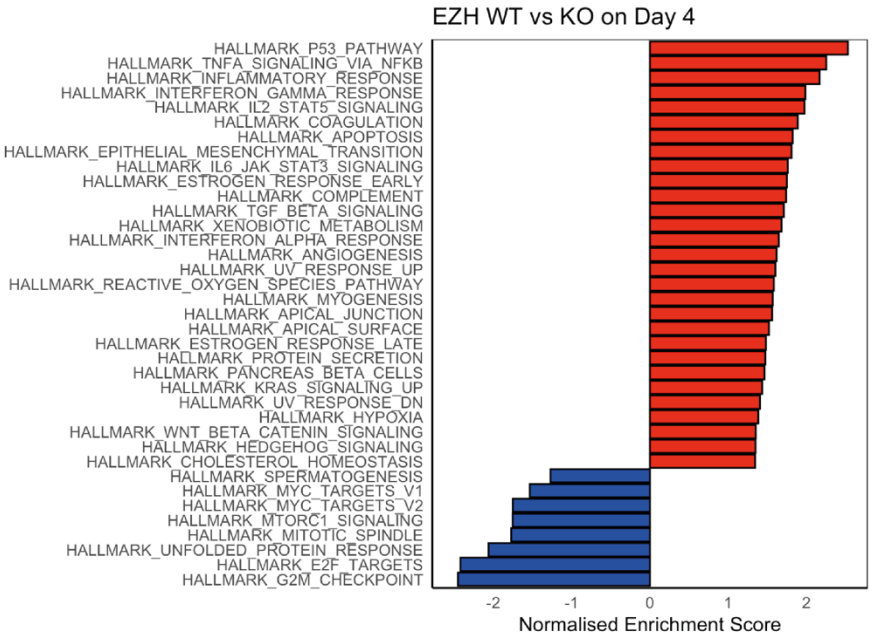

Supplementary Figure 4: GSEA of EZH1/2 KO to the WT cells

GSEA of EZH1/2 KO mESCs compared to the WT cells reveals 29 enriched (red) and 8 depleted pathways (blue).

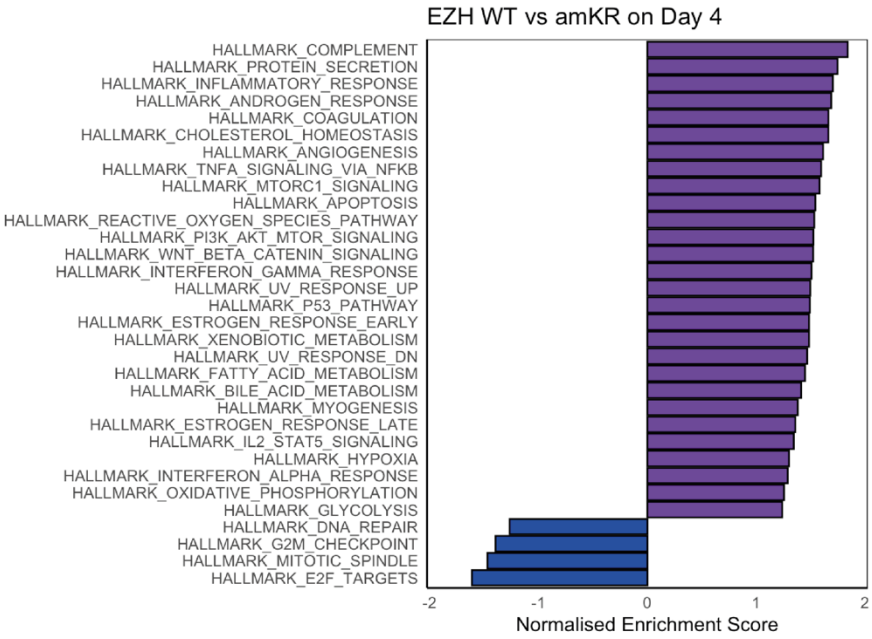

Supplementary Figure 5: GSEA of EZH2amKR compared to the WT cells

GSEA of EZH2^{amKR} compared to the WT show 28 enriched (purple) and 4 depleted pathways (blue).

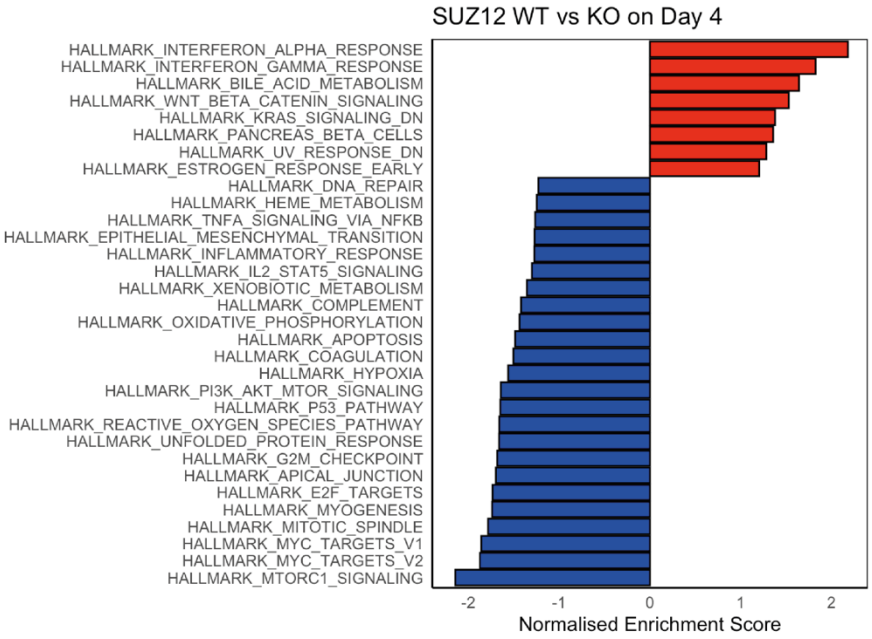

Supplementary Figure 6: Comparison GSEA of SUZ12 KO to the WT cells

GSEA of SUZ12 KO cells compared to the WT mESCs reveal 8 entiched (red) and 24 depleted pathways (blue).

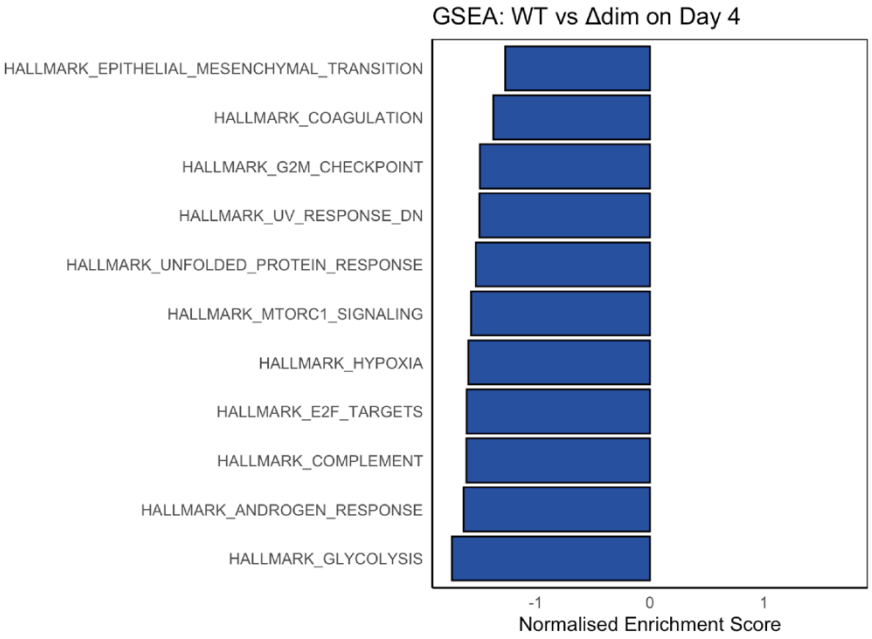

Supplementary Figure 7: Comparison GSEA of SUZ12$^{\Delta dim}$ to the WT rescued cell

GSEA comparison of SUZ12$^{\Delta dim}$ compared to WT rescue cells show 11 depleted pathways (blue).